Lehrstuhl für Netzwerktheorie und Signalverarbeitung

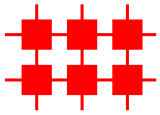

Forschungsberichte

Herausgeber: Prof. Dr. techn. Dr. h.c. Josef A. Nossek

Bernhard Lehmeyer

Receiver and Transmitter Topologies

Institute for Circuit Theory and Signal Processing
Munich University of Technology

Receiver and Transmitter Topologies

Bernhard Lehmeyer

Vollständiger Abdruck der von der Fakultät für Elektrotechnik und Informationstechnik der Technischen Universität München zur Erlangung des akademischen Grades eines

Doktor-Ingenieurs

genehmigten Dissertation.

Vorsitzender: Prof. Dr.-Ing. Josef Kindersberger
Prüfer der Dissertation:

1. Prof. Dr. techn. Dr. h.c. Josef A. Nossek
2. Prof. Dr.-Ing. Berthold Lankl

Die Dissertation wurde am 10.7.2018 bei der Technischen Universität München eingereicht und durch die Fakultät für Elektrotechnik und Informationstechnik am 7.8.2018 angenommen.

Contents

Acknowledgements

On 19 October 2005 at semester beginning I joined the very first lecture as a enrolled student of this university. The Professor there had a brilliant lecture style and told us about Ludwig Boltzmann and his motto: „Nothing is more practical than a good theory “. When looking at the lecture notes he cited Alexander Friedrich Ladislaus Roda Roda: „Aus einem Buch abschreiben: ein Plagiat. Aus zwei Büchern abschreiben: ein Essay. Aus drei Büchern abschreiben: eine Doktordissertation. Aus vier Büchern abschreiben: ein fünftes gelehrtes Buch.“ The years went by so fast and now I am writing the last part of this thesis, thinking how it all began. Back in 2012 Univ.-Prof. Dr. techn. Dr. h.c. Josef A. Nossek offered me a position as a research engineer and teaching assistant at his renown Institute for Circuit Theory and Signal Processing at Technical University of Munich. During many years he contributed as great teacher and brilliant supervisor of my doctoral thesis in many ways to my work of the past years. He always had time and an open door for me at the institute and to develop this thesis. His way of asking the right questions at the right time and his ability to create a working environment and atmosphere always motivated me. Besides for technical problems he had an open ear for any kind of problem, too. Without his commitment and professional attitude this doctoral thesis would not have been possible. I would like to thank Univ.-Prof. Dr. techn. Dr. h.c. Josef A. Nossek and PD. Dr.-Ing Michel T. Ivrlač for supervising my Ph.D. thesis and taking their time to guide and support me throughout the duration of this work. They always made it possible to share and discuss ideas and problems. Furthermore, they showed a lot of patience when proofreading my research papers. I would like to express my gratitude to Univ.-Prof. Dr.-Ing Berthold Lankl for the opportunity to work in his group and his encouragement and support. I thank also Prof. Dr.-Ing. habil. Markus Becherer, Prof. Dr. techn. Dr. h.c. Peter Russer, PD Dr. habil. Johannes Russer, Dr.-Ing. Christian Hofmann, Dr.-Ing. Amine Mezghani, Dr.-Ing. Hans Brunner and Dr.-Ing. Israa Slim and M.Sc. Michael Haider for all our discussions on several subjects and their interest in my work. I like to thank Dr.-Ing. Rainer Pauli, Dr.-Ing. Manfred Gloger and Univ.-Prof. Dr.-Ing. Walter Entenmann for the long fruitful discussions about the history of electrical engineering. It really helped me understanding how new ideas and inventions have been generated. During the time when I was working towards the doctoral degree, I had the pleasure to meet a variety of collegues and friends. I want to thank all of them for making my life more colorful. I also want to thank the non-academic staff, especially Elizabeth Soeder, Lida Barth, Hartmut Peters, Sergey Fedorov and Ali Yilmazcan. Johannes Bastl, who now is doctoral candidate at RWTH Aachen contributed to this

thesis as master student. I would like to thank him for his patience with my special ideas and the late night discussions.

It is impossible to put in words how much I owe my parents. I am so grateful for all that they did for me and I thank them in every possible way. Their kindness, love and selflessness have always matured me throughout my life. Last but not least, I want to thank my family, especially my mother, my father my sister and my girlfriend Annika, for having supported me throughout my studies and for having been always by my side.

Munich, March 2018

Bernhard Lehmeyer

1. Introduction

1.0.1 Mile Stones in Research

With the beginning of the 20th century, the commercial use of wireless telegraphy started. The theory was funded by James Clerk Maxwell (13 June 1831-5 November 1879), a Scottish scientist [1] in the field of mathematical physics [2]. In his work from 1865 [3] Maxwell derives an electromagnetic wave equation with a velocity for light in close agreement with measurements made by following experiments, deducing that light is an electromagnetic wave. „A Treatise on Electricity and Magnetism" [4] his fundamental work published and written in 1873, introduced the use of vector fields, and his labels have been perpetuated. It was Heinrich Rudolf Hertz [5], who finally succeed in 1886 in proofing the existence of electromagnetic waves in experiments between 1885 and 1889. Therefore, first antennas were built by Hertz in 1888. As transmitter served a Hertzian dipole with spark gap, alternating current (AC) decoupled by inductors from a supply battery. The spark itself has a partial negative resistance, which deattenuates the connected dipole, and makes it oscillating. As a receiver he generally preferred a resonator of circular, square, or octagonal form, with a spark gap. The gap could be adjusted by a micrometer and observed by lenses or a microscope. Care was taken that the oscillator and the corresponding resonators should precisely be tuned to the same frequency. For the first time a signal was transmitted and received in the lecture room at *Physikalisches Institut at Karlsruhe*. While Guglielmo Marconi at the beginning optimized his transmitters in an empirical way, Karl Ferdinand Braun was the first one to obtain well calculated power matching by introducing a matching transformer. Since that time, lots of inventions and research activities have improved receiver and transmitters for efficiency, power consumption, device life time and data throughput. A big milestone in wireless communication was the invention of the electron valve. This invention evolved in three stages. The first step was the invention of the incandescent light bulb by Thomas Alva Edison in 1879. Unfortunately, the glass of these early bulbs turned black after several hours of use. An additional electrode should prevent this effect by catching the disposed metal atoms, what finally led to John Ambrose Fleming's invention of the vacuum electron diode, called thermoionic valve in 1904. The third step was the introduction of a control grid by Lee de Forest in 1906. The grid Audion, later called triode, was the first device to amplify, albeit only slightly, the strength of received radio signals. In 1928 Hans Rukop wrote in his booklet „25 Jahre Telefunken" [6] about wireless telegraphy as an extremely fast moving business due to its gradient of rapid research. A new age began with the invention of the field effect transistor by Julius Edgar Lilienfeld in 1925 [7] and the invention of the bipolar transistor in

the winter of 1947 by John Bardeen, William Shockley and Walter Brattain at Bell Labs [8][9]. The extremely reduced size compared to electron tubes which led to an integration of large numbers of tiny transistors into a small chip results in circuits that are orders of magnitude smaller, cheaper, and faster than those constructed of discrete electronic components. Also in 1947, Bell Labs was the first to propose a cellular radio telephone network. The primary innovation was the development of a network of small overlapping cell sites supported by a call switching infrastructure that tracks users as they move through a network and passes their calls from one site to another without dropping the connection. Not all inventions and great researchers of the past could be mentioned in this short summary. Research in mobile communication is going on all over the world, there are still bottlenecks to be removed and limits to be pushed to a higher level. This work shows just a few aspects of actual research.

1.0.2 Modern Research

Nowadays, some of the main hardware bottlenecks for the data throughput in a modern mobile communication system are:

- the power efficiency of the transmit amplifier
- decoupling and matching of the antenna array
- the noise floor and dynamic range of the receiver frontend

Today, each smart device is microprocessor controlled. Whenever a digital signal processor (DSP) is available, it will be used for compressing and modulation purposes. Behind a digital to analog converter (DAC) for the transmit case or analog to digital converter (ADC) in the receive case, the world is analog. This thesis deals with the analog parts of a transceiver system. A block diagram will help identifying the signal path according to the order of the chapters. Fig. 1.1 shows a transmitter and a receiver block diagram. The digital signal is fed to a DSP unit, a DAC feeds the processed analog signal to a power amplifier (PA), where the output filter obtains antenna power matching. In the case of multiple signal chains in combination with a transmit antenna array, the band pass filter would additionally decouple the antenna elements, chapter 3. The same appeals to antenna and input filter of the receiver. But here a special way of matching should be chosen as shown in chapter 5. For optimizing the following low noise amplifier, a precise knowledge of the noise parameters is elementary. Therefore a novel measurement method is shown in chapter 6. For a higher power efficiency factor, due to economical reasons, a highly efficient transmit amplifier is essential, chapter 2 and beam forming should be obtained e.g. by a Butler matrix circuit in chapter 4. At the end, the summary, chapter 7, shows what was achieved.

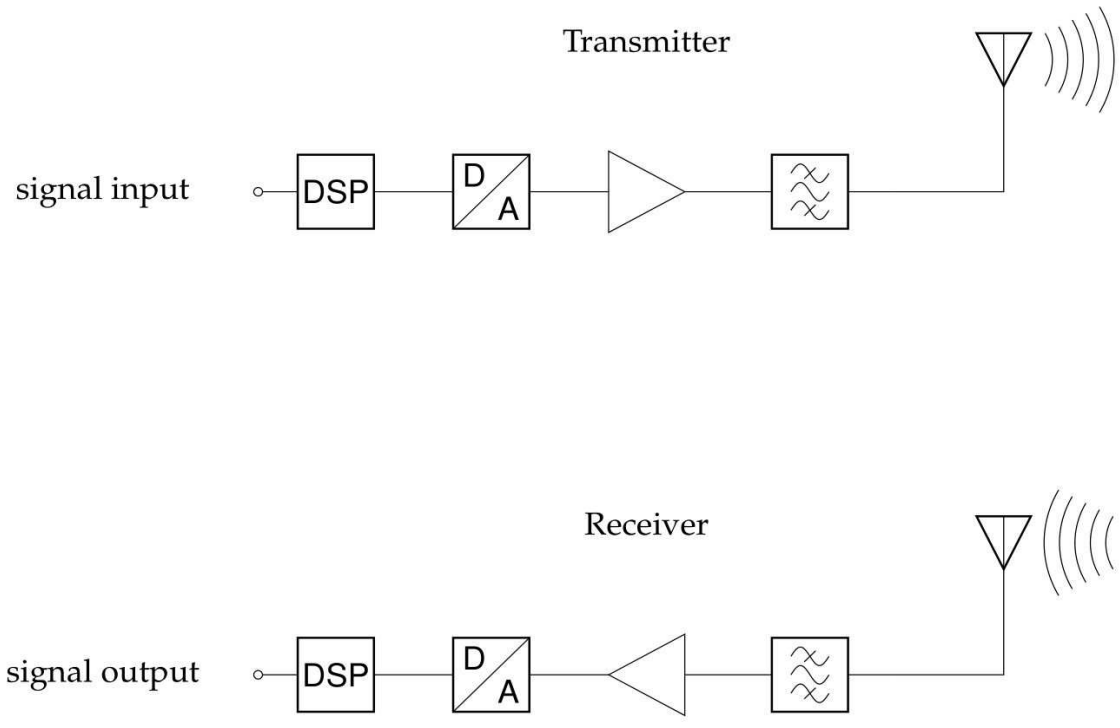

Fig. 1.1. Transmitter and receiver block diagram

2. Amplifier Concepts

2.1 Introduction

THERE are at least ten lettered classes of radio frequency (RF) power amplifiers [10] and several combinations of those classes. This complexity is funded by the different possible operating modes of transistors. In one time interval a transistor can act as controlled resistor, high resistance current source, low resistance switch or as voltage controlled capacitor. These modes of operation can be combined within a period, leading to different amplifier classes.

2.1.1 Classical Concepts from A through F

Widely established concepts from A to F including combinations of those classes are discussed and analyzed. For each class an implementation has been simulated and the efficiency was calculated out of the operating parameters. The classes are split into two groups: the linear amplifiers, class A through B and the switching mode amplifiers, class C through F. Finally, the findings out of these considerations led to a new invention.

2.1.2 Class M

In this part of the chapter, a recently patented switched mode amplifier topology for RF purposes is considered. For this new concept only one externally controlled switching element is necessary, while the second element obtains self controlled switching. Therefore, the typical problems of push-pull operation will not occur. Energy of not required harmonics can be recycled and fed back to the power supply unit itself. Both amplifier and energy recycling circuit are discussed, implemented and simulated.

2.2 Class A Concept

According to the established definition, the linear amplifier classes from A to B are considered to be working with a sinusoidal excitation. In a class A amplifier the amplifying device usually is a single transistor, e.g. field effect transistor (FET) or bipolar transistor, which is conducting for the whole period, that is $0° - 360°$. Class A with operating resistor is the oldest amplifier topology, its efficiency of $\eta_A < 25\%$ the lowest.

2.2.1 Mathematical Analysis

For analysis, a simple class A amplifier, Fig 2.1, with signal source v_{sig}, supply voltage V_{B} and the operating resistor R is considered. As amplifying element an n-channel metall oxide field effect transistor (MOS-FET), optimized for a big linear operating area is used. The operating point diagram, Fig 2.2 shows the characteristics of the Helmholtz Thevenin source circuit, connected to drain and source of the transistor. The ideal point of operation (OP) is located at the middle of the characteristic transfer curve, where the current is I_{OP}, while the voltage is V_{OP}.

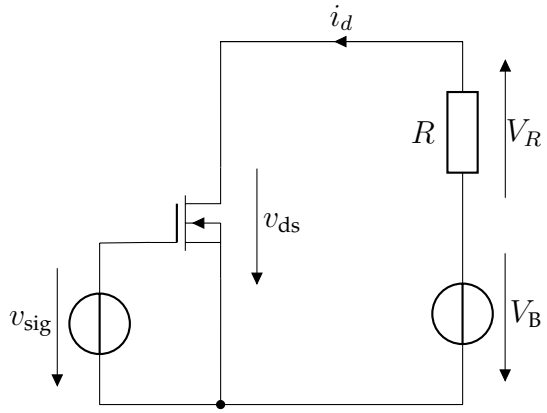

Fig. 2.1. Class A amplifier

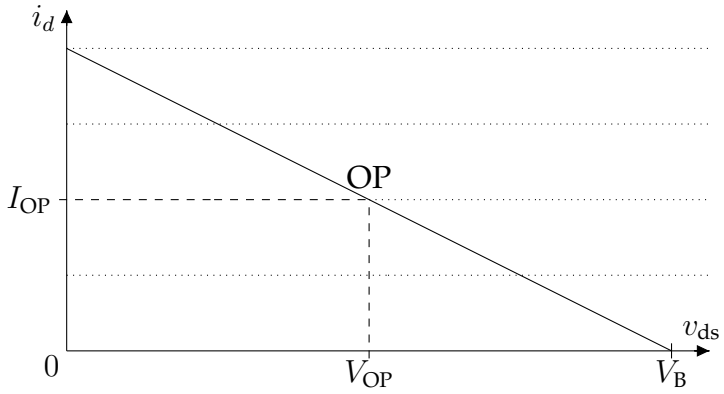

Fig. 2.2. Operating point diagram, class A

For a sinusoidal excitation $i_{\text{d}}(t)$ and v_{ds} are defined in the following way:

$$i_{\text{d}}(t) = I_{\text{OP}}(1 + \sin \omega t) \tag{2.1}$$

The point of operation is:

$$v_{\text{ds}} = V_{\text{OP}}(1 - \sin \omega t) \tag{2.2}$$

$$V_{\text{OP}} = \frac{1}{2} V_{\text{B}} = I_{\text{OP}} \cdot R \tag{2.3}$$

Therefore, the dissipated power of the transistor P_T is:

$$\begin{aligned} P_\mathrm{T} &= \frac{1}{\mathrm{T}}\int_0^\mathrm{T} i_\mathrm{d}(t)v_\mathrm{ds}(t)\mathrm{d}t = \frac{V_\mathrm{B}^2}{4R}\cdot\frac{1}{\mathrm{T}}\int_0^\mathrm{T}(1-\sin^2\omega t)\mathrm{d}t \\ &= \frac{V_\mathrm{B}^2}{4R\mathrm{T}}\int_0^\mathrm{T}(1-\frac{1}{2}(1-\cos 2\omega t))\mathrm{d}t = \frac{V_\mathrm{B}^2}{4R}\cdot\frac{1}{\mathrm{T}}\cdot\frac{\mathrm{T}}{2} = \frac{V_\mathrm{B}^2}{8R} \end{aligned} \tag{2.4}$$

The power supplied by the source P_B is:

$$P_\mathrm{B} = \frac{1}{\mathrm{T}}\int_0^\mathrm{T} i_d(t)V_\mathrm{B}\mathrm{d}t = \frac{V_\mathrm{B}^2}{2R\mathrm{T}}\int_0^\mathrm{T}(1+\sin\omega t)\mathrm{d}t = \frac{V_\mathrm{B}^2}{2R}. \tag{2.5}$$

The power P_R transformed into heat by the resistor

$$\begin{aligned} P_\mathrm{R} &= \frac{1}{\mathrm{T}}\int_0^\mathrm{T} i_\mathrm{d}^2(t)R\,\mathrm{d}t = \frac{V_\mathrm{B}^2}{4R\mathrm{T}}\int_0^\mathrm{T}(1+\sin\omega t)^2\mathrm{d}t \\ &= \frac{V_\mathrm{B}^2}{4R\mathrm{T}}\int_0^T(1+2\sin\omega t+\sin^2\omega t)\,\mathrm{d}t = 3\frac{V_\mathrm{B}^2}{8R}. \end{aligned} \tag{2.6}$$

P_DC is the DC component, transformed into heat, P_T is dissipated by the transistor, P_AC is the desired output power

$$P_\mathrm{R} = P_\mathrm{DC} + P_\mathrm{AC} = \frac{V_\mathrm{B}^2}{4R} + \frac{V_\mathrm{B}^2}{8R}. \tag{2.7}$$

$$P_\mathrm{DC} + P_\mathrm{AC} + P_\mathrm{T} = P_\mathrm{R} + P_\mathrm{T} = P_\mathrm{B} \tag{2.8}$$

So, the efficiency η is calculated to

$$\eta = \frac{P_\mathrm{AC}}{P_\mathrm{B}} = \frac{1}{4} \mathrel{\hat{=}} 25\%. \tag{2.9}$$

2.2.2 Class A design example

In a typical broadband design, often used in preamplifiers or as general purpose driver stage, an operating resistor is used, Fig. 2.3. The output is DC protected as in most amplifiers, so half the AC power will be dissipated in the operating resistor and $\eta_\mathrm{max} = 12.5\%$. A further problem is caused by the non linear transfer curve of the transistor. For a low distortion only a part of the transfer curve of Fig. 2.2 can be used.

The circuit is simple, distortion is low and its efficiency is very bad, Fig 2.4 shows the small output current i_AR and the much higher collector current i_AT.

Fig. 2.5 shows v_AN, the collector voltage and v_AR, the output voltage over the load resistor.

2.2.3 Class A with Transformer

Operating point adjustment calculations of the previously discussed narrow band amplifier apply to the topology with output transformer as well, Fig. 2.6. This kind of circuit is found as intermediate frequency (IF) stage in receivers, or as audio power stage in tube circuits, where the transformer usually is the bandwidth limiting device.

In this case the efficiency is 50%, also.

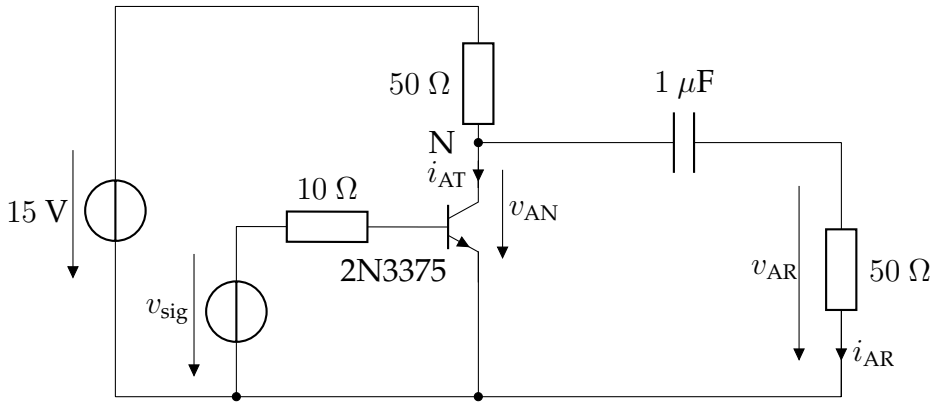

Fig. 2.3. Class A amplifier

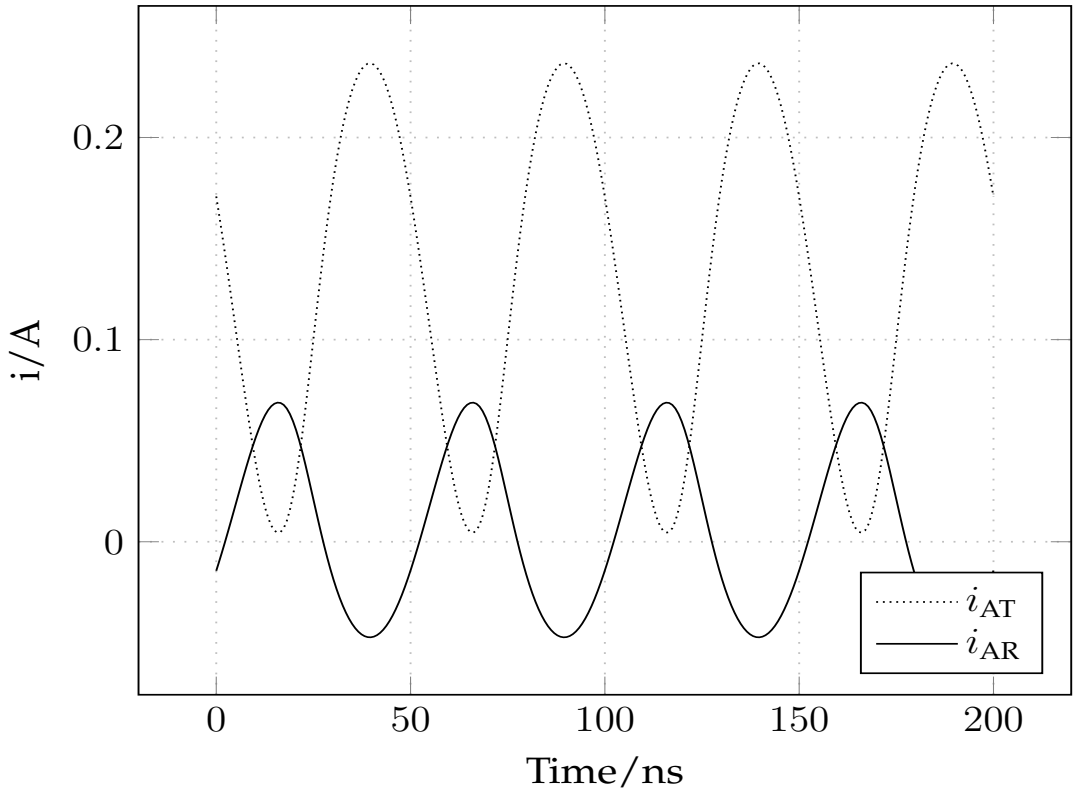

Fig. 2.4. The currents at the class A amplifier

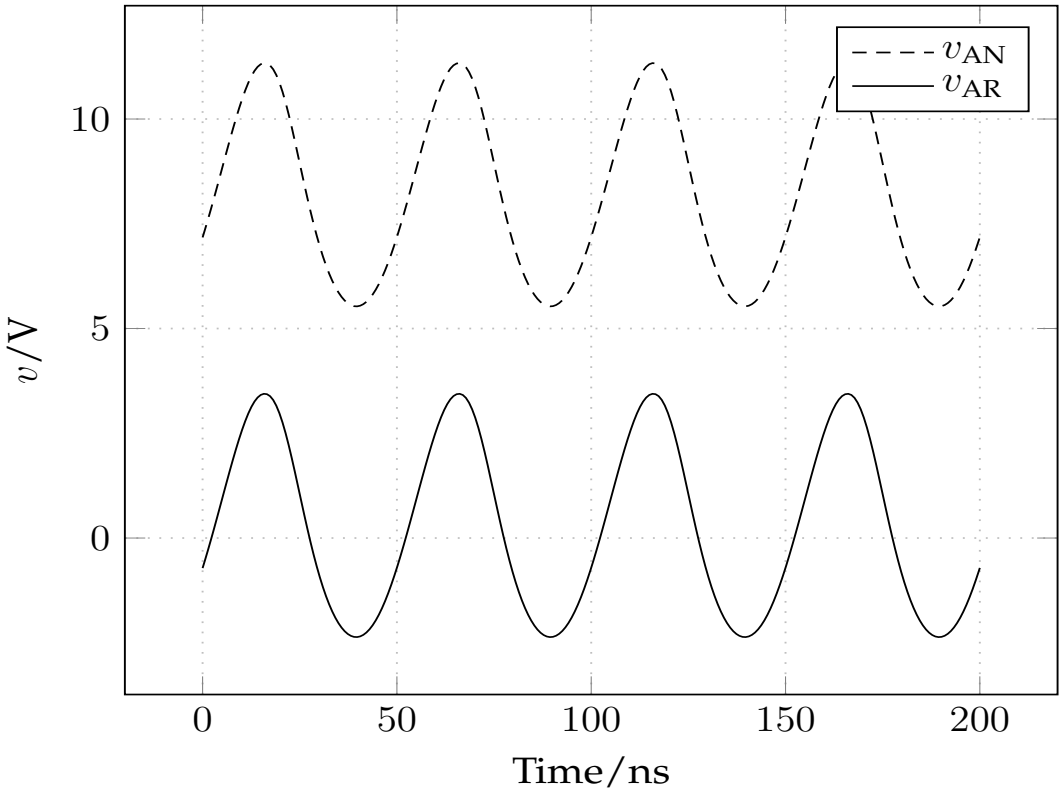

Fig. 2.5. Class A amplifier, voltages.

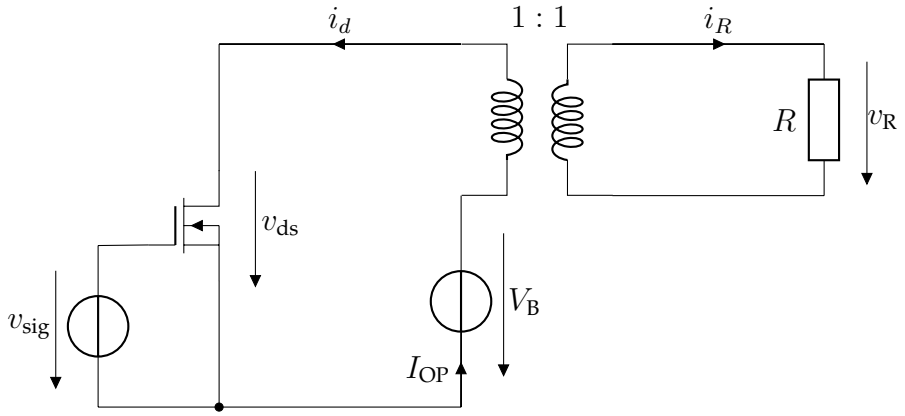

Fig. 2.6. Class A amplifier with transformer

2.2.4 Class A_L with Inductive Supply Coupling

In many cases a broad amplifier bandwidth or low frequency (LF) operation are not necessary, these degrees of freedom can be used for power saving. For RF purposes, the efficiency is increased by inductive coupling, Fig. 2.7. Such a circuit is found both in RF preamplifiers and in RF power stages. In a model, composed of ideal lumped elements, the inductor $L_S \to \infty$ acts as constant current source, providing the current I_{OP}. If the transistor is turned on completely, it is conducting the whole current $2 \cdot I_{OP} = i_d$. In the turn off case, the drain-source voltage rises until the load resistor takes over the whole current, Fig. 2.8. In this case the optimal operating point current I_{OP} is:

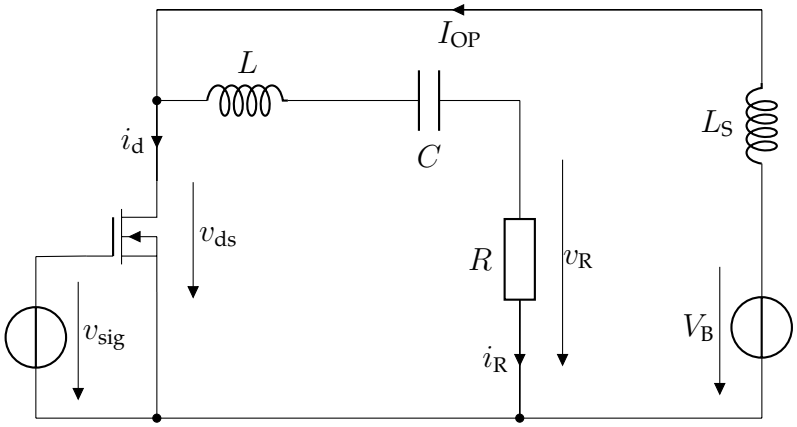

Fig. 2.7. Class A narrow band amplifier

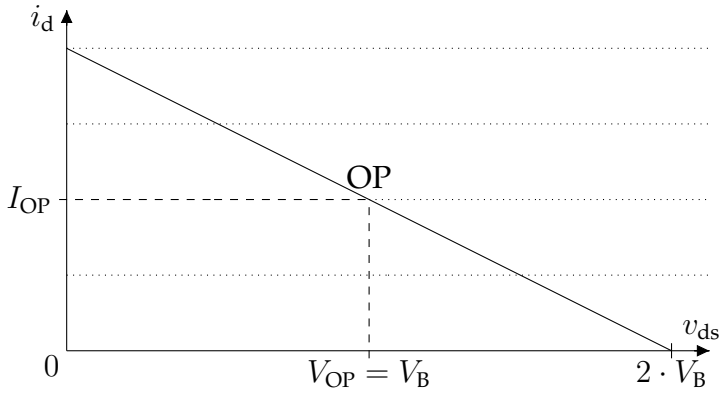

Fig. 2.8. Operating point diagram narrow band class A

$$i_d(t) = I_{OP}(1 + \sin \omega t), \quad I_{OP} = \frac{V_B}{R}. \tag{2.10}$$

Because of the output filter network, the voltage v_R and the current i_R at the load resistance are a pure AC voltage and a bigger part of the transistor transfer curve is usable without increasing the distortion, if a suitable low pass filter is used.

$$v_R(t) = i_R(t)R = -I_{OP} \cdot R \sin(\omega t). \tag{2.11}$$

The current provided by the supply I_{OP} remains constant

$$I_{OP} = i_d(t) + i_R(t) = \text{const.}, \tag{2.12}$$

therefore the powers are described by

$$P_{\mathrm{T}} = \frac{V_{\mathrm{B}}^2}{2R}, \quad P_{\mathrm{B}} = V_{\mathrm{B}} I_{\mathrm{OP}} = \frac{V_{\mathrm{B}}^2}{R}, \quad P_{\mathrm{R}} = P_{\mathrm{AC}} = \frac{V_{\mathrm{B}}^2}{2R}. \tag{2.13}$$

The efficiency is calculated to

$$\eta = \frac{1}{2} \mathrel{\hat{=}} 50\% \tag{2.14}$$

2.2.5 Class A_L design example

A simple transmit amplifier is considered as design example Fig. 2.9.

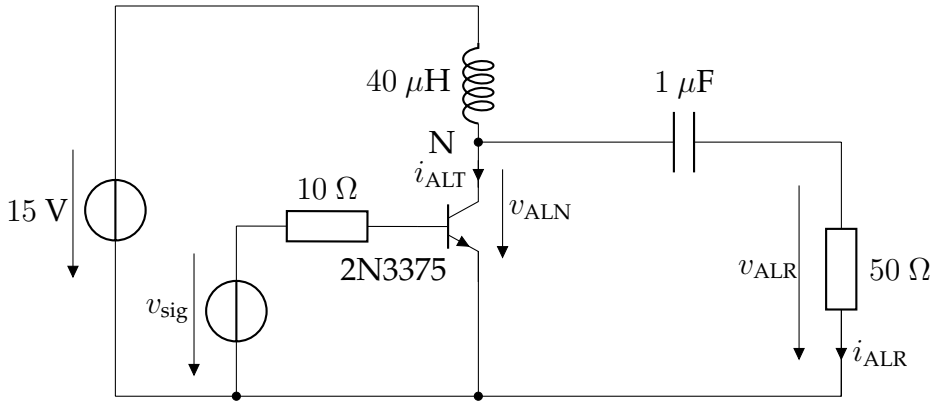

Fig. 2.9. Class A_L amplifier

The efficiency of the circuit according to Fig. 2.9 is much higher than the efficiency of the circuit according to Fig. 2.3. Fig 2.10 shows the output current i_{ALR} through the load resistor and the collector current i_{ALT}.

The DC is insulated by a capacitor as Fig. 2.11 shows, where v_{ALN} is the collector voltage and v_{ALR} the output voltage.

2.2.6 Alternative Definition

Based on efficiency analysis, there is a better definition for the amplifier class, that is independent of excitation. In amplifiers of class A the average value of the supplied power is P_{B} is independent of the curve shape of the input signal v_{sig}, as long as its DC component in the time interval of analysis is zero, as well.

$$0 = \frac{1}{T} \int_0^T v_{\mathrm{sig}} \, \mathrm{d}t \quad \Rightarrow \quad P_{\mathrm{B}} \neq f(v_{\mathrm{sig}}) \tag{2.15}$$

2.3 Class B Concept

In a class B amplifier, Fig. 2.12, usually two transistors in push-pull configuration are used, Fig. 2.13. In this case the transistors are conducting in an alternating way, the first transistor from $0° - 180°$ while the second transistor from $180° - 360°$ within each period. Since two transistors are used now, i_{d1} is the drain current of transistor T1 and i_{d2} is the drain current of transistor T2.

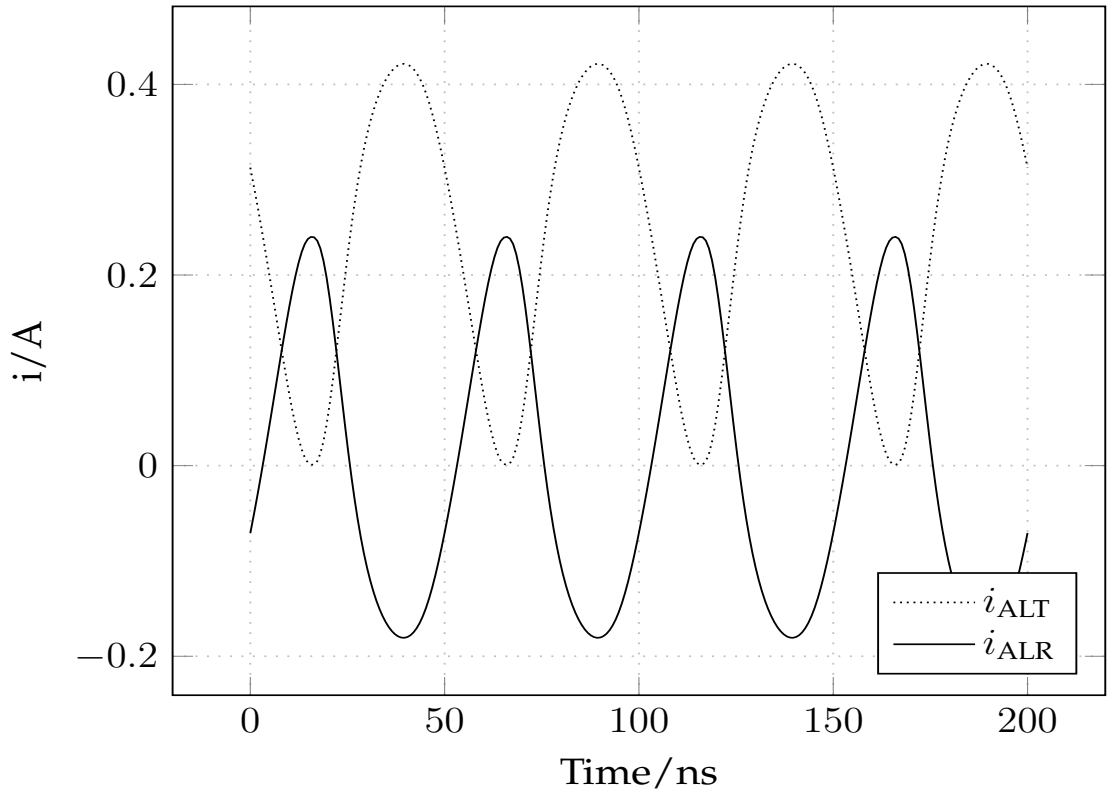

Fig. 2.10. The currents at the class A_L amplifier

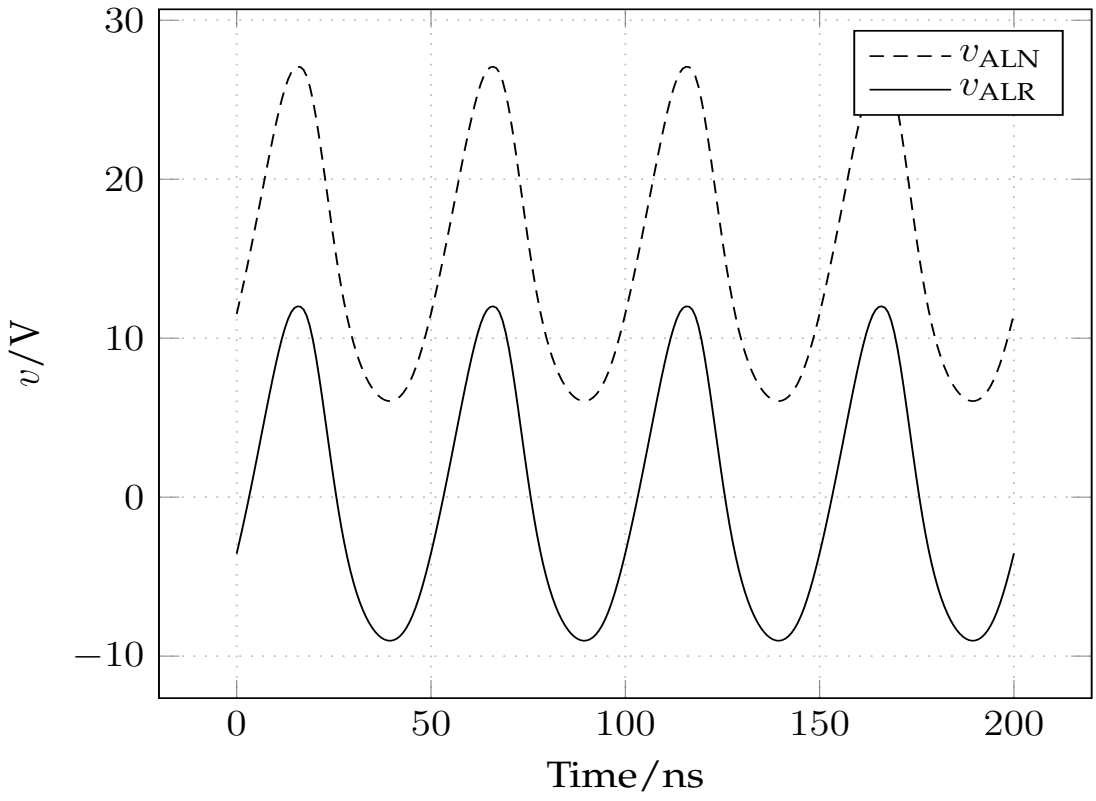

Fig. 2.11. Class A_L amplifier, voltages.

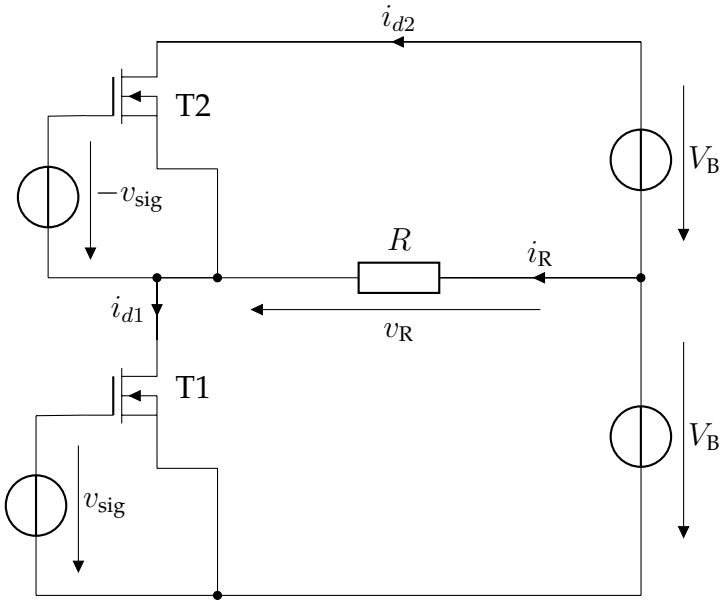

Fig. 2.12. Class B push-pull amplifier

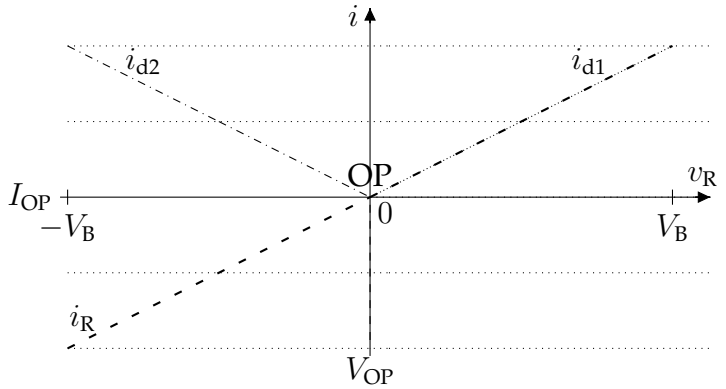

Fig. 2.13. Operating point diagram, class B amplifier

2.3.1 Mathematical Modeling

In the following subsection class B amplifiers without quiescent current $I_{\text{OP}} = 0$ are considered. The push-pull amplifier is fed by two supply voltage sources, both transistors are excited with alternate phase, Fig. 2.12. While transistor 1 is conducting, transistor 2 is turned off, and vice versa, Fig. 2.13. For the positive half wave appeals

$$i_{\text{d1}} = \frac{V_{\text{B}}}{R} \sin \omega t \ \geq 0, \quad i_{\text{d2}} = 0, \tag{2.16}$$

while during the negative half wave the other transistor starts conducting

$$i_{\text{d2}} = \frac{V_{\text{B}}}{R} \sin \omega t \ \geq 0, \quad i_{\text{d1}} = 0. \tag{2.17}$$

$$P_{\text{R}} = P_{\text{AC}} = \frac{2}{T} \int_0^{\frac{T}{2}} \frac{V_{\text{B}}^2}{R} \sin^2 \omega t \, \mathrm{d}t = \frac{2V_{\text{B}}^2}{RT} \cdot \frac{1}{2} \cdot \frac{T}{2} = \frac{V_{\text{B}}^2}{2R} \tag{2.18}$$

$$P_{\text{B}} = \frac{2}{T} \int_0^{\frac{T}{2}} \frac{V_{\text{B}}^2}{R} \sin \omega t \, \mathrm{d}t = \frac{2V_{\text{B}}^2}{RT} \left[-\cos \omega t \frac{1}{\omega} \right]_0^{\frac{T}{2}} = 2\frac{V_{\text{B}}^2}{R\pi} \tag{2.19}$$

$$\eta_{\text{B}} = \frac{P_{\text{R}}}{P_{\text{B}}} = \frac{\pi}{4} \hat{=} 78,5\% \tag{2.20}$$

2.3.2 Class B design example

Class B amplifiers are found in a servo controller or an operational amplifier (OpAmp) output stage for example. Since npn/nmos transistors are faster compared to pnp/pmos transistors of the same technology process, for RF class B amplifiers usually, npn/nmos transistors are typically used. In the example Fig. 2.14, the sources v_{sig} and $-v_{\text{sig}}$ provide 20 MHz sine wave control signals, superposed by a 0.6 V DC bias voltage. Now, the

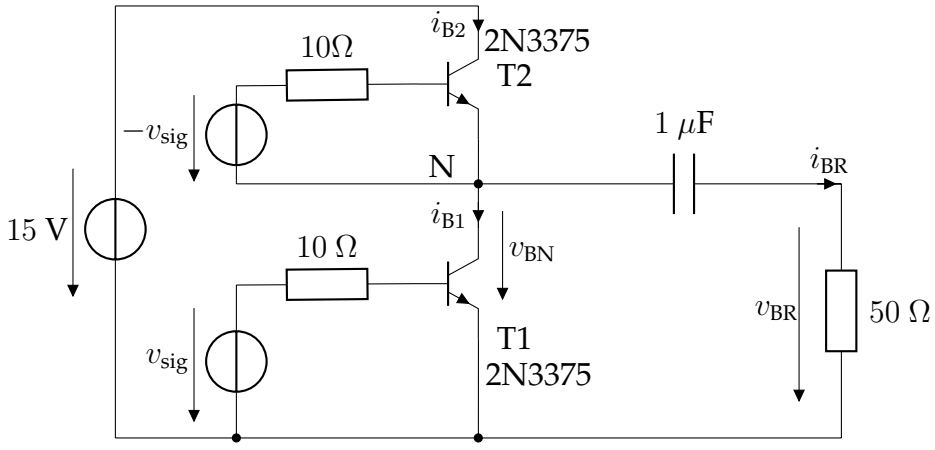

Fig. 2.14. Class B amplifier.

effort and distortion are higher, but its efficiency is very much higher, Fig 2.15 shows the output current i_{BR} and the collector currents i_{B1} and i_{B2}. The nonlinear behavior at the zero crossing is good visible, Fig 2.15, Fig. 2.16. The DC is insulated by a capacitor as Fig. 2.16 shows, where v_{BN} is the collector voltage and v_{BR} the output voltage.

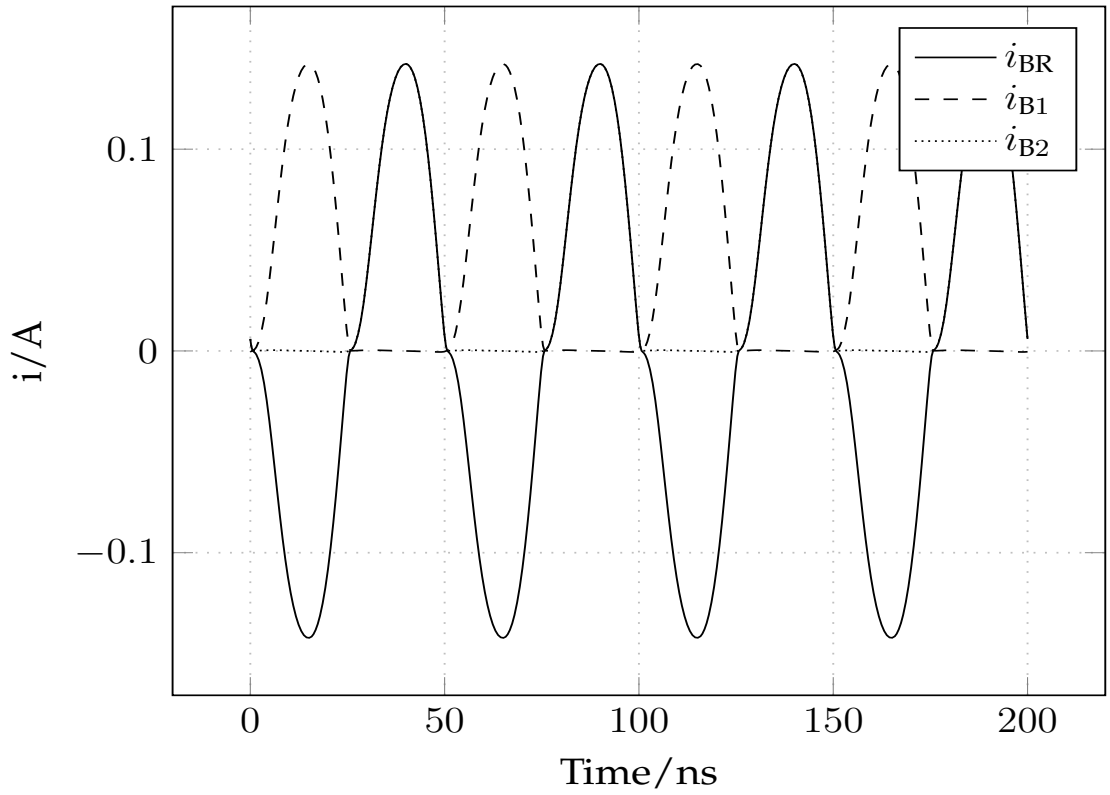

Fig. 2.15. Class B amplifier, currents.

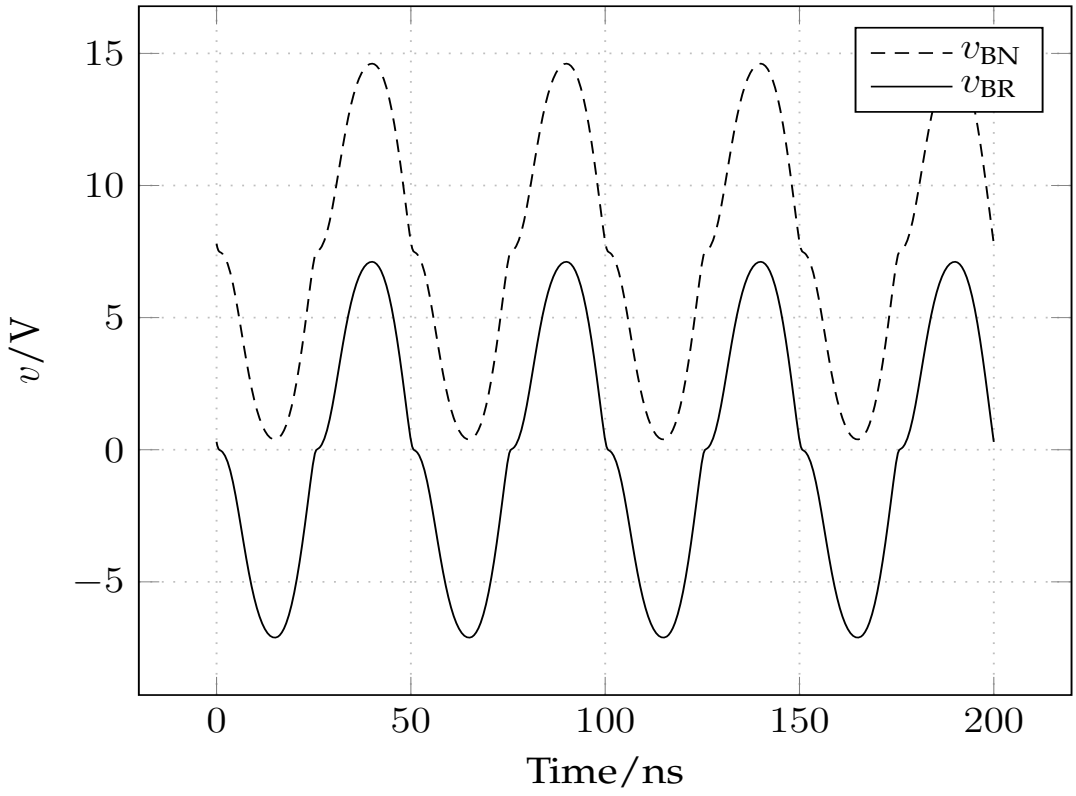

Fig. 2.16. Class B amplifier, voltages.

2.3.3 Class AB Operation

Between class A and B, with respect to the operating point, class AB is located. In a class AB amplifier each transistor must be conducting for more than half a period, but less than one whole period of time. With typical commercial products, efficiency of class B is at $\eta_B < 75\%$, in class AB operation, it is $\eta_A < \eta_{AB} < \eta_B$.

2.3.4 Class AB design example

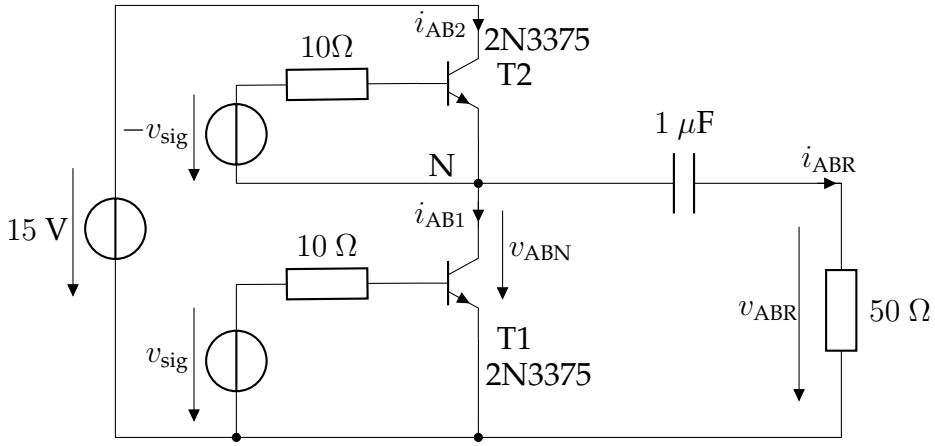

Fig. 2.17. Class AB amplifier.

Almost all typical high fidelity (HIFI) amplifiers are class AB. The distortion is much lower compared to class B, but its efficiency is a bit lower, Fig 2.17. Fig. 2.18 shows the output current i_{ABR} and the collector currents i_{AB1} and i_{AB2}. In the example Fig. 2.17, the sources v_{sig} and $-v_{sig}$ provide 20 MHz sine wave control signal, superposed by a 0.72 V DC bias voltage. The DC is insulated by a capacitor as Fig. 2.19 shows, where v_{ABN} is the collector voltage and v_{ABR} the output voltage.

2.4 Design Comparison of linear Amplifier Classes

Table 2.1 shows the operating parameters of the example circuits shown in Fig. 2.3, Fig. 2.9, Fig. 2.17 and Fig. 2.14. $P(15\text{ V})$ is the supply power, $P(\text{be}_{T1})$ and $P(\text{be}_{T2})$ are the powers dissipated in the base emitter diodes of the transistors, $P(50\ \Omega)$ is the output power and

$$G = \frac{P(50\ \Omega)}{P(\text{be}_{T1}) + P(\text{be}_{T2})}, \tag{2.21}$$

is the achieved power gain. In difference to a low frequency FET amplifier, the input signal power cannot be neglected with a bipolar transistor RF amplifier, so the efficiency η is defined as follows:

$$\eta = \frac{P(50\ \Omega)}{P(\text{be}_{T1}) + P(\text{be}_{T2}) + P(15\text{ V}) - P(V_2)}, \tag{2.22}$$

where $P(V_2)$ is the recovered power in the later discussed class M topology. The biggest problem of real implemented class A amplifiers is the non linear behavior of transistors.

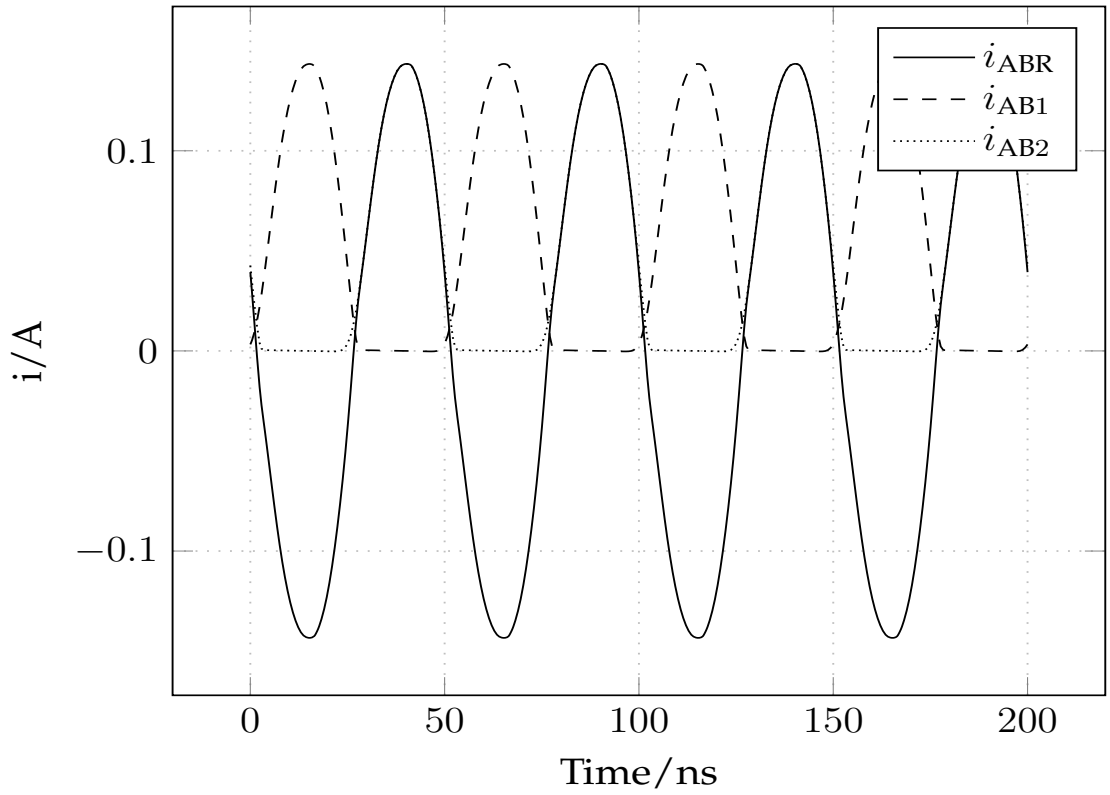

Fig. 2.18. Class AB amplifier, currents.

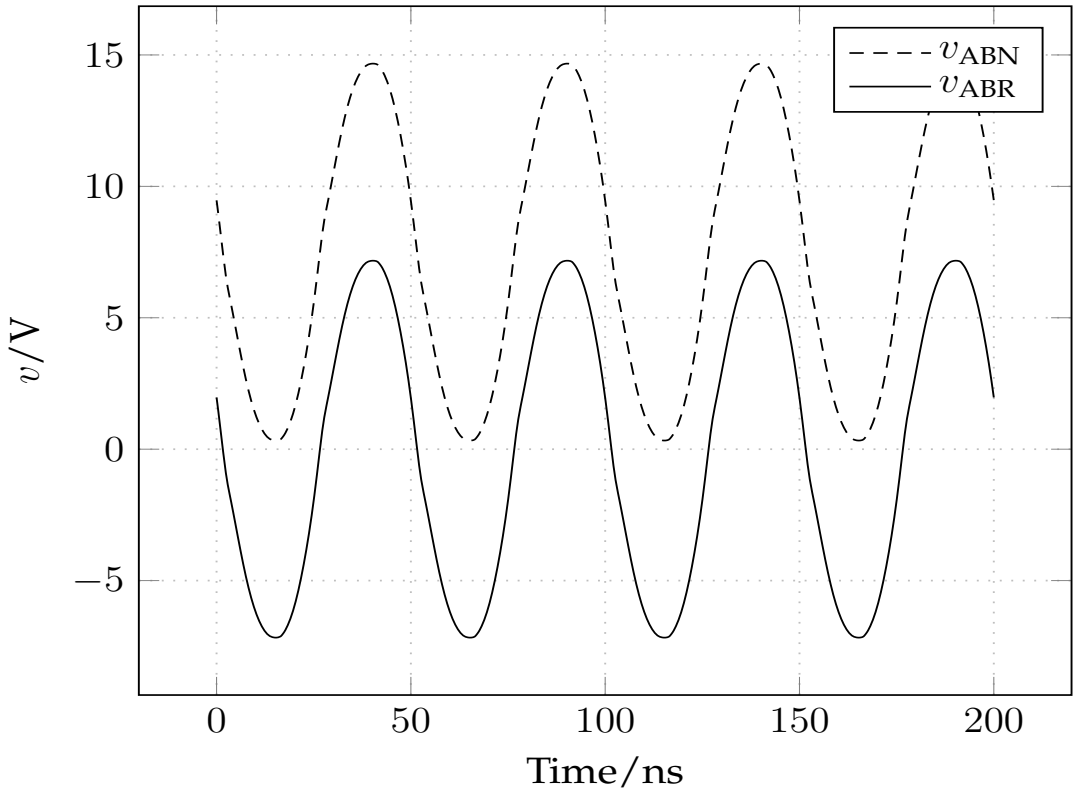

Fig. 2.19. Class AB amplifier, voltages .

Class	A	A_L	AB	B
$P(15\ V)$	2.043 W	3.614 W	735.4 mW	622.1 mW
$P(be_{T1})$	16.9 mW	44.5 mW	6.85 mW	4.17 mW
$P(be_{T2})$	-	-	6.85 mW	4.17 mW
$P(50\ \Omega)$	86.187 mW	1.106 W	553.6 mW	467.1 mW
η	4.2 %	30.2 %	73.9 %	74.1 %
G	5.1	24.9	40.4	56.0

Table 2.1. Efficency analysis

Because of this reason, only a small part of the transistors output transfer curve can be used as an operating area, when low distortion is desired. Class A in Table 2.1 shows that linearity has to be dearly bought for an extremely low efficiency with this considerable bad concept. A_L is much better, but this concept e.g. cannot be used for amplifying DC. The linear operating area can be doubled by using a second transistor for forming a push-pull configuration. The quiescent current can be very much lower then. Here also applies the rule, a better linearity has to be dearly bought with a higher quiescent current. For an application one has to figure out the requirements of linearity and efficiency before choosing the topology. If it is acceptable, the quiescent current can be put to a very low value and then a class AB topology would be the best compromise between high efficiency and low distortion.

2.4.1 Change Over Between Linear and Switched Concepts

Sometimes the difference between a linear and a nonlinear amplifier circuit is the choice of the operating point only. Fig. 2.21 shows an example for the circuit in Fig. 2.20. Here the operating point is chosen such that no quiescent current i_d would occur, if $v_{sig} \to 0$ applies. With v_{sig} containing a negative DC component, the conducting time of the transistor can be decreased. Instead of class A, the resulting topology is called class C.

2.5 Class C Concept

Class C means one transistor conducting less than $180°$ in one period, according to the old definition. Class C amplifiers usually are single ended amplifiers, designed for RF purposes. The input signal is typically sinusoidal, the driver stages often are linear amplifiers of class A, AB or B. A band limiting output filter is needed, because the class C power stage is non linear. Efficiency typically is $\eta_C < 80\%$. All discussed amplifiers achieve less than $\eta = 100\%$ with ideal elements conceptional.

2.6 Switched Amplifiers

In switched amplifiers usually special switching transistors are taken, optimized for a low on drain source resistance $R_{DS\,ON}$ and a short rise- and fall time. With respect to this fact, for theoretical analysis of the basic concept, the transistors are replaced by switches. In general there are two categories of switched amplifiers. The single ended switched amplifier Fig 2.22 and the switched push-pull amplifier, Fig 2.23. An efficiency of theoretically

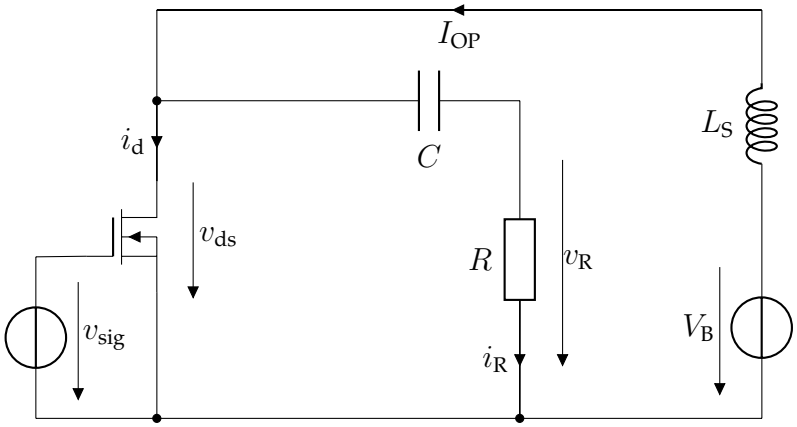

Fig. 2.20. Narrow band amplifier, class C

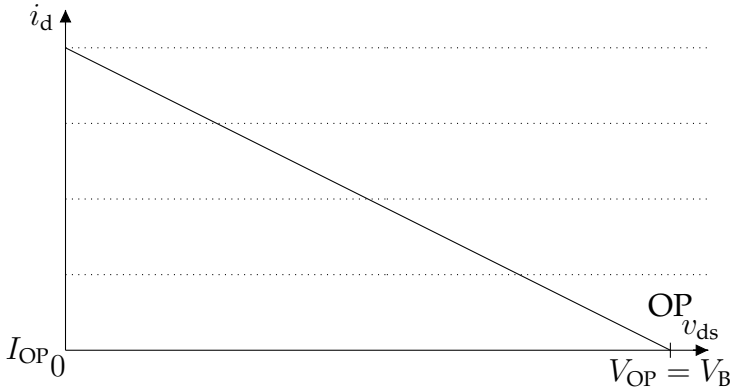

Fig. 2.21. Operating point diagram, class C

100% is achieved, much higher than each theoretical optimum for linear amplifier topologies. Established examples for the single ended switched amplifier topology, Fig 2.22, are the classes C, E, F and for the switched push-pull amplifier, Fig 2.23, class D and the newly invented classes M and N, which will be introduced later.

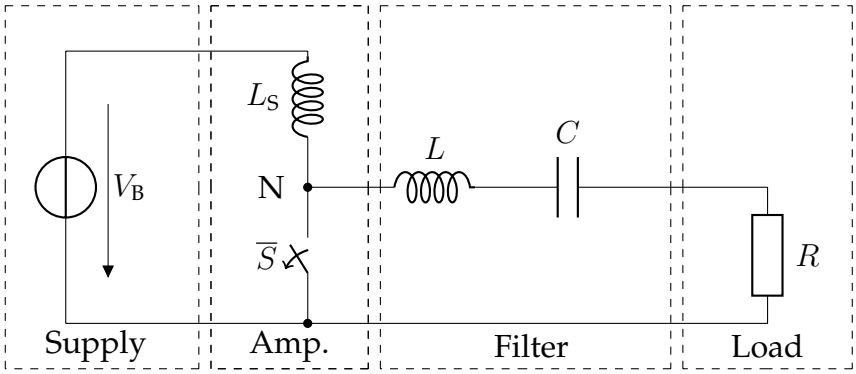

Fig. 2.22. Switched single ended amplifier

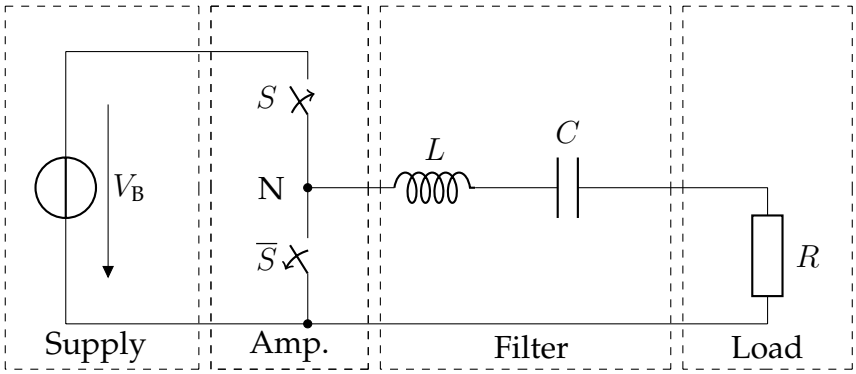

Fig. 2.23. Switched push-pull amplifier

2.6.1 Switched Class C Concept

Many commercial RF class C amplifiers are destroyed in a very easy way by disconnecting the load, e.g. the antenna. The following considerations help understanding this effect. The class C amplifier turns into a switched amplifier, if a square wave control signal is applied. Especially the design of switching RF amplifiers e.g. class C [11][12][13][14] leads to serious issues, that are only visible when real transistor models are considered. The single ended amplifier in Fig. 2.24 includes one power transistor and a voltage source with a series inductor, which is sized such, that the current flowing through is almost constant. In the operating frequency band this inductor transforms the voltage source into a current source. In the ideal case, its impedance in the operating frequency range is infinite. Fig 2.24 shows an example for a simple single ended amplifier with 15 V power supply, a 40 μH series inductor and a LC output network with 50 Ω load, where v_{sq} is the square wave control signal. Fig. 2.25 shows the output current i_{CR} and the collector current i_{CT}. The DC is insulated by a capacitor as Fig. 2.26 shows, where v_{CN} is the collector voltage and v_{CR} the output voltage. The key problem is node N switching between about

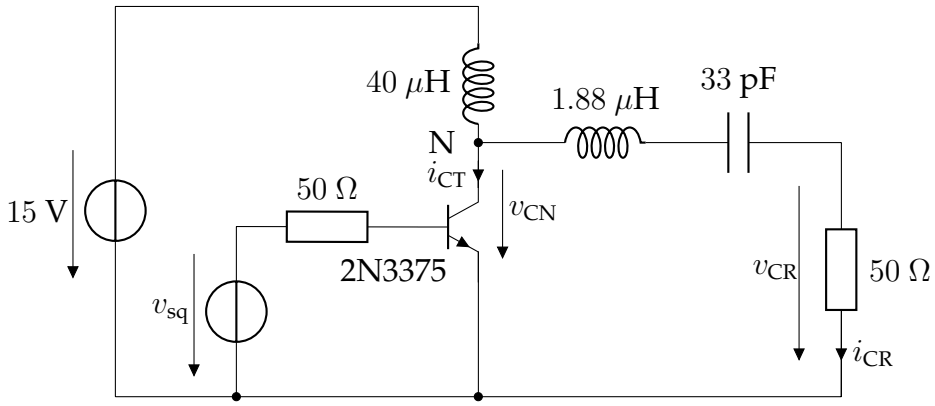

Fig. 2.24. Class C amplifier

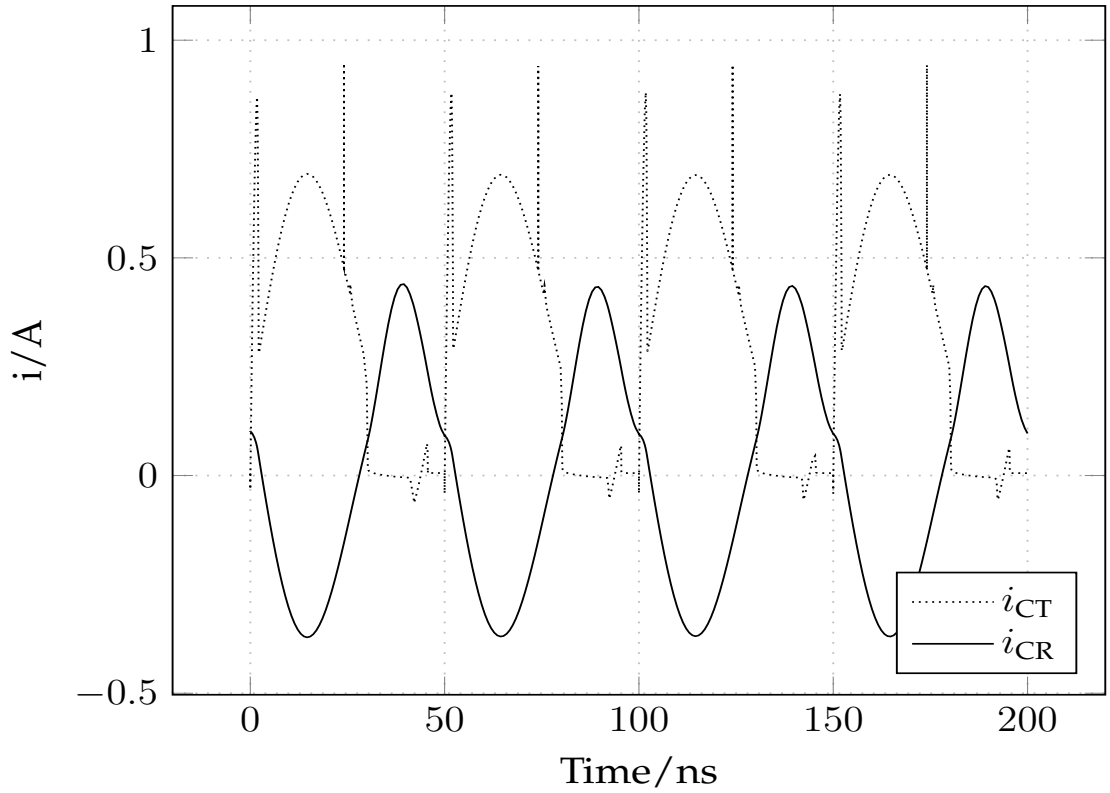

Fig. 2.25. The currents at the class C amplifier

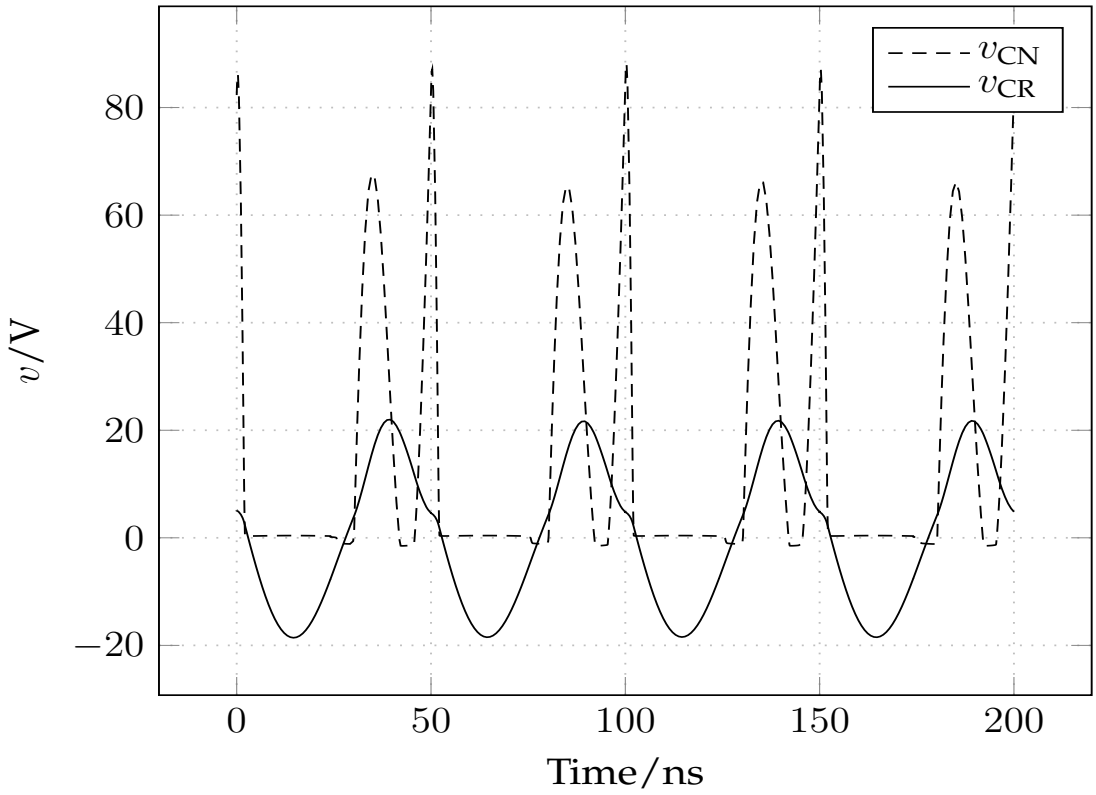

Fig. 2.26. Class C amplifier, high voltage peaks at node N.

$0\ \Omega$ in each negative half wave and almost $\infty\ \Omega$ at each positive half wave, leading to an extremely asymmetric output voltage at node N, Fig. 2.26, necessitating a high-voltage capable transistor, Fig. 2.24. All following amplifier classes show ideas to overcome this key problem for saver operation and higher efficiency.

2.6.2 Class E Concept

Much saver transmit power amplifiers are class E types. A possible method of avoiding high voltage peaks is lowering the impedance at node N when the transistor is turned off. Therefore, a 27 pF capacitor is connected between node N and ground, Fig. 2.27, leading the class E topology [15][16][17][18]. The capacitive component of the impedance at node N is increased until the switch off voltage peak reaches a tolerable level, Fig. 2.29. Ideally switching occurs at the time instant when the voltage at node N is zero. If this time is not hit exactly, current peaks occur, seen in Fig. 2.28. In the example the amplifier consumes 5.1 W at an output power of 4.1 W, leading to an efficiency of $78\ \%$, Table 2.3. Fig. 2.28 shows the output current i_{ER}, the collector current i_{ET} and the capacitor current i_{EC}. The DC is insulated by a capacitor as Fig. 2.29 shows, where v_{EN} is the collector voltage and v_{ER} the output voltage.

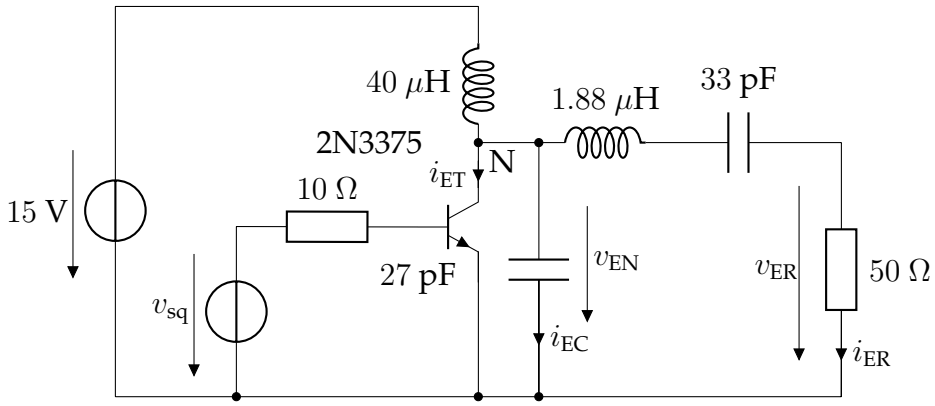

Fig. 2.27. Class E amplifier.

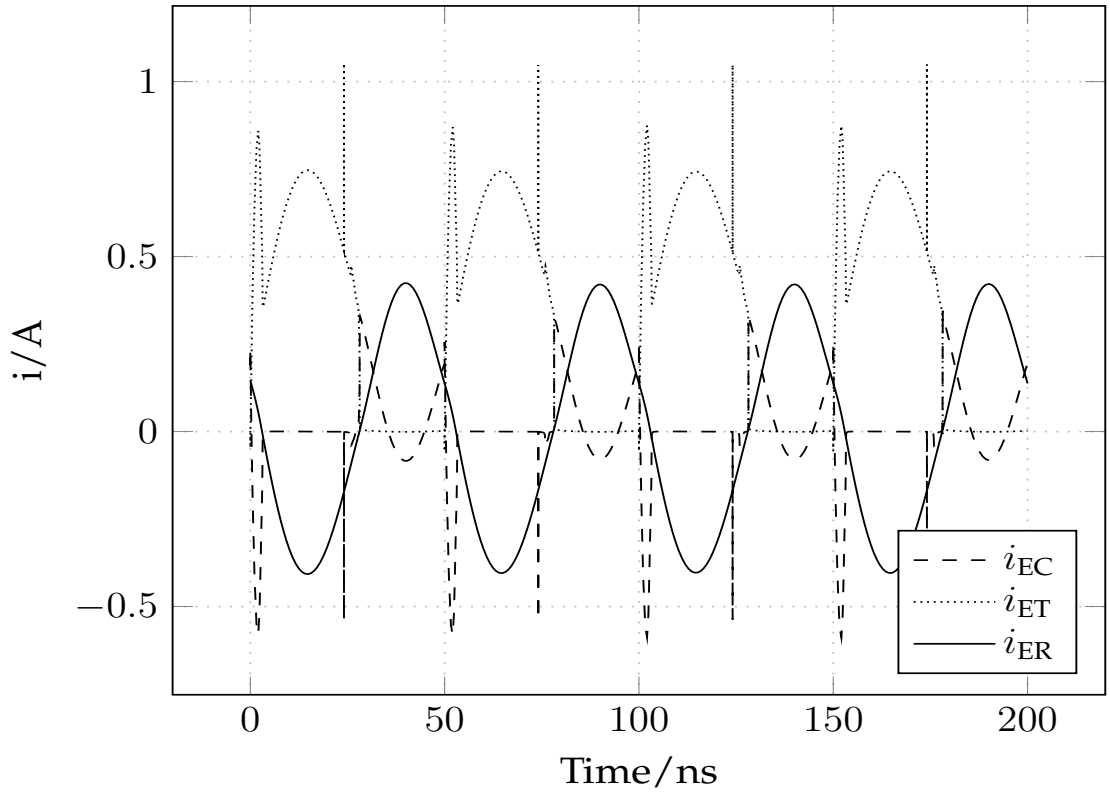

Fig. 2.28. The currents at the class E amplifier

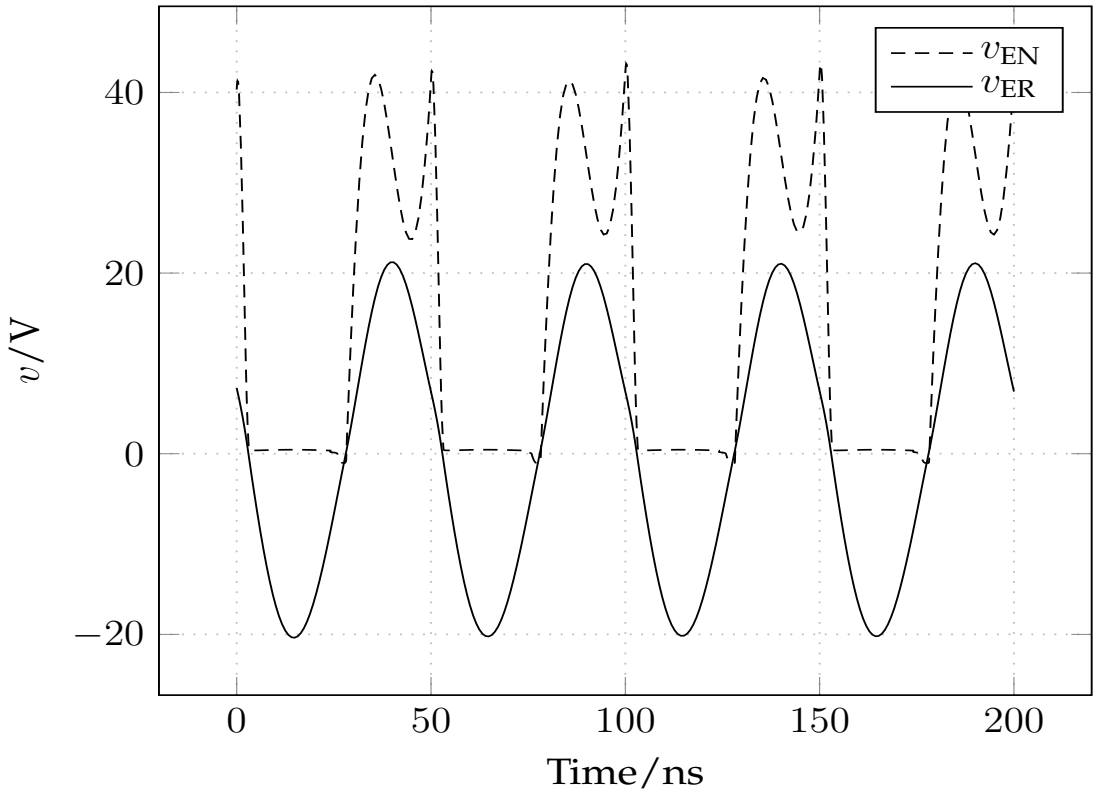

Fig. 2.29. Class E amplifier, voltage peaks at node N.

2.7 Class F Concept

The class F amplifier seems to be a basically academic topology, extremely rare in use. According to class F concept [19][20], a filter network is used for shorting the even harmonics at node N, for achieving a rectangular waveform at this node, Fig. 2.30. This is achieved by series resonators tuned to the even multiples of the fundamental frequency, also acting like band-stop filters and short-circuit the even harmonics. Parallel resonators tuned to the odd harmonic frequencies, which act like band-stop filters, are used to prevent the odd harmonics from reaching the output node. A series resonator C_0 , L_0 tuned to the fundamental frequency feeds the output signal to the load. Even though considerable high voltage peaks at node N can occur. There are two major disadvantages of this class F concept: On the one hand the network theoretical effort for synthesis is huge compared to other concepts, on the other hand reactances of high quality factor and high voltage resistant transistors are needed.

Fig. 2.30 shows a practical, simplified implementation of a class F amplifier [21] [22] [23]. Table 2.2 shows the values of the used capacitors in the implementation Fig. 2.30, where C_0 and L_0 are the reactances of the output network, while C_x and L_x for $x \in [1, ..., 8]$ are the reactances of the shorting network. This means eight serial resonators are connected in parallel here, represented by C_n and L_n for a better visualization. An additional small 14.4 pF capacitor also helps increasing the efficiency [24]. Fig. 2.31 shows the output current i_{FR}, the collector current i_{FT} and the resonator current i_{FC}. The DC is insulated

Capacitor	Value	Inductor	Value
C_0	33 pF	L_0	1.88 μH
C_1	$C_0/2$	L_1	$L_0/2$
C_2	$C_0/4$	L_2	$L_0/4$
C_3	$C_0/6$	L_3	$L_0/6$
C_4	$C_0/8$	L_4	$L_0/8$
C_5	$C_0/10$	L_5	$L_0/10$
C_6	$C_0/12$	L_6	$L_0/12$
C_7	$C_0/14$	L_7	$L_0/14$
C_8	$C_0/16$	L_8	$L_0/16$

Table 2.2. Class F reactance values

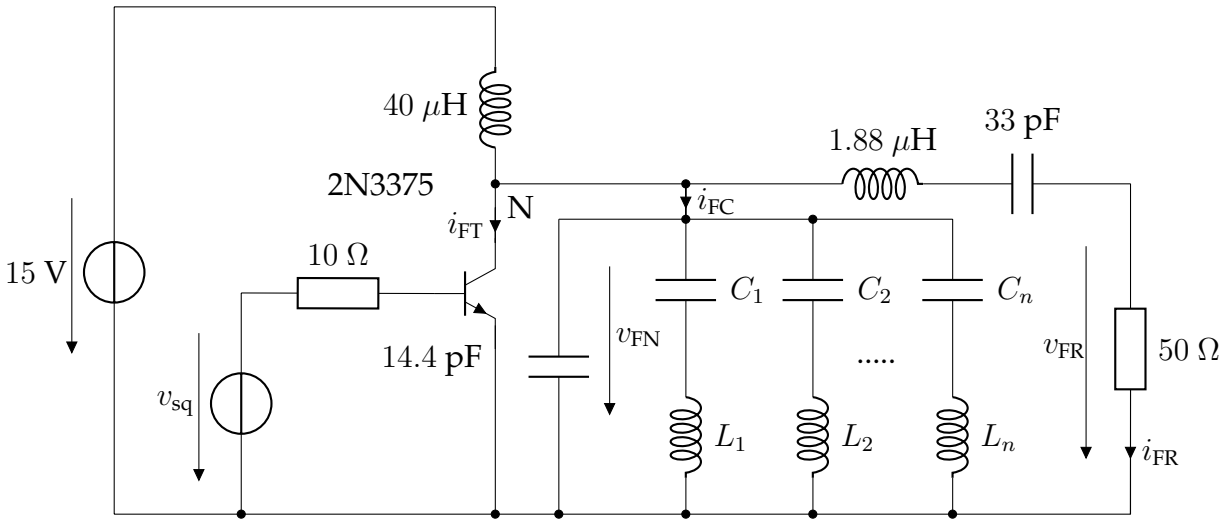

Fig. 2.30. Class F amplifier.

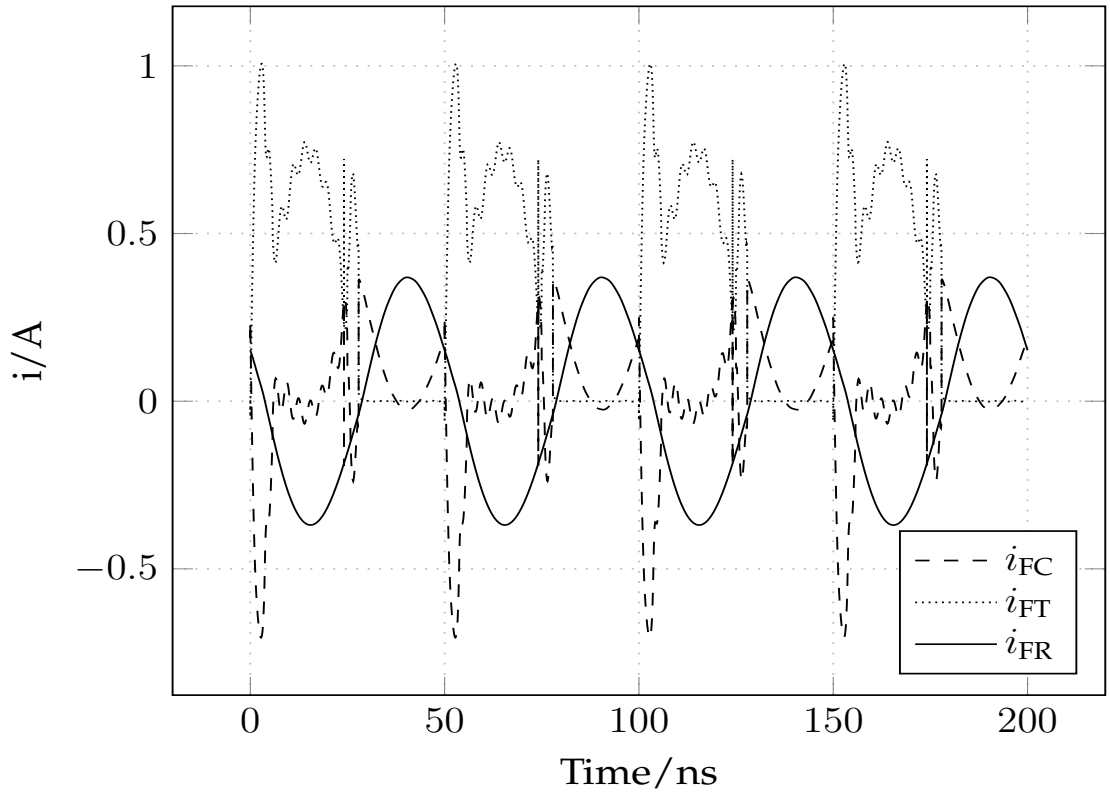

Fig. 2.31. The currents at the class F amplifier

by a capacitor as Fig. 2.32 shows, where v_{FN} is the collector voltage and v_{FR} the output voltage.

2.8 Class D Concept

This topology is used in induction ovens, solar power inverters and lamp or computer supplies as well. Evidently, two transistors should be used in push-pull configuration when ever possible [25][26][27], which is the case in the class D amplifier. Then, the small signal impedance of node N is always $0\ \Omega$ in the ideal case. Fig. 2.33 shows a simple push-pull amplifier with a 15 V power supply, two npn transistors operating in push-pull configuration and the same output network topology as used in Fig. 2.23. Fig 2.34 shows the output current i_{DR} and the collector currents i_{D1} and i_{D2}. The DC is insulated by a capacitor as Fig. 2.35 shows, where v_{DN} is the collector voltage and v_{DR} the output voltage. Importantly, cases with both transistors conducting at the same time must be prevented as shown in Fig. 2.34, due to the high cross currents that reduce the efficiency and might lead to thermal destruction. In addition, the transistors are not allowed to be completely switched off at the same time as well. Controlling the transistors for the perfect timing is the real problem of class D. Usually timing errors in the controlling system are the most probable reason for defective devices. At higher frequencies, the transistors need a longer time for turning off, than for switching on, because of the minority carriers needing time for recombining. In several cases, the controlling of the upper transistor T2, Fig. 2.33, is achieved by a transformer or a driver stage supplied by charge pumps. Fig. 2.34 shows

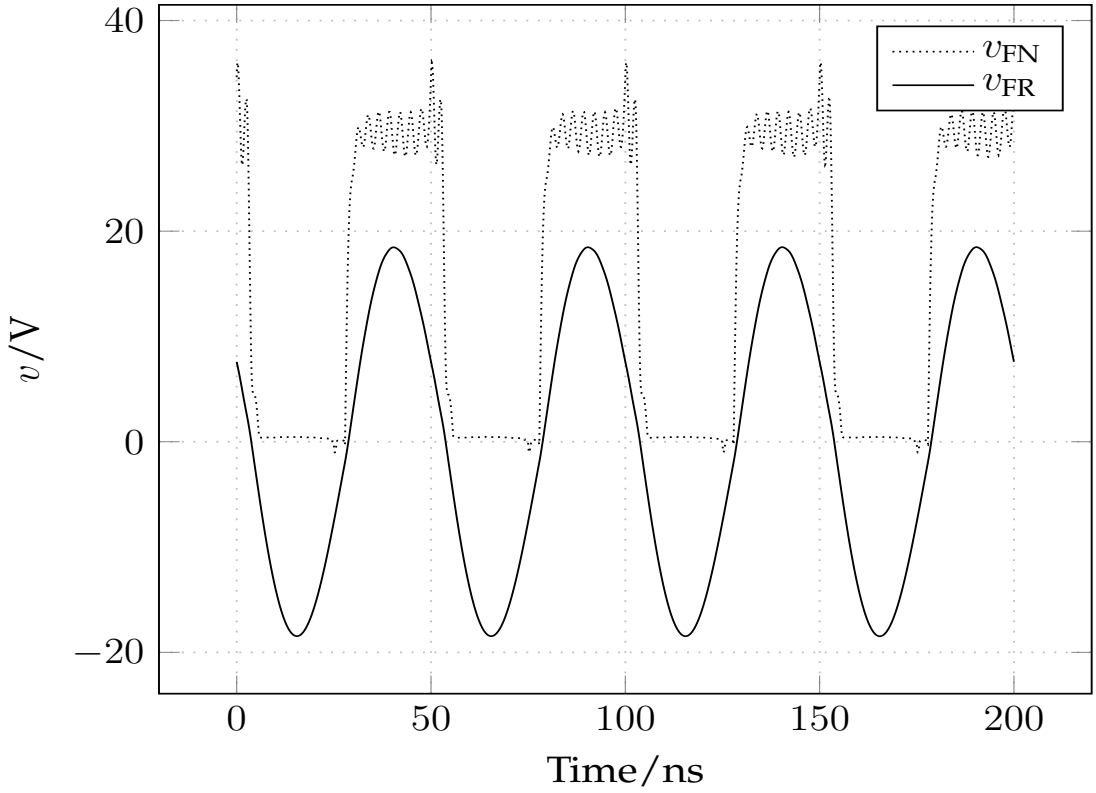

Fig. 2.32. Class F amplifier, voltages.

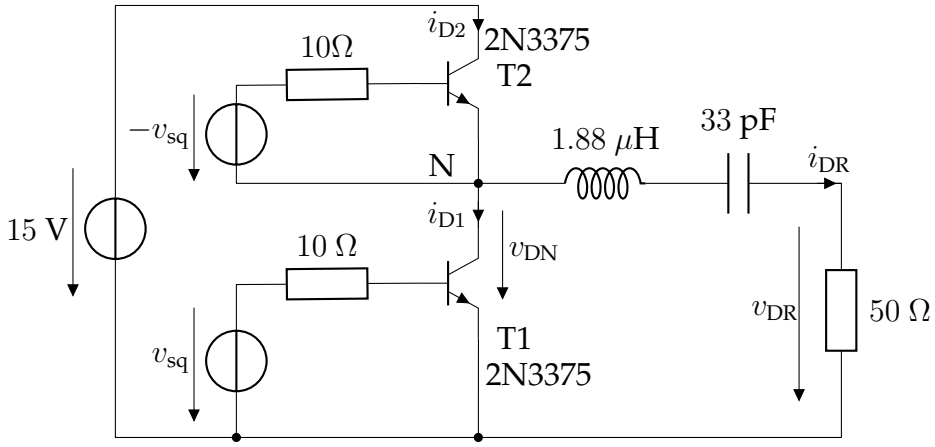

Fig. 2.33. Class D amplifier.

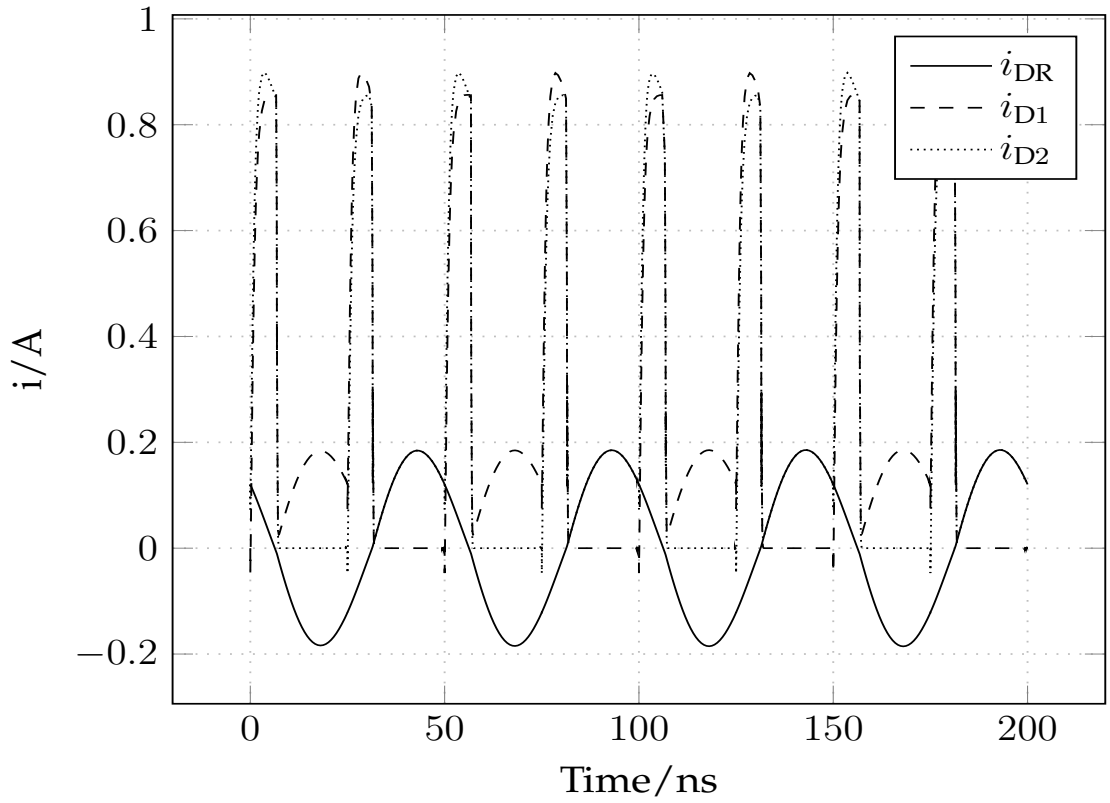

Fig. 2.34. Class D amplifier, currents.

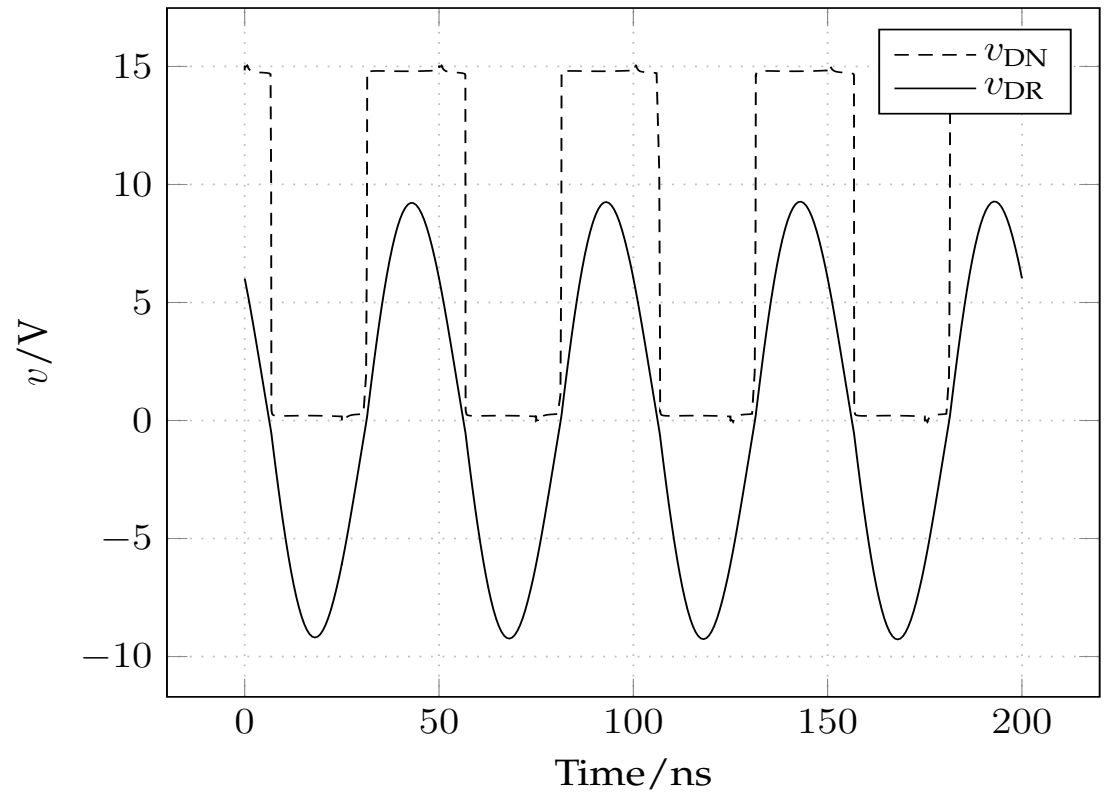

Fig. 2.35. Class D amplifier, voltages.

the currents of the amplifier, Fig. 2.33, while Fig. 2.35 shows the voltages. With both transistors conducting at the same time, the cross current is enormously increasing leading to a huge dissipation power at high operating frequencies. In such a case the amplifier consumes 3.77 W at an output power of 848 mW. The efficiency $\eta = 21\%$ is even lower than in a class A amplifier. The effort of implementing a class D amplifier has no benefit if the operating frequency gets to high as this example shows.

2.9 The New Concept: Class M

Considering a Schottky diode as a switching device [28][29][30], the charge carrier transport is mainly achieved by minority carriers. Therefore, it can change its state extremely fast between low and high resistance. It is therefore convenient to replace the upper transistor, which is difficult to be controlled, by a Schottky diode.

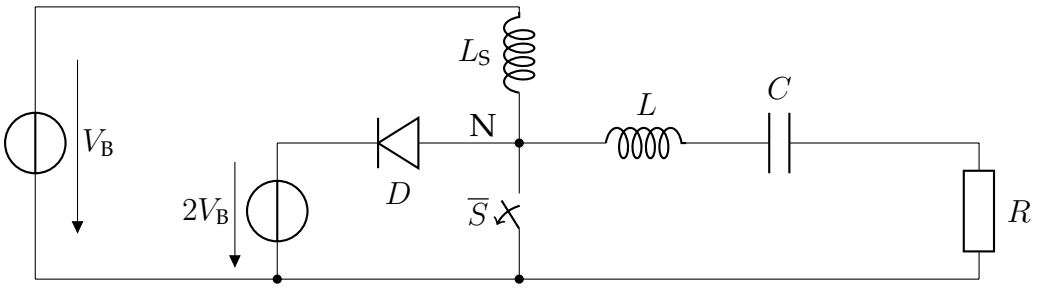

Fig. 2.36. The basic concept of an automatic push-pull amplifier.

If the transistor switches off, the voltage at node N will rise at twice the value of the supply voltage V_B, providing a symmetric output signal, then. The reflected not required power will be fed back by diode D in a source with twice the supply voltage, Fig 2.36. In this case the reflected energy is not transformed into heat, instead it can be used as supply energy once more.

2.10 Simulation of the Class M Amplifier

The example Class M amplifier includes a 15 V supply source and a source $V_2 \approx 30$ V for energy recycling. The exact value of V_2 is adjusted for highest efficiency, Table 2.3. Taking advantage of the diode self control, a push-pull driver stage is avoided, while still preserving the push-pull effect. The lumped element values have to be chosen such that the diode remains in its low ohmic state with the transistor turned off to guarantee symmetric half waves. Efficiency will reach its optimum, if the current flow keeps the diode in the low ohmic state at its minimum, Fig. 2.38. Fig 2.38 shows the output current i_{MR}, the collector current i_{MC} and the diode current i_{MD}. The DC is insulated by a capacitor as Fig. 2.39 shows, where v_{MN} is the collector voltage and v_{MR} the output voltage. Voltage at node N is a symmetrical square wave, Fig. 2.39, the drain current is a positive sine wave, the current through the diode is a negative sine half wave. v_{MN} is provided with the amplitude voltage value related to the supply voltage and twice the voltage compared to the established push-pull concepts. Due to the power recycling concept, smaller transistors, dissipating less power, can be used. In simulation, circuit Fig. 2.37 reached an efficiency

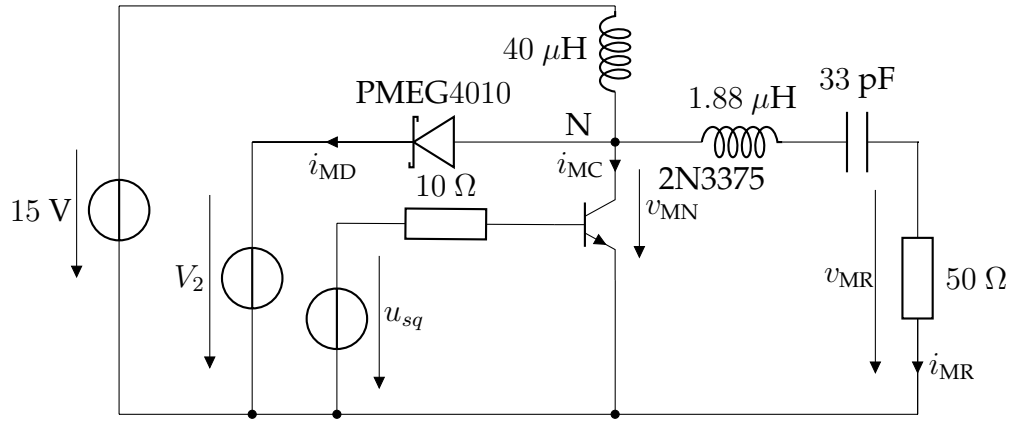

Fig. 2.37. Class M amplifier.

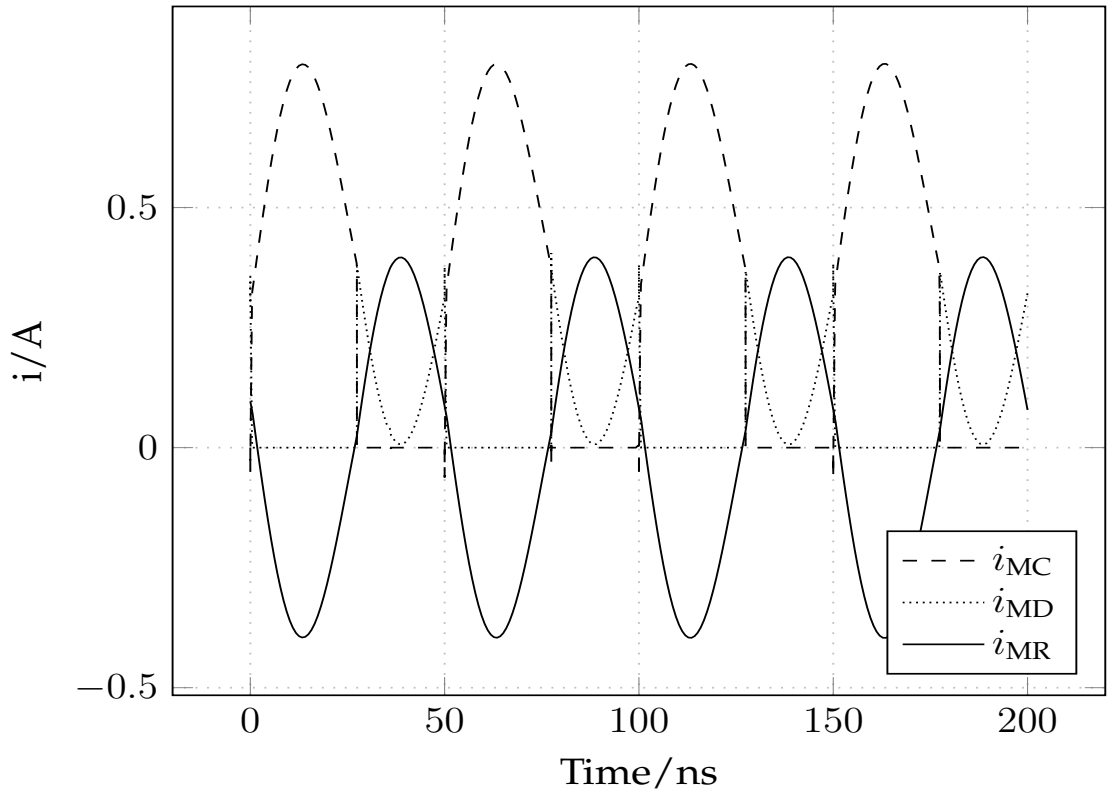

Fig. 2.38. The currents at the class M amplifier.

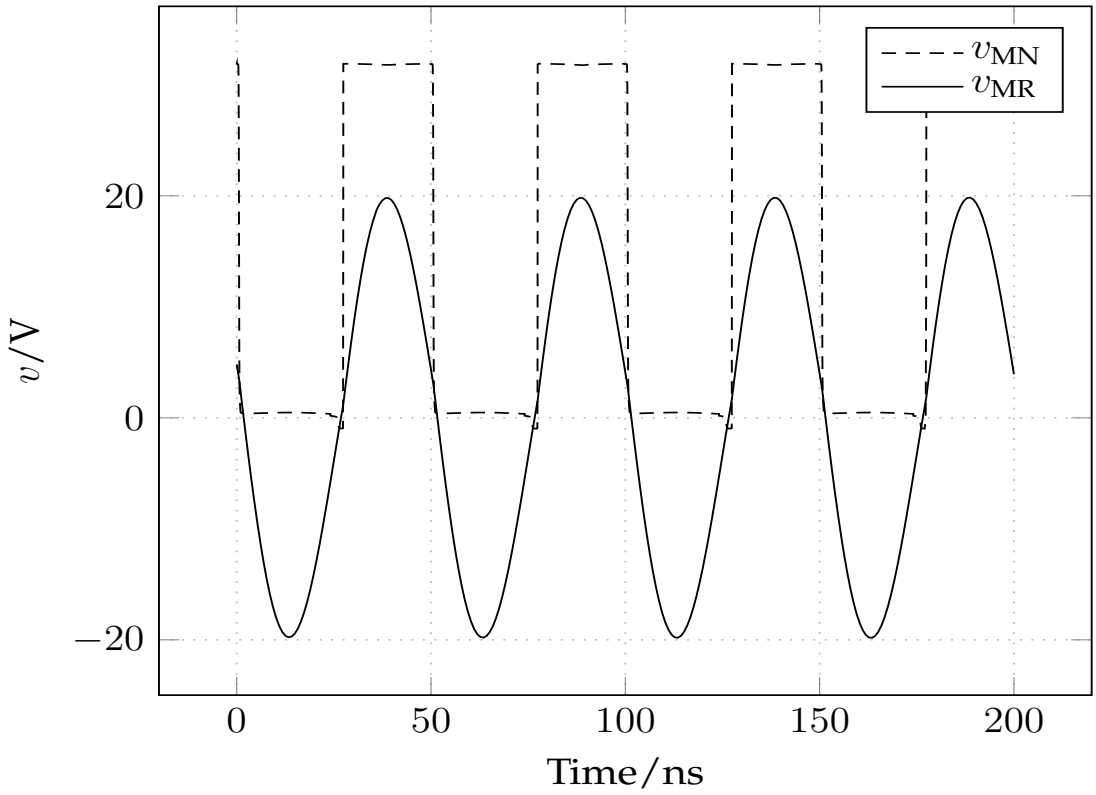

Fig. 2.39. Class M implementation, voltages.

of about $\eta = 96\%$. The consumed power was 5.89 W, the recycled power 1.97 W and the output power 3.99 W.

2.11 Energy Recycling

Because not in all devices twice the supply voltage at a special power value is required, there is the possibility of using a special circuit for energy recycling.

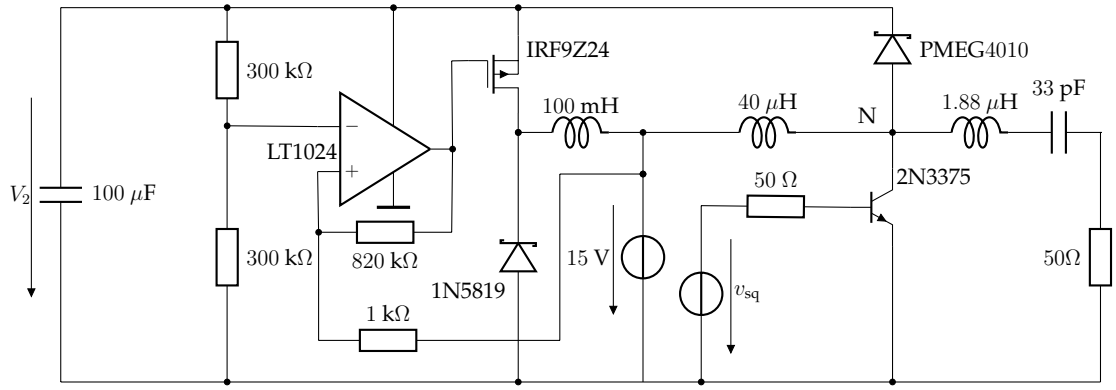

Fig. 2.40. Automatic push-pull amplifier with energy recycling unit.

Fig. 2.40 shows a class M amplifier with energy recycling circuit. With a voltage divider consisting of two 300 kΩ resistors, the input voltage is sensed and compared with

the 15 V supply voltage serving as reference voltage. The OpAmp LT1024 in Schmitt trigger configuration regulates its supply voltage to 30 V by which it is fed. Diode 1N5819 and the 100 mH inductor are the power unit of a buck converter together with the p channel MOS-FET. The efficiency of the whole circuit turns to be $\eta = 95\%$ then.

2.11.1 Efficiency Analysis by Simulation

All switched mode amplifier classes are compared in Table 2.3 regarding their parameters, where $P(15\text{ V})$ is the supply power, $P(V_2)$ the recycled power, $P(\text{be}_{\text{T1/2}})$ the control signal power at the base emitter diode and $P(50\ \Omega)$ the output power.

Class	C	D	E	F	M
$P(15\text{ V})$	4.8192 W	3.7657 W	5.0985 W	5.1585 W	5.8921 W
$V(V_2)$	-	-	-	-	31.1 V
$P(V_2)$	-	-	-	-	1.973 W
$P(\text{be}_{\text{T1}})$	218.8 mW	147.1 mW	207.88 mW	198.59 mW	206.19 mW
$P(\text{be}_{\text{T2}})$	-	147.1 mW	-	-	-
$P(50\ \Omega)$	3.5725 W	848.32 mW	4.1257 W	3.3966 W	3.9913 W
G	16.3	2.9	19.8	17.1	19.4
η	70.9 %	20.9 %	77.8 %	63.4 %	96.8 %

Table 2.3. Efficency analysis

A class C amplifier as shown in Table 2.3 is an extremely problematic topology. This is the reason, why class E and F have been created. Both of them avoid high drain-source voltage spikes by design, where class E uses a single capacitor, while class F uses an LC network. Class F is a complex and costly concept, whereas many commercial RF amplifiers are class E due to its simplicity. In every hardware setup, a parasitic capacitance between switching node and ground will occur, e.g. as transistor parasitics or winding capacitances within the choke. That means, when considering the capacitance to be the defining feature for class E operation mode, class C would only exist theoretically. As discussed before, class D is not always an advantageous design. In an RF design the efficiency will suffer a lot, when the transistors are operating close to their transition frequency. When the main target parameters for an application are efficiency and robustness, then the choice would be a class M amplifier. The efficiency can be increased a lot, when the energy reflected by the load is fed back to the power supply.

2.12 Sine Wave Excited Efficiency Analysis by Simulation

For this analysis, the amplifier is controlled with a sinusoidal signal $u_{\text{sin}} = 1\text{ V} \cdot \sin(2\pi t \cdot 1\text{ MHz}) + 2,67\text{ V}$. Since the considerations apply both to bipolar transistors and MOS-FET, here, Fig. 2.41, Fig. 2.42, MOS-FET transistors have been used.

Table 2.4 shows the efficiency of the design, Fig. 2.41, in dependence of the real valued control source impedance R_1. Table 2.5 shows the efficiency of the design Fig. 2.42 in dependence of the real valued control source impedance R_1. The optimum value of V_2 is dependent on the wave form of the control signal, Table 2.5. Comparing Table 2.4 and Table 2.5 leads to the finding that class M offers a higher efficiency in each single configuration.

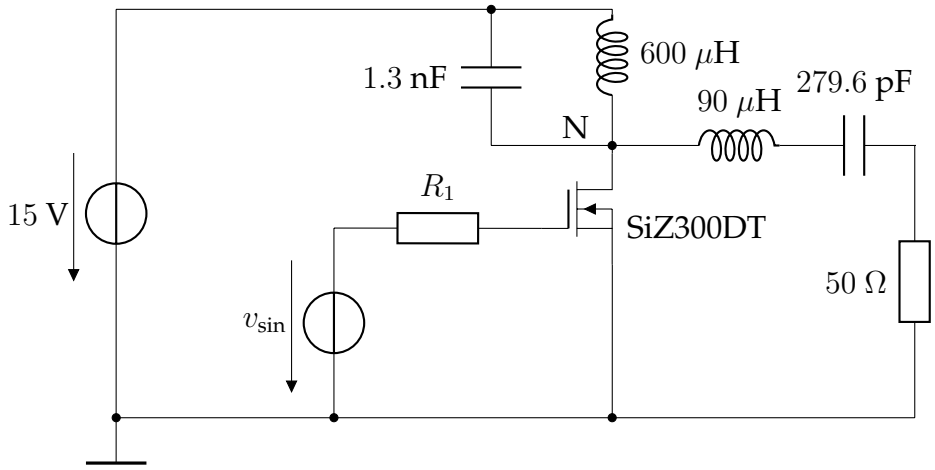

Fig. 2.41. Class C implementation

Class C				
R_1	0 Ω	5 Ω	50 Ω	100 Ω
$P(15V)$	5.31 W	5.41 W	5.93 W	6.26 W
$P(u_{\sin})$	887 μW	1.31 mW	3.07 mW	3.59 mW
$P(50\Omega)$	3.90 W	3.96 W	4.18 W	4.16 W
G	4397	3023	1362	1159
η	73.4 %	73.2 %	70.5 %	66.4 %

Table 2.4. Efficency analysis class C

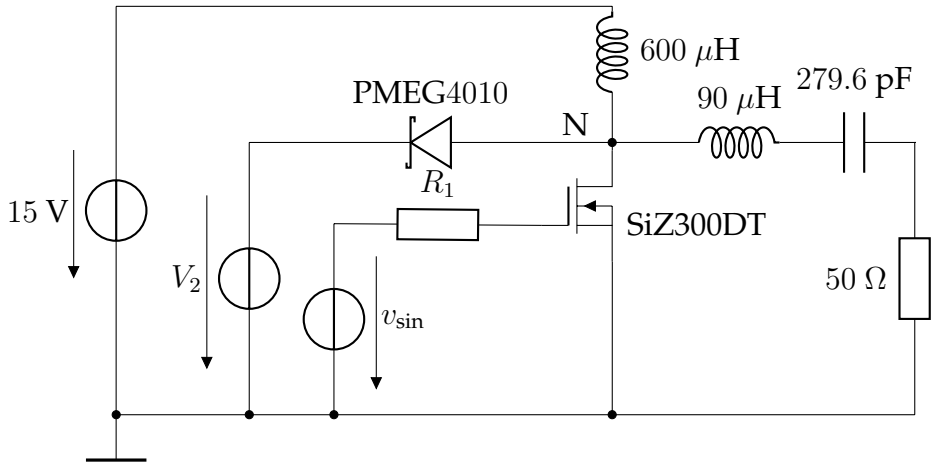

Fig. 2.42. Class M implementation

Class M				
R_1	0 Ω	5 Ω	50 Ω	100 Ω
$P(15V)$	5.69 W	5.80 W	6.06 W	6.16 W
V_2	29.8 V	30.2 V	32.6 V	34.9 V
$P(V_2)$	1.68 W	1.51 W	824 mW	413 mW
$P(v_{\text{sin}})$	390 μW	831 μW	2.87 mW	3.58 mW
$P(50\Omega)$	3.63 W	3.72 W	4.06 W	4.21 W
G	9308	4477	1415	1176
η	90.5 %	86.7 %	77.5 %	73.2 %

Table 2.5. Efficiency analysis, class M

2.13 Measurements

For a quick evaluation, a test realization was implemented using a driver stage similar to the circuit described in [31]. The control signal was provided by the function generator HP 3314A, the output power was measured with an RF thermocouple power meter [32], while for the DC parameters a Keithley 172 DMM was used. Selected transistors, silver wire coils and low loss silver mica capacitors helped increasing the efficiency. Since a suitable Schottky diode was not available, a selected base emitter diode of a transistor was preferred, so the optimum point of operation moved to higher voltages and the peak efficiency was a bit lower than in the simulation, as Table 2.6 shows.

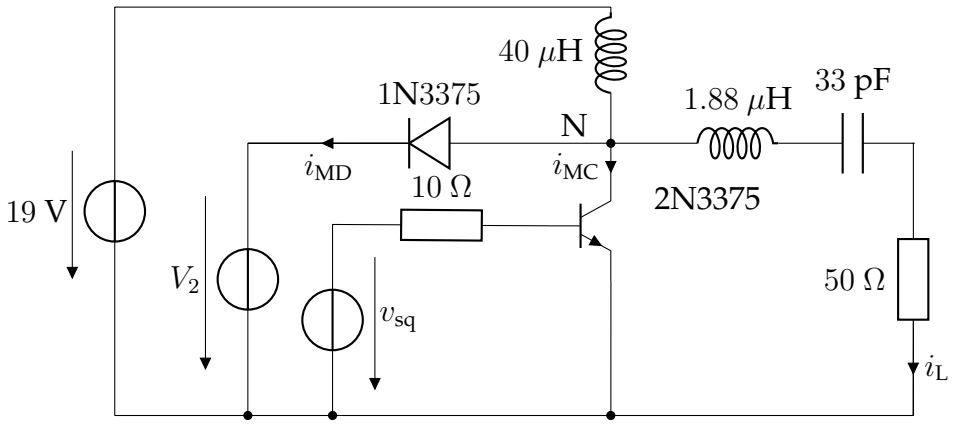

Fig. 2.43. An example of the automatic push-pull amplifier.

Class M	Mesurement
$P(19\text{ V})$	8.4 W
$V(V_2)$	38 V
$P(V_2)$	2.3 W
$P(\text{be}_{\text{T1}})$	300 mW
$P(50\ \Omega)$	5.8 W
G	19.33
η	91 %

Table 2.6. Efficency analysis

Up to now, the highest efficiency with transistors of type 2N3375 has been reached at a current consumption of 440 mA and 19 V supply voltage and an input signal of 20 MHz with $\eta = 91\ \%$ for the class M prototype.

2.14 Another New Concept: Class N

Class M topology discussed in subsection 2.9 feeds back energy at twice the supply voltage. Without the LC output network, this topology behaves like a boost converter. It is also possible generating a square wave signal at node N while feeding back energy at the half value of the original supply voltage. Fig. 2.44 shows class N topology. In comparison to class M, the elements $D,\ L_\mathrm{S}$ and S changed their location clockwise. Fig 2.46

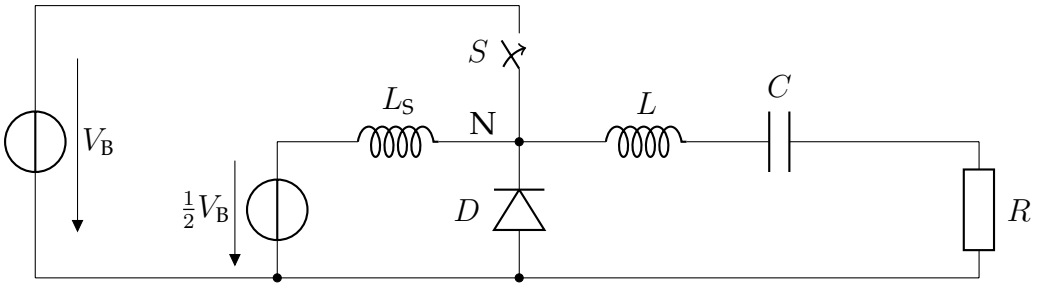

Fig. 2.44. Automatic push-pull amplifier, class N

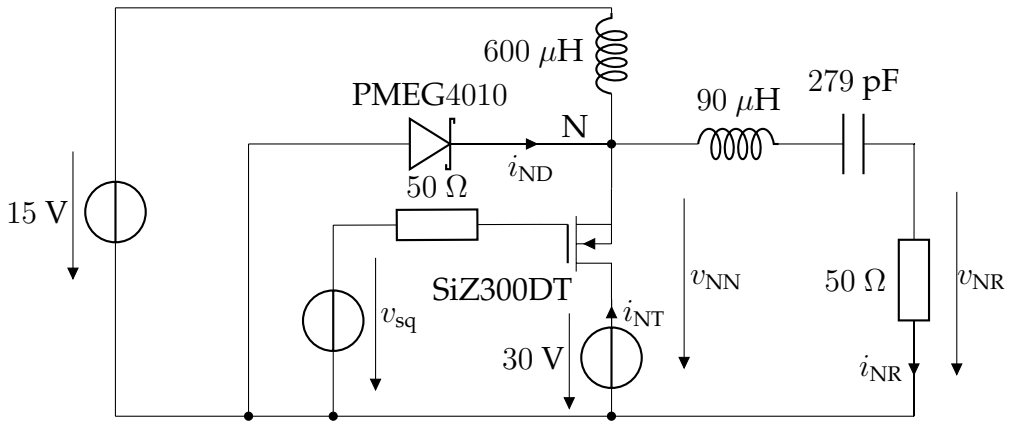

Fig. 2.45. Class N amplifier

shows the output current i_NR, the drain current i_NT and the diode current i_ND. The DC component is blocked by a capacitor as Fig. 2.47 shows, where v_NN is the collector voltage and v_NR the output voltage. According to the simulation an efficiency of $\eta = 98.5\ \%$ was achieved. In this circuit a bigger edge frequency is reached with the transistor acting as source follower.

2.15 Optimum Size of RF Power Components

After reviewing established PA topologies, the novel class M concept was introduced. The topology has been optimized theoretically [33]. This section is a summary of the findings during this master's thesis. As a further step towards a practical implementation of the

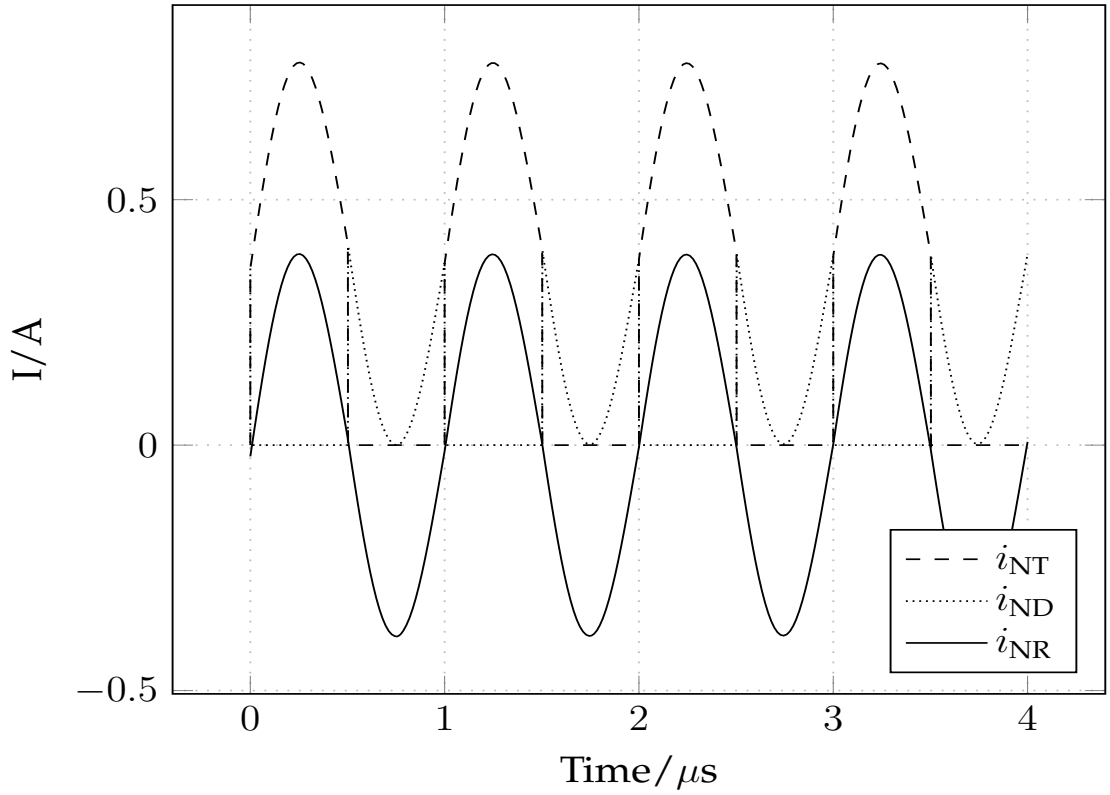

Fig. 2.46. Class N amplifier, current

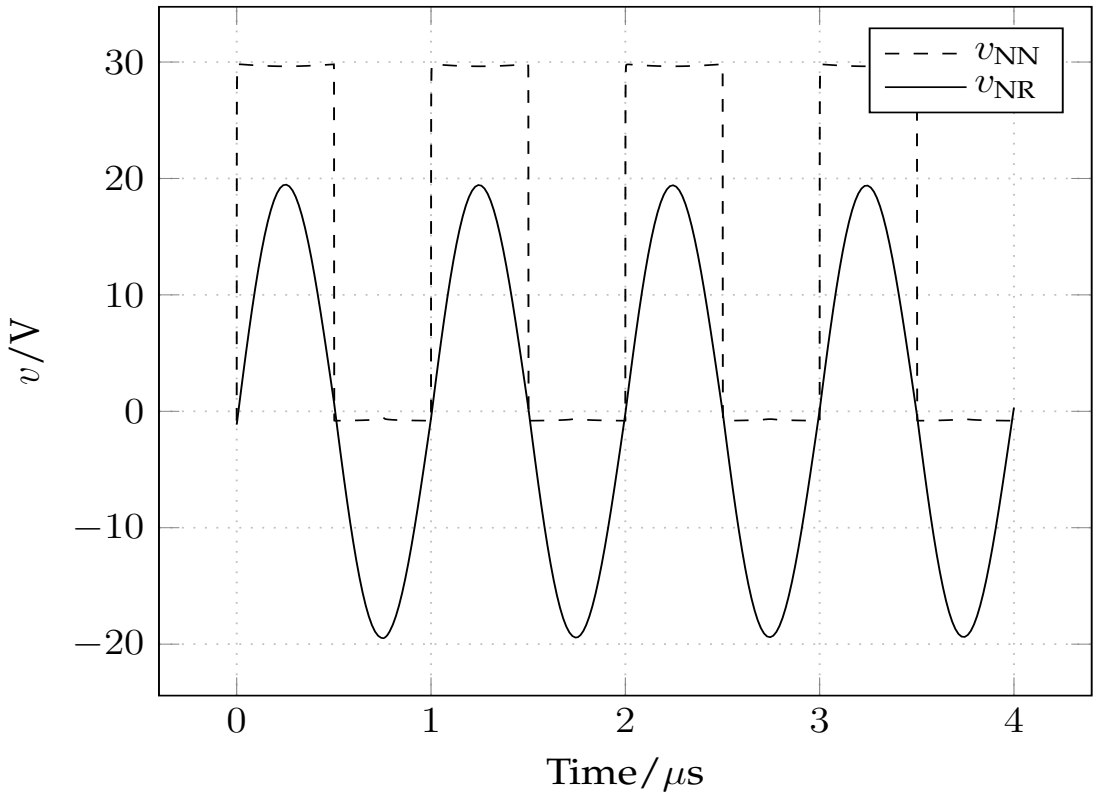

Fig. 2.47. Class N amplifier, voltage at Node N

class M amplifier, all different circuit components will be examined, especially regarding their non-idealities. Beside the passive components, which are just treated in order to provide a complete picture, the focus will be on the semiconductor devices involved in the class M amplifier. The following discussion should on the one hand raise the awareness of the behavior and the deployability of the presented circuits' components in the context of RF power applications and on the other hand serve as a feasibility analysis of class M concept in order to evaluate its practical relevance.

2.15.1 Detailed Class M Amplifier Analysis

The previous results motivate analyzing the impact of diode and transistor size on class M amplifier performance. As a first step towards finding an answer to the question, if an optimal scaling of the switching devices exists for the class M amplifier in Fig. 2.48, its operation is analyzed in detail.

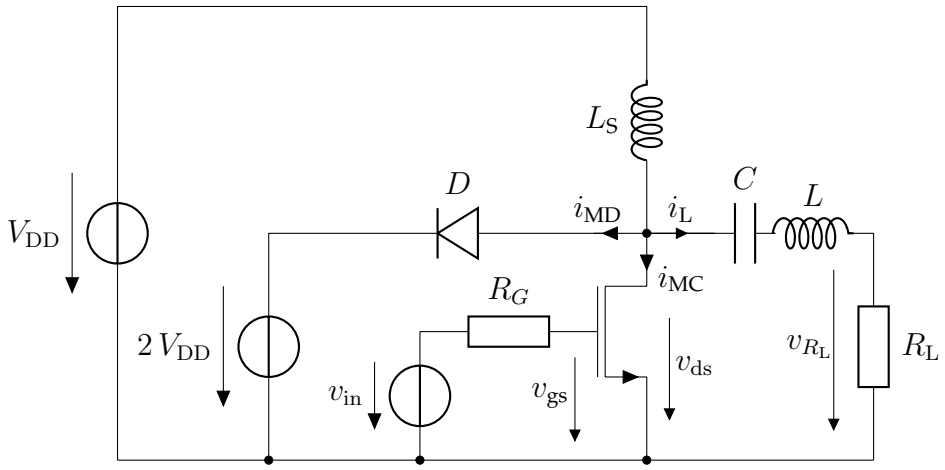

Fig. 2.48. Class M power amplifier analysis

The FET comprises a non-zero input capacitance, which requires a non-zero generator resistance R_G in order to guarantee a non-zero time constant and thus finite current transients. The ideal waveforms of the voltages and currents at the drain node are shown qualitatively in Fig. 2.49.

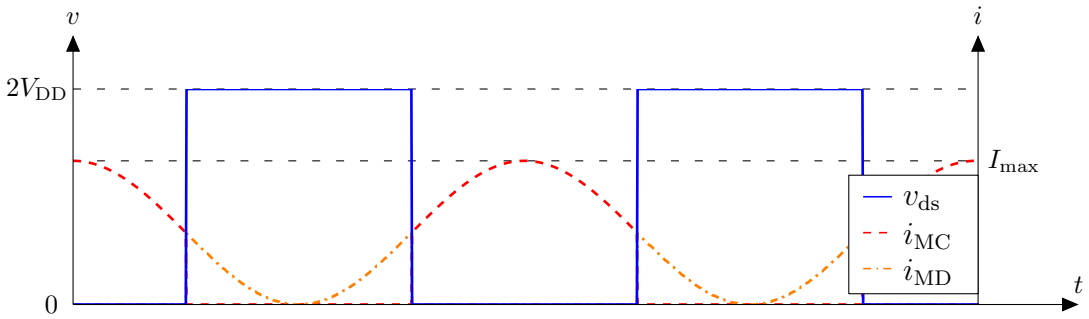

Fig. 2.49. Class M voltage and current waveforms

The drain-source voltage (solid) is shaped as the desired square wave. The dashed curve is the drain current i_{MC} of the transistor, which is essentially zero while v_{ds} is greater

than zero. During the off-phase of the transistor, the diode takes over the current (dash-dotted curve) and during the residual time of the signal period it is reversely biased. The combination of the drain current and the current through the diode results in the desired sinusoidal current through the load resistance R_{L}. In order to explain the waveforms from Fig. 2.49 the important parts of the class M amplifier are reviewed. Proper class M operation in steady state is assumed meaning that the voltage v_{ds} between drain and source of the transistor hereafter is a square wave ranging between 0 and $2V_{\mathrm{DD}}$ with a frequency of f_0.

2.15.2 Output Filter

First of all the impact of the LC series resonator at the output is considered, which is depicted in Fig. 2.50 together with the load resistor R_{L}. The following equations describe

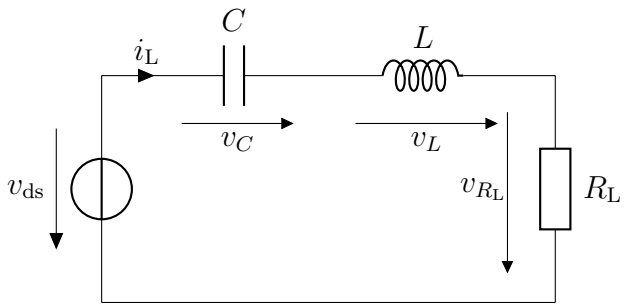

Fig. 2.50. Class M output filter

the behavior of the resistive and reactive components:

$$\frac{\mathrm{d}}{\mathrm{d}t}v_C = \frac{1}{C}i_{\mathrm{L}}, \tag{2.23}$$

$$v_L = L\frac{\mathrm{d}}{\mathrm{d}t}i_{\mathrm{L}}, \tag{2.24}$$

$$v_{R_{\mathrm{L}}} = R_{\mathrm{L}}i_{\mathrm{L}}. \tag{2.25}$$

Based on Kirchhoff's Voltage Law,

$$v_{\mathrm{ds}} = v_C + v_L + v_{R_{\mathrm{L}}}, \tag{2.26}$$

the second order differential equation

$$\frac{\mathrm{d}}{\mathrm{d}t}v_{ds} = \frac{1}{C}i_{\mathrm{L}} + R_{\mathrm{L}}\frac{\mathrm{d}}{\mathrm{d}t}i_{\mathrm{L}} + L\frac{\mathrm{d}^2}{\mathrm{d}t^2}i_{\mathrm{L}}, \tag{2.27}$$

is set up. As shown in section 2.9, the output filter is chosen such, that the output current is the fundamental sine wave and harmonics can be neglected. Fig. 2.51 shows the transfer curve for the transfer function

$$H(\mathrm{j}\omega) = \frac{R_{\mathrm{L}}}{R_{\mathrm{L}} + \mathrm{j}\omega L + \frac{1}{\mathrm{j}\omega C}}, \quad v(\omega) = 20 \cdot \log\left|\frac{H(\mathrm{j}\omega)}{H(\mathrm{j}\omega_0)}\right| \mathrm{dB}, \tag{2.28}$$

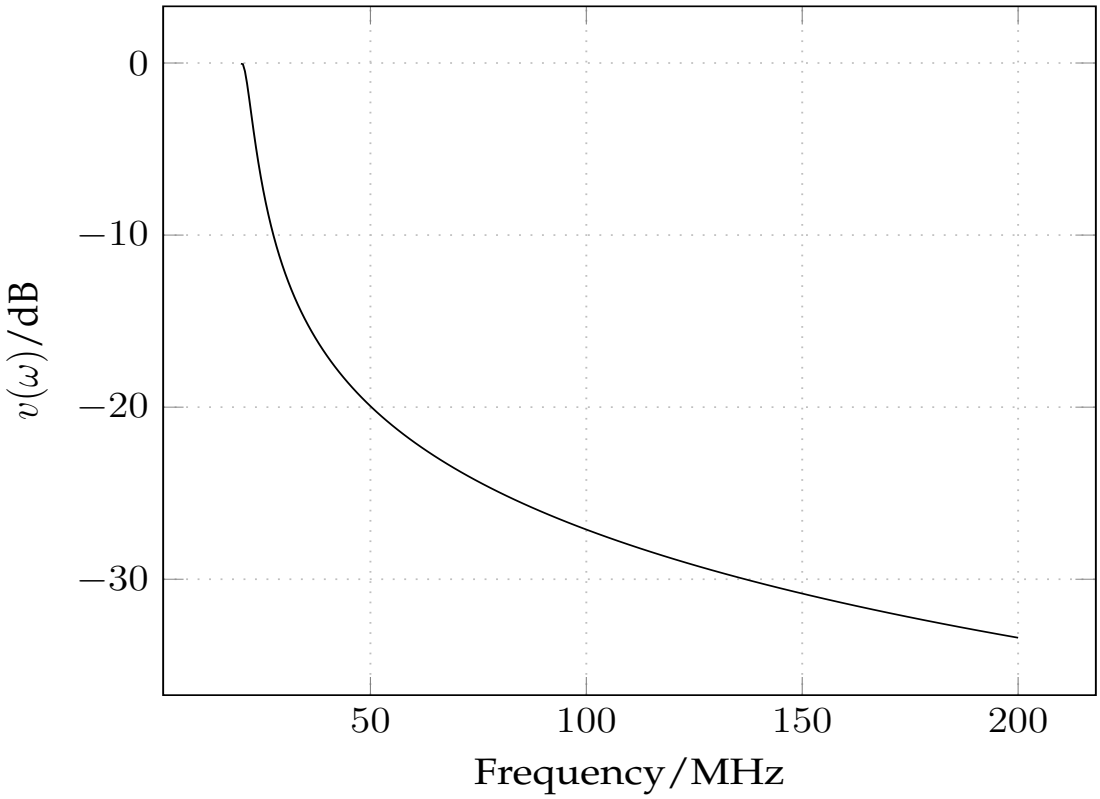

Fig. 2.51. Output filter transfer curve

of the filter implemented in the circuit of Fig. 2.37 from 20 MHz up to 200 MHz. At 60 MHz the attenuation is 22 dB, so the output signal is approximately sinusoidal and the complex phasor calculation is allowed to be used.

$$i = \frac{V_0}{|Z|}\sin(\omega t - \phi), \tag{2.29}$$

using the following definitions [34, p.153], where $|Z|$ is the absolute impedance value and ϕ the phase angle:

$$Z = R_\mathrm{L} + \mathrm{j}X = |Z|e^{\mathrm{j}\phi} \tag{2.30}$$

$$|Z| = \sqrt{R_\mathrm{L}^2 + X^2} \tag{2.31}$$

$$X = \omega L - \frac{1}{\omega C} \tag{2.32}$$

$$\tan(\phi) = \frac{X}{R_\mathrm{L}} = \frac{\omega L - \frac{1}{\omega C}}{R_\mathrm{L}} \tag{2.33}$$

The resonance condition $X = 0$, where the amplitude of the current i is maximal, results in the definition of the resonance frequency ω_0.

$$X = \omega_0 L - \frac{1}{\omega_0 C} = 0 \qquad\qquad \omega_0 = \frac{1}{\sqrt{LC}} \tag{2.34}$$

At resonance frequency, the phase shift ϕ between the voltage across the RLC series resonator and the current is zero. In the case of the class M amplifier the excitation voltage v_{ds} is a square wave, thus it is the sum of the sine waves at the odd harmonics of the fundamental frequency. Only that part of the signal will pass through the RLC-filter unchanged, whose frequency equals the resonance frequency and all other signal parts will be attenuated and phase shifted. Consequently, the only effectual voltage component across the R_{L} for the LC circuit tuned to $f_0 = \frac{1}{2\pi\sqrt{LC}}$ is the sine wave at the fundamental frequency causing an in-phase sinusoidal current through the load. As the RLC-filter attenuates any signal parts apart from the resonance frequency and therefore also DC, the sinusoidal load current is bias-free. Under resonance conditions, the amplitude $\hat{I}$ of the load current is solely determined by V_{DD} and the load resistance R_{L} using (2.29) and the definition of κ_{ssq} from (2.36),

$$\hat{I} = \frac{\kappa_{\mathrm{ssq}} \cdot V_{\mathrm{DD}}}{R_{\mathrm{L}}}, \tag{2.35}$$

$$\kappa_{\mathrm{ssq}} = \frac{4}{\pi} \approx \frac{1}{0.7854} \approx 1.273. \tag{2.36}$$

For an amplifier implementation, the output filter bandwidth B_{w} is chosen according to the application. With the help of the quality factor

$$Q = \frac{f_0}{B_{\mathrm{w}}}, \tag{2.37}$$

and its direct expression, the parameters of the circuit components are calculated

$$Q = \frac{1}{R_{\mathrm{L}}}\sqrt{\frac{L}{C}} = \frac{\omega_0 L}{R_{\mathrm{L}}} = \frac{1}{\omega_0 R_{\mathrm{L}} C}. \tag{2.38}$$

2.15.3 DC-Feed Network

Reconsidering Fig. 2.49, the currents through the diode and the transistor add up to a sinusoid. This combined current equals the load current but contains a DC component of $\hat{I} = I_{\max}/2$ as it cannot drop below zero due to the fact that besides leakage currents neither a diode nor a n-channel FET conducts negative currents. As described above, the RLC-filter at the the output however allows only AC components at its resonance frequency to pass and therefore blocks any DC currents. In order to fulfill Kirchhoff's Current Law at the drain node, the DC offset $I_{\max}/2$ has to be delivered by the DC-feed network consisting of V_{DD} and L_{S}. Based on the differential description of the inductance

$$v_{L_{\mathrm{S}}} = L_{\mathrm{S}} \frac{\mathrm{d}}{\mathrm{d}t} i_{L_{\mathrm{S}}}, \tag{2.39}$$

the integral form can be written as follows

$$i_{L_{\mathrm{S}}}(t) = i_{L_{\mathrm{S}},0} + \frac{1}{L_{\mathrm{S}}} \int_{t_0}^{t} v_{L_{\mathrm{S}}}(\tau) d\tau. \tag{2.40}$$

After a certain time of settling at t_0, the integral part evaluated over one signal period is zero due to the symmetry of the voltage $v_{L_{\mathrm{S}}}$, which is a square wave ranging between

$-V_{\mathrm{DD}}$ and $+V_{\mathrm{DD}}$. Consequently, after t_0 the energy stored in the inductor does not change from period to period.

$$E_{L_\mathrm{S}}(t) = \frac{1}{2} L_\mathrm{S} i_{L_\mathrm{S}}^2(t) = \frac{1}{2} L_\mathrm{S} i_{L_\mathrm{S}}^2(t+T) = E_{L_\mathrm{S}}(t+T) \tag{2.41}$$

During the positive half wave of v_{L_S}, the inductor current rises and the stored energy is increased by some ΔE. In the other half of the signal period, this process is reversed and ΔE is passed on to the amplifier circuit. After the settling, i_{L_S} can be viewed as almost constant under the condition that L_S is sufficiently large. (2.40) with L_S in the denominator implies, that for large inductance values, the change in current is small and therefore ΔE is small compared to the overall energy stored in the inductor. Due to the relatively small changes in i_{L_S} the DC-feed inductor L_S and the voltage source V_{DD} can be replaced by a single ideal current source of constant value $I_{\mathrm{OP}} = I_{\max}/2$ that equals the average current through the inductor.

2.15.4 Power Efficiency

With the previous insights, the class M operation can be explained from the viewpoint of energy. During the transistor's off-phase, the energy stored in the DC-feed inductor L_S decreases, while during the transistor's on-phase the stored inductor energy increases. So, the total stored energy does not change over one signal period with the system in steady state operation. Therefore, ΔE is the entire energy drawn from the power supply in one signal period. This energy is proportionally distributed over the different spectral components of the square wave at the drain node. Which part of the energy is passed on to the load, is determined depending on which frequency components can pass the RLC-filter. The key feature of class M concept is that energy of all other spectral components reflected by the output filter is not transformed into heat loss inside the transistor, but fed back to the power supply via the diode. As a side effect, the energy recovery protects the amplifier from destruction in case of a mismatched load as the reflected power is kept away from the transistor and redirected to the supply. Of course, a small part of ΔE will unavoidably be transformed into heat, but these losses are due to finite on- and off-resistances and switching speeds of the circuit components, and are not caused by the amplifier topology. Given a signal period of T, the energy consumption E_{OP} from the supply, where I_{OP} is the supply current, the energy E_{in} drawn from the signal source, the output energy E_{load} and the recovered energy E_{r} can be specified by

$$E_{\mathrm{OP}} = \int_{t_0}^{t_0+T} I_{\mathrm{OP}} \cdot v_{\mathrm{ds}}(t) dt, \tag{2.42}$$

$$E_{\mathrm{in}} = \int_{t_0}^{t_0+T} \frac{v_{\mathrm{in}}(t)\left(v_{\mathrm{gs}}(t) - v_{\mathrm{in}}(t)\right)}{R_{\mathrm{G}}} dt, \tag{2.43}$$

$$E_{\mathrm{load}} = \int_{t_0}^{t_0+T} \frac{v_{R_\mathrm{L}}^2(t)}{R_{\mathrm{L}}} dt, \tag{2.44}$$

$$E_r = \int_{t_0}^{t_0+T} 2 V_{\mathrm{DD}} i_{\mathrm{MD}}(t) dt, \tag{2.45}$$

$$\tag{2.46}$$

$$\eta_{\mathrm{ClassM}} = \frac{E_{\mathrm{load}}}{E_{\mathrm{OP}} - E_{\mathrm{r}}} \tag{2.47}$$

and

$$\mathrm{PAE}_{\mathrm{ClassM}} = \frac{E_{\mathrm{load}} - E_{\mathrm{in}}}{E_{\mathrm{OP}} - E_{\mathrm{r}}}. \tag{2.48}$$

The previous formulas highlight the fundamental difference between the class M amplifier and other switched-mode PA concept: The idea of energy recovery. In the denominator, the recovered energy is subtracted from the DC power consumption leading to a high efficiency.

2.16 Simulating Class M Operation with Linear Models

2.16.1 Parameters

The general degrees of freedom during the amplifier design are:

1) Diode area A_j and FET dimensions W, L
2) Operating frequency f_0
3) Load impedance (R_{L} and filter Q), supply voltage V_{DD} and the DC-feed inductance L_{S}
4) Signal source (waveform, amplitude V_G, R_{G})

In order to reduce the number of unknowns and thereby the complexity of the analysis, the different system aspects from the above list are reviewed and decisions are made, which parameters are to be left free and which are to be defined. If not explicitly declared otherwise, the values specified hereafter apply for all later simulations.

2.16.2 Size of The Switching Devices

The influence of the diode and transistor size on the amplifier behavior is eminently pronounced. Thus A_{j} and W are among the most important parameters for the intended investigation. In general, this is also true for the transistor length L. Nevertheless, L is fixed to the minimum value L_{min} of the technology node due to the fact that in the used transistor model an increase in L will lead to an augmentation of the transistor resistance and the parasitic capacitances and therefore always to a degradation of the system performance. In more sophisticated transistor models with included short channel effects, an increasing L may possibly improve the transistor properties.

2.16.3 Operating Frequency

Like other switched-mode PA topologies, the class M amplifier exhibits a close to hundred percent efficiency when realized at low frequencies, where the imperfections and parasitics of the involved components are negligible. One goal of this work is examining the class M concept also at higher frequencies. The operating frequency is therefore an important degree of freedom.

2.16.4 Load Impedance and Supply Voltage

Load impedance and supply voltage basically determine the achievable output power. Under ideal conditions, the power delivered to the load reads

$$P_{\mathrm{load}} = \frac{\left(\kappa_{\mathrm{ssq}} V_{\mathrm{DD}}\right)^2}{2R_{\mathrm{L}}}. \tag{2.49}$$

For scaling the available output power, one of the parameters V_{DD} and R_{L} is sufficient. By choice, V_{DD} is set to $10\ \mathrm{V}$ and R_{L} remains a free variable. The inductance L_{S} is determined based on the operating frequency; the larger f_0 the smaller L_{S} needs to be. Used values are for instance $L_{\mathrm{S}} = 50\ \mu\mathrm{H}$ at $10\ \mathrm{MHz}$, $L_{\mathrm{S}} = 5\ \mu\mathrm{H}$ at $100\ \mathrm{MHz}$, et cetera. The influence of the filter bandwidth on the system performance has to be eliminated when comparing the amplifier for varying load resistances and different frequencies. Therefore, a constant quality factor $Q = 10$ is specified. Despite of the possibility to extract any of the odd harmonics, we will restrict the discussion to the fundamental sine wave at f_0, to which the resonance frequency of the filter is tuned.

2.16.5 Signal Source

As the class M amplifier is non-linear with respect to the signal envelope, the waveform of the input signal can be chosen freely. The waveform of the input voltage is set to a square wave with amplitude V_{DD}, which enables the fastest possible switching as well as driving the transistor strongly into the linear region. The generator resistance R_{G} primarily affects the time constant at the gate node and thus the switching speed of the transistor. Changes in R_{G} will for sure move the optimal point, however the general behavior of the class M amplifier, meaning the dependencies on A_{j}, W, f_0 and R_{L}, are not changed. For the intended investigation of the class M concept, the choice of R_{G} is of no particular interest and therefore $R_{\mathrm{G}} = 5\ \Omega$ is determined.

2.17 Simplifications and Simulation Procedure

Analyzing the class M amplifier in LTspice by Linear Technology (SPICE) by manually varying the different variables is an extremely tedious and thus not feasible approach. Furthermore, numerical issues and convergence problems may arise due to the non-linearity of the circuit, which will complicate the identification of consistent parameter dependencies. In the previous part the benefits of using linear models in matrix laboratory (MATLAB) when it comes to manifold parameter variations or optimization were demonstrated. Especially the parameter dependencies always come out consistent and clear. Thus several adjustments and simplifications will be necessary. Considering all reactive components from the basic class M amplifier in Fig. 2.48 and all parasitic elements originating from the the transistor and the diode, reveals that the amplifier comprises in total the following seven reactances:

- the DC-feed inductor L_{S}
- the LC filter consisting of L and C
- the parasitic diode capacitance C_{d}
- the parasitic FET capacitances C_{gs}, C_{ds} and C_{gd}

Even if the piecewise device models are used, the required effort for deriving the system descriptions for the different phases of the switching is unacceptable. It is out of all proportion to the possible advantages of a MATLAB implementation over simply using SPICE. Simplifications leading to a reduction of the system order are therefore indispensable for an analytical approach. Besides the three parasitic capacitances of the switching devices, which are of major interest and therefore have to remain in the circuit, all other reactances are possible candidates for a replacement. All assumptions and simplifications introduced are of course to be verified in the end by comparative simulations. Steady state conditions are always assumed in following.

2.17.1 Output Filter Replacement

Finding a replacement for the RLC-filter at the output is highly desirable, as two reactances could be potentially removed and the system thereby could by simplified tremendously. In principle, the effect of the output filter can be emulated under the condition that the waveform of the drain-source voltage v_{ds} is known. By applying the fourier transform (FT) to v_{ds} the amplitudes of its spectral components are obtained. Then the factor of attenuation and the phase shift for each spectral component is determined by evaluating the frequency dependent impedance of the RLC filter for all found frequencies in the spectrum. The amplitudes of the spectral components together with the impedance of the RLC network yield all spectral components of the load current, which added up result in the overall load current. Once the load current is known, the RLC network can be substituted by a current source, whose current equals the calculated load current. Obviously, the load current is a result of the simulation and cannot be predicted a priori. Determining the load current turns out to be a chicken-and-egg problem: For the calculation of the load current the drain source voltage has to be known. But in order to obtain v_{ds} we already have to known the load current, because the linear device models are initialized based on the current flowing through it. Without a proper linearization point for the switching devices, a correct calculation of v_{ds} is not possible. As a solution to this problem of cause and effect, the following iterative simulation procedure was developed. Based on the predefinition, that the output filter is tuned to the fundamental frequency f_0, the amplitude of the resulting ideal output current is determinable solely based on the supply voltage, the ratio κ_{ssq} between a square wave and its related fundamental sine component and the load resistance R_{L} (see 2.35). As all of these three parameters are known, the ideal output current can be estimated a priori. Using this (or any other realistic) estimation of the current $i_{\mathrm{L}}^{(1)}$, the linear device models are initialized with the average of the estimated current being used as a pseudo bias point. Then the switching is simulated for the first time. Due to the imperfections of the semiconductor components, the resulting waveform $v_{ds}^{(1)}$ of the drain-source voltage will deviate from the ideal square wave and will be closer to reality. The simulated drain-source voltage is periodically continued and its spectrum is analyzed using the FT. Afterwards, the load current is calculated using the FT results as described above yielding a new estimation of the load current $i_{\mathrm{L}}^{(2)}$. Finally, the calculation of the drain source-voltage is restarted with the new estimate $i_{\mathrm{L}}^{(2)}$ resulting in a better estimation $v_{ds}^{(2)}$. This procedure is repeated several times, until a the estimation $i_{\mathrm{L}}^{(n)}$ and the resulting current $i_{\mathrm{L}}^{(n+1)}$ are nearly equal. Between the single iterations the amplitude

of the estimated current is adjusted in the following way: If the resulting current is larger than the estimation, the estimated current is increased; if the resulting current is lower than the estimation, the estimated current is decreased. The termination criterion is defined such that the relative deviation of the peak values of the estimated and the resulting current lies below $1\ \%$. For the comparative simulations with SPICE the output filter is not replaced by a current source. In this way the developed simulation procedure can be verified.

2.17.2 DC-Feed Network Replacement

A great advantage of this idealization is the reduced settling time of the system during the simulation, as the current through the inductance L_S does not have to build up, which usually takes some time due to its large value. Fig. 2.52 shows the resulting circuit.

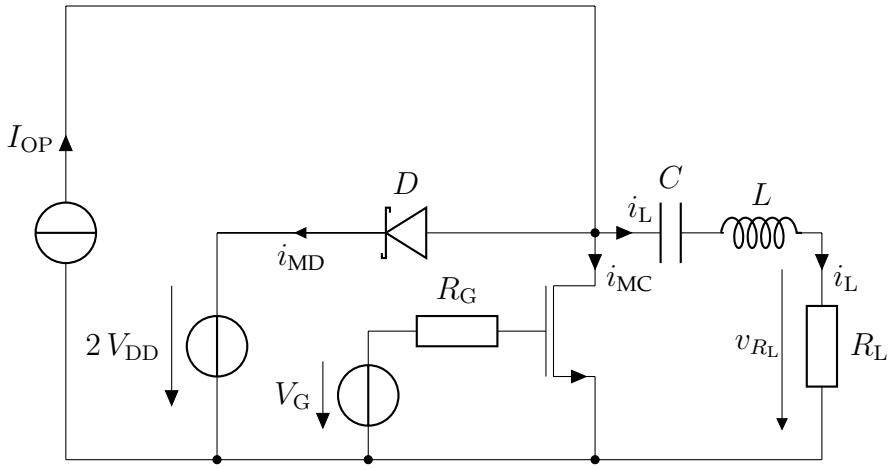

Fig. 2.52. Idealized class M power amplifier

The arising question is, what is the value of I_OP? Like for the output current above, its value cannot be determined a priori. Two different approaches are possible.

2.17.3 Option A: Identify I_OP with the Peak Output Current

The only clue regarding the problem of estimating I_OP is provided by the waveforms of the ideal class M amplifier. Lacking any other option, it is assumed that $I_\mathrm{OP} \approx \hat{I}_\mathrm{load}$ is valid also in the case of non-ideal components. The iterative computation of the load current introduced in the previous subsection provides therefore also the value of I_OP. For the reference simulations in SPICE the value of I_OP were adjusted, until the peak output current and I_OP roughly coincide within a tolerance of less than 1 %.

2.17.4 Option B: Co-Simulations in LTSpice

A different approach is using SPICE for computing the value of I_OP and fed the result to the MATLAB simulation. The idea behind this approach becomes apparent, when optimization is considered: In the proximity of the nominal point simulated by in SPICE, the deviation of the original non-linear circuit and its linear approximation is small. Around the nominal point the linearized circuit is optimized and the result is fed back to the SPICE

simulation for the computation of the next nominal point. During the single iteration steps, it can be verified, whether an improvement was actually achieved. For a reasonable estimation for arbitrary parameter values an interpolation of a sufficiently high number of sampling points is used. As the estimation of the on-resistances of the diode and the transistor is not very accurate and therefore the interpolated values from SPICE are used. This especially is necessary for the FET, as the Shichman-Hodges equations predict the on-resistance quite bad. In fact, also in the implementation of option A an adjustment of $R_{ds,\,ON}$ based on SPICE simulation data is necessary in order to obtain correct results.

The two different approaches will be compared as part of the analysis of the simulation results. It should be emphasized that the underlying circuits in SPICE are different for the two options: option B exhibits the original DC-feed network, while option A uses I_{DC}, the idealization of the current source I_{OP}.

2.17.5 Simplified Class M Amplifier

The aforementioned simplifications are applied to the equivalent class M amplifier circuit in Fig. 2.53. Therefore, the two current sources can be taken together, resulting in the circuit from Fig. 2.54. Since the three parasitic transistor capacitances C_{gs}, C_{gd} and C_{ds} are connected as a loop, one capacitor voltage is redundant and one capacitor can be replaced by a controlled current source:

$$v_4 = v_2 - v_1, \quad \frac{\mathrm{d}}{\mathrm{d}t}v_4 = \frac{\mathrm{d}}{\mathrm{d}t}v_2 - \frac{\mathrm{d}}{\mathrm{d}t}v_1, \quad i_4 = \frac{C_{\mathrm{gd}}}{C_{\mathrm{ds}}}i_2 - \frac{C_{\mathrm{gd}}}{C_{\mathrm{gs}}}i_1. \tag{2.50}$$

The current source I_0 is defined by

$$I_0 = I_{\mathrm{DC}} - I_{\mathrm{load}}. \tag{2.51}$$

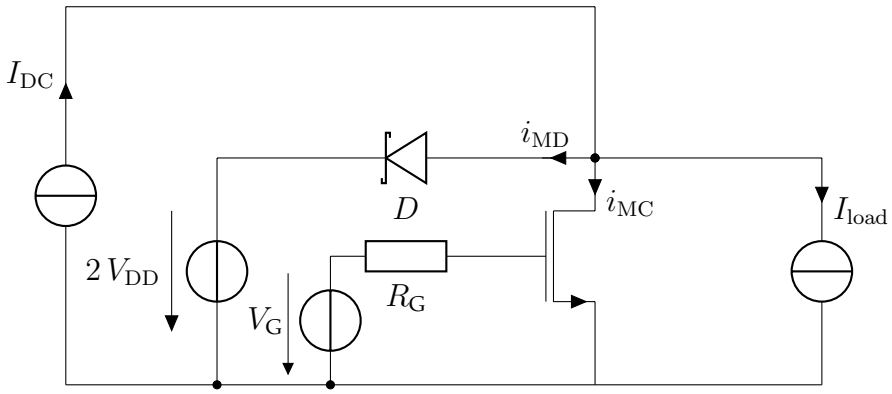

Fig. 2.53. Class M amplifier: DC-feed network and output filter replaced

2.18 Circuit Analysis

Finally, the number of reactances was reduced to three; only the parasitic capacitances are still present in the circuit. Now applying the linear device models on the circuit in Fig. 2.54 results in Fig. 2.55.

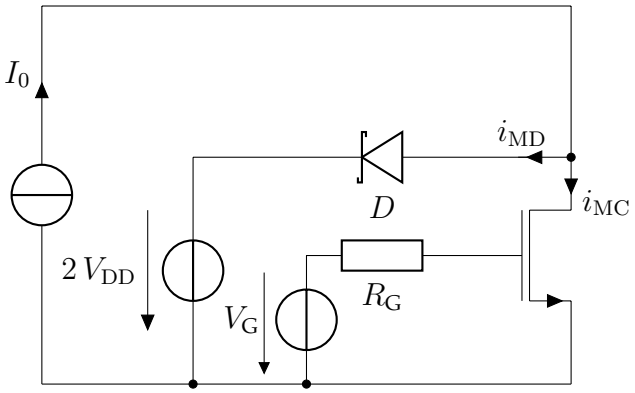

Fig. 2.54. Simplified Class M Amplifier

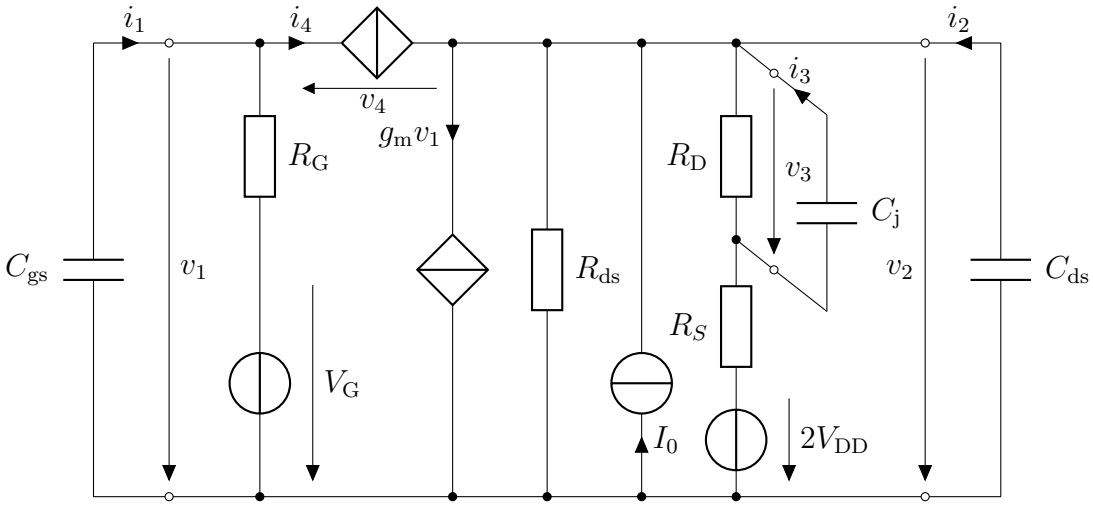

Fig. 2.55. Class M Amplifier: Equivalent Circuit for Saturation Region

We only look at the saturation region, the descriptions for cutoff and linear region are deducible from the saturation region description by adjusting R_{ds} to the respective values and setting $g_{\mathrm{m}} = 0$.

For the sake of readability the description of the resistive part is written down line by line and not in matrix-vector-notation.

$$v_1 = i_1 \cdot R_\mathrm{G}\left(1+\frac{C_\mathrm{gd}}{C_\mathrm{gs}}\right) - i_2 \cdot R_\mathrm{G}\frac{C_\mathrm{gd}}{C_\mathrm{ds}} + V_\mathrm{G} \tag{2.52}$$

$$\begin{aligned} v_2 = &-i_1 \cdot \frac{R_\mathrm{ds}(R_\mathrm{D}+R_\mathrm{S})}{R_\mathrm{D}+R_\mathrm{S}+R_\mathrm{ds}}\left[\frac{C_\mathrm{gd}}{C_\mathrm{gs}} + g_\mathrm{m}R_\mathrm{G}\left(1+\frac{C_\mathrm{gd}}{C_\mathrm{gs}}\right)\right] \\ &+ i_2 \cdot \frac{R_\mathrm{ds}(R_\mathrm{D}+R_\mathrm{S})}{R_\mathrm{D}+R_\mathrm{S}+R_\mathrm{ds}}\left[1+\frac{C_\mathrm{gd}}{C_\mathrm{ds}}\left(1+g_\mathrm{m}R_\mathrm{G}\right)\right] \\ &+ i_3 \cdot \frac{R_\mathrm{ds}(R_\mathrm{D}+R_\mathrm{S})}{R_\mathrm{D}+R_\mathrm{S}+R_\mathrm{ds}}\left(1-\frac{R_\mathrm{S}}{R_\mathrm{D}+R_\mathrm{S}}\right) \\ &+ \frac{R_\mathrm{ds}(R_\mathrm{D}+R_\mathrm{S})}{R_\mathrm{D}+R_\mathrm{S}+R_\mathrm{ds}}\left[\frac{2V_\mathrm{DD}}{R_\mathrm{D}+R_\mathrm{S}} - g_\mathrm{m}V_\mathrm{G} + I_0\right] \end{aligned} \tag{2.53}$$

$$\begin{aligned} v_3 = &-i_1 \cdot \frac{R_\mathrm{ds}R_\mathrm{D}}{R_\mathrm{D}+R_\mathrm{S}+R_\mathrm{ds}}\left[\frac{C_\mathrm{gd}}{C_\mathrm{gs}} + g_\mathrm{m}R_\mathrm{G}\left(1+\frac{C_\mathrm{gd}}{C_\mathrm{gs}}\right)\right] \\ &+ i_2 \cdot \frac{R_\mathrm{ds}R_\mathrm{D}}{R_\mathrm{D}+R_\mathrm{S}+R_\mathrm{ds}}\left[1+\frac{C_\mathrm{gd}}{C_\mathrm{ds}}\left(1+g_\mathrm{m}R_\mathrm{G}\right)\right] \\ &+ i_3 \cdot \left(\frac{R_\mathrm{ds}R_\mathrm{D}}{R_\mathrm{D}+R_\mathrm{S}+R_\mathrm{ds}}\left(1-\frac{R_\mathrm{S}}{R_\mathrm{D}+R_\mathrm{S}}\right) + \frac{R_\mathrm{D}R_\mathrm{S}}{R_\mathrm{D}+R_\mathrm{S}}\right) \\ &+ \frac{R_\mathrm{ds}R_\mathrm{D}}{R_\mathrm{D}+R_\mathrm{S}+R_\mathrm{ds}}\left[\frac{2V_\mathrm{DD}}{R_\mathrm{D}+R_\mathrm{S}} - g_\mathrm{m}V_\mathrm{G} + I_0\right] - \frac{2V_\mathrm{DD}R_\mathrm{D}}{R_\mathrm{D}+R_\mathrm{S}} \end{aligned} \tag{2.54}$$

The values of all voltage-dependent capacitances are again fixed for the voltage in the middle of the switching edge, as changing their values would require a time consuming recalculation of the eigenvalues and eigenvectors.

2.19 Accordance of Spice and MATLAB Simulation Results

Due to the numerous possible combinations of the parameters R_L, W, A_j we restrict the comparison of SPICE and MATLAB results to the following settings: $f_0 = 100\ \mathrm{MHz}$, $R_\mathrm{L} = 50\,\Omega$, $\lambda_W = 10000$ and λ_A ranges between 0.01 and 0.25, where λ_A is the area scaling factor, λ_W the width scaling factor, W the channel width and A_j the actual diode area [33, p.41].

2.19.1 Option A

The simulation results are summarized in Table 2.7, where for each value of λ_A the upper line represents the SPICE results and the lower line the MATLAB results. Within acceptable tolerances the results show great accordance. Nevertheless, the results do not meet the expectations, as the output power gets bigger and bigger the smaller the diode area is chosen. The found behavior can be reconstructed with the real amplifier circuit comprising L_S and V_DD. In order to come up with the same result, the value of the single supply voltage has to be increased while the value of double supply voltage remains unchanged. If the supply voltage is sufficiently increased, v_ds also drops never below twice the supply voltage during the second half of the period. The definition $I_\mathrm{OP} = \hat{I}_\mathrm{load}$ entails that the supply current is always as big as needed. Obviously, this is an illegitimate

λ_A	P_{DC}	P_r	P_{load}	η	I_{DC}
0.01	2.9623 W	888.82 mW	1.8165 W	87.61 %	270 mA
	2.8931 W	832.70 mW	1.7986 W	87.29 %	268 mA
0.05	2.6267 W	819.39 mW	1.6636 W	92.05 %	258 mA
	2.5846 W	778.63 mW	1.6501 W	91.37 %	257 mA
0.1	2.5615 W	748.64 mW	1.6393 W	90.43 %	256 mA
	2.5227 W	738.70 mW	1.6269 W	91.19 %	255 mA
0.25	2.4183 W	522.95 mW	1.5966 W	84.24 %	252 mA
	2.3961 W	607.31 mW	1.5881 W	88.78 %	252 mA

Table 2.7. Simulation results for the simplified class M amplifier (Option A)

over-idealization, as the original DC-feed network comprising L_{S} cannot provide arbitrary currents for a fixed supply voltage. Precisely this is the error in option A: The adjustment of I_{OP} leads implicitly to an increased supply voltage. Despite of its accuracy and independence from SPICE co-simulations, the model based on option A is therefore not usable, as a constant V_{DD} was postulated.

2.19.2 Option B

In Table 2.8 the figures simulated in SPICE and in MATLAB compared.

λ_A	P_{DC}	P_r	P_{load}	η	I_{DC}
0.01	2.2488 W	608.60 mW	1.4402 W	87.81 %	242.5 mA
	2.2436 W	536.9 mW	1.4350 W	84.08 %	242.1 mA
0.05	2.3820 W	638.10 mW	1.5798 W	90.59 %	251.9 mA
	2.3449 W	604.33 mW	1.5399 W	88.47 %	248.9 mA
0.1	2.4528 W	628.20 mW	1.6125 W	88.36 %	254.1 mA
	2.4087 W	594.3 mW	1.6079 W	88.62 %	253.8 mA
0.25	2.7800 W	763.50 mW	1.5985 W	79.27 %	252.8 mA
	2.7048 W	724.66 mW	1.6250 W	82.07 %	255 mA

Table 2.8. Simulation results for the simplified class M amplifier (Option B)

In the nominal points the accordance is adequate, but not as high as expected. Additionally, close to switching edges voltage peaks arise.

2.20 Optimal Class M Amplifier

The efficiency optimization of the class M amplifier, regardless of whether drain efficiency or power added efficiency (PAE) is considered, is a multivariate optimization problem. The optimization problem can be generally written down as follows: The objective function f is either the drain efficiency η or the PAE. As stated above, f_0 is no optimization variable but a free parameter, as we want to observe how the optimal point changes depending on the operating frequency.

2.21 Extreme Parameter Values

The consequences of setting the three parameters A_j, W R_L to extreme, meaning very small or very big, values are discussed. There are three branches connected to the DC-feed network:

- energy recovery branch with the diode and current i_r
- pull down branch with the transistor and current i_d
- load branch with the load resistor and current i_L

For given parameters A_j, W and R_L, a specific impedance level ensues in each branch. As we will see, whenever the one branch becomes very low-ohmic or very high-ohmic compared to the two remaining branches, the behavior of the entire amplifier is determined by this branch.

2.21.1 Diode Branch

If the diode is very small the energy recovery branch becomes high-ohmic resulting in large voltage spikes at the drain node. In the limit the on-resistance gets so high that it equals an open-circuit and the circuit behaves the same way, as if no diode was there at all. This operating state corresponds to class C operation and the circuit is no longer a class M amplifier. In contrast, a diode of very large area exhibits an extremely high capacitance. Under this conditions, the circuit does nothing else but generating blind current and the effective voltage of v_ds becomes zero letting the load current vanish.

2.21.2 Transistor Branch

Small FETs are not capable of pulling v_ds down close to ground potential. Thus in the limit the voltage swing of v_ds and with it the output current becomes virtually zero. Huge parasitic capacitances resulting from a large transistor lead to the same effect as a large diode capacitance. The impedance at the drain node is so low that no matter what current flows, v_ds stays close to zero. Again, there is no output power available.

2.21.3 Load Branch

For $R_\mathrm{L} \to \infty$ the behavior of the circuit is like there was no load connected (open circuit). The drain-source voltage is a perfect square wave, but no power is extracted from it. For small values of R_L the impedance is low compared to the other two branches no matter which size the diode and the transistor are. Due to the resulting high currents, the effective value of v_ds vanishes. The limit $R_\mathrm{L} = 0$ results per definition in $P_{load} = 0$, as the power consumption of a short circuit is always zero.

From this short discussion it is evident that for extreme parameter values the output power vanishes. The only exception is the small diode, but in this case the circuit leaves class M operation and large unwanted voltage spikes arise. This insight suggests the assumption that somewhere in between the extreme choices of the parameter an optimum exists.

2.22 Existence of an Optimal Point

A large number of ≈ 400 sampling points were simulated in SPICE at $100\,\mathrm{MHz}$ by sweeping R_L, λ_W and λ_A over a wide range. Now, one parameter is varied while the other two remain constant. In this way, the dependence of the efficiency on each single parameter is illustrated.

Parameter	Sim I	Sim II	Sim III
λ_A	0.001-0.5	0.1	0.1
λ_W	10000	500-30000	10000
R_L	50 Ω	50 Ω	10-120 Ω

Table 2.9. Class M Simulation Parameters

In Fig. 2.56 to Fig. 2.58 the simulated drain and power added efficiencies are depicted. The single points are interpolated for a better visibility of the overall behavior of the circuit.

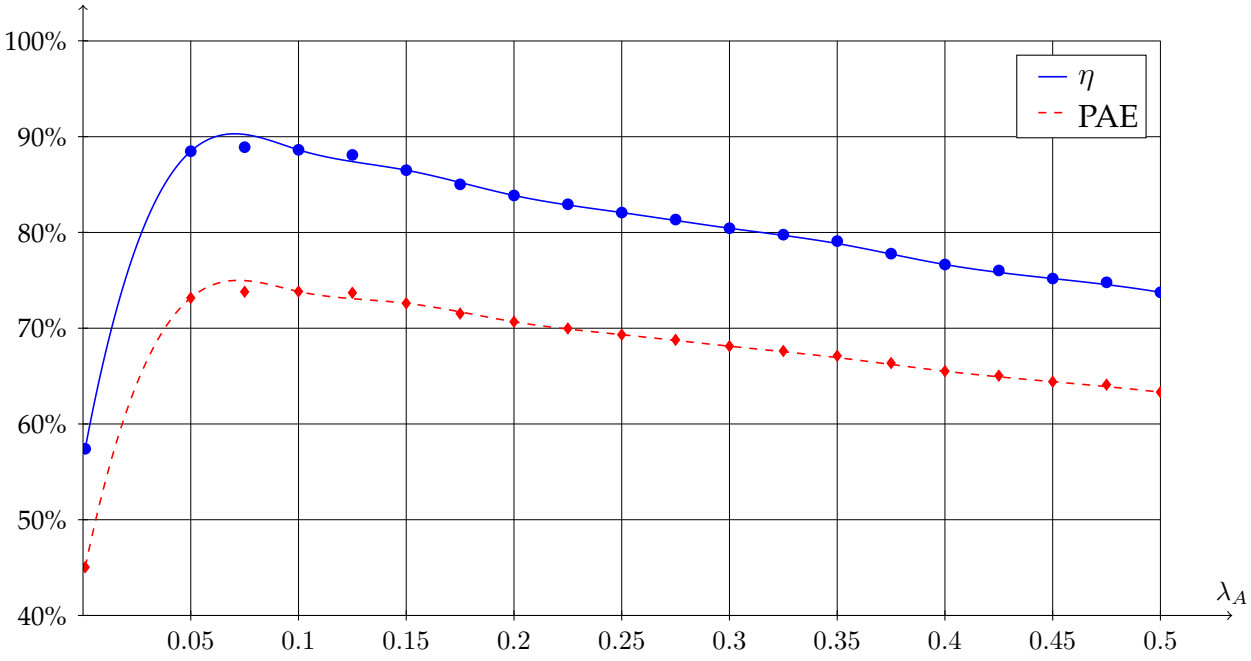

Fig. 2.56. Class M: Efficiency versus Diode Size

For all three parameters it is found, that there is one unique value where the efficiency is highest. This finding proves the proposition, that the extreme values of R_L, W and A_j are not optimal. Furthermore, the optimal points of η and PAE do not coincide leaving

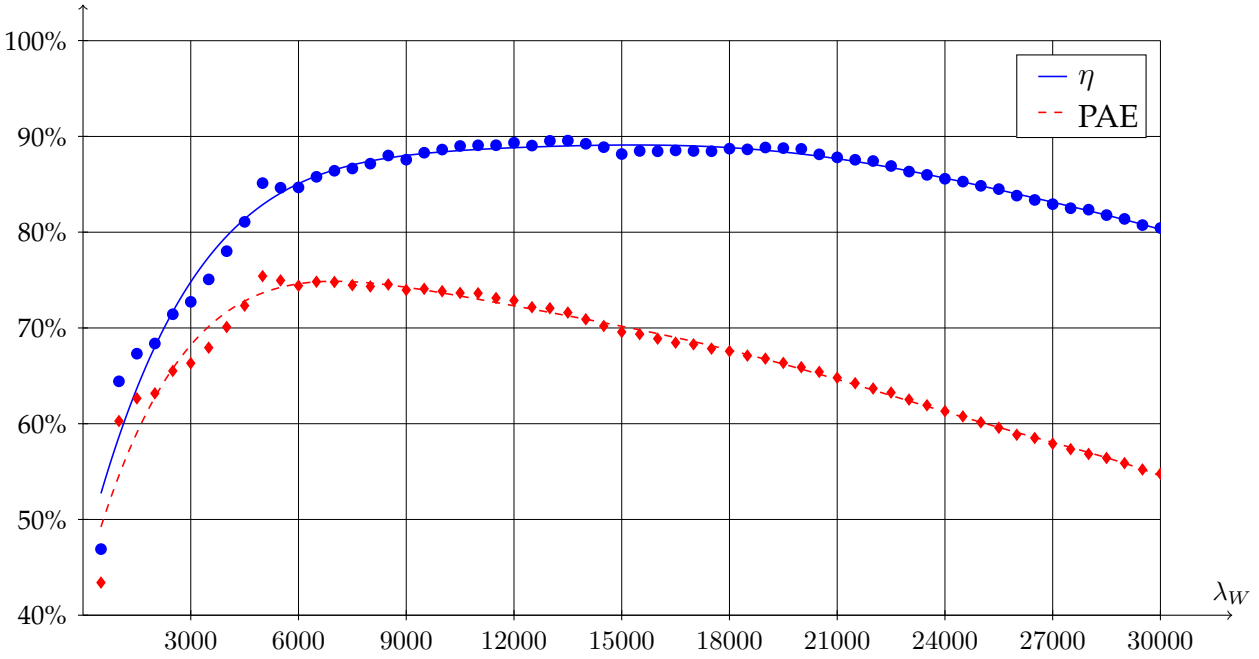

Fig. 2.57. FET Switching: Efficiency versus Transistor Size

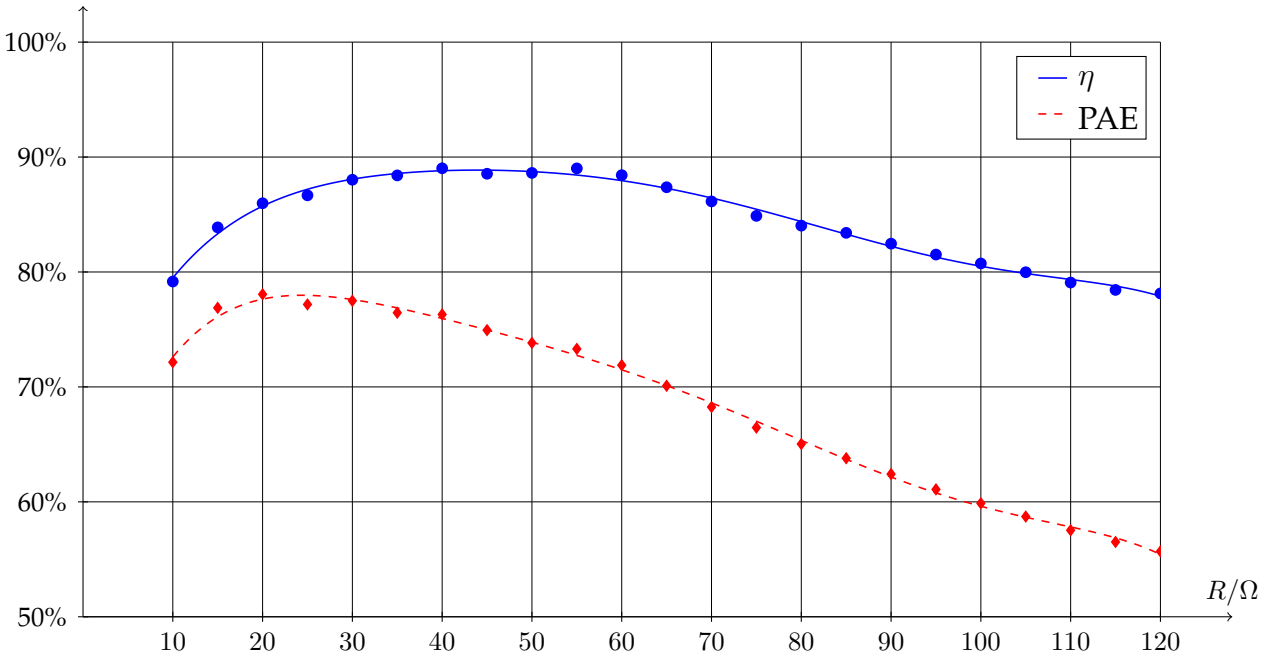

Fig. 2.58. FET Switching: Efficiency versus Load Resistance

room for trading them both off against each other. The strong dependency of the amplifier efficiency on each parameter allows the conclusion that there must exist one unique global optimum when all three parameters are concurrently considered. Against expectations, the simulation results of the model do not everywhere show a monotonic dependence on the circuit parameters, especially if the step size between to adjacent points is small. Despite of being an essentially linear model, no consistent curvature is found. As

a result additional local optima appear in the curves from Fig. 2.56 to Fig. 2.58. There are strong indications, that this global optimum exists, but despite the applied simplifications the developed model is not capable of making it appear without ambiguity. This circumstance prevents non-gradient based optimization algorithms[1] like the Downhill-Simplex from finding the global optimum, we are interested in. Further efforts are necessary in order to refine the model to make it applicable for a full optimization.

The strong dependency of the amplifier efficiency on each parameter allows the conclusion, that there must exist one unique global optimum when all three parameters are concurrently considered.

2.23 Conclusion

New amplifier topologies called class M and class N have been presented. Simulations measurements and optimization for evaluating the performance have been carried out. Compared to existing concepts, the efficiency is higher, the design is easier and the operation is safe with lower cost components. Due to the encouraging results, using class M in transmit amplifiers seems to be promising for many applications, suggesting further investigations.

[1] The calculation of the amplifier efficiency is a complex iterative procedure involving the solution of linear differential equations. Obviously, there are no gradients available to this objective function. Therefore, only algorithms that do not rely on gradients are applicable.

3. Decoupling and Matching Network for Symmetric Three-Ports

3.1 Motivation

COUPLING is the main effect, that cannot be neglected within a super gain antenna array. In such an array, the spacing between the elements is smaller than the wave length λ. In this case, the values for the coupling have about the same dimension as the diagonal elements of the antenna admittance matrix $\boldsymbol{Y}_{\mathrm{A}}$. If one will go for single port matching, that means matching each port on its own and completely neglecting the coupling, array gain would be lost. The decupling and matching network (DMN) should be optimized for low losses, so it is convenient choosing a reactance only design. Two ways of designing a DMN will be shown: The first one is the direct analytical design out of the antenna admittance matrix $\boldsymbol{Y}_{\mathrm{A}}$, section 3.2. The second one is the design optimized for low losses. Here, section 3.6, a stripline element design is optimized for lowest losses. This is achieved by using a small number of stripline elements and connecting them as short as possible. According to the needed degrees of freedom for the design and the two possibilities of connecting three points among each other, star and triangle are the resulting geometries.

3.2 Direct DMN Topology

Consider an antenna array composed of three equal monopole wires which are mounted normal to a circular ground plane and located at the corners of an equilateral triangle. When the centers of the triangle and of the circular ground plane coincide, the environment of each monopole looks the same as for each other monopole, at least in empty space or when other obstacles are located at enough distance. In such a situation, the three excitation ports form a symmetric 3-port. In the following, the design of a DMN by Dr. Michel Ivrlač is described, that can be used in conjunction with such a symmetric 3-port. Fig. 3.1 shows the structure of the proposed linear, reciprocal and (ideally) loss-less DMN 6-port. Its degrees of freedom must be designed such that when ports 1, 2, and 3 are connected to the antenna arrays excitation ports, the remaining ports 4, 5 and 6, become electrically decoupled and present a prescribed impedance. The design of the DMN takes care that it can be realized using planar micro-strip technology. This means that only those connections are allowed between the 6 ports which do not lead to cross-overs of micro-strip

wires. In the following, we first synthesize the network and then look at its realization using lumped lossless and lossy componets respectively.

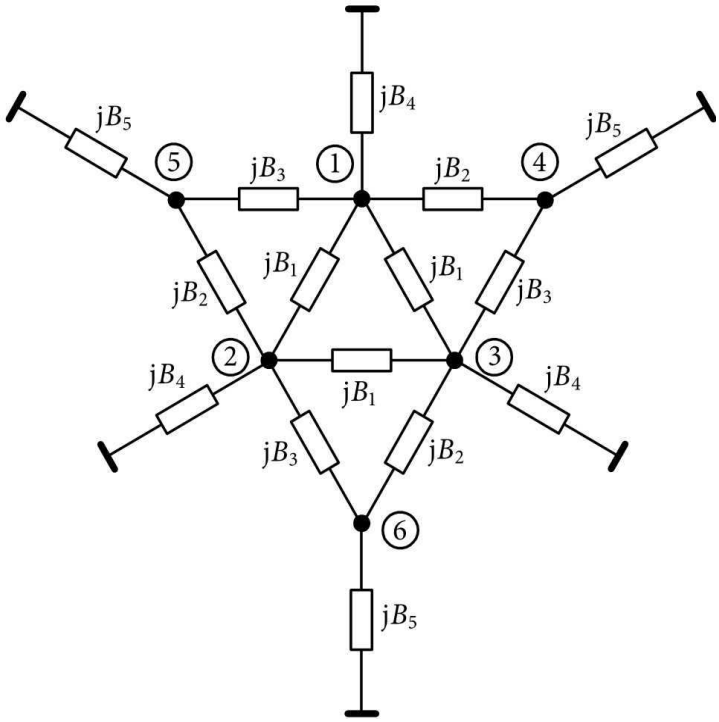

Fig. 3.1. Network structure of the proposed decoupling and matching 6-port.

3.2.1 Network Synthesis

Because all symmetric multiports can be parametrized by two complex parameters for instance, the value of the all-equal main-diagonal components and the value of the all-equal off-diagonal components of any matrix description of the linear symmetric multiport it requires at least four real-valued degrees of freedom to a) remove the coupling, and b) to set the impedance of the decoupled ports to a prescribed value. We propose a network structure, which actually uses five real-valued degrees of freedom, the susceptances $B_1, ..., B_5$, but has a convenient structure, which is shown in Fig. 3.1. It consists, in total, of 15 (ideally) loss-less reactances. Numbering the ports according to the encircled numerals in Fig. 3.1, it is easy to see that the admittance matrix $\boldsymbol{Y}_{\mathrm{M}}$ of the DMN can be expressed as

$$\boldsymbol{Y}_{\mathrm{M}} = \mathrm{j} \begin{bmatrix} \boldsymbol{A} & \boldsymbol{B}^{\mathrm{T}} \\ \boldsymbol{B} & \boldsymbol{C} \end{bmatrix}, \tag{3.1}$$

where the real valued matrices $\boldsymbol{A}$, $\boldsymbol{B}$ and $\boldsymbol{C}$ are given by

$$\boldsymbol{A} = \begin{bmatrix} 2B_1 + B_2 + B_3 + B_4 & -B_1 & -B_1 \\ -B_1 & 2B_1 + B_2 + B_3 + B_4 & -B_1 \\ -B_1 & -B_1 & 2B_1 + B_2 + B_3 + B_4 \end{bmatrix}, \tag{3.2}$$

$$\boldsymbol{B} = \begin{bmatrix} -B_2 & 0 & -B_3 \\ -B_3 & -B_2 & 0 \\ 0 & -B_3 & -B_2 \end{bmatrix}, \tag{3.3}$$

and

$$\boldsymbol{C} = \begin{bmatrix} B_2 + B_3 + B_5 & 0 & 0 \\ 0 & B_2 + B_3 + B_5 & 0 \\ 0 & 0 & B_2 + B_3 + B_5 \end{bmatrix}. \tag{3.4}$$

If one connects to the ports 1, 2 and 3, a linear 3-port with admittance matrix $\boldsymbol{Y}_{\mathrm{A}}$, then the remaining ports (4, 5 and 6) form another 3-port with admittance matrix:

$$\boldsymbol{Y} = \mathrm{j}\boldsymbol{C} + \boldsymbol{B}(\boldsymbol{Y}_{\mathrm{A}} + \mathrm{j}\boldsymbol{A})^{-1}\boldsymbol{B}^{\mathrm{T}}. \tag{3.5}$$

Because the antenna array 3-port is symmetric, $\boldsymbol{Y}_{\mathrm{A}}$ has the following structure:

$$\boldsymbol{Y}_{\mathrm{A}} = \begin{bmatrix} \alpha & \beta & \beta \\ \beta & \alpha & \beta \\ \beta & \beta & \alpha \end{bmatrix}, \tag{3.6}$$

where $\alpha,\ \beta\ \in \mathbb{C} \cdot \Omega^{-1}$. Let us now choose $\boldsymbol{A}$ such, that

$$\boldsymbol{A} = -\mathrm{Im}\{\boldsymbol{Y}_{\mathrm{A}}\}. \tag{3.7}$$

From (3.2), (3.6), (3.7), this means that

$$B_1 = \mathrm{Im}\{\beta\}, \tag{3.8}$$

$$B_2 + B_3 + B_4 = -\mathrm{Im}\{\alpha + 2\beta\}. \tag{3.9}$$

Substituting (3.7) into (3.5) then shows that

$$\boldsymbol{Y} = \mathrm{j}\boldsymbol{C} + \boldsymbol{B}(\mathrm{Re}\{\boldsymbol{Y}_{\mathrm{A}}\}^{-1})\boldsymbol{B}^{\mathrm{T}}. \tag{3.10}$$

Expressing the inverse of the real-part of $\boldsymbol{Y}_{\mathrm{A}}$ in the form

$$(\mathrm{Re}\{\boldsymbol{Y}_{\mathrm{A}}\})^{-1} = \begin{bmatrix} a & b & b \\ b & a & b \\ b & b & a \end{bmatrix}, \tag{3.11}$$

where $a, b \in \mathbb{R} \cdot \Omega$, it follows

$$\boldsymbol{B}\,(\mathrm{Re}\{\boldsymbol{Y}_{\mathrm{A}}\})^{-1}\,\boldsymbol{B}^{\mathrm{T}} = \begin{bmatrix} \gamma & \xi & \xi \\ \xi & \gamma & \xi \\ \xi & \xi & \gamma \end{bmatrix}, \tag{3.12}$$

where

$$\xi = B_2 B_3 a + \left(B_2^2 + B_2 B_3 + B_3^2\right) b, \tag{3.13}$$

while the value of γ will be considered later. For port decoupling, we must have

$$\xi = 0, \tag{3.14}$$

which translates into

$$B_3 = -B_2 \frac{a + b \pm \sqrt{a^2 + 2ab - 3b^2}}{2b}. \tag{3.15}$$

Because B_3 must be real-valued, we have to restrict ourselves to the case where

$$a^2 + 2ab - 3b^2 \geq 0. \tag{3.16}$$

It seems that this is fulfilled in practice, especially for compact arrays. Using (3.15) in (3.12) then reveals that

$$\gamma = -B_2 \frac{(a^2 + ab - 2b^2)\left(a + b \pm \sqrt{a^2 + 2ab - 3b^2}\right)}{2b^2}. \tag{3.17}$$

In order to obtain

$$\boldsymbol{Y} = (G + \mathrm{j}B) \begin{bmatrix} 1 & 0 & 0 \\ 0 & 1 & 0 \\ 0 & 0 & 1 \end{bmatrix}, \tag{3.18}$$

where $G, B \in \mathbb{R} \cdot \Omega^{-1}$, are prescribed values of the decoupled ports conductance and susceptance, we choose

$$\gamma = G. \tag{3.19}$$

With (3.16) then follows that

$$B_2 = \pm \sqrt{\frac{2b^2}{(a^2 + ab - 2b^2)\left(a + b \pm \sqrt{a^2 + 2ab - 3b^2}\right)}}, \tag{3.20}$$

where the two $\pm$ symbols can be applied independently of each other. Hence, there are up to four solutions for B_2 , and one can choose whichever is more convenient. From (3.4), (3.10), (3.12), (3.14), (3.18) and (3.19), it finally follows that

$$B_5 = B - B_2 - B_3. \tag{3.21}$$

3.3 The Proposed Algorithm

This completes the synthesis of the network, which we summarize for convenience: Given

$$\boldsymbol{Y}_{\mathrm{A}} = \begin{bmatrix} \alpha & \beta & \beta \\ \beta & \alpha & \beta \\ \beta & \beta & \alpha \end{bmatrix}, \quad \left(\mathrm{Re}\{\boldsymbol{Y}_{\mathrm{A}}\}\right)^{-1} = \begin{bmatrix} a & b & b \\ b & a & b \\ b & b & a \end{bmatrix}, \tag{3.22}$$

and $G \in \mathbb{R}^+ \cdot \Omega^{-1}$, $\quad B \in \mathbb{R} \cdot \Omega^{-1}$ and letting:

$$B_1 = \mathrm{Im}\{\beta\}, \tag{3.23}$$

$$B_2 = \pm \sqrt{\frac{2b^2 G}{(a^2 + ab - 2b^2)\left(a + b \pm \sqrt{a^2 + 2ab - 3b^2}\right)}}, \tag{3.24}$$

$$B_3 = -B_2 \frac{a + b \pm \sqrt{a^2 + 2ab - 3b^2}}{2b}, \tag{3.25}$$

$$B_4 = -\mathrm{Im}\{\alpha + 2\beta\} - B_2 - B_3, \tag{3.26}$$

$$B_5 = B - B_2 - B_3, \tag{3.27}$$

results in the admittance matrix of the 3-port formed by ports $4,\ 5$ and 6 given by

$$\boldsymbol{Y} = (G + \mathrm{j}B) \begin{bmatrix} 1 & 0 & 0 \\ 0 & 1 & 0 \\ 0 & 0 & 1 \end{bmatrix}, \tag{3.28}$$

when the 3-port with admittance matrix $\boldsymbol{Y}_{\mathrm{A}}$ is connected to the ports $1,\ 2$ and 3 of the DMN from Fig 3.1. Note that the $\pm$ operator in front of the square root in the expression for B_3 is identical to the $\pm$ operator in front of the inner square root in the expression for B_2 . That is, the same sign must be chosen for both!

3.3.1 Example

Three monopoles of length 18.5 mm and diameter of 3 mm are placed at the corners of an equilateral triangle at a distance of 19.2 mm a part (measured from the center of one monopole to the center of another monopole wire). They are mounted normal to a circular ground plane of 100 mm radius. The center of the triangle is co-located with the center of the circular ground plane. At a frequency of 3.6 GHz, full-wave electromagnetic analysis delivers the admittance matrix

$$\boldsymbol{Y}_{\mathrm{A}} = 10^{-3}\Omega^{-1} \begin{bmatrix} 19.6 & 8.65 & 8.65 \\ 8.65 & 19.6 & 8.65 \\ 8.65 & 8.65 & 19.6 \end{bmatrix} - \mathrm{j} \cdot 10^{-3}\Omega^{-1} \begin{bmatrix} 10.3 & 13.4 & 13.4 \\ 13.4 & 10.3 & 13.4 \\ 13.4 & 13.4 & 10.3 \end{bmatrix}, \tag{3.29}$$

and,

$$\alpha = (19.6 - \mathrm{j} \cdot 10.3)\, 10^{-3}\Omega^{-1}, \quad a = 69.9\ \Omega, \tag{3.30}$$

$$\beta = (8.65 + \mathrm{j} \cdot 13.4)10^{-3}\Omega^{-1}, \quad b = -21.4\ \Omega. \tag{3.31}$$

We prescribe

$$G = 20 \text{ x } 10^{-3}\ \Omega^{-1} \text{and} \quad B = 0 \tag{3.32}$$

From these data we can compute the degrees of freedom for the DMN as

$$\begin{aligned} B_1 &= -13.38 \text{ x } 10^{-3}\ \Omega^{-1}, & L_1 &= 3.29 \text{ nH}, \\ B_2 &= +10.19 \text{ x } 10^{-3}\ \Omega^{-1}, & C_2 &= 0.45 \text{ pF}, \\ B_3 &= +16.98 \text{ x } 10^{-3}\ \Omega^{-1}, & C_3 &= 0.75 \text{ pF}, \\ B_4 &= +9.938 \text{ x } 10^{-3}\ \Omega^{-1}, & C_4 &= 0.44 \text{ pF}, \\ B_5 &= -27.17 \text{ x } 10^{-3}\ \Omega^{-1}, & L_5 &= 1.63 \text{ nH}, \end{aligned}$$

yielding the desired admittance matrix of

$$\boldsymbol{Y} = 0.02\ \Omega^{-1} \begin{bmatrix} 1 & 0 & 0 \\ 0 & 1 & 0 \\ 0 & 0 & 1 \end{bmatrix}, \tag{3.33}$$

which corresponds to uncoupled ports with a port input impedance of $50\ \Omega$.

3.4 Results of Simulation

3.4.1 Lossless DMN

Here, microwave studio by Computer Simulation Technology (MWS) antenna array simulation results have been used for a DMN analysis with advanced design system by Keysight (ADS) and SPICE. Fig. 3.3 shows the matching, while Fig. 3.4 shows the decoupling obtained for ideal lossless lumped elements within the DMN.

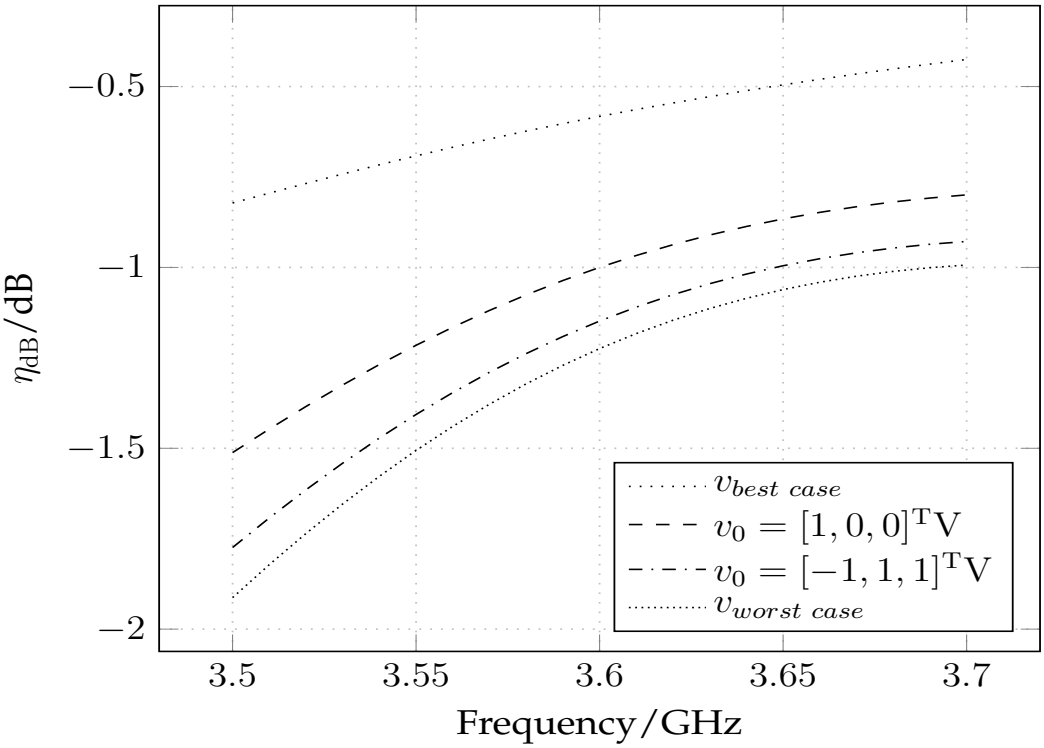

$v_{best\ case} = [(0, 5774), (0, 5774), (0, 5774)]^{\mathrm{T}}\mathrm{V}$
$v_{worst\ case} = [(0, 2887 - \mathrm{j}0, 5), (0, 2887 - \mathrm{j}0, 5), (0, 5774)]^{\mathrm{T}}\mathrm{V}$
Fig. 3.2. Losses obtained for lossy lumped elements

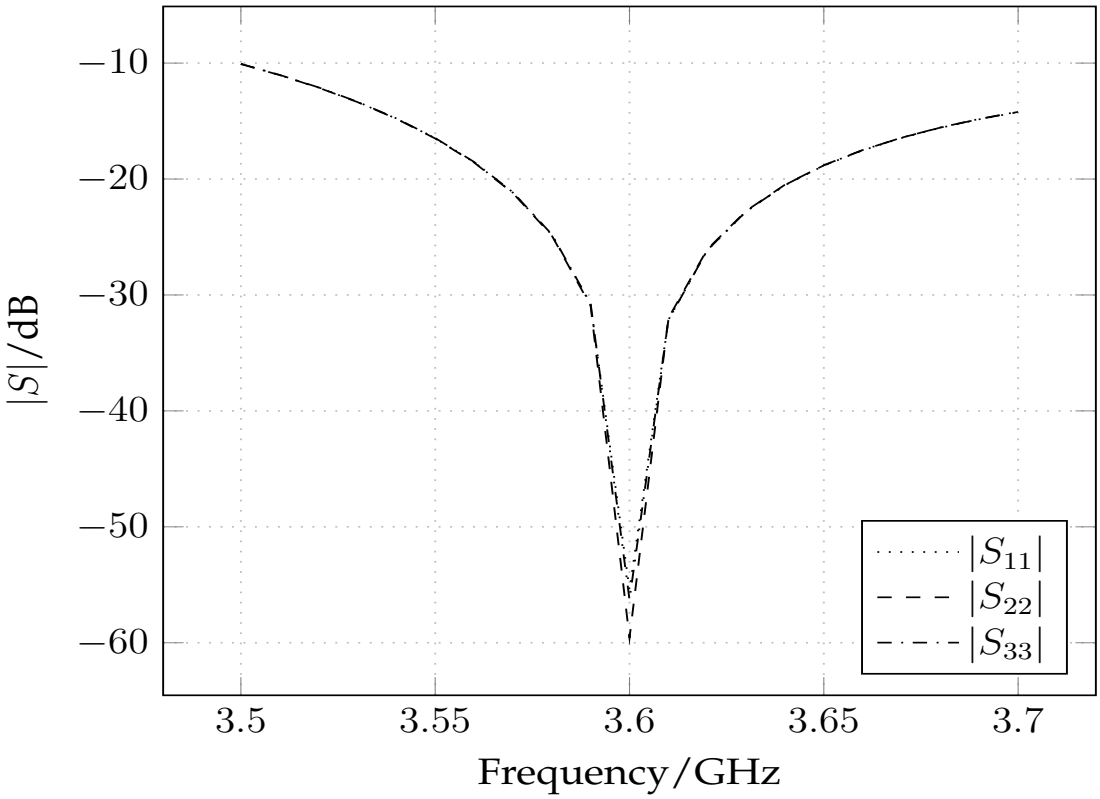

Fig. 3.3. Matching obtained for lossless lumped elements

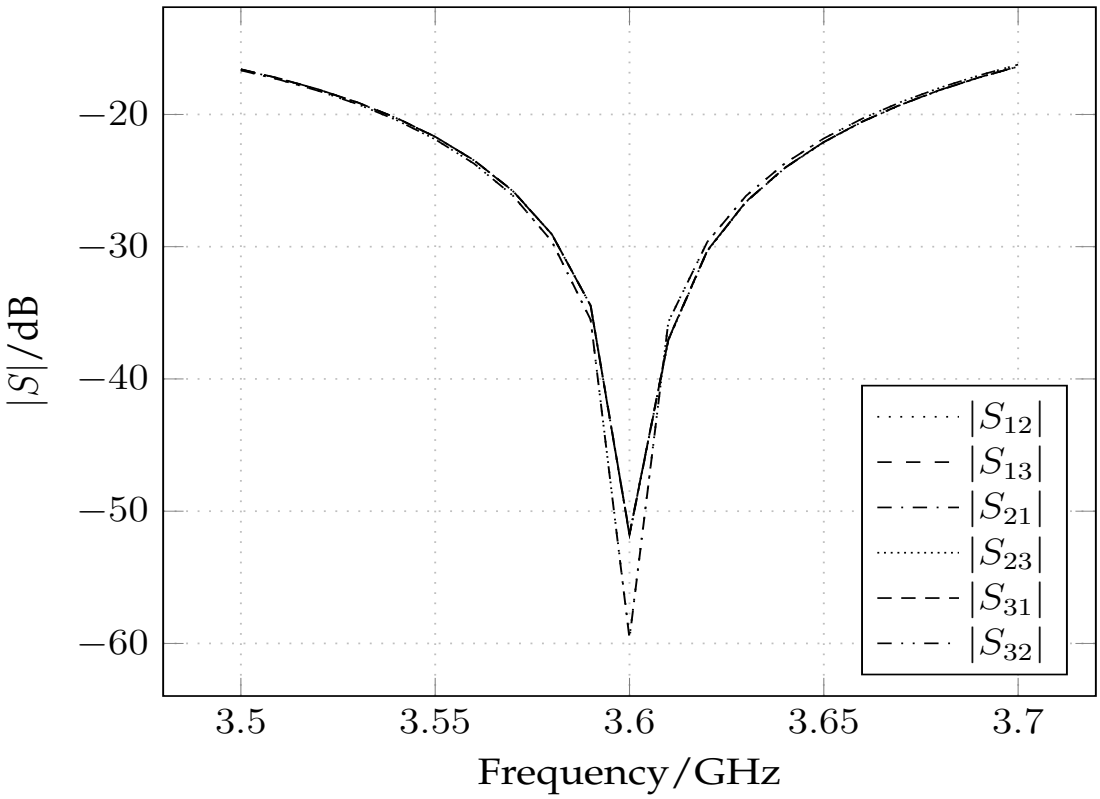

Fig. 3.4. Decoupling obtained for lossless lumped elements

3.4.2 Lossy DMN

A more common case is for sure a look into a lossy DMN, e.g. with $Q = 30$ for each reactive element. Fig. 3.5 shows the matching, while Fig. 3.6 shows the losses obtained for lossy lumped elements within the DMN, where $\eta_{\mathrm{dB}} = 10 \log \frac{P_{\mathrm{out}}}{P_{\mathrm{in}}}$. P_{in} is the sum input power into the three ports $4, 5$ and 6, while P_{out} is the sum output power to the antenna array, Fig. 3.2. Here, the losses for the best case, worst case and different beam forming vectors have been calculated according to section 3.9.3.

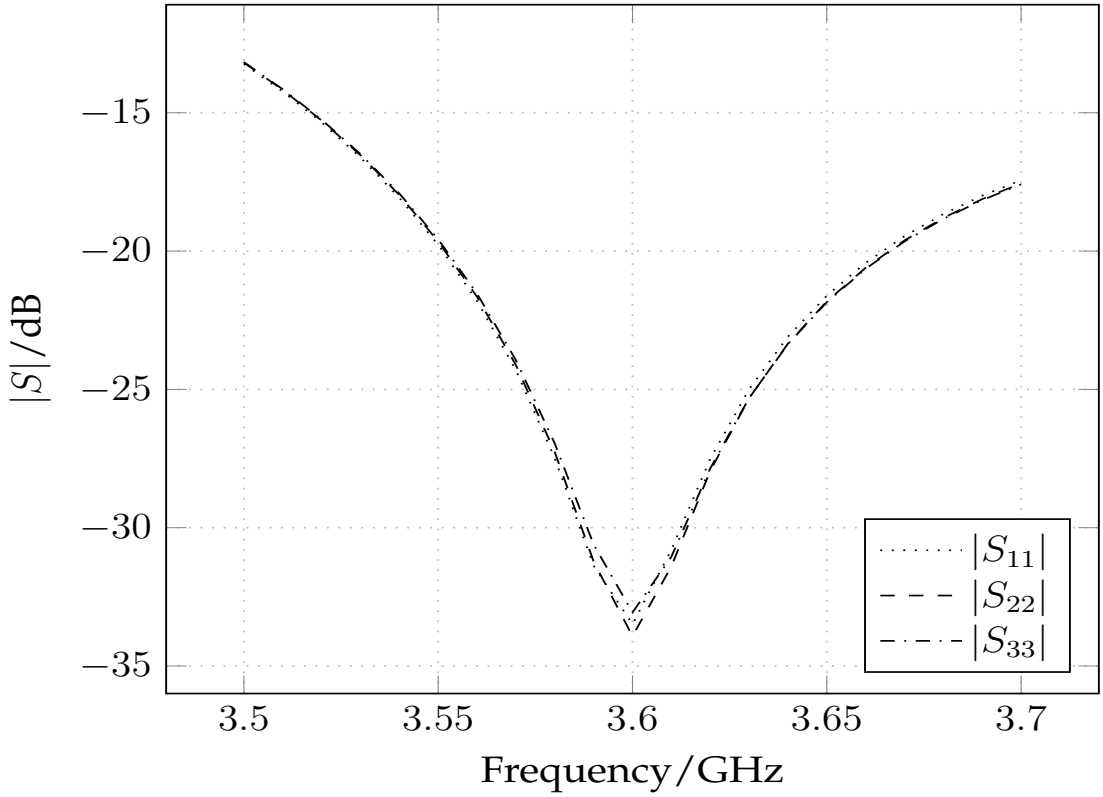

Fig. 3.5. Matching obtained for lossy lumped elements

3.5 Direct DMN Transmission Line Solution

In the circuit from Fig. 3.1, the admittances $\mathrm{j}B_i$, with $i \in \{1, ..., 5\}$,can be realized by using transmission lines as the basic design element. If the required bandwidth is not too large, such a design can then conveniently be implemented in micro-strip technology. The basic building block is a quarter-wavelength $(\lambda/4)$ transmission line, which can be described by

$$\boldsymbol{A}_{\lambda/4} = \mathrm{j} \begin{bmatrix} 0 & Z_0 \\ Z_0^{-1} & 0 \end{bmatrix}, \tag{3.34}$$

where Z_0 is the transmission line's characteristic impedance. Another simple 2-port which consists only of a single parallel admittance Y, has got the chain matrix

$$\boldsymbol{A}_Y = \begin{bmatrix} 1 & Z_0 \\ Y & 1 \end{bmatrix}. \tag{3.35}$$

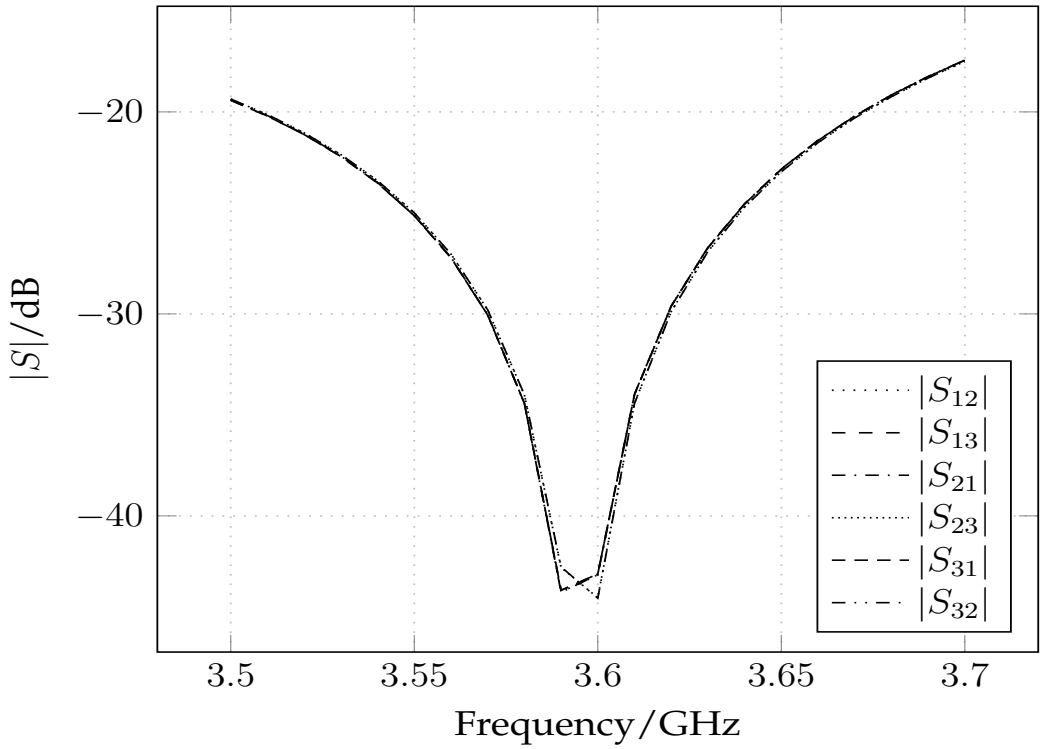

Fig. 3.6. Decoupling obtained for lossy lumped elements

Consequently, the cascade shown in Fig. 3.7 can be described by the chain matrix

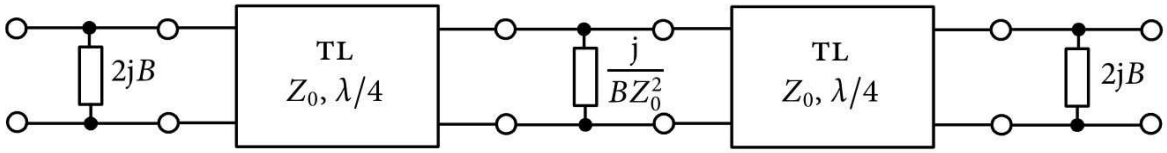

Fig. 3.7. A chain of 5 simple 2-ports which implement a floating admittance jB.

$$\boldsymbol{A} = \boldsymbol{A}_{2\mathrm{j}B}\boldsymbol{A}_{\lambda/4}\boldsymbol{A}_{\lambda/(BZ_0^2)}\boldsymbol{A}_{\lambda/4}\boldsymbol{A}_{2\mathrm{j}B} = \begin{bmatrix} 1 & -\mathrm{j}/B \\ 0 & 1 \end{bmatrix}. \tag{3.36}$$

Because this is exactly the chain matrix of a floating admittance jB, one can realize the DMN from Fig. 3.1 in the way shown in Fig. 3.8. Compared with the original design from Fig. 3.1, the circuit in Fig. 3.8 uses grounded reactances instead of floating ones, and employs to this end a total of 18 quarter-wavelength transmission lines. While the number of the reactances is still the same, their values are changed according to:

$$B_{\mathrm{I}} = \frac{1}{B_1 Z_0^2}, \tag{3.37}$$

$$B_{\mathrm{II}} = \frac{1}{B_2 Z_0^2}, \tag{3.38}$$

$$B_{\mathrm{III}} = \frac{3}{B_2 Z_0^2}, \tag{3.39}$$

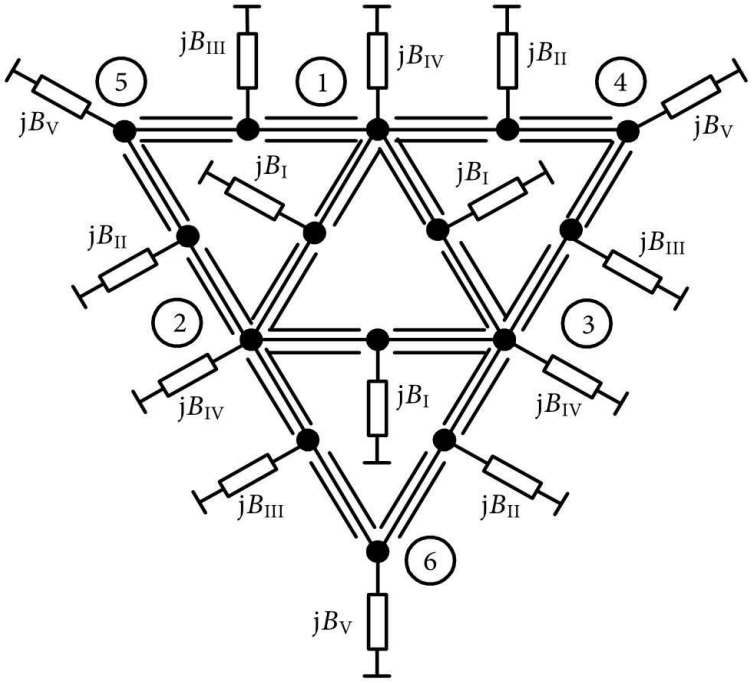

Fig. 3.8. A circuit equivalent to the one from Fig. 3.1, but which uses only grounded reactances (instead of floating ones) and quarter wavelength transmission lines.

$$B_{\mathrm{IV}} = 4B_1 + 2B_2 + 2B_3 + B_4, \tag{3.40}$$

$$B_{\mathrm{V}} = 2B_2 + 2B_3 + B_5. \tag{3.41}$$

Because all reactances are returned to ground it is easy to realize them again by use of transmission lines which run open (or are shorted) at one end. This results in the circuit shown in Fig. 3.9. The lengths $l_{\mathrm{I}}, ..., l_{\mathrm{V}}$, of the open (or shorted) transmission lines have to be set appropriately such that the required admittances $\mathrm{j}B_{\mathrm{I}}, ..., \mathrm{j}B_{\mathrm{V}}$ are produced at their other ends, respectively. An ideal transmission line is described by

$$\begin{bmatrix} v_1 \\ i_1 \end{bmatrix} = \begin{bmatrix} \cos(2\pi l/\lambda) & \mathrm{j}Z_0 \sin(2\pi l/\lambda) \\ \mathrm{j}Z_0^{-1}\sin(2\pi l/\lambda) & \cos(2\pi l/\lambda) \end{bmatrix} \begin{bmatrix} v_2 \\ -i_2 \end{bmatrix}, \tag{3.42}$$

where v_1 and i_1 are the complex phasors of the voltage and current at one end of the line and v_2 and i_2 are the respective complex phasors for the other end. In the following, we assume that the transmission lines are *open-circuited* at one end. Setting $i_2 = 0$, it then follows from (3.42) that the other end of the transmission line acts as an admittance

$$Y = \frac{\mathrm{j}}{Z_0}\tan(2\pi l/\lambda), \tag{3.43}$$

where l is the length of the transmission line. Setting $Y = \mathrm{j}B$, it follows that the length must be set according to

$$l_\eta = \frac{\lambda_\eta}{2\pi}\arctan(B_\eta Z_{0,\eta}), \quad \text{where } \eta \in \{\mathrm{I}, \mathrm{II}, \mathrm{III}, \mathrm{IV}, \mathrm{V}\}. \tag{3.44}$$

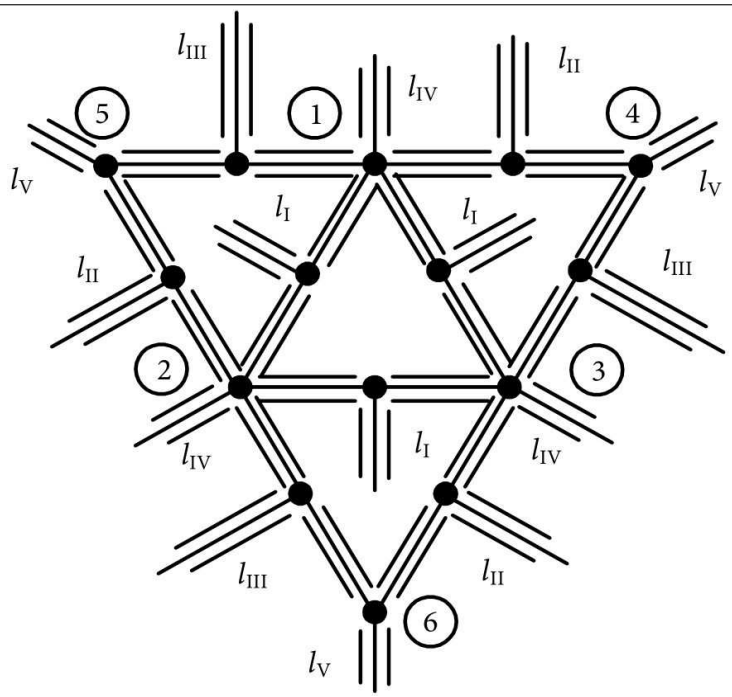

Fig. 3.9. A circuit equivalent to the one from Fig. 3.1, but which uses only transmission lines.

In case the length comes out negative, one has to add $\lambda/2$ so long until the result is positive. The characteristic impedances $Z_{0,\eta}$ can be chosen independently from each other and of the characteristic impedance Z_0 of the quarter-wavelength transmission lines. Note that the wavelength λ_η on the transmission line usually depends on its characteristic impedance.

3.6 Star and Triangle DMN Topology

Consider an antenna array composed of three equal monopole wires as in (3.2). The centers of the triangle and of the circular ground plane coincide and the environment of each monopole looks the same as described in (3.2). Therefore, the three excitation ports form a symmetric 3-port. In the following, another design of a DMN that can be used in conjunction with such a symmetric 3-port is described.

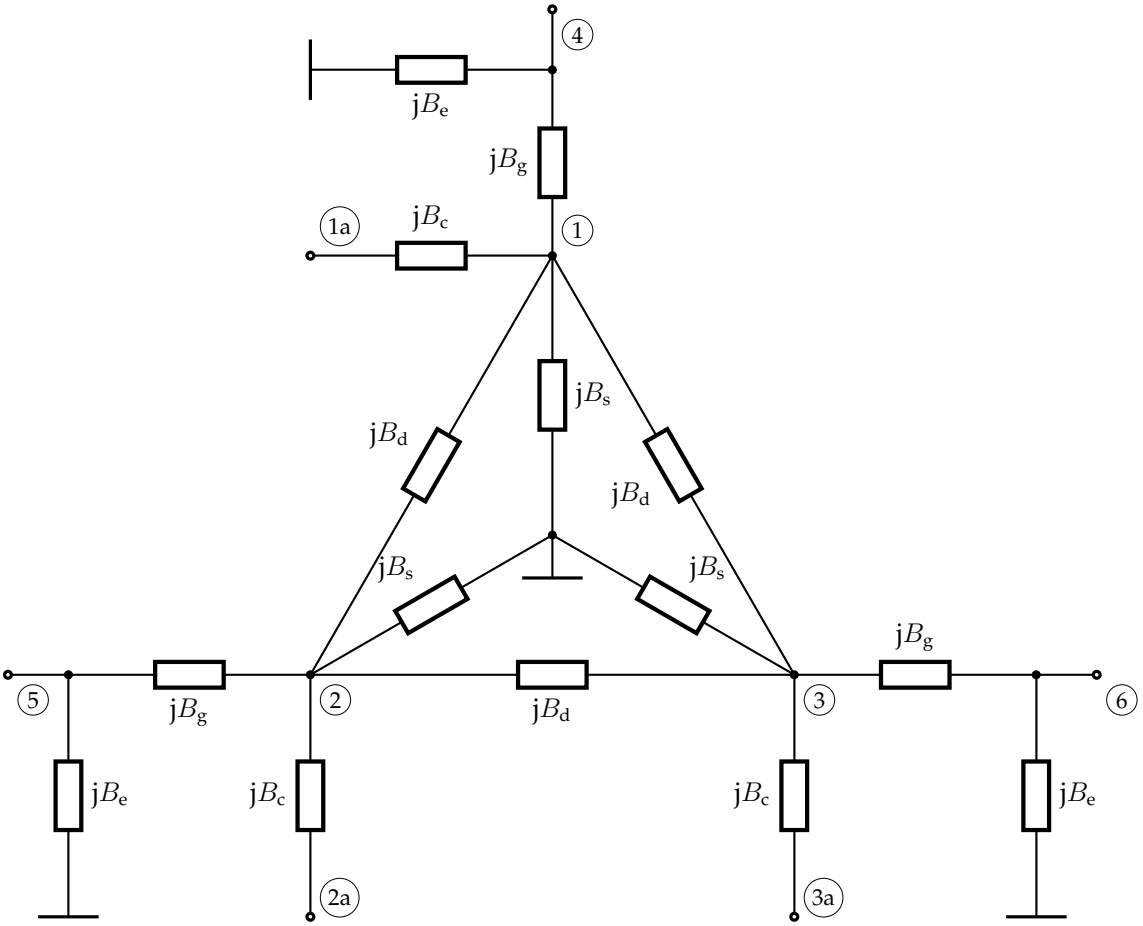

Fig. 3.10. Network structure of the proposed decoupling and matching 6-port.

Fig. 3.10 shows the structure of the proposed linear, reciprocal and (ideally) loss-less DMN 6-port realized with lumped elements. Its degrees of freedom must be designed such that when ports 1a, 2a, and 3a are connected to the antenna arrays excitation ports, the amplifier ports 4, 5 and 6, become electrically decoupled and present a prescribed impedance, optimal for beeing connected to amplifier ports.
The design of the DMN takes care, that it can be realized using planar micro-strip technology. This means, that only those connections are allowed between the 6 ports, which do not lead to cross-overs of micro-strip lines. In the following, we first synthesize the network and then look at its realization using lumped lossless and lossy componets respectively.

3.7 Star and Triangle DMN Network Synthesis

3.7.1 Design With Lumped Components

All symmetric multiports can be parametrized by two complex parameters. For instance, by the value of the all-equal main-diagonal components and by the value of the all-equal off-diagonal components of any matrix description of the linear symmetric multiport. This requires at least four real-valued degrees of freedom to a) remove the coupling and b) to set the impedance of the decoupled ports to a prescribed value. We propose a network structure, which actually uses five real-valued degrees of freedom, the susceptances $B_\mathrm{c}, ..., B_\mathrm{s}$, but has a convenient structure which is shown in Fig. 3.10. It consists, in total, of 15 (ideally) loss-less reactances. In the following step, the series reactances B_c are neglected, they are later used for modifying the original antenna matrix $\boldsymbol{Y}_\mathrm{A}$ into $\boldsymbol{Y}_\mathrm{B}$ for making the design algorithm similar to (3.2). This is the reason, why the antenna is connected to the ports 1a, 2a and 3a while the ports 1, 2 and 3 were introduced for the sake of analytical simplicity. Numbering the ports according to the encircled numerals in Fig. 3.10, it is easy to see, that the admittance matrix $\boldsymbol{Y}_\mathrm{M}$ of the DMN can be expressed as

$$\boldsymbol{Y}_\mathrm{M} = \mathrm{j}\begin{bmatrix} \boldsymbol{A} & \boldsymbol{B}^\mathrm{T} \\ \boldsymbol{B} & \boldsymbol{C} \end{bmatrix}, \tag{3.45}$$

where the real valued matrices $\boldsymbol{A}$, $\boldsymbol{B}$ and $\boldsymbol{C}$ are given by

$$\boldsymbol{A} = \begin{bmatrix} 2B_\mathrm{d} + B_\mathrm{s} + B_\mathrm{g} & -B_\mathrm{d} & -B_\mathrm{d} \\ -B_\mathrm{d} & 2B_\mathrm{d} + B_\mathrm{s} + B_\mathrm{g} & -B_\mathrm{d} \\ -B_\mathrm{d} & -B_\mathrm{d} & 2B_\mathrm{d} + B_\mathrm{s} + B_\mathrm{g} \end{bmatrix}, \tag{3.46}$$

$$\boldsymbol{B} = \begin{bmatrix} -B_\mathrm{g} & 0 & 0 \\ 0 & -B_\mathrm{g} & 0 \\ 0 & 0 & -B_\mathrm{g} \end{bmatrix}, \tag{3.47}$$

and

$$\boldsymbol{C} = \begin{bmatrix} B_\mathrm{g} + B_\mathrm{e} & 0 & 0 \\ 0 & B_\mathrm{g} + B_\mathrm{e} & 0 \\ 0 & 0 & B_\mathrm{g} + B_\mathrm{e} \end{bmatrix}. \tag{3.48}$$

If one connects to the ports 1, 2 and 3, a linear 3-port with admittance matrix $\boldsymbol{Y}_\mathrm{A}$, then the remaining ports (4, 5 and 6) form another 3-port with admittance matrix

$$\boldsymbol{Y} = \mathrm{j}\boldsymbol{C} + \boldsymbol{B}(\boldsymbol{Y}_\mathrm{A} + \mathrm{j}\boldsymbol{A})^{-1}\boldsymbol{B}^\mathrm{T}. \tag{3.49}$$

Because the antenna array 3-port is symmetric, $\boldsymbol{Y}_\mathrm{A}$ has the following structure:

$$\boldsymbol{Y}_\mathrm{A} = \begin{bmatrix} \alpha & \beta & \beta \\ \beta & \alpha & \beta \\ \beta & \beta & \alpha \end{bmatrix}, \tag{3.50}$$

where $\alpha,\ \beta\ \in \mathbb{C} \cdot \Omega^{-1}$. Let us now choose A such that

$$\boldsymbol{A} = -\mathrm{Im}\{\boldsymbol{Y}_\mathrm{A}\}. \tag{3.51}$$

From (3.46), (3.50), (3.51), this means that

$$B_{\mathrm{d}} = \mathrm{Im}\{\beta\} \tag{3.52}$$

and

$$B_{\mathrm{s}} + B_{\mathrm{g}} = -\mathrm{Im}\{\alpha + 2\beta\}. \tag{3.53}$$

Substituting (3.51) into (3.49) then shows that

$$\boldsymbol{Y} = \mathrm{j}\boldsymbol{C} + \boldsymbol{B}(\mathrm{Re}\{\boldsymbol{Y}_{\mathrm{A}}\}^{-1})\boldsymbol{B}^{\mathrm{T}}. \tag{3.54}$$

Expressing the inverse of the real-part of $\boldsymbol{Y}_{\mathrm{B}}$ in the form:

$$(\mathrm{Re}\{\boldsymbol{Y}_{\mathrm{A}}\})^{-1} = \begin{bmatrix} a & b & b \\ b & a & b \\ b & b & a \end{bmatrix}, \tag{3.55}$$

where $a, b \in \mathbb{R} \cdot \Omega$, it follows, that

$$\boldsymbol{B}\,(\mathrm{Re}\{\boldsymbol{Y}_{\mathrm{A}}\})^{-1}\,\boldsymbol{B}^{\mathrm{T}} = \begin{bmatrix} \gamma & \xi & \xi \\ \xi & \gamma & \xi \\ \xi & \xi & \gamma \end{bmatrix}, \tag{3.56}$$

where

$$\xi = B_g^2 b, \tag{3.57}$$

while the value of γ will be considered later. For port decoupling, we must have

$$\xi = 0. \tag{3.58}$$

Usually the design will start with a given antenna array described by

$$\boldsymbol{Z}_{\mathrm{B}} = \boldsymbol{Y}_{\mathrm{B}}^{-1} = \begin{bmatrix} \lambda & c & c \\ c & \lambda & c \\ c & c & \lambda \end{bmatrix}, \tag{3.59}$$

$$\boldsymbol{Y}_{\mathrm{A}}^{-1} = \boldsymbol{Y}_{\mathrm{B}}^{-1} + \frac{1}{\mathrm{j}B_{\mathrm{c}}} \cdot \mathbf{1} = \begin{bmatrix} d & c & c \\ c & d & c \\ c & c & d \end{bmatrix}, \tag{3.60}$$

where

$$d = \lambda + \frac{1}{\mathrm{j}B_{\mathrm{c}}}, \tag{3.61}$$

which translates into

$$\mathrm{Re}\{\beta\} = \mathrm{Re}\left\{\frac{c^2 - cd}{d^3 + 2c^3 - 3c^2 d}\right\}\Bigg|_{B_{\mathrm{c}}} = 0, \tag{3.62}$$

it follows,

$$b = 0 \tag{3.63}$$

and

$$\gamma = B_{\mathrm{g}}^2 a. \tag{3.64}$$

In order to obtain

$$\boldsymbol{Y} = (G + \mathrm{j}B) \begin{bmatrix} 1 & 0 & 0 \\ 0 & 1 & 0 \\ 0 & 0 & 1 \end{bmatrix}, \tag{3.65}$$

where $G, B \in \mathbb{R} \cdot \Omega^{-1}$, are prescribed values of the decoupled ports' conductance and susceptance, we choose

$$\gamma = G. \tag{3.66}$$

With (3.64) then follows that

$$B_{\mathrm{g}} = \pm\sqrt{\frac{G}{a}}, \tag{3.67}$$

where the $\pm$ symbols lead to two solutions for B_{g} , and one can choose whichever is more convenient. From (3.48), (3.54), (3.56), (3.58), (3.65) and (3.66) it finally follows, that

$$B_{\mathrm{e}} = -B_{\mathrm{g}}. \tag{3.68}$$

For solving (3.62) the real part must be separated, therefore

$$\lambda = x + \mathrm{j}y, \qquad y' = y - \frac{1}{B_{\mathrm{c}}}, \qquad c = u + \mathrm{j}v, \tag{3.69}$$

are defined and plugged into (3.62)

$$\mathrm{Re}\{\beta\} = \mathrm{Re}\left\{ \frac{(u+\mathrm{j}v)^2 - (u+\mathrm{j}v)(x+\mathrm{j}y')}{(x+\mathrm{j}y')^3 + 2(u+\mathrm{j}v)^3 - 3(u+\mathrm{j}v)^2(x+\mathrm{j}y')} \right\}\Bigg|_{B_{\mathrm{c}}} = 0. \tag{3.70}$$

The numerator of (3.70) becomes

$$num = \left(u^2 - v^2 - ux + vy'\right) + \mathrm{j}\left(2uv - uy' - xv\right). \tag{3.71}$$

Each term not containing y' is now substituted, resulting in

$$num = (vy' + A) + \mathrm{j}\left(C - uy'\right). \tag{3.72}$$

The denominator is

$$\begin{aligned} denom = {} & x^3 - 3xy'^2 + 2\left(u^3 - 3uv^2\right) - 3\left(x\left(u^2 - v^2\right) - 2y'uv\right) \\ & + \mathrm{j}\left(3x^2y' - y'^3 + 2\left(3u^2v - v^3\right) - 3\left(2uvx - y'\left(u^2 - v^2\right)\right)\right). \end{aligned} \tag{3.73}$$

Each term not containing y' is now substituted

$$denom = -3xy'^2 + 6uvy' + B + \mathrm{j}\left(-y'^3 + 3\left(x^2 - u^2 + v^2\right)y' + D\right),$$

with a further substitution, the denominator is

$$denom = -3xy'^2 + 6uvy' + B + \mathrm{j}\left(-y'^3 + Ey' + D\right).$$

Now, the formula for y' is complete

$$\begin{aligned} 0 = {} & uy'^4 - (3vx + C)\,y'^3 + \left(6uv^2 - 3Ax - Eu\right)y'^2 \\ & + (6Auv + Bv + CE + Du)\,y' + AB - CD, \end{aligned} \tag{3.74}$$

since its degree is 4, there are four solutions.

3.7.2 The Proposed Algorithm

This completes the synthesis of the network, which we summarize for convenience: Given $\boldsymbol{Y}_{\mathrm{A}}$ and G:

$$\boldsymbol{Y}_{\mathrm{A}}^{-1} = \boldsymbol{Y}_{\mathrm{B}}^{-1} + \frac{1}{B_{\mathrm{c}}} \cdot \mathbf{1} = \begin{bmatrix} d & c & c \\ c & d & c \\ c & c & d \end{bmatrix}, \tag{3.75}$$

such, that

$$\mathrm{Re}\left\{ \frac{c^2 - cd}{d^3 + 2c^3 - 3c^2 d} \right\} \Bigg|_{B_{\mathrm{c}}} = 0 \tag{3.76}$$

is fulfilled, then $b = 0$.

$$\boldsymbol{Y}_{\mathrm{A}} = \begin{bmatrix} \alpha & \beta & \beta \\ \beta & \alpha & \beta \\ \beta & \beta & \alpha \end{bmatrix}, \quad (\mathrm{Re}\{\boldsymbol{Y}_{\mathrm{A}}\})^{-1} = \begin{bmatrix} a & b & b \\ b & a & b \\ b & b & a \end{bmatrix}, \tag{3.77}$$

$G \in \mathbb{R}^{+} \cdot \Omega^{-1}, \quad B \in \mathbb{R} \cdot \Omega^{-1}$ and letting:

$$B_{\mathrm{d}} = \mathrm{Im}\{\beta\} \tag{3.78}$$

$$B_{\mathrm{g}} = \pm\sqrt{\frac{G}{a}} \tag{3.79}$$

$$B_{\mathrm{s}} = -\mathrm{Im}\{\alpha + 2\beta\} - B_{\mathrm{g}} \tag{3.80}$$

$$B_{\mathrm{e}} = -B_{\mathrm{g}} \tag{3.81}$$

results in the admittance matrix of the 3-port formed by ports $4,\ 5$ and 6 given by

$$\boldsymbol{Y} = (G + \mathrm{j}B) \begin{bmatrix} 1 & 0 & 0 \\ 0 & 1 & 0 \\ 0 & 0 & 1 \end{bmatrix}, \tag{3.82}$$

when the 3-port with admittance matrix $\boldsymbol{Y}_{\mathrm{B}}$ is connected to the ports $1,\ 2$ and 3 of the DMN from Fig 3.10.

3.7.3 Strip-line Implementation

In any practical implementation, the DMN must be connected with the antenna array. The length of the connection lines, e.g. strip lines, are not negligible, because of their impedance transformation. On the other hand lumped inductors have a limited quality factor Q, which usually is lower, than the Q of ceramic multilayer capacitors. Therefore, we aim at replacing many of the lumped reactances by strip lines. We start with the topology shown in Fig. 3.11, which will be called „decoupler“.

This circuit is described by its nodal admittance matrix

$$\boldsymbol{Y}_{\mathrm{Q}} = \mathrm{j} \begin{bmatrix} 2B_{\mathrm{d}} + B_{\mathrm{s}} & -B_{\mathrm{d}} & -B_{\mathrm{d}} \\ -B_{\mathrm{d}} & 2B_{\mathrm{d}} + B_{\mathrm{s}} & -B_{\mathrm{d}} \\ -B_{\mathrm{d}} & -B_{\mathrm{d}} & 2B_{\mathrm{d}} + B_{\mathrm{s}} \end{bmatrix}. \tag{3.83}$$

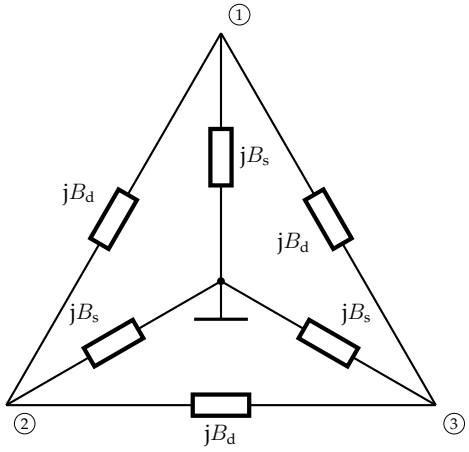

Fig. 3.11. Lumped Elements Decoupler

The reactances B_s can easily be replaced by shorted strip lines

$$B_s = -\frac{1}{Z_\mathrm{ss} \tan \beta_\mathrm{p} l_\mathrm{ss}}. \tag{3.84}$$

Where Z_ss and l_ss are impedance and length of this strip line, β_p is its phase constant. Replacing B_d by strip line is not as simple. When looking to the general matrix description of transmission lines,

$$\boldsymbol{A}_\mathrm{L} = \begin{bmatrix} \cos \beta_\mathrm{p} l & \mathrm{j} Z_0 \sin \beta_\mathrm{p} l \\ \frac{\mathrm{j} \sin \beta_\mathrm{p} l}{Z_0} & \cos \beta_\mathrm{p} l \end{bmatrix}, \tag{3.85}$$

after converting to an admittance matrix

$$\boldsymbol{Y}_\mathrm{L} = \begin{bmatrix} \frac{1}{\mathrm{j} Z_0 \tan \beta_\mathrm{p} l} & -\frac{1}{\mathrm{j} Z_0 \sin \beta_\mathrm{p} l} \\ -\frac{1}{\mathrm{j} Z_0 \sin \beta_\mathrm{p} l} & \frac{1}{\mathrm{j} Z_0 \tan \beta_\mathrm{p} l} \end{bmatrix} \neq \mathrm{j} \begin{bmatrix} B_\mathrm{d} & -B_\mathrm{d} \\ -B_\mathrm{d} & B_\mathrm{d} \end{bmatrix}, \tag{3.86}$$

one will come to the conclusion, this is not possible. A grounded reactance an be replaced by a stripline element, while a floating reactance cannot be replaced. After introducing a new fourth node in the center by opening the ground connection, Fig. 3.12 we obtain a new nodal admittance matrix (3.87).

$$\boldsymbol{Y}_{4\mathrm{Q}} = \begin{bmatrix} \frac{2}{\mathrm{j} Z_\mathrm{d} \tan \beta_\mathrm{d} l_\mathrm{d}} + \frac{1}{\mathrm{j} Z_s \tan \beta_s l_s} & -\frac{1}{\mathrm{j} Z_\mathrm{d} \sin \beta_\mathrm{d} l_\mathrm{d}} & -\frac{1}{\mathrm{j} Z_\mathrm{d} \sin \beta_\mathrm{d} l_\mathrm{d}} & -\frac{1}{\mathrm{j} Z_\mathrm{s} \sin \beta_\mathrm{s} l_\mathrm{s}} \\ -\frac{1}{\mathrm{j} Z_\mathrm{d} \sin \beta_\mathrm{d} l_\mathrm{d}} & \frac{2}{\mathrm{j} Z_\mathrm{d} \tan \beta_\mathrm{d} l_\mathrm{d}} + \frac{1}{\mathrm{j} Z_\mathrm{s} \tan \beta_\mathrm{s} l_\mathrm{s}} & -\frac{1}{\mathrm{j} Z_\mathrm{d} \sin \beta_\mathrm{d} l_\mathrm{d}} & -\frac{1}{\mathrm{j} Z_\mathrm{s} \sin \beta_\mathrm{s} l_\mathrm{s}} \\ -\frac{1}{\mathrm{j} Z_\mathrm{d} \sin \beta_\mathrm{d} l_\mathrm{d}} & -\frac{1}{\mathrm{j} Z_\mathrm{d} \sin \beta_\mathrm{d} l_\mathrm{d}} & \frac{2}{\mathrm{j} Z_\mathrm{d} \tan \beta_\mathrm{d} l_\mathrm{d}} + \frac{1}{\mathrm{j} Z_\mathrm{s} \tan \beta_\mathrm{s} l_\mathrm{s}} & -\frac{1}{\mathrm{j} Z_\mathrm{s} \sin \beta_\mathrm{s} l_\mathrm{s}} \\ -\frac{1}{\mathrm{j} Z_\mathrm{s} \sin \beta_\mathrm{s} l_\mathrm{s}} & -\frac{1}{\mathrm{j} Z_\mathrm{s} \sin \beta_\mathrm{s} l_\mathrm{s}} & -\frac{1}{\mathrm{j} Z_\mathrm{s} \sin \beta_\mathrm{s} l_\mathrm{s}} & \frac{3}{\mathrm{j} Z_\mathrm{s} \tan \beta_\mathrm{s} l_\mathrm{s}} \end{bmatrix} \tag{3.87}$$

Here, l_d, β_d and Z_d are length, phase constant and impedance of the dotted triangle strip line elements, l_s, β_s and Z_s are length, phase constant and impedance of the dashed star elements.

Because node 4 will have no other connection than to node $1, 2$ and 3 the 4x4 matrix $\boldsymbol{Y}_{4\mathrm{Q}}$ can be converted to a 3x3 matrix, identical to $\boldsymbol{Y}_\mathrm{Q}$ and the circuit in Fig. 3.13,

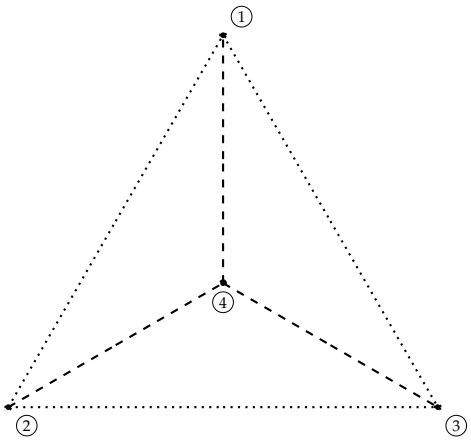

Fig. 3.12. 4-Node Strip Line Decoupler

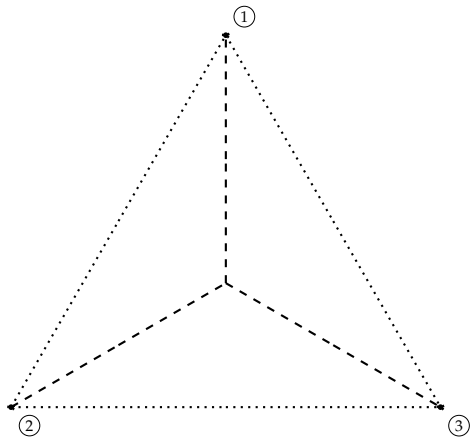

Fig. 3.13. 3-Node Strip Line Decoupler

$$\boldsymbol{Y}_{\mathrm{Q}} = \begin{bmatrix} \frac{2}{\mathrm{j}Z_{\mathrm{d}}\tan\beta_{\mathrm{d}}l_{\mathrm{d}}} + \frac{1}{\mathrm{j}Z_{\mathrm{s}}\tan\beta_{\mathrm{s}}l_{\mathrm{s}}} - \frac{2}{\mathrm{j}3Z_{\mathrm{s}}\sin 2\beta_{\mathrm{s}}l_{\mathrm{s}}} & -\frac{1}{\mathrm{j}Z_{\mathrm{d}}\sin\beta_{\mathrm{d}}l_{\mathrm{d}}} - \frac{2}{\mathrm{j}3Z_{\mathrm{s}}\sin 2\beta_{\mathrm{s}}l_{\mathrm{s}}} & -\frac{1}{\mathrm{j}Z_{\mathrm{d}}\sin\beta_{\mathrm{d}}l_{\mathrm{d}}} - \frac{2}{\mathrm{j}3Z_{\mathrm{s}}\sin 2\beta_{\mathrm{s}}l_{\mathrm{s}}} \\ -\frac{1}{\mathrm{j}Z_{\mathrm{d}}\sin\beta_{\mathrm{d}}l_{\mathrm{d}}} - \frac{2}{\mathrm{j}3Z_{\mathrm{s}}\sin 2\beta_{\mathrm{s}}l_{\mathrm{s}}} & \frac{2}{\mathrm{j}Z_{\mathrm{d}}\tan\beta_{\mathrm{d}}l_{\mathrm{d}}} + \frac{1}{\mathrm{j}Z_{\mathrm{s}}\tan\beta_{\mathrm{s}}l_{\mathrm{s}}} - \frac{2}{\mathrm{j}3Z_{\mathrm{s}}\sin 2\beta_{\mathrm{s}}l_{\mathrm{s}}} & -\frac{1}{\mathrm{j}Z_{\mathrm{d}}\sin\beta_{\mathrm{d}}l_{\mathrm{d}}} - \frac{2}{\mathrm{j}3Z_{\mathrm{s}}\sin 2\beta_{\mathrm{s}}l_{\mathrm{s}}} \\ -\frac{1}{\mathrm{j}Z_{\mathrm{d}}\sin\beta_{\mathrm{d}}l_{\mathrm{d}}} - \frac{2}{\mathrm{j}3Z_{\mathrm{s}}\sin 2\beta_{\mathrm{s}}l_{\mathrm{s}}} & -\frac{1}{\mathrm{j}Z_{\mathrm{d}}\sin\beta_{\mathrm{d}}l_{\mathrm{d}}} - \frac{2}{\mathrm{j}3Z_{\mathrm{s}}\sin 2\beta_{\mathrm{s}}l_{\mathrm{s}}} & \frac{2}{\mathrm{j}Z_{\mathrm{d}}\tan\beta_{\mathrm{d}}l_{\mathrm{d}}} + \frac{1}{\mathrm{j}Z_{\mathrm{s}}\tan\beta_{\mathrm{s}}l_{\mathrm{s}}} - \frac{2}{\mathrm{j}3Z_{\mathrm{s}}\sin 2\beta_{\mathrm{s}}l_{\mathrm{s}}} \end{bmatrix}. \tag{3.88}$$

It is important to mention, that in the topology, Fig. 3.11, the imaginary part of the coupling is compensated by B_{d}, the triangle element only. In Fig. 3.13 both, triangle and star elements do that job. Replacing the lumped element decoupler, Fig. 3.11, by the strip line decoupler, Fig. 3.13, we set (3.83) equal to (3.88) and get

$$2\mathrm{j}B_{\mathrm{d}} + \mathrm{j}B_{\mathrm{s}} = \frac{2}{\mathrm{j}Z_{\mathrm{d}}\tan\beta_{\mathrm{d}}l_{\mathrm{d}}} + \frac{1}{\mathrm{j}Z_{\mathrm{s}}\tan\beta_{\mathrm{s}}l_{\mathrm{s}}} - \frac{2}{\mathrm{j}3Z_{\mathrm{s}}\sin 2\beta_{\mathrm{s}}l_{\mathrm{s}}}, \tag{3.89}$$

$$2B_{\mathrm{d}} + B_{\mathrm{s}} = -\frac{2}{Z_{\mathrm{d}}\tan\beta_{\mathrm{d}}l_{\mathrm{d}}} - \frac{1}{Z_{\mathrm{s}}\tan\beta_{\mathrm{s}}l_{\mathrm{s}}} + \frac{2}{3Z_{\mathrm{s}}\sin 2\beta_{\mathrm{s}}l_{\mathrm{s}}}, \tag{3.90}$$

for the diagonal elements and

$$-\mathrm{j}B_{\mathrm{d}} = -\frac{1}{\mathrm{j}Z_{\mathrm{d}}\sin\beta_{\mathrm{d}}l_{\mathrm{d}}} - \frac{2}{\mathrm{j}3Z_{\mathrm{s}}\sin 2\beta_{\mathrm{s}}l_{\mathrm{s}}}, \tag{3.91}$$

$$B_{\mathrm{d}} = -\frac{1}{Z_{\mathrm{d}}\sin\beta_{\mathrm{d}}l_{\mathrm{d}}} - \frac{2}{3Z_{\mathrm{s}}\sin 2\beta_{\mathrm{s}}l_{\mathrm{s}}}, \tag{3.92}$$

for the non diagonal elements. Putting (3.92) into (3.90) leads to

$$B_{\mathrm{s}} = \frac{2(1-\cos\beta_{\mathrm{d}}l_{\mathrm{d}})}{Z_{\mathrm{d}}\sin\beta_{\mathrm{d}}l_{\mathrm{d}}} - \frac{\cos\beta_{\mathrm{s}}l_{\mathrm{s}}}{Z_{\mathrm{s}}\sin\beta_{\mathrm{s}}l_{\mathrm{s}}} + \frac{4}{3Z_{\mathrm{s}}\sin 2\beta_{\mathrm{s}}l_{\mathrm{s}}}, \tag{3.93}$$

while

$$\cot\frac{\beta_{\mathrm{d}}l_{\mathrm{d}}}{2} = \frac{\sin\beta_{\mathrm{d}}l_{\mathrm{d}}}{1-\cos\beta_{\mathrm{d}}l_{\mathrm{d}}} \tag{3.94}$$

helps simplifying it:

$$B_{\mathrm{s}} = \frac{2}{Z_{\mathrm{d}}\cot\frac{\beta_{\mathrm{d}}l_{\mathrm{d}}}{2}} - \frac{\cos\beta_{\mathrm{s}}l_{\mathrm{s}}}{Z_{\mathrm{s}}\sin\beta_{\mathrm{s}}l_{\mathrm{s}}} + \frac{4}{3Z_{\mathrm{s}}\sin 2\beta_{\mathrm{s}}l_{\mathrm{s}}}. \tag{3.95}$$

Z_d is now separated:

$$\frac{2}{Z_\mathrm{d}\cot\frac{\beta_\mathrm{d}l_\mathrm{d}}{2}} = B_\mathrm{s} + \frac{\cos\beta_\mathrm{s}l_\mathrm{s}}{Z_\mathrm{s}\sin\beta_\mathrm{s}l_\mathrm{s}} - \frac{4}{3Z_\mathrm{s}\sin 2\beta_\mathrm{s}l_\mathrm{s}}. \tag{3.96}$$

$$Y_\mathrm{d} = \frac{1}{Z_\mathrm{d}} = \frac{\cot\frac{\beta_\mathrm{d}l_\mathrm{d}}{2}}{2}\left(B_\mathrm{s} + \frac{1}{Z_\mathrm{s}\tan\beta_\mathrm{s}l_\mathrm{s}} - \frac{4}{3Z_\mathrm{s}\sin 2\beta_\mathrm{s}l_\mathrm{s}}\right) \tag{3.97}$$

And from (3.92) we get

$$\frac{1}{Z_\mathrm{d}\sin\beta_\mathrm{d}l_\mathrm{d}} = -\frac{2}{3Z_\mathrm{s}\sin 2\beta_\mathrm{s}l_\mathrm{s}} - B_\mathrm{d} \text{ and} \tag{3.98}$$

$$Y_\mathrm{d} = \frac{1}{Z_\mathrm{d}} = \sin\beta_\mathrm{d}l_\mathrm{d}\left(-\frac{2}{3Z_\mathrm{s}\sin 2\beta_\mathrm{s}l_\mathrm{s}} - B_\mathrm{d}\right). \tag{3.99}$$

3.8 Star and Triangle DMN Example

Three monopoles of length 18.5 mm and diameter of 3 mm are placed at the corners of an equilateral triangle distance of 20.83 mm a part (measured from the center of one monopole to the center of another monopole wire). They are mounted normal to a circular ground plane of 100 mm radius. The center of the triangle is co-located with the center of the circular ground plane. At a frequency of 3.6 GHz, full-wave electromagnetic analysis delivers the admittance matrix

$$\boldsymbol{Y}_\mathrm{B} = 10^{-3}\,\Omega^{-1}\begin{bmatrix} 57.1 & 33.8 & 33.8 \\ 33.8 & 57.1 & 33.8 \\ 33.8 & 33.8 & 57.1 \end{bmatrix} + \mathrm{j}10^{-3}\,\Omega^{-1}\begin{bmatrix} 9.9 & 27.6 & 27.6 \\ 27.6 & 9.9 & 27.6 \\ 27.6 & 27.6 & 9.9 \end{bmatrix}. \tag{3.100}$$

With (3.74) B_c is calculated,

$$\begin{aligned} B_\mathrm{cC} &= +106.42 \text{ x } 10^{-3}\,\Omega^{-1}, & C_\mathrm{cC} &= 4.7 \text{ pF} \\ B_\mathrm{cL} &= -33.0325 \text{ x } 10^{-3}\,\Omega^{-1}, & L_\mathrm{cL} &= 1.338 \text{ nH} \\ B_\mathrm{cRL} &= (-7.8382 - \mathrm{j}4.2262) \text{ x } 10^{-3}\,\Omega^{-1} \\ B_\mathrm{c\text{-}RL} &= (-7.8382 + \mathrm{j}4.2262) \text{ x } 10^{-3}\,\Omega^{-1}. \end{aligned}$$

There are four solutions existing, B_cC (C = capacitive), B_cL (L = inductive), B_cRL (RL = negative resistive and inductive), $B_\mathrm{c\text{-}RL}$ (-RL = resistive and inductive). Here $B_\mathrm{c} = +106.42 \text{ x } 10^{-3}\,\Omega^{-1}$ is chosen, equating to $C_\mathrm{c} = 4.70$ pF, leading to

$$\boldsymbol{Y}_\mathrm{A} = 10^{-3}\,\Omega^{-1}\begin{bmatrix} 31.4 & 0 & 0 \\ 0 & 31.4 & 0 \\ 0 & 0 & 31.4 \end{bmatrix} + \mathrm{j}10^{-3}\,\Omega^{-1}\begin{bmatrix} 12.4 & 25.4 & 25.4 \\ 25.4 & 12.4 & 25.4 \\ 25.4 & 25.4 & 12.4 \end{bmatrix} \tag{3.101}$$

and

$$\alpha = (31.4 + \mathrm{j}12.4) \text{ x } 10^{-3}\,\Omega^{-1}, \quad a = 31.8\,\Omega. \tag{3.102}$$

$$\beta = \mathrm{j}25.4 \text{ x } 10^{-3}\,\Omega^{-1} \text{ and } \quad b = 0\,\Omega. \tag{3.103}$$

3.8.1 Lumped Lossless Elements

We prescribe

$$G = 20 \text{ x } 10^{-3}\ \Omega^{-1}, \quad B = 0. \tag{3.104}$$

From these data we can compute the lumped element values for the DMN as

$$\begin{aligned} B_{\mathrm{d}} &= +25.40 \text{ x } 10^{-3}\ \Omega^{-1}, & C_d &= 1.12 \text{ pF} \\ B_{\mathrm{g}} &= -25.06 \text{ x } 10^{-3}\ \Omega^{-1}, & L_g &= 1.76 \text{ nH} \\ B_{\mathrm{s}} &= -38.17 \text{ x } 10^{-3}\ \Omega^{-1}, & L_s &= 1.13 \text{ nH} \\ B_{\mathrm{e}} &= +25.06 \text{ x } 10^{-3}\ \Omega^{-1}, & C_e &= 1.10 \text{ pF} \end{aligned}$$

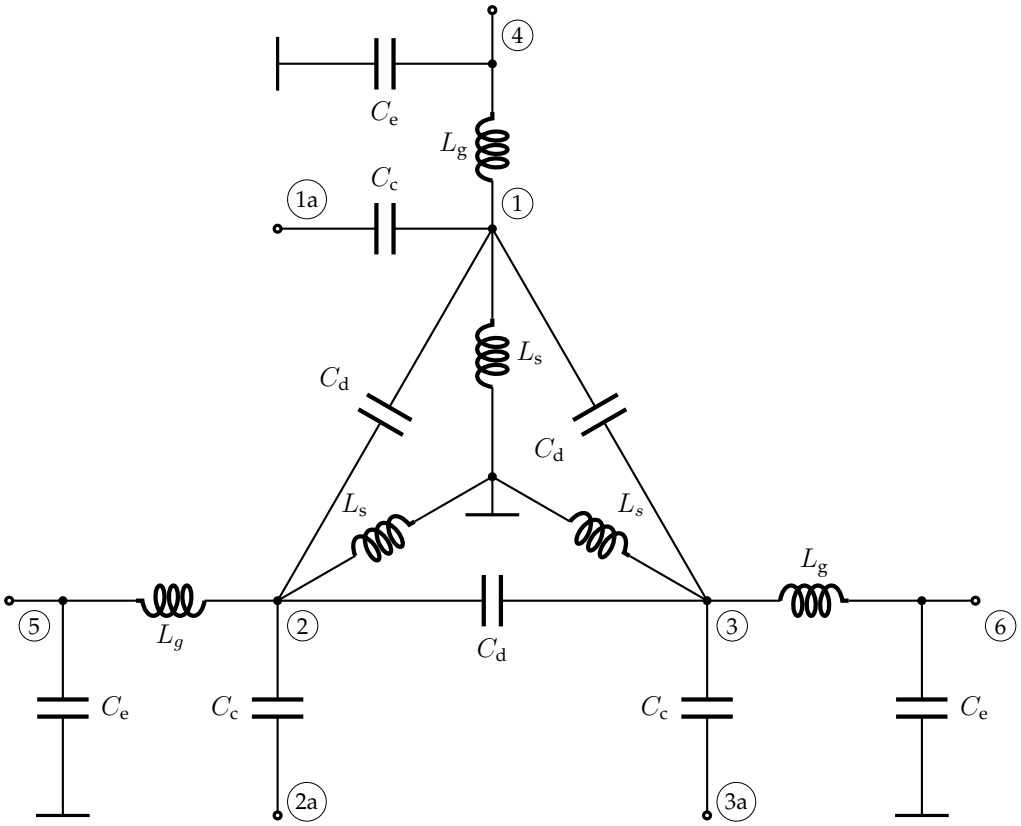

Fig. 3.14. Network structure of the proposed decoupling and matching 6-port.

Fig. 3.14 shows the network yielding the desired admittance matrix of

$$\boldsymbol{Y} = 0.02\ \Omega^{-1} \begin{bmatrix} 1 & 0 & 0 \\ 0 & 1 & 0 \\ 0 & 0 & 1 \end{bmatrix}, \tag{3.105}$$

which corresponds to uncoupled ports with a port input impedance of $50\ \Omega$. For a commercial design striplines and surface mounted device (SMD) capacitors would be used, due to low losses and small size.

3.8.2 Lossy Stripline Elements With SMD Capacitors

This design starts with $\boldsymbol{Y}_{\mathrm{A}}$, where the real parts of the coupling are $0\ \Omega^{-1}$. A triangle is now chosen to be the layout. Therefore,

$$l_{\mathrm{d}} = \sqrt{3} \cdot l_{\mathrm{s}}. \tag{3.106}$$

The triangle distance should be the same as the one of the given antenna array

$$l_{\mathrm{d}} = 20.83\ \mathrm{mm}. \tag{3.107}$$

The whole circuit is optimized for lowest losses at 3.6 GHz with the ADS simulation. As given requirement, the matching and decoupling should be as good as possible within a bandwidth of 100 MHz. For achieving these goals, a suboptimal matching is chosen. This means the matching is not perfect at one frequency. In the Smith-Chart, the impedance curve is a loop around the point of optimal matching. It seems obvious, that connection lines from the array to the amplifiers are needed anyway, so a floating strip line design was chosen. Because this strip line also does not behave like an ideal inductor and the suboptimal matching, the capacitor C_{e} changes, Fig. 3.15.

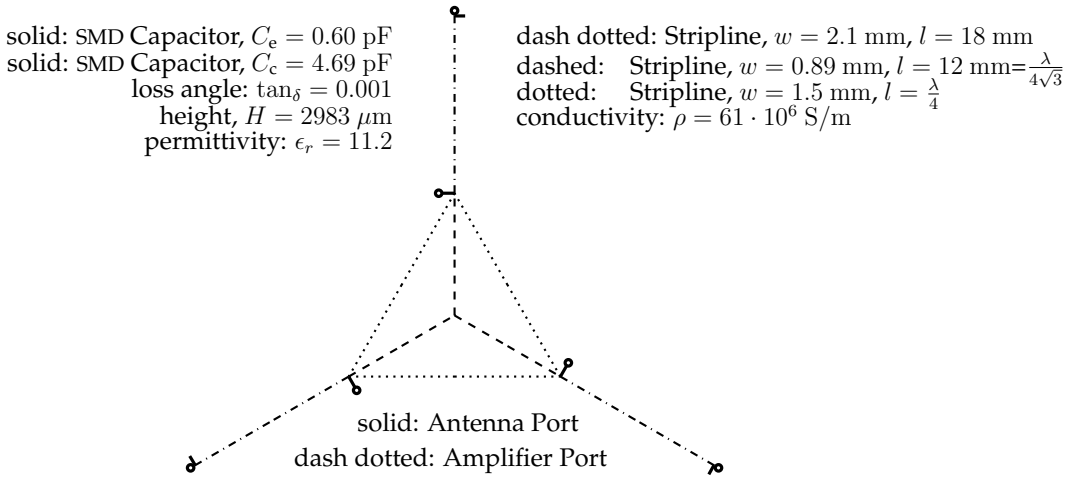

Fig. 3.15. 2-Dimensional DMN Layout

Therefore, the parameters are:

$$\begin{aligned}
\beta_{\mathrm{d}} &= 0.2097\ \frac{\mathrm{rad}}{\mathrm{mm}}, \\
\beta_{\mathrm{s}} &= 0.2055\ \frac{\mathrm{rad}}{\mathrm{mm}}, \\
Z_{\mathrm{d}} &= 64.3\ \Omega, \\
Z_{\mathrm{s}} &= 76.9\ \Omega
\end{aligned}$$

and the lossless $\boldsymbol{Y}_{\mathrm{Q}}$ for these optimization goals is

$$\boldsymbol{Y}_{\mathrm{Q}} = \mathrm{j}10^{-3}\,\Omega^{-1} \begin{bmatrix} -3.6 & -25.4 & -25.4 \\ -25.4 & -3.6 & -25.4 \\ -25.4 & -25.4 & -3.6 \end{bmatrix}. \tag{3.108}$$

When connecting $\boldsymbol{Y}_{\mathrm{Q}}$ in parallel to $\boldsymbol{Y}_{\mathrm{A}}$, there will be no coupling anymore. After introducing losses $\boldsymbol{Y}_{\mathrm{Ql}}$ generated from ADS differs by a real valued part of the diagonal elements from the lossless one $\boldsymbol{Y}_{\mathrm{Q}}$,

$$\boldsymbol{Y}_{\mathrm{Ql}} = 10^{-3}\,\Omega^{-1} \begin{bmatrix} 0.2 & 0 & 0 \\ 0 & 0.2 & 0 \\ 0 & 0 & 0.2 \end{bmatrix} + \mathrm{j}10^{-3}\,\Omega^{-1} \begin{bmatrix} -3.6 & -25.4 & -25.4 \\ -25.4 & -3.6 & -25.4 \\ -25.4 & -25.4 & -3.6 \end{bmatrix}. \tag{3.109}$$

3.8.3 Stripline Decoupler

As already shown, C_{d} and L_{s} in Fig. 3.14 can together be replaced by stripline elements. Two degrees of freedom, l_{d} and l_{s} are used to adjust the size of the decoupler to perfectly fit below the antenna array. For the calculation of Z_{d} and Z_{s}, β_{d} and β_{s} are taken from section 3.8.2.

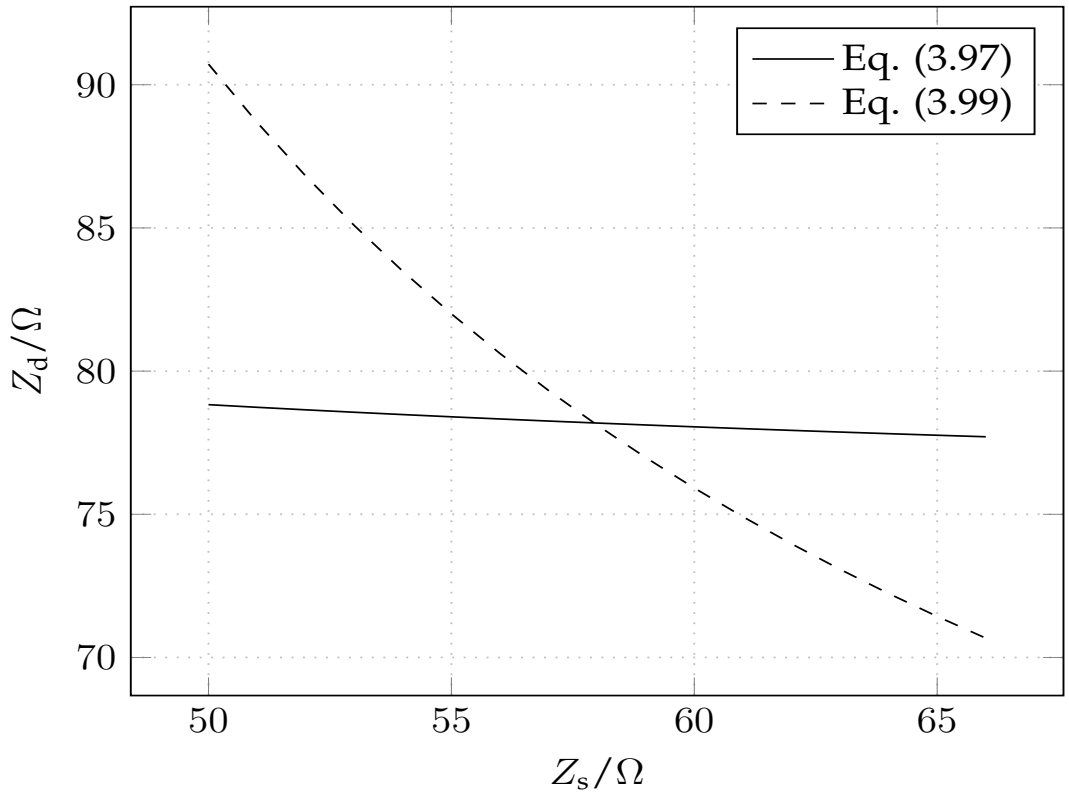

Fig. 3.16. Impedance Z_{d} in dependence on Z_{s} calculated with (3.97)

When choosing both impedances, that (3.97) and (3.99) are fulfilled as Fig. 3.16 shows, the micro stripline decoupler is identical to the lumped elements decoupler.

3.9 Star and Triangle DMN Results of Simulation

3.9.1 Lossless Lumped Elements DMN

Computer Simulation Technology (CST) antenna array results have been used for a DMN analysis with ADS and SPICE. Fig. 3.18 shows the matching, while Fig. 3.19 shows the decoupling obtained for ideal lossless lumped elements within the DMN. During the simulations it became apparent, that the star and triangle circuit is more robust against element value tolerances and has a bigger bandwidth compared to the results shown in 3.4.1.

3.9.2 Lossy Strip Line/SMD Capacitor DMN

A more common case is for sure a look into a lossy DMN, as shown in Fig. 3.15. Fig. 3.20 shows the matching, Fig. 3.21 the decoupling, while Fig. 3.17 shows the losses obtained for lossy lumped elements within the DMN, where $\eta_{\mathrm{dB}} = 10 \log \frac{P_{\mathrm{out}}}{P_{\mathrm{in}}}$. P_{in} is the sum input power into the three ports $4, 5$ and 6, while P_{out} is the sum output power to the antenna array, Fig. 3.17. Here, the losses for the best case and the worst case have been calculated according to section 3.9.3.

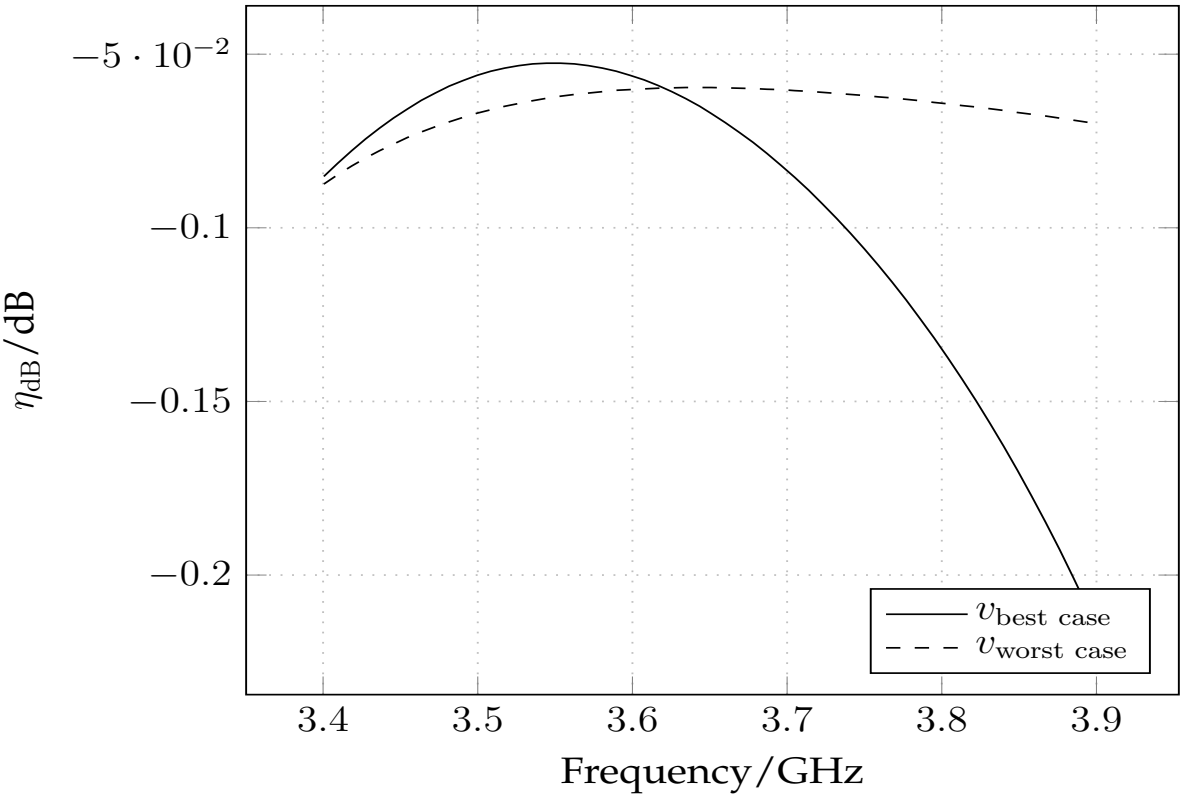

$v_{\mathrm{best\ case}} = [0.4083 + 0.4864\,\mathrm{j}; -0.5761 - 0.4864\,\mathrm{j}; 0.1678]^{\mathrm{T}}\mathrm{V}$
$v_{\mathrm{worst\ case}} = [(0,5774), (0,5774), (0,5774)]^{\mathrm{T}}\mathrm{V}$
Fig. 3.17. Losses obtained for DMN shown in Fig. 3.15

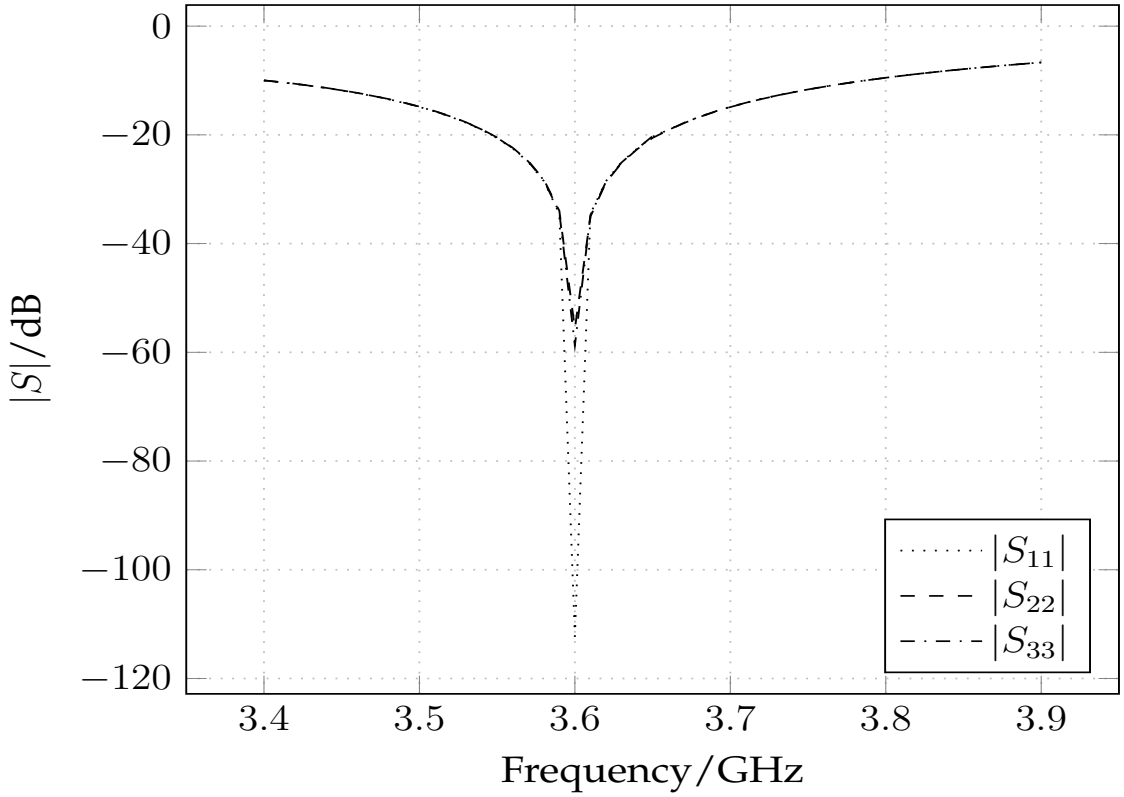

Fig. 3.18. Matching obtained for lossless lumped elements

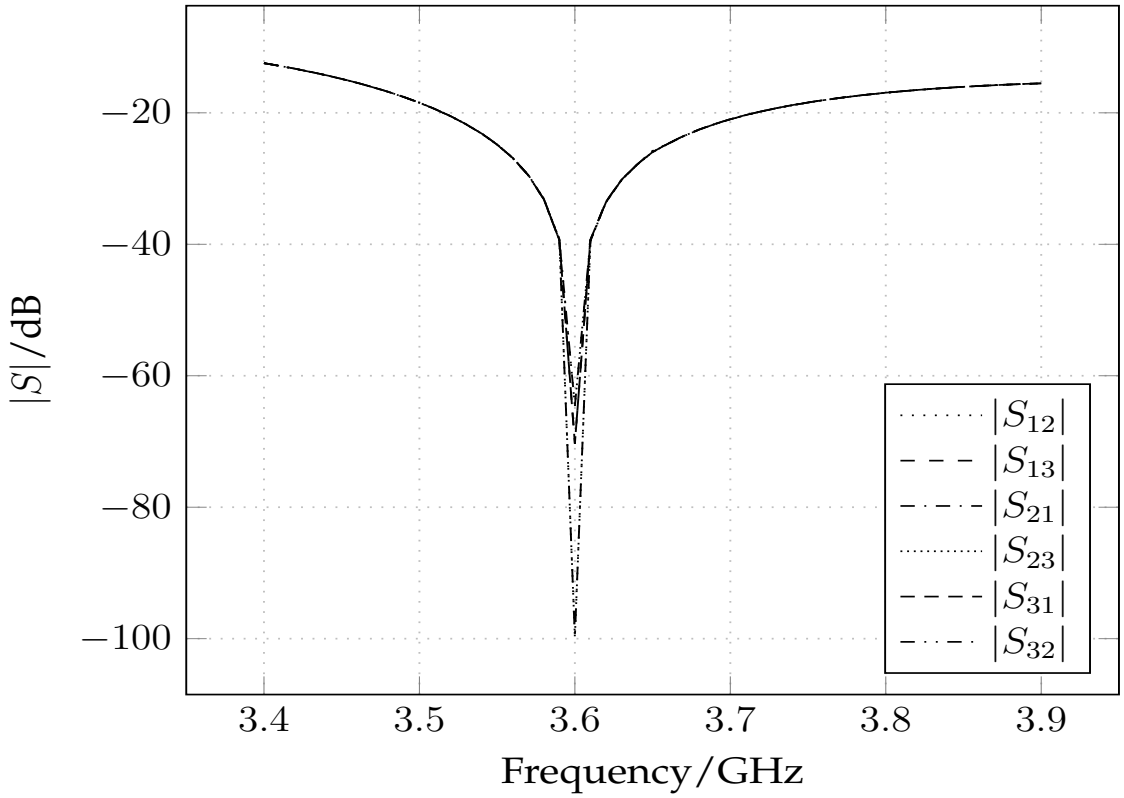

Fig. 3.19. Decoupling obtained for lossless lumped elements

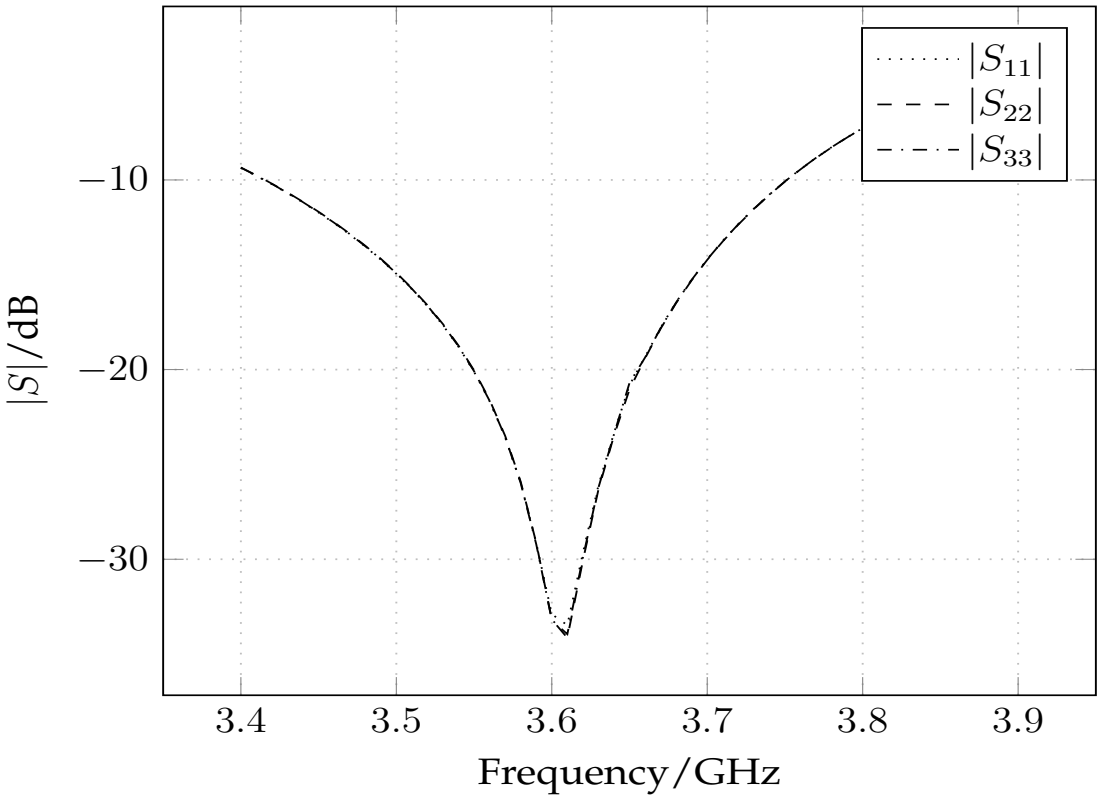

Fig. 3.20. Matching obtained for DMN shown in Fig. 3.15

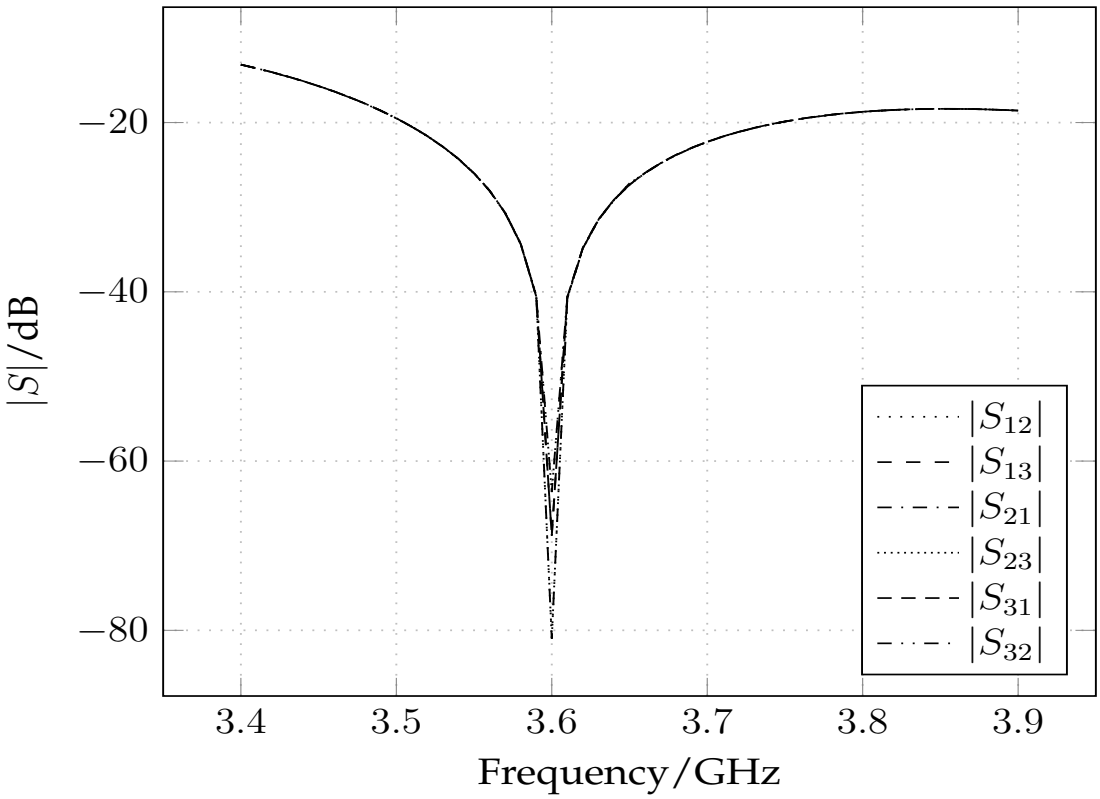

Fig. 3.21. Decoupling obtained for DMN shown in Fig. 3.15

3.9.3 Calculation of Losses

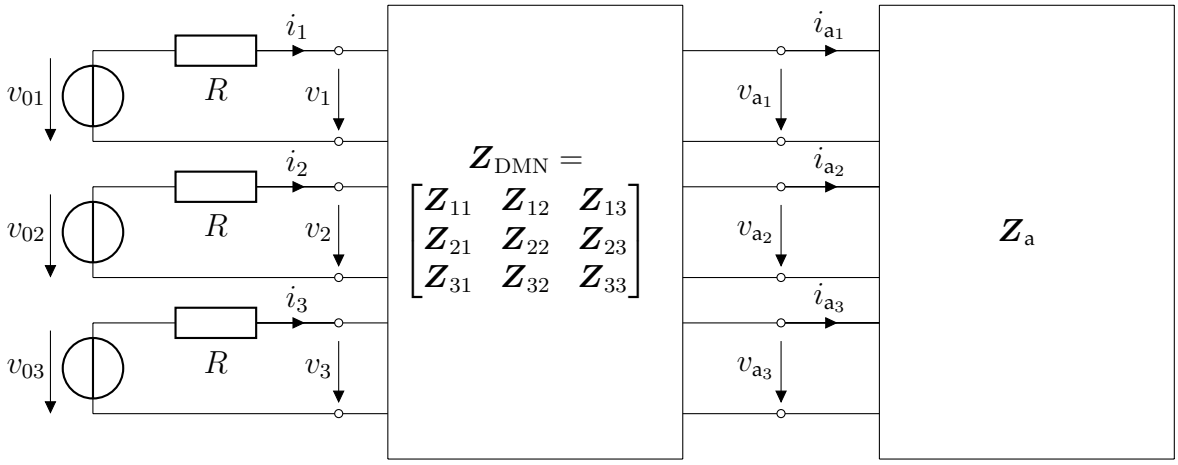

Fig. 3.22. Antenna array $\boldsymbol{Z}_{\mathrm{a}}$ driven by signal sources via $\boldsymbol{Z}_{\mathrm{DMN}}$.

For power considerations, the model shown in Fig. 3.22 is taken, where $\boldsymbol{v}_0$ is the virtual ideal source input voltage, $\boldsymbol{v}$ the real input voltage of the source including a resistance R and $\boldsymbol{v}_{\mathrm{a}}$ is the output voltage.

$$\boldsymbol{v}_0 = [v_{01}, v_{02}, v_{03}]^{\mathrm{T}}, \quad \boldsymbol{v} = [v_1, v_2, v_3]^{\mathrm{T}}, \quad \boldsymbol{v}_{\mathrm{a}} = [v_{\mathrm{a}1}, v_{\mathrm{a}2}, v_{\mathrm{a}3}]^{\mathrm{T}} \tag{3.110}$$

$\boldsymbol{i}$ and $\boldsymbol{i}_{\mathrm{a}}$ are input and output current of the DMN.

$$\boldsymbol{i} = [i_1, i_2, i_{i3}]^{\mathrm{T}}, \quad \boldsymbol{i}_{\mathrm{a}} = [i_{\mathrm{a}_1}, i_{\mathrm{a}_2}, i_{\mathrm{a}_3}]^{\mathrm{T}}, \quad \boldsymbol{v}_0 = \boldsymbol{v} + R\mathbf{1} \cdot \boldsymbol{i}, \quad \boldsymbol{v}_{\mathrm{a}} = \boldsymbol{Z}_{\mathrm{a}} \cdot \boldsymbol{i}_{\mathrm{a}} \tag{3.111}$$

For the calculation, the impedance matrix description is used.

$$\begin{bmatrix} \boldsymbol{v} \\ \boldsymbol{v}_{\mathrm{a}} \end{bmatrix} = \begin{bmatrix} \boldsymbol{Z}_{11} & \boldsymbol{Z}_{12} \\ \boldsymbol{Z}_{21} & \boldsymbol{Z}_{22} \end{bmatrix} \cdot \begin{bmatrix} \boldsymbol{i} \\ -\boldsymbol{i}_{\mathrm{a}} \end{bmatrix} \tag{3.112}$$

The dissipated power P_{diss} is the difference between input and output power:

$$P_{\mathrm{diss}} = \mathrm{Re}\{\boldsymbol{v}^{\mathrm{H}}\boldsymbol{i} - \boldsymbol{v}_{\mathrm{a}}^{\mathrm{H}}\boldsymbol{i}_{\mathrm{a}}\}. \tag{3.113}$$

$$\boldsymbol{Z}_{\mathrm{a}}\boldsymbol{i}_{\mathrm{a}} = \boldsymbol{Z}_{21}\boldsymbol{i} - \boldsymbol{Z}_{22}\boldsymbol{i}_{\mathrm{a}}, \quad \boldsymbol{i}_{\mathrm{a}} = (\boldsymbol{Z}_{\mathrm{a}} + \boldsymbol{Z}_{22})^{-1}\boldsymbol{Z}_{21}\boldsymbol{i} = \boldsymbol{F} \cdot \boldsymbol{i} \tag{3.114}$$

The voltage $\boldsymbol{v}$ is dependent on the load consisting of $\boldsymbol{Z}_{\mathrm{a}}$ and $\boldsymbol{Z}_{\mathrm{DMN}}$

$$\boldsymbol{v} = (\boldsymbol{Z}_{11} - \boldsymbol{Z}_{12}(\boldsymbol{Z}_{\mathrm{a}} + \boldsymbol{Z}_{22})^{-1}\boldsymbol{Z}_{21})\boldsymbol{i} = \boldsymbol{Z}_{\mathrm{in}}^{\mathrm{T}}\boldsymbol{i} = \boldsymbol{Z}_{\mathrm{in}}\boldsymbol{i} = (\boldsymbol{Z}_{11} - \boldsymbol{Z}_{12}\boldsymbol{F})\boldsymbol{i}. \tag{3.115}$$

$$\boldsymbol{i} = \frac{1}{R}(\boldsymbol{v}_0 - \boldsymbol{v}), \quad \boldsymbol{v} = \boldsymbol{Z}_{\mathrm{in}}(R \cdot \mathbf{1} + \boldsymbol{Z}_{\mathrm{in}})^{-1}\boldsymbol{v}_0 = \boldsymbol{D} \cdot \boldsymbol{v}_0 \tag{3.116}$$

$$\boldsymbol{v}^{\mathrm{H}}\boldsymbol{i} = \frac{1}{R}\boldsymbol{v}_0^{\mathrm{H}}\boldsymbol{D}^{\mathrm{H}}(\mathbf{1} - \boldsymbol{D})\boldsymbol{v}_0, \quad \boldsymbol{D} = \boldsymbol{Z}_{\mathrm{in}}(R\mathbf{1} + \boldsymbol{Z}_{\mathrm{in}})^{-1} \tag{3.117}$$

$$\boldsymbol{v}^{\mathrm{H}}\boldsymbol{i} = \boldsymbol{v}_0^{\mathrm{H}}\boldsymbol{A}\boldsymbol{v}_0, \quad \boldsymbol{A} = \frac{1}{R}\boldsymbol{D}^{\mathrm{H}}(\mathbf{1} - \boldsymbol{D}) \tag{3.118}$$

$$\boldsymbol{v}_\mathrm{a} = \boldsymbol{Z}_\mathrm{a}\boldsymbol{i}_\mathrm{a} = \boldsymbol{Z}_\mathrm{a}(\boldsymbol{Z}_\mathrm{a} + \boldsymbol{Z}_{22})^{-1}\boldsymbol{Z}_{21}\boldsymbol{i} = \boldsymbol{Z}_\mathrm{a}\boldsymbol{F}\frac{1}{R}(\mathbf{1} - \boldsymbol{D})\boldsymbol{v}_0 \tag{3.119}$$

$$\boldsymbol{i}_\mathrm{a} = \frac{1}{R}\boldsymbol{F}(\mathbf{1} - \boldsymbol{D})\boldsymbol{v}_0, \quad \boldsymbol{v}_\mathrm{a}^\mathrm{H}\boldsymbol{i}_\mathrm{a} = \frac{1}{R^2}(\mathbf{1} - \boldsymbol{D}^\mathrm{H})\boldsymbol{F}^\mathrm{H}\boldsymbol{Z}_\mathrm{a}^*\boldsymbol{F}(\mathbf{1} - \boldsymbol{D})\boldsymbol{v}_0 = \boldsymbol{v}_0^\mathrm{H}\boldsymbol{B}\boldsymbol{v}_0 \tag{3.120}$$

$$\boldsymbol{B} = \frac{1}{R^2}(\mathbf{1} - \boldsymbol{D}^\mathrm{H})\boldsymbol{F}^\mathrm{H}\boldsymbol{Z}_\mathrm{a}^*\boldsymbol{F}(\mathbf{1} - \boldsymbol{D}) \tag{3.121}$$

$$P_\mathrm{diss} = P_\mathrm{in} - P_\mathrm{out} = \frac{1}{2}\boldsymbol{v}_0^\mathrm{H}(\boldsymbol{A} + \boldsymbol{A}^\mathrm{H})\boldsymbol{v}_0 - \frac{1}{2}\boldsymbol{v}_0^\mathrm{H}(\boldsymbol{B} + \boldsymbol{B}^\mathrm{H})\boldsymbol{v}_0 \tag{3.122}$$

$$\eta_\mathrm{dB} = 10 \cdot \log_{10}\left|\frac{P_\mathrm{out}}{P_\mathrm{in}}\right|, \quad P_\mathrm{in} = \frac{1}{2}\boldsymbol{v}_0^\mathrm{H}(\boldsymbol{A} + \boldsymbol{A}^\mathrm{H})\boldsymbol{v}_0, \quad P_\mathrm{out} = \frac{1}{2}\boldsymbol{v}_0^\mathrm{H}(\boldsymbol{B} + \boldsymbol{B}^\mathrm{H})\boldsymbol{v}_0 \tag{3.123}$$

$$\boldsymbol{C} = (\boldsymbol{A} + \boldsymbol{A}^\mathrm{H}) - (\boldsymbol{B} + \boldsymbol{B}^\mathrm{H}) = \boldsymbol{C}^\mathrm{H} = \boldsymbol{Q}\boldsymbol{\Lambda}\boldsymbol{Q}^\mathrm{H} \tag{3.124}$$

$$\boldsymbol{Q} = [\boldsymbol{q}_1, \boldsymbol{q}_2, \boldsymbol{q}_3], \quad \lambda_1 \geq \lambda_2 \geq \lambda_3 > 0 \tag{3.125}$$

$$P_\mathrm{diss\ max} = \Lambda_{11} \quad \text{for} \quad \boldsymbol{v}_0 = \boldsymbol{q}_1, \quad ||\boldsymbol{v}_0||_2^2 = 1 \tag{3.126}$$

$$P_\mathrm{diss\ min} = \Lambda_{33} \quad \text{for} \quad \boldsymbol{v}_0 = \boldsymbol{q}_3, \quad ||\boldsymbol{v}_0||_2^2 = 1 \tag{3.127}$$

3.10 Measurements

During summer 2017, antenna arrays and DMNs have been implemented and measured by Jonas Kornprobst and Prof. Dr. -Ing. Thomas Eibert.

3.10.1 Direct DMN Design According to 3.2

The layout of the micro stripline DMN and antenna array, designed by Dr. Michel Ivrlač, are shown in Fig. 3.23. The distance between the centers of the monopoles is $0.25\ \lambda$, free space wavelength at 3.6 GHz. The ground plane is made of aluminium, as DMN substrate copper coated RO3003 is used. For lower losses, caused by skin effect, the antenna elements were made of silver coated copper. The fabricated prototype corresponding to the model is seen in Fig. 3.24.

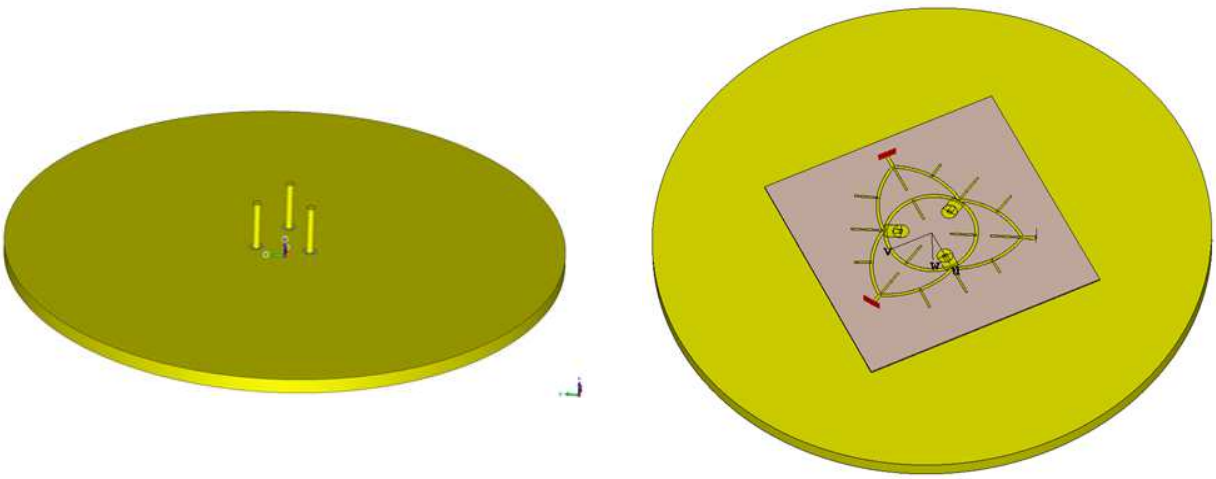

Fig. 3.23. Model of three-element array with direct DMN.

Fig. 3.24. Fabricated prototype of three-element array with direct DMN.

The measured S-parameters for matching, Fig. 3.28 and decoupling, Fig. 3.29 of the prototype are compared to simulation results regarding matching in Fig. 3.25 and decoupling in Fig. 3.26. The agreement between measured and simulated results is very good. The achieved bandwidth is close to 200 MHz with the previosly defined design goal of -16 dB, which is assumed for the input matching as well as for the coupling between the feed ports. This DMN exhibits a double resonant behavior, which is responsible for the large bandwidth. In this case, the point of optimum decoupling in Fig. 3.26 is not achieved at the same frequency as the point of optimum matching in Fig. 3.25 is.

The three-dimensional radiation pattern of one single antenna element is shown in Fig. 3.27. Therefore, one feed port has been excited with a $50\ \Omega$ source, while the other ports were terminated with $50\ \Omega$ resistors. Due to losses in the DMN and the antenna structure of about -0.24 dB, the efficiency is considerably high, but it is slightly worse than for the array DMN combinations to be considered in later sections.

The optimized horizontal realized array gain due to the simulated element radiation patterns is displayed in Fig. 3.30. The optimization has been performed for every desired azimuth scan direction based on the beam-forming procedure as discussed in [35]. The beam-forming procedure works with one horizontal pattern cut, for an angle of $\vartheta = 70^o$ in the considered case, and maximizes the power density in a given horizontal direction for a given input power. Two different reference patterns are considered in Fig. 3.30. The right side of the figure shows the realized gain, whereas an averaged horizontal cut of one element for the elevation angle of $\vartheta = 70^o$ has been taken as reference in the left side of the figure. This reference pattern has a certain directivity due to vertical beam-forming and leads, thus, to a lower array gain. As also discussed earlier, the array gain exhibits some oscillations dependent on the radiation angle, which is due to the variations in the single element patterns of the array.

Fig. 3.31 shows the measurement setup for the radiation pattern measurements in the anechoic chamber of the chair of high frequency engineering (HFT) at technical university of Munich (TUM). The array on its device holder is mounted on the spherical positioner. Tunable phase shifters and attenuators are used to adjust the excitation weights of the

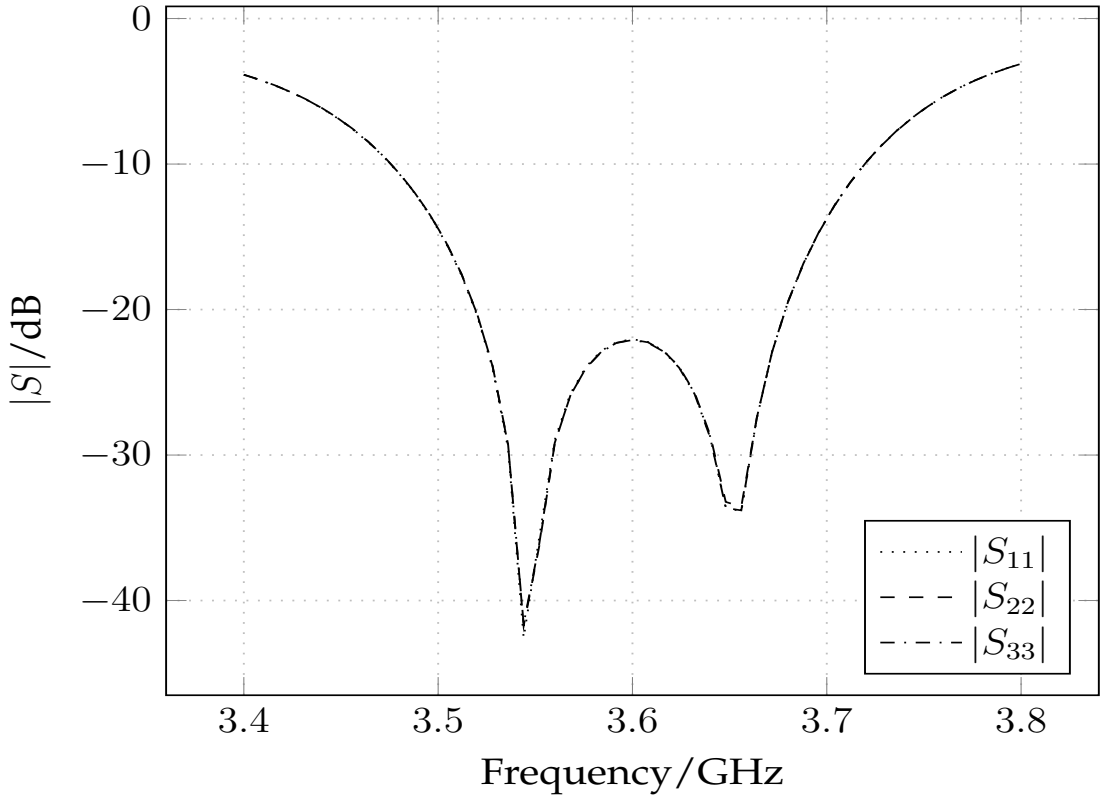

Fig. 3.25. Matching obtained for direct DMN simulation

array elements. On the opposite side of the anechoic chamber, the reference antenna including its positioner is located. Here, a well characterized Yagi antenna was used. Outside the anechoic chamber is the rack with network analyzer and the measurement control computer.

Fig. 3.32 displays measured single element pattern cuts of the array and compares them with the corresponding results from simulations. During the measurements, all ports were terminated with $50\ \Omega$ resistors and the port corresponding to the measured element was excited. The upper left chart shows all three measured element pattern cuts with their mean beams directed to $\varphi = 0°$ and the three remaining charts compare the individual element pattern measurements to the simulation. The three element patterns show good agreement among each other and the agreement of the measurements and the simulations is even more remarkable.

Fig. 3.33 shows the optimized horizontal realized array gain obtained from the optimization with the measured array element pattern, for a fixed elevation angle of $\vartheta = 70°$. Measured curves agree well with the corresponding results from simulated patterns.

For verifying the beam forming behavior of the fabricated prototype, three different excitation vectors (azimuth angles $0°, 300°$ and $330°$) were hard-wired by a feed network consisting of power dividers, adjustable phase shifters and attenuators. The optimum beam forming vectors according to [35] were generated while therefore the resulting array radiation patterns were measured in the anechoic chamber.

Fig. 3.34 shows the obtained excitation weights for the three angles and the array patterns obtained from the measurements with these excitation weights. The realized max-

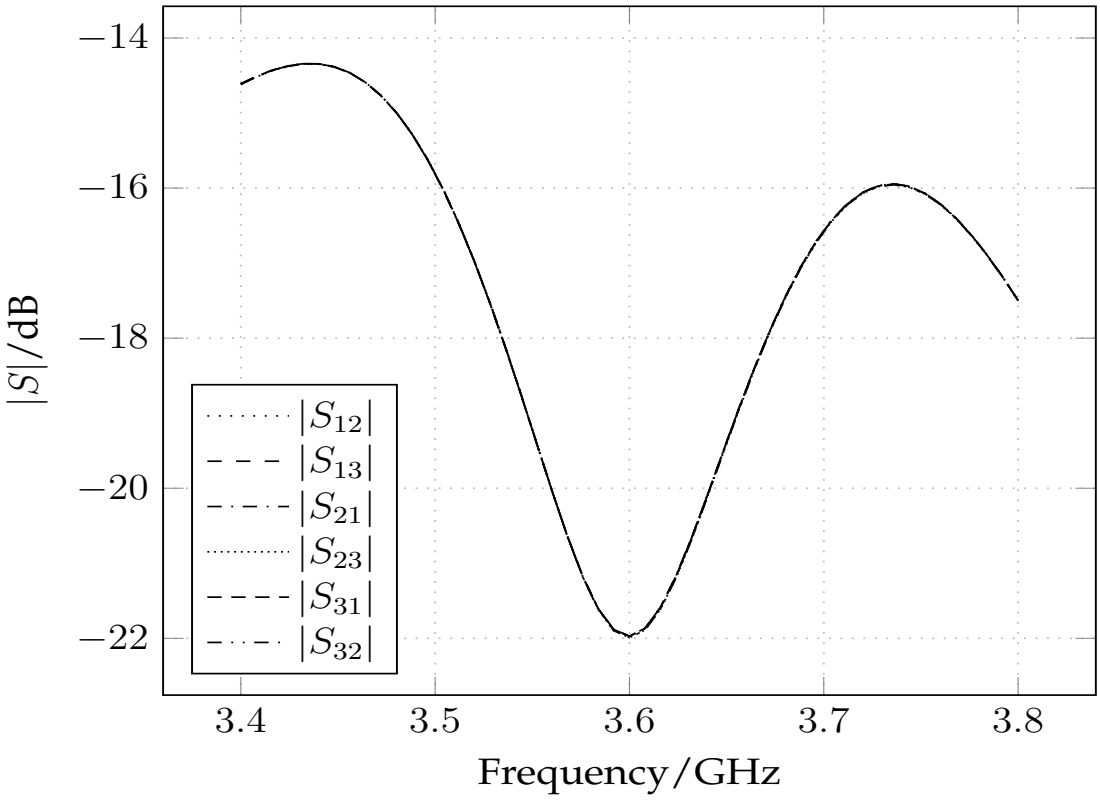

Fig. 3.26. Decoupling obtained for direct DMN simulation

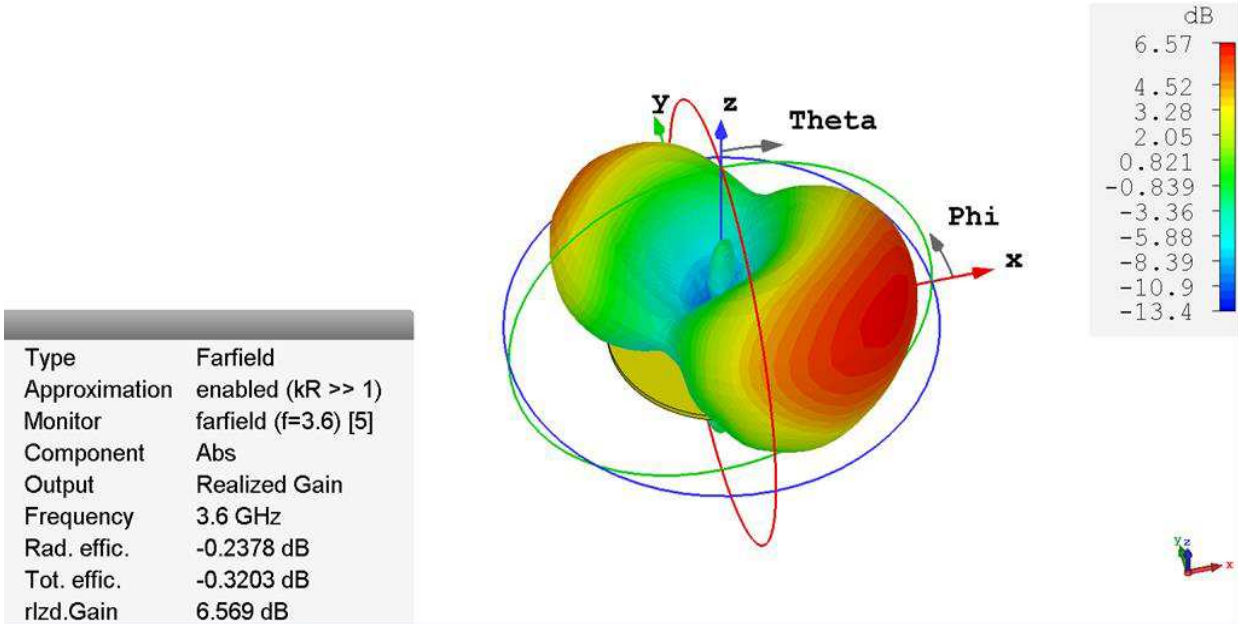

Fig. 3.27. Three-dimensional element pattern of three-element array with direct DMN, simulated.

imum gain of all three cuts is close to the theoretically expected value. The shapes of the three patterns show differences, but this is also expected for the chosen main beam angles.

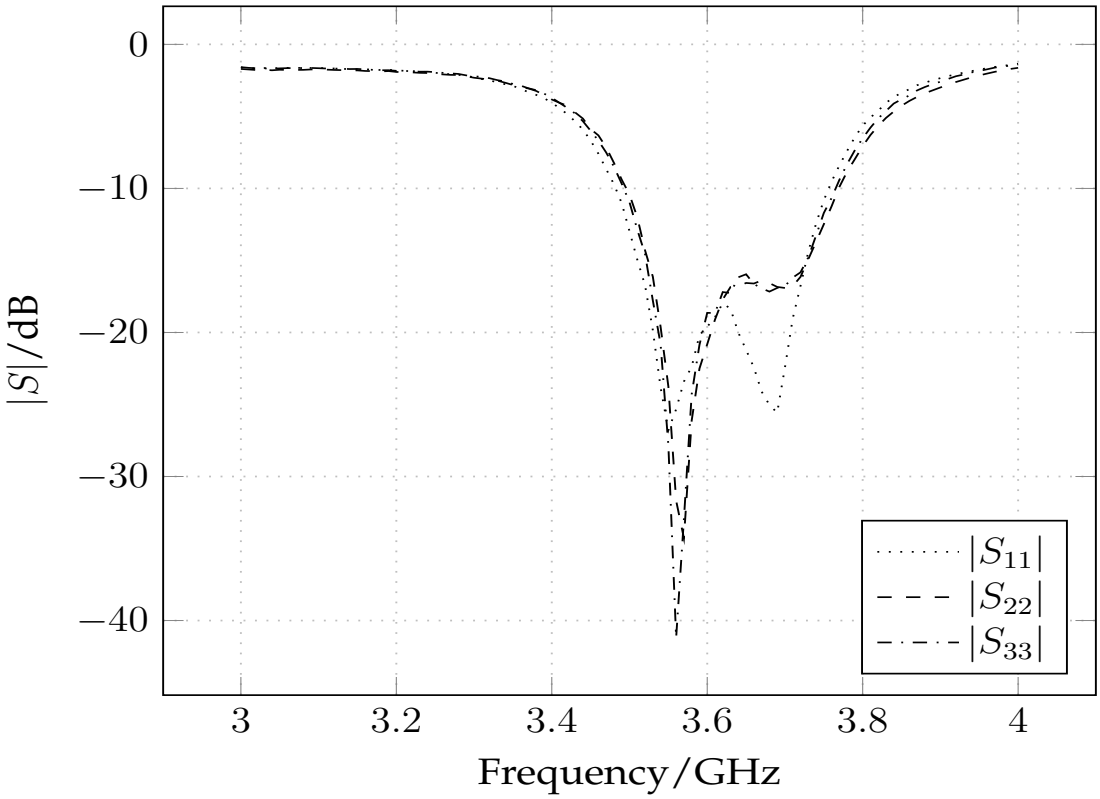

Fig. 3.28. Matching obtained for direct DMN measurement

3.10.2 Star triangle DMN Design According to 3.6

The layout of the DMN in micro-strip technology and the arrangement of the array elements is shown in Fig. 3.35, where the distance between the centers of the monopoles is about $0.26\ \lambda$ free space wavelength at 3.6 GHz. Fig. 3.36 shows the fabricated prototype.

The measured S-parameters for matching, Fig. 3.39 and decoupling, Fig. 3.40 of the prototype are compared to simulation results regarding matching in Fig. 3.37 and decoupling in Fig. 3.38. Measured and simulated results agree very good while the achieved bandwidth is about 100 MHz, with the previosly defined design goal of -16 dB for the input matching as well as for the coupling between the feed ports. In comparison to typical compact antenna array systems, here the bandwidth is very broad.

A characteristic three-dimensional radiation pattern of one radiation element of the array is shown in Fig. 3.41, where one of the feed ports has been excited with a $50\ \Omega$ source and the other two ports were terminated with $50\ \Omega$ resistors. The here indicated radiation efficiency is excellent (due to losses in the DMN and the antenna structure). The positive value of about $+0.03$ dB is resulting from numerical inaccuracies.

The optimized horizontal realized array gain due to the simulated element radiation patterns is displayed in Fig. 3.42. The optimization has been performed for every desired azimuth scan direction based on the beam-forming procedure as discussed in [35]. The beam-forming procedure works with one horizontal pattern cut, for an angle of $\vartheta = 70^o$ in the considered case, and maximizes the power density in a given horizontal direction for a given input power (sum of accepted power at all three antenna array element ports). Two different reference patterns are considered in Fig. 3.42. The right side of the figure shows

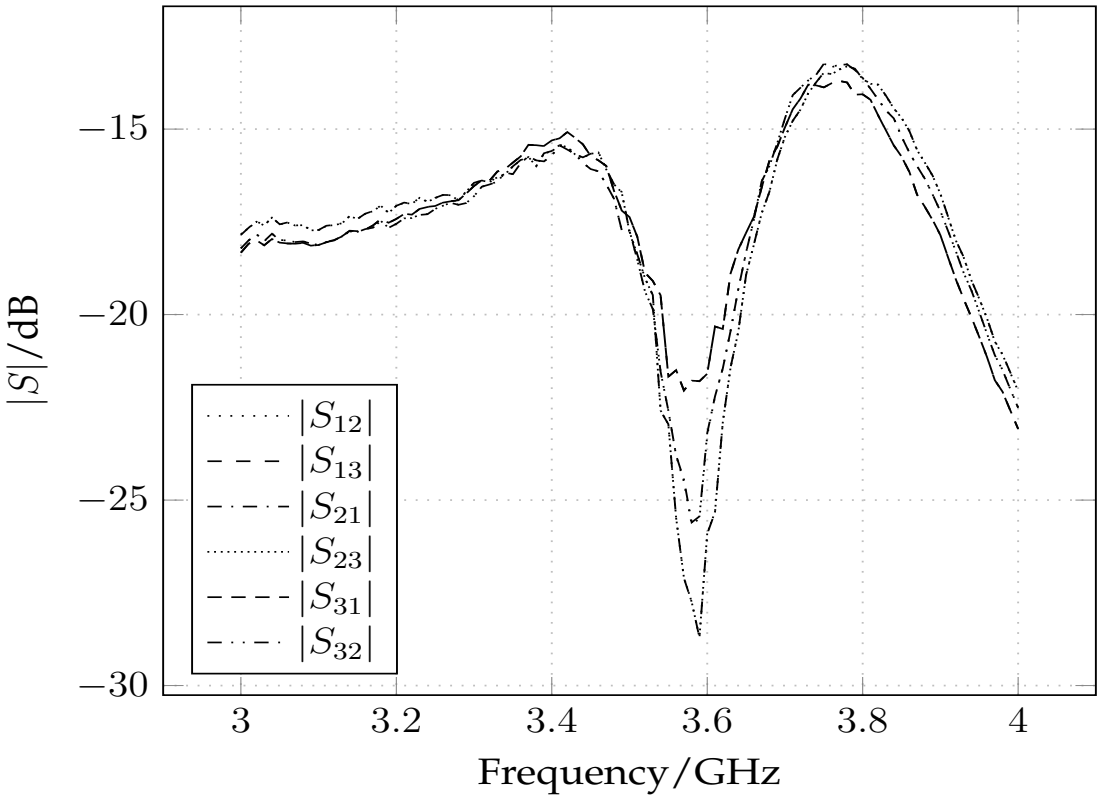

Fig. 3.29. Decoupling obtained for direct DMN measurement

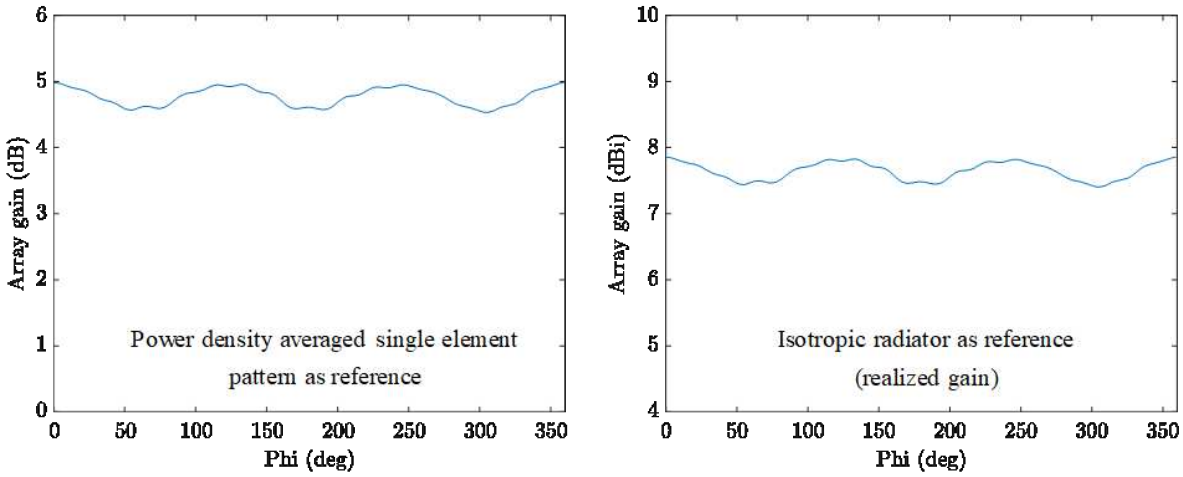

Fig. 3.30. Optimized horizontal realized array gain of three-element array with direct DMN, based on simulated element patterns, for a fixed elevation angle of $\vartheta = 70°$.

the realized gain, whereas an averaged horizontal cut of one element for the elevation angle of $\vartheta = 70^o$ has been taken as reference in the left side of the figure. This reference pattern has a certain directivity, due to vertical beam-forming and leads to a lower array gain. As also discussed earlier, the array gain exhibits some oscillations, dependent on the radiation angle, which is due to the variations in the single element patterns of the array.

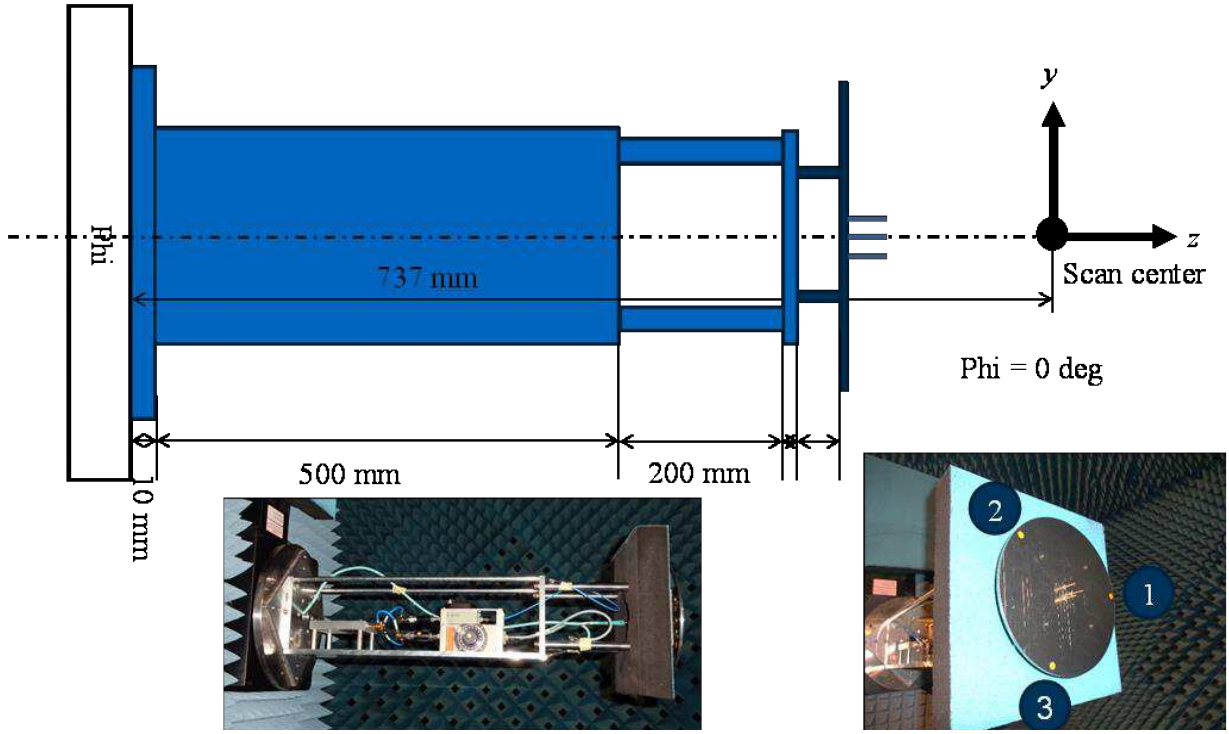

Fig. 3.31. Measurement setup of three-element array with direct DMN, seen in the anechoic chamber of TUM.

Fig. 3.43 shows measured single element pattern cuts of the array and compares them to the corresponding results from simulations. During the measurements, all ports were terminated with $50\ \Omega$ and the port corresponding to the measured element was excited. The upper left chart shows all the three measured element pattern cuts with their mean beams directed to $\varphi = 0°$ and the three remaining charts compare the individual element pattern measurements to the simulation. The three element patterns show good agreement among each other and the agreement of the measurements and the simulations is even more remarkable.

Fig. 3.44 shows the horizontal optimized realized gain cut of the three-element array with triangle-star DMN in comparison to results based on measured element patterns to results based on simulated element patterns, for a fixed elevation angle of $\vartheta = 70°$. The comparison to the corresponding results from simulated patterns indicates very good agreement. To verify the beam forming behavior of the fabricated prototype, three different beam forming vectors (azimuth angles $0°, 300°$ and $330°$) were hard-wired by using a feed network, consisting of a power divider as well as adjustable phase shifters and attenuators. Array excitation coefficients according to [35] were generated while the resulting array radiation patterns have been measured in the anechoic chamber.

Fig. 3.45 shows the obtained excitation weights for the three angles together with the array patterns obtained from the measurements with these excitation weights. The realized maximum gain of all three cuts is very equal to the expected values. The shapes of the three patterns show differences, but this is expected for the chosen main beam angles.

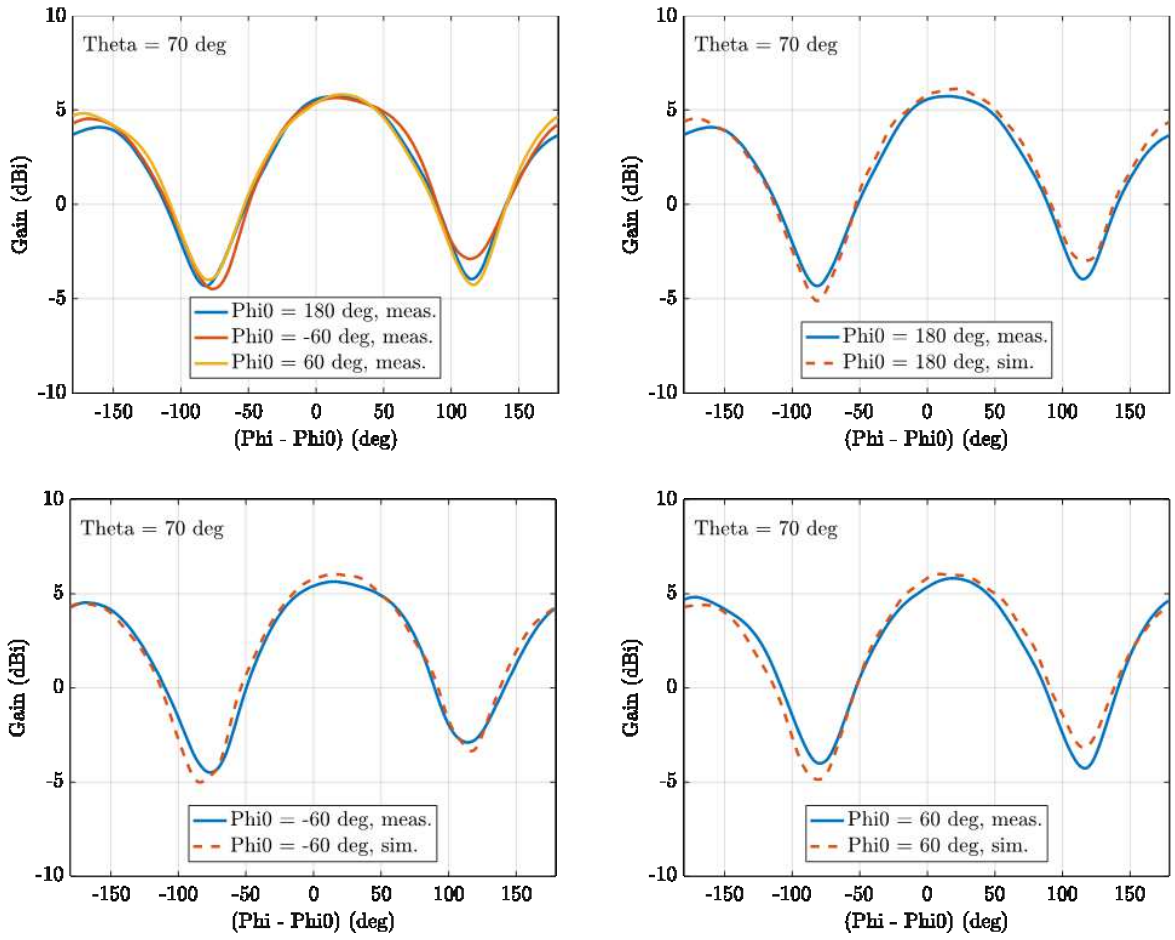

Fig. 3.32. Measured element pattern cuts of the three-element array with direct DMN, im comparison with simulated results.

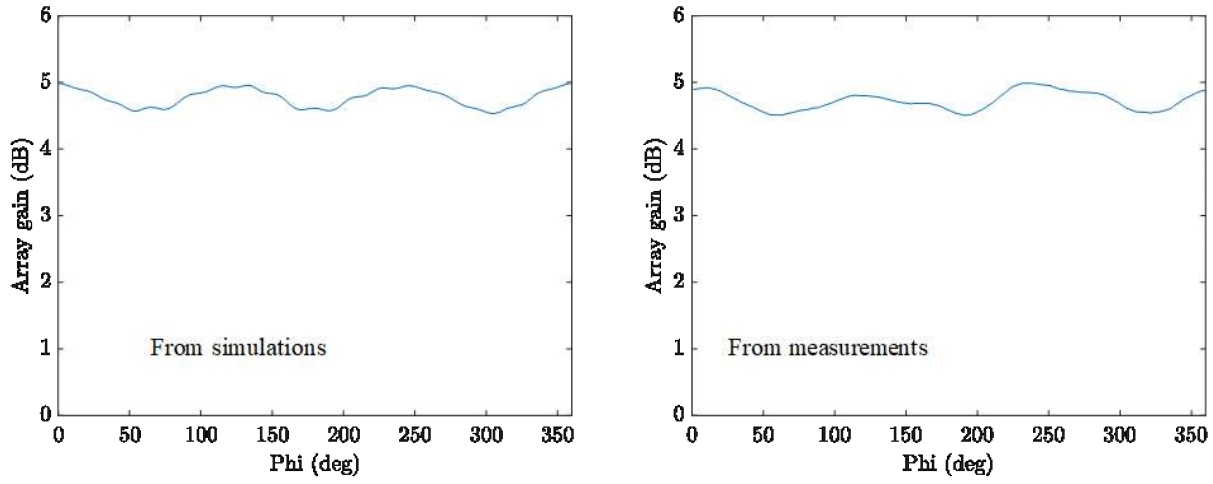

Fig. 3.33. Horizontal optimized realized gain cut of three-element array

$$\varphi_0 = 0°, \quad w_0 = \begin{pmatrix} 8.99\mathrm{e}^{\,\mathrm{j}\cdot 7.50°} \\ 4.99\mathrm{e}^{-\mathrm{j}\cdot 71.37°} \\ 9.71\mathrm{e}^{-\mathrm{j}\cdot 116.67°} \end{pmatrix}$$

$$\varphi_0 = 330°, \quad w_0 = \begin{pmatrix} 7.14\mathrm{e}^{\,\mathrm{j}\cdot 109.79°} \\ 4.23\mathrm{e}^{\,\mathrm{j}\cdot 112.61°} \\ 11.45\mathrm{e}^{\,\mathrm{j}\cdot 4.75°} \end{pmatrix}$$

$$\varphi_0 = 300°, \quad w_0 = \begin{pmatrix} 3.93\mathrm{e}^{\,\mathrm{j}\cdot 61.61°} \\ 7.59\mathrm{e}^{\,\mathrm{j}\cdot 129.39°} \\ 11.27\mathrm{e}^{\,\mathrm{j}\cdot 3.94°} \end{pmatrix}$$

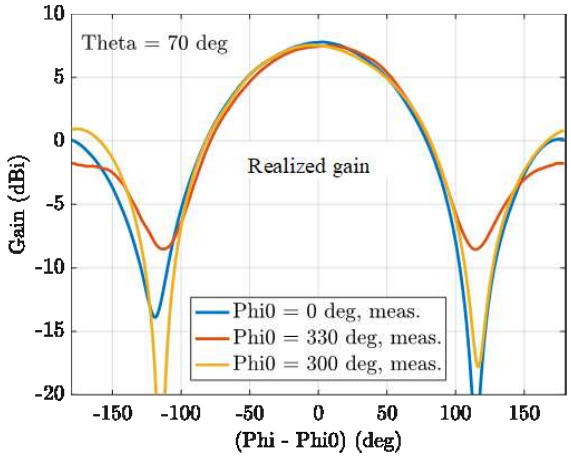

Fig. 3.34. Measured array pattern cuts of three-element array with direct DMN: Fed with optimized beam-forming weights as shown in the figure for three different azimuth angles, for a fixed elevation angle of $\vartheta = 70°$.

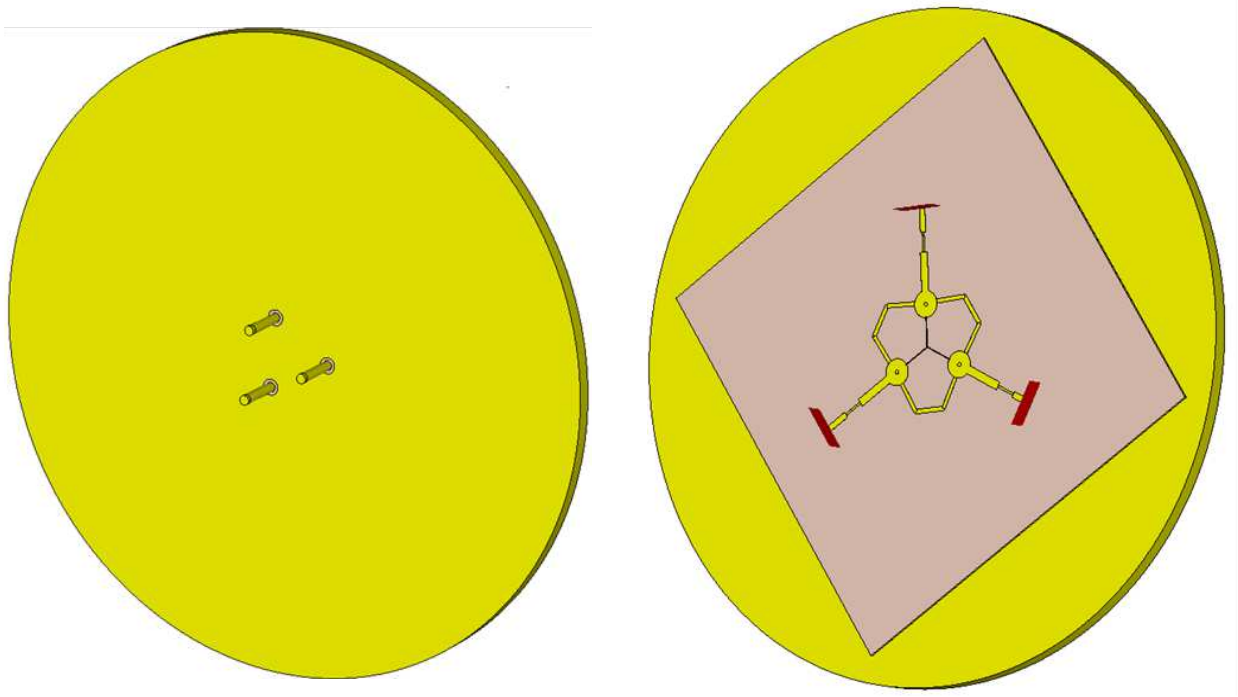

Fig. 3.35. Model of three-element array with triangle-star DMN.

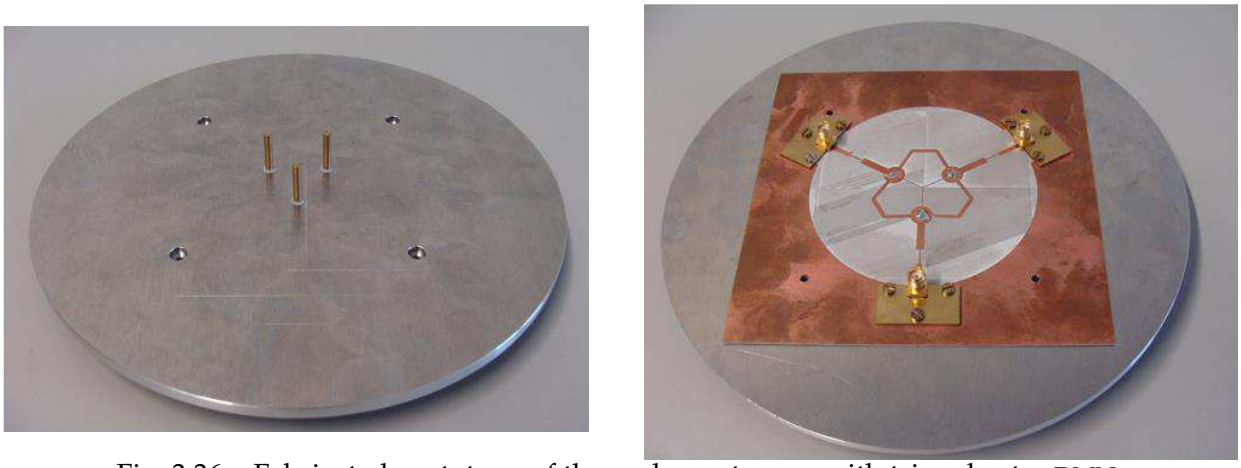

Fig. 3.36. Fabricated prototype of three-element array with triangle-star DMN.

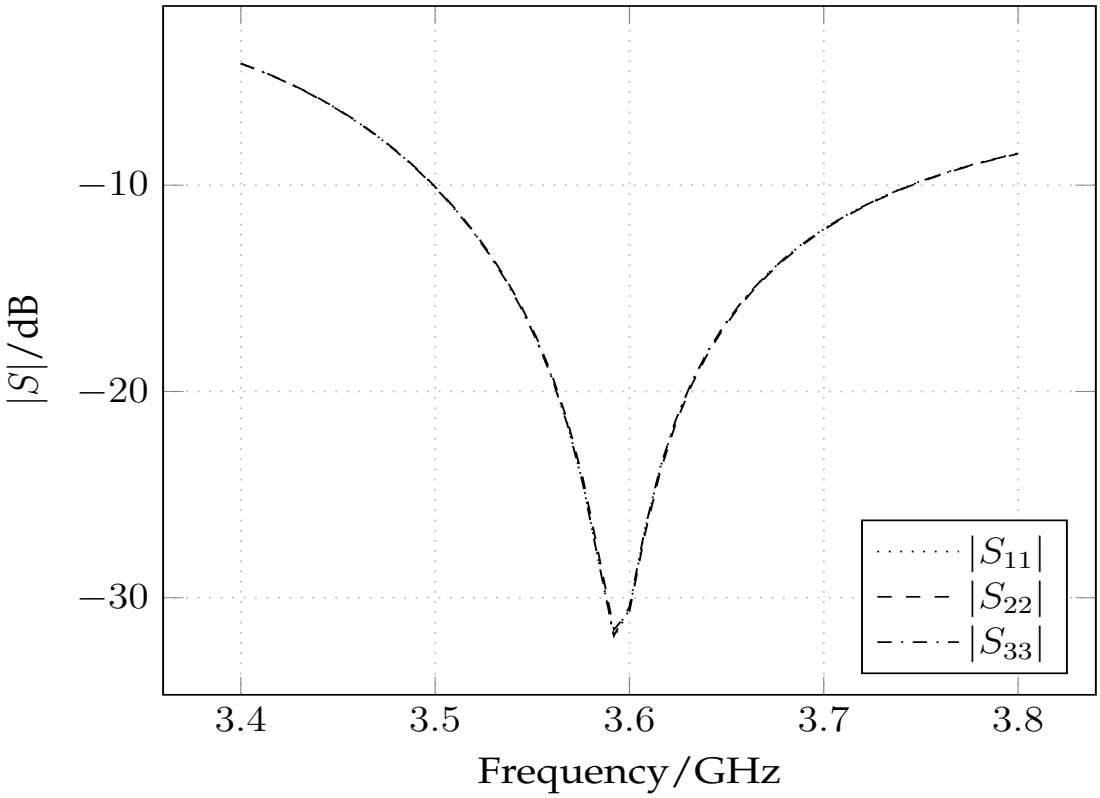

Fig. 3.37. Matching obtained for triangle-star DMN simulation

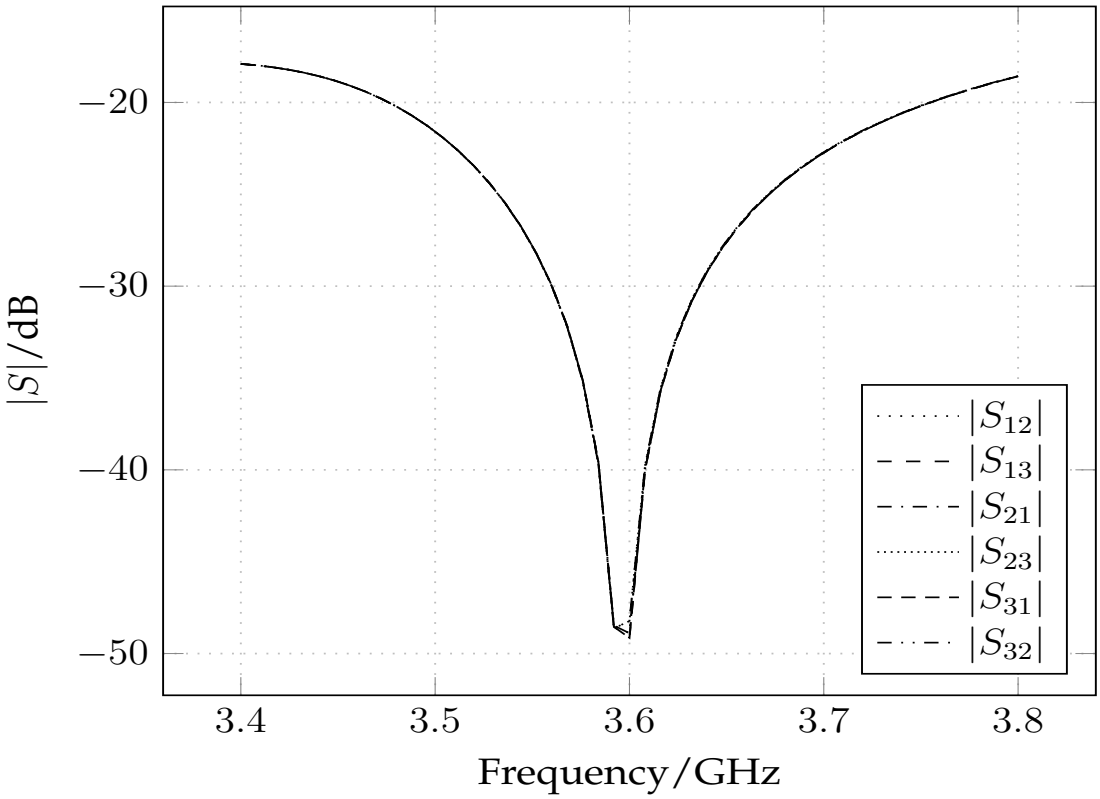

Fig. 3.38. Decoupling obtained for triangle-star DMN simulation

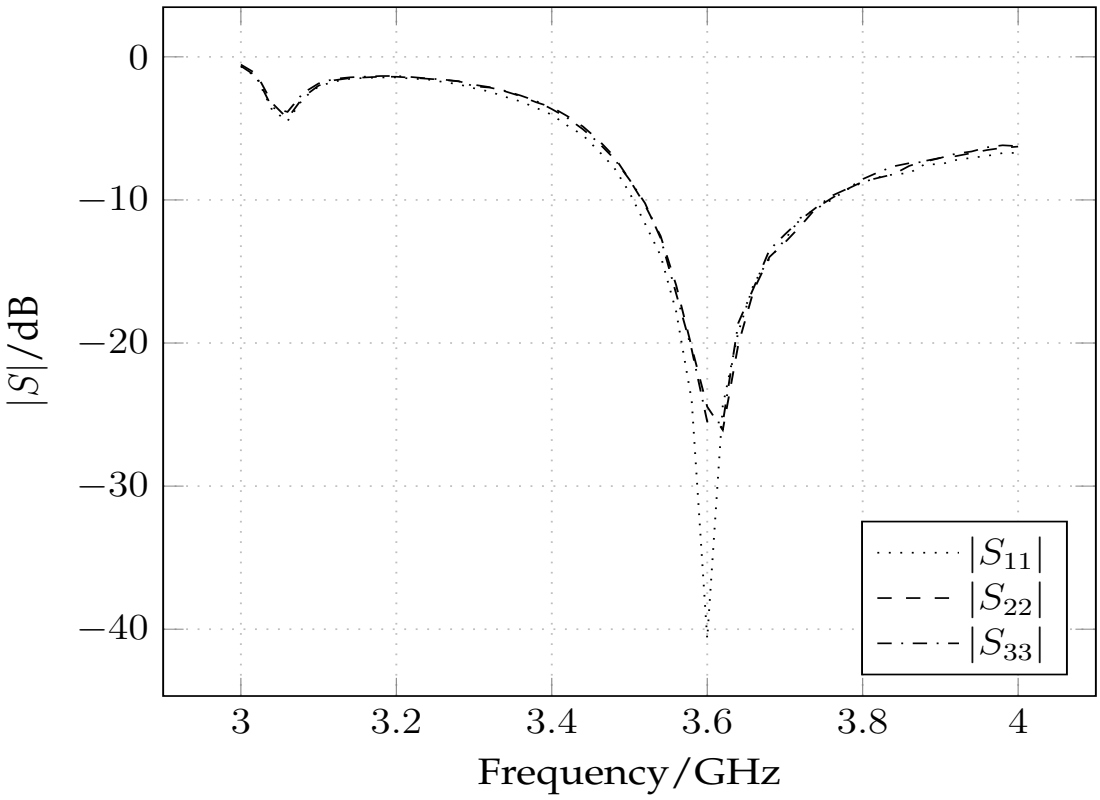

Fig. 3.39. Matching obtained for triangle-star DMN measurement

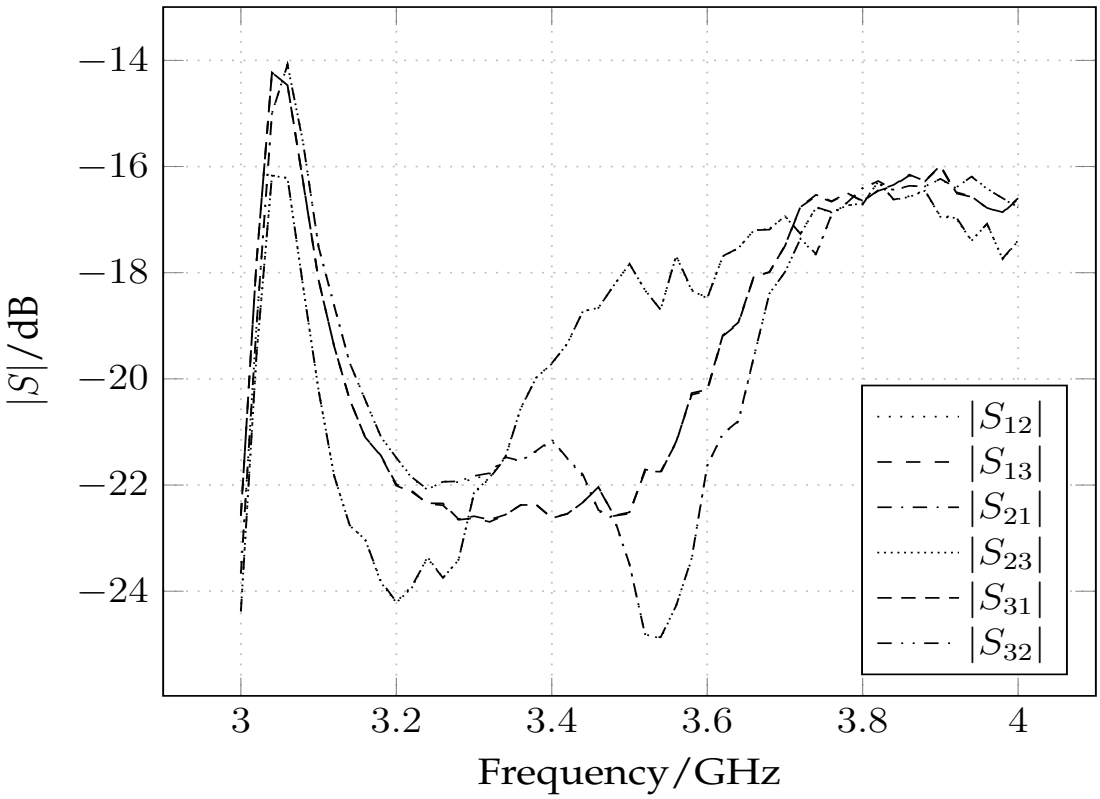

Fig. 3.40. Decoupling obtained for triangle-star DMN measurement

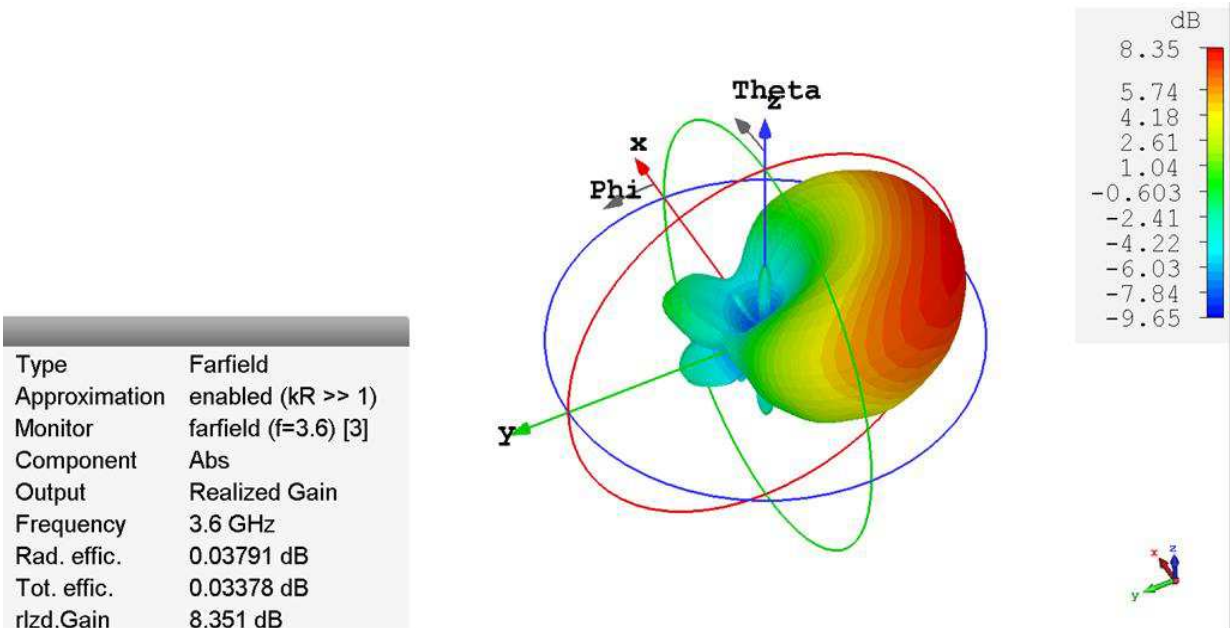

Fig. 3.41. Three-dimensional element pattern of three-element array with triangle-star DMN, simulated.

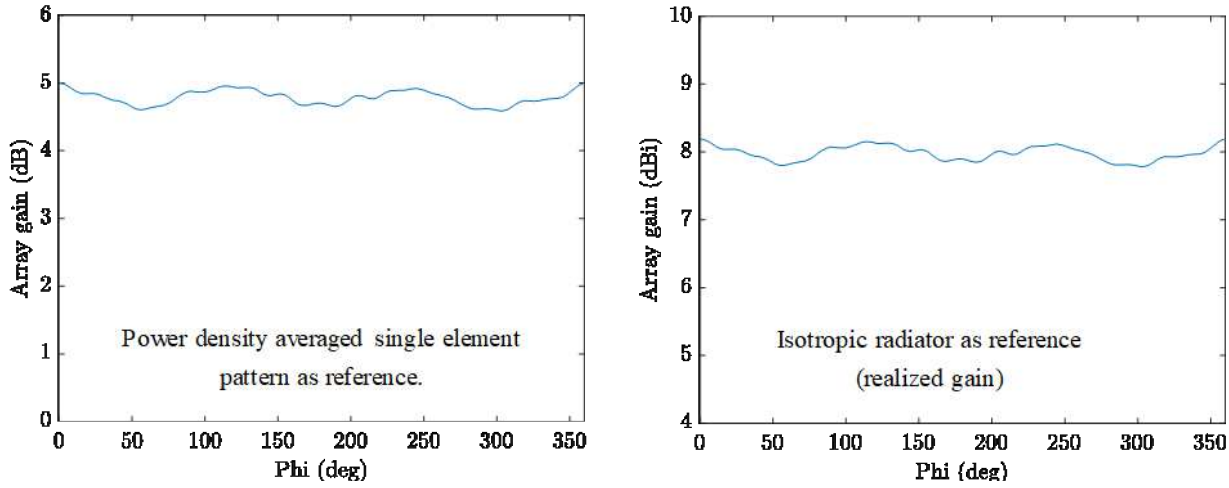

Fig. 3.42. Optimized horizontal realized array gain of three-element array with triangle-star DMN

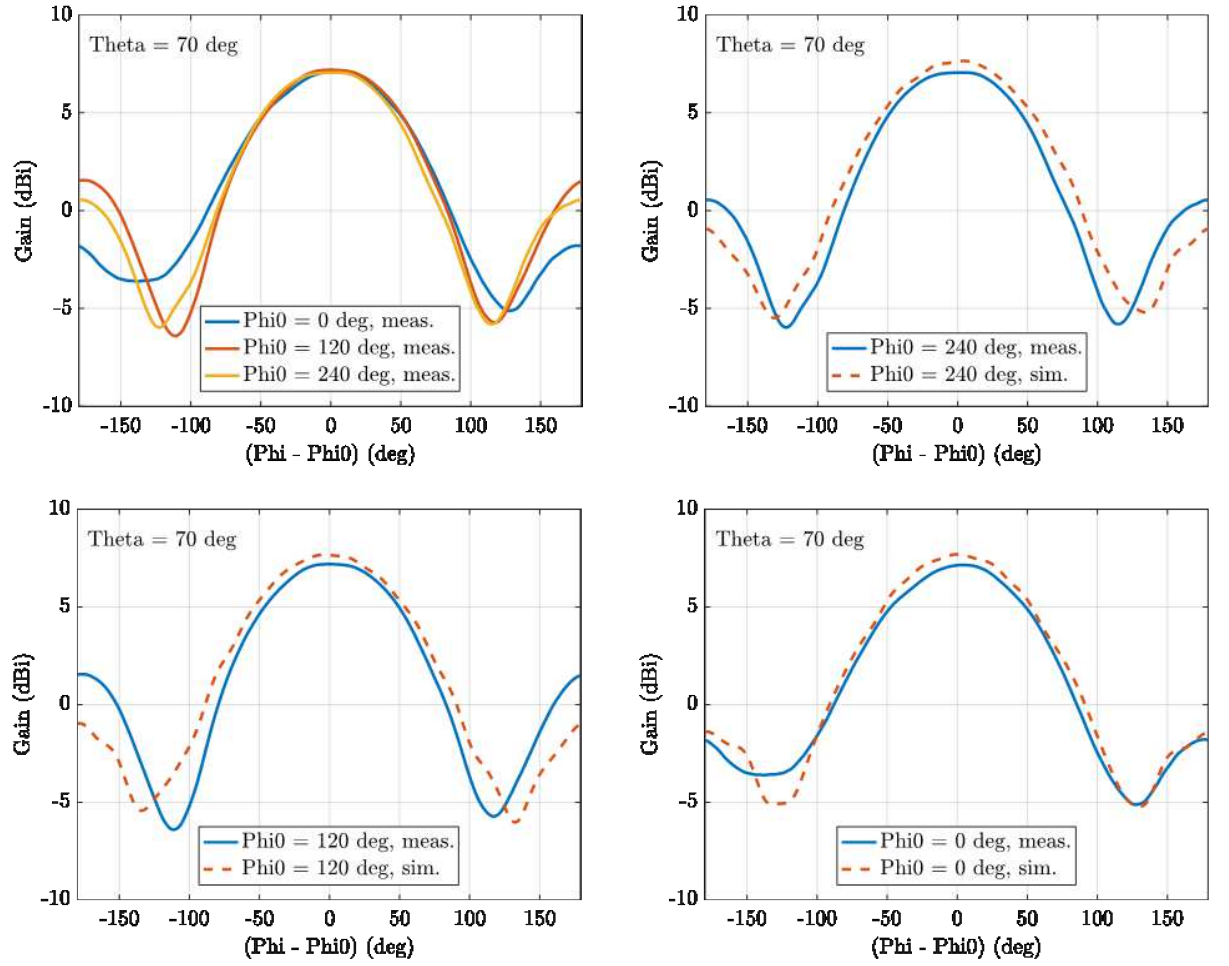

Fig. 3.43. Measured element pattern cuts of the three-element array with triangle-star DMN, in comparison with simulated results.

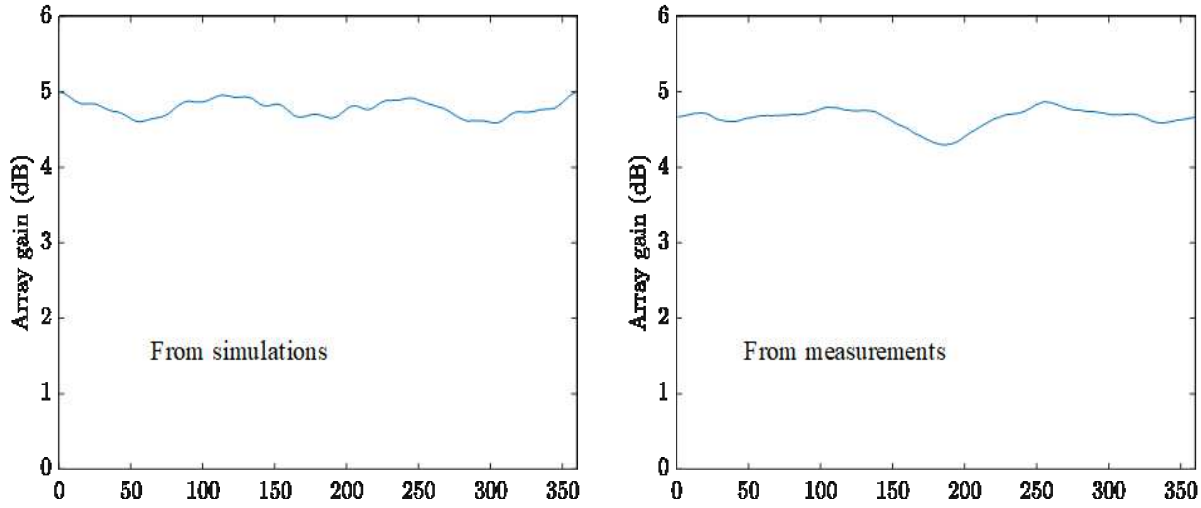

Fig. 3.44. Horizontal optimized realized gain cut of three-element array with triangle-star

$$\varphi_0 = 0°, \quad w_0 = \begin{pmatrix} 13.45\mathrm{e}^{-\mathrm{j}\cdot 1.22°} \\ 3.12\mathrm{e}^{\,\mathrm{j}\cdot 131.11°} \\ 3.08\mathrm{e}^{\,\mathrm{j}\cdot 142.83°} \end{pmatrix}$$

$$\varphi_0 = 330°, \quad w_0 = \begin{pmatrix} 12.01\mathrm{e}^{-\mathrm{j}\cdot 1.40°} \\ 4.71\mathrm{e}^{\,\mathrm{j}\cdot 49.40°} \\ 5.79\mathrm{e}^{\,\mathrm{j}\cdot 176.76°} \end{pmatrix}$$

$$\varphi_0 = 300°, \quad w_0 = \begin{pmatrix} 9.04\mathrm{e}^{-\mathrm{j}\cdot 1.31°} \\ 8.31\mathrm{e}^{-\mathrm{j}\cdot 1.90°} \\ 7.03\mathrm{e}^{\,\mathrm{j}\cdot 170.08°} \end{pmatrix}$$

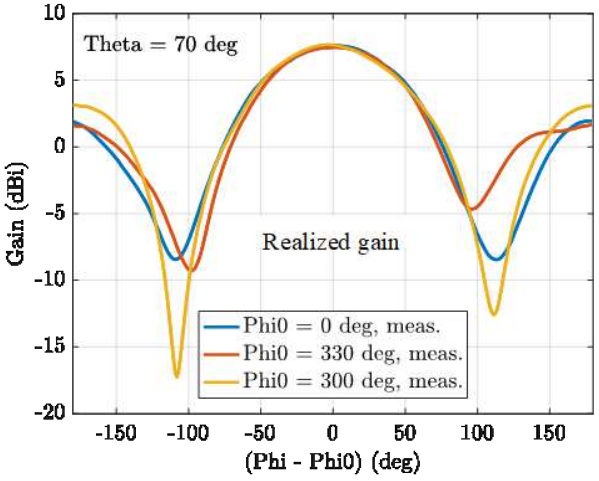

Fig. 3.45. Measured array pattern cuts of three-element array with triangle-star DMN: Fed with optimized beam-forming weights as shown in the figure for three different azimuth angles, for a fixed elevation angle of $\vartheta = 70°$.

3.11 Conclusion

Two ways of designing a DMN have been shown. The direct analytical design is easy to understand and shows the increase of array gain. When solutions for the equations of the direct design do not exist, or a low loss stripline design is desired, the star triangle topology is the design one should go for. Calculation, simulation and measurements agree very well. As the results show a DMN makes an antenna array much more efficient.

4. Analog Beam Forming

FOR a higher data throughput with limited frequency bandwidth and multiple users, beam forming is essential. There are two different basic concepts for analog beam forming, either working with adjustable phase shifters, or with in hardware implemented matrices, representing a choice of fixed beam forming vectors. Advantages of the hardware implemented discrete fourier transform (DFT) matrices concept are:

- A control circuit including wires to adapt phase shifters is not necessary
- No combining losses, even if multiple beams are used simultaneously
- Lower losses than with adjustable phase shifters

The design chosen here uses the column vectors of the DFT matrix as beamforming vectors for a sub array with 8 antennas. At first, a lossless ideal four port 3 dB splitter is considered, Fig. 4.1. All its ports are matched, the power is distributed to two loads at port 2 and 3 uniformly, while port 4 will remain powerless. That means, when amplifiers are connected to port 1 and 4, Fig. 4.2, their ports will be decoupled. A lossless ideal splitter is needed with all its ports matched, where the power is distributed to n loads uniformly. A possible solution of creating such a desired 3 dB hybrid is taking a $90°$ hybrid, Fig. 4.3 and connect it to additional delay lines, Fig. 4.4. Fig. 4.3 shows a simple micro strip line structure, optimized for low losses. The unwanted phase shift is compensated with delay lines, where j is equal to an electrical length of $\frac{1}{4}\,\lambda$, -1 is equal to an electrical length of $\frac{1}{2}\,\lambda$ and -j is equal to an electrical length of $\frac{3}{4}\,\lambda$ in Fig. 4.4. For bigger beam forming structures the so designed 3 dB hybrids and delay elements are used according to the following theory description in Fig. 4.5 and Fig. 4.6.

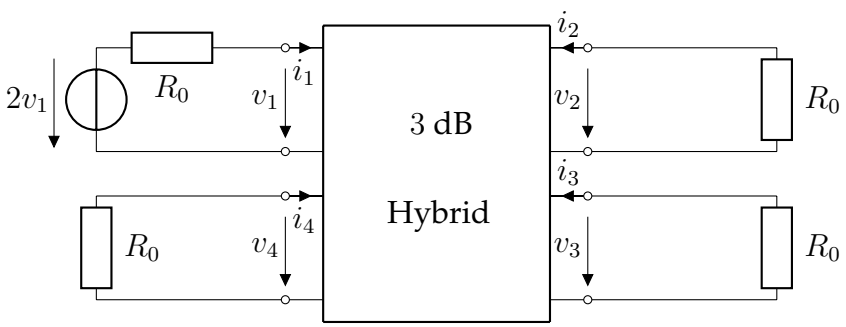

Fig. 4.1. 3 dB hybrid with single source, used as power splitter

For distributing the power to n loads $2^m - 1$ 3 dB hybrids are needed. One 3 dB Hybrid in strip line technology may occupy an area of $\sim (\frac{\lambda}{2}$ x $\frac{\lambda}{2})$, which at 30 GHz and $\epsilon_r \approx 2$ will be approximately $(3,5$ x $3,5)$ mm^2,

$$\boldsymbol{S}_{3\text{ dB}} = \frac{1}{\sqrt{2}} \begin{bmatrix} 0 & 1 & -1 & 0 \\ 1 & 0 & 0 & 1 \\ -1 & 0 & 0 & 1 \\ 0 & 1 & 1 & 0 \end{bmatrix}, \quad \boldsymbol{S}_{90^\circ} = \frac{1}{\sqrt{2}} \begin{bmatrix} 0 & -\mathrm{j} & -1 & 0 \\ -\mathrm{j} & 0 & 0 & -1 \\ -1 & 0 & 0 & -\mathrm{j} \\ 0 & -1 & -\mathrm{j} & 0 \end{bmatrix}. \tag{4.1}$$

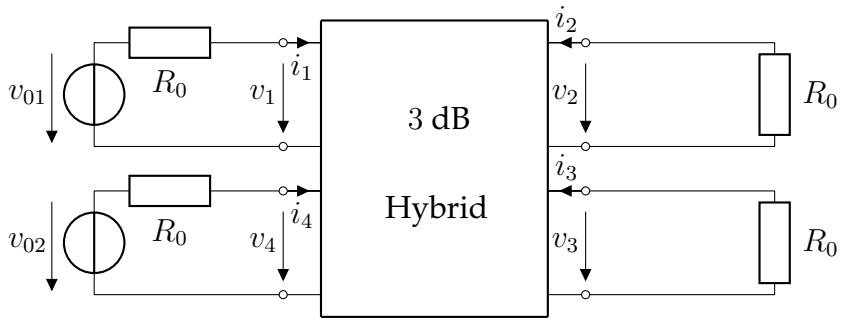

Fig. 4.2. 3 dB hybrid with two sources, used as power distributor

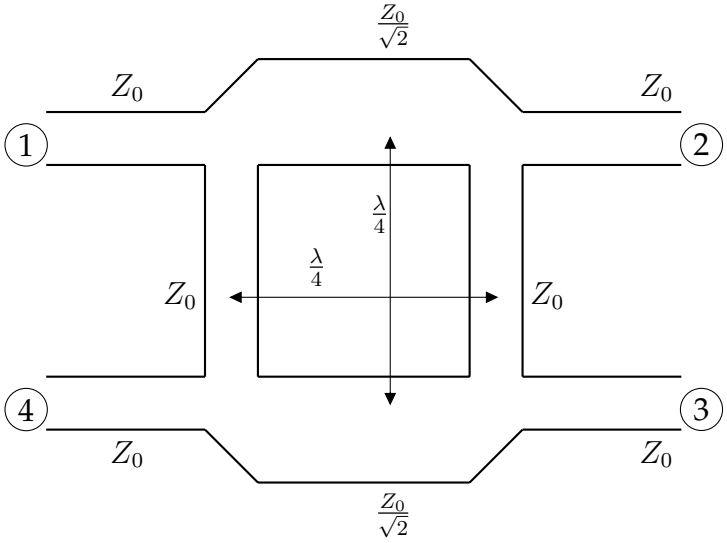

Fig. 4.3. 90° hybrid layout example

Here the DFT is expressed as multiplication $\boldsymbol{b} = \boldsymbol{W}\boldsymbol{a}$, where $\boldsymbol{a}$ is the original input signal, $\boldsymbol{W}$ is the NxN DFT matrix and $\boldsymbol{b}$ is the DFT of the signal. Hereby, $\omega = e^{-2\mathrm{j}\pi/N}$ is the primitive root of unity. Regarding the example Fig 4.6, according to (4.6), here a multiplication of w is equal to a phase rotation of 45°.

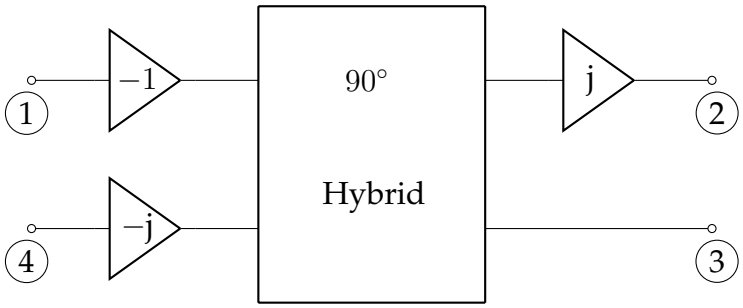

Fig. 4.4. 3 dB hybrid

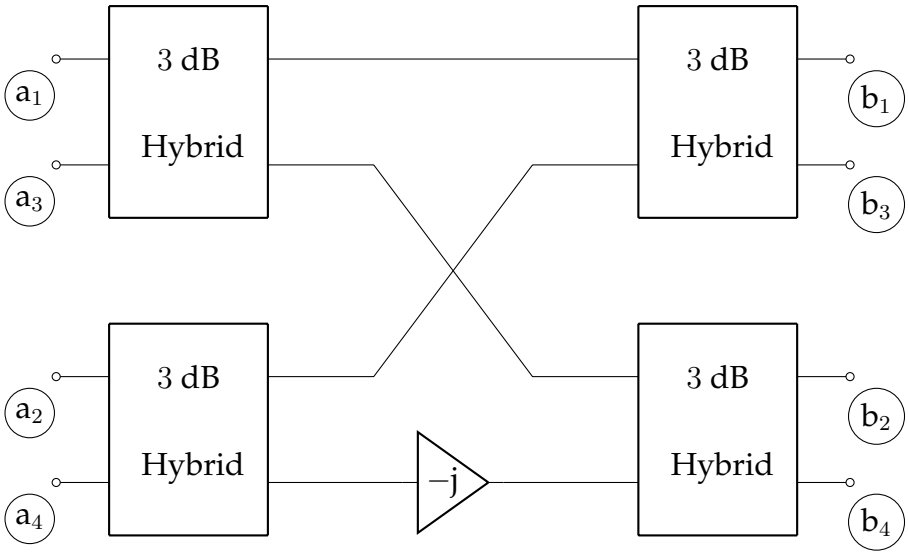

Fig. 4.5. 4 channel analog beam former

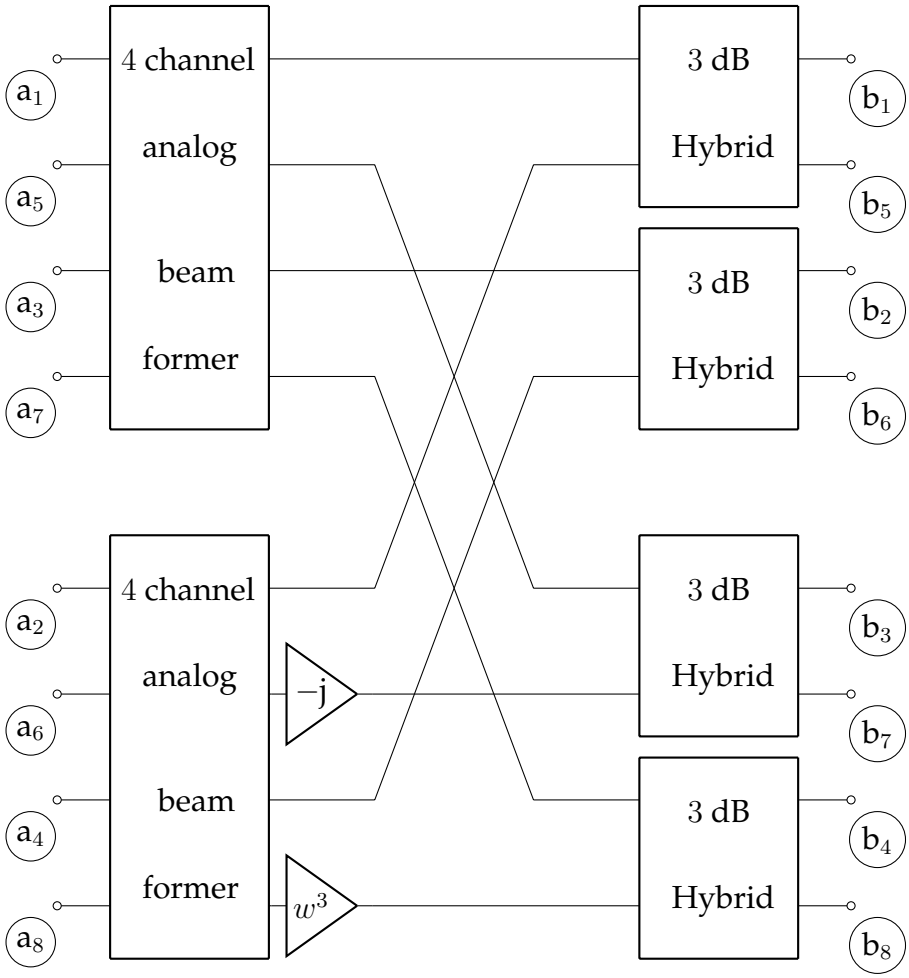

Fig. 4.6. 8 channel analog beam former

$$\boldsymbol{W} = \frac{1}{\sqrt{8}} \begin{bmatrix} 1 & 1 & 1 & 1 & 1 & 1 & 1 & 1 \\ 1 & w & w^2 & w^3 & w^4 & w^5 & w^6 & w^7 \\ 1 & w^2 & w^4 & w^6 & w^8 & w^{10} & w^{12} & w^{14} \\ 1 & w^3 & w^6 & w^9 & w^{12} & w^{15} & w^{18} & w^{21} \\ 1 & w^4 & w^8 & w^{12} & w^{16} & w^{20} & w^{24} & w^{28} \\ 1 & w^5 & w^{10} & w^{15} & w^{20} & w^{25} & w^{30} & w^{35} \\ 1 & w^6 & w^{12} & w^{18} & w^{24} & w^{30} & w^{36} & w^{42} \\ 1 & w^7 & w^{14} & w^{21} & w^{28} & w^{35} & w^{42} & w^{49} \end{bmatrix} \tag{4.2}$$

$$\boldsymbol{a}^{\mathrm{T}} = [a_1, a_2, ..., a_8]\,, \quad \boldsymbol{b}^{\mathrm{T}} = [b_1, b_2, ..., b_8]\,, \quad \boldsymbol{b} = \boldsymbol{W}\boldsymbol{a} \tag{4.3}$$

With a Butler matrix, the transmit signals from RF- chains can be distributed to the N antenna elements theoretically without losses. The received signals are combined to the input of the RF chain without degrading the noise figure. Since real world hybrids are not lossless, the last units in the network should be the high power amplifiers per antenna and the first units in the receiver chain the low noise amplifier (LNA)s per antenna element. Beam patterns may be optimized, but are not adaptive and can be chosen from an optimized, but fixed grid of beams. It is much easier connecting data streams to certain Butler matrix inputs than adapting phase shifters. For an NxN beam former, $\frac{N}{2}\log_2 N$ hybrids are needed.

4.1 Simulation

For the simulation, a design center frequency of 30 GHz was chosen. The substrate parameters of RO3003 have been used, while the thickness of the silver metal layer on top was 50 μm. For the ground plane on the bottom side, the parameters of silver were chosen, too. The RO3003 substrate was 50 μm thick. According to the CST implementation, 1.638 mm is equal to 0.25 λ wavelength at 30 GHz. A wave impedance of 50 Ω is achieved at a top layer conductor width of 0.1118 mm for a micro stripline. With these parameters first, a $90°$ hybrid according to Fig. 4.3 was implemented. Fig. 4.7 shows the phase of S_{11}, S_{21}, S_{31} and S_{41}, while Fig. 4.8 shows good matching of port 1 with $|S_{11}|$ lower than -30 dB and an even better decoupling $|S_{41}|$ of about -38 dB. The power is distributed to two ports as indicated in Fig. 4.9. An ideal single input-, two output splitter would have an output power of -3 dB at each port. Here, the attenuation due to lossy substrate and metal layers and radiation is 0.1 dB for $|S_{31}|$ and 0.25 dB for $|S_{21}|$.

As next step, according to Fig. 4.4, a 3 dB hybrid was implemented with CST. With the S-paramters from the CST simulation for the 3 dB hybrids, the circuit shown in Fig. 4.6 was simulated with ADS. Fig. 4.10 shows the phase with port 1 as reference, ... Fig. 4.17 shows the phase with port 8 as reference. Fig. 4.18 shows the attenuation with port 1 as reference, ... Fig. 4.25 shows the attenuation with port 8 as reference.

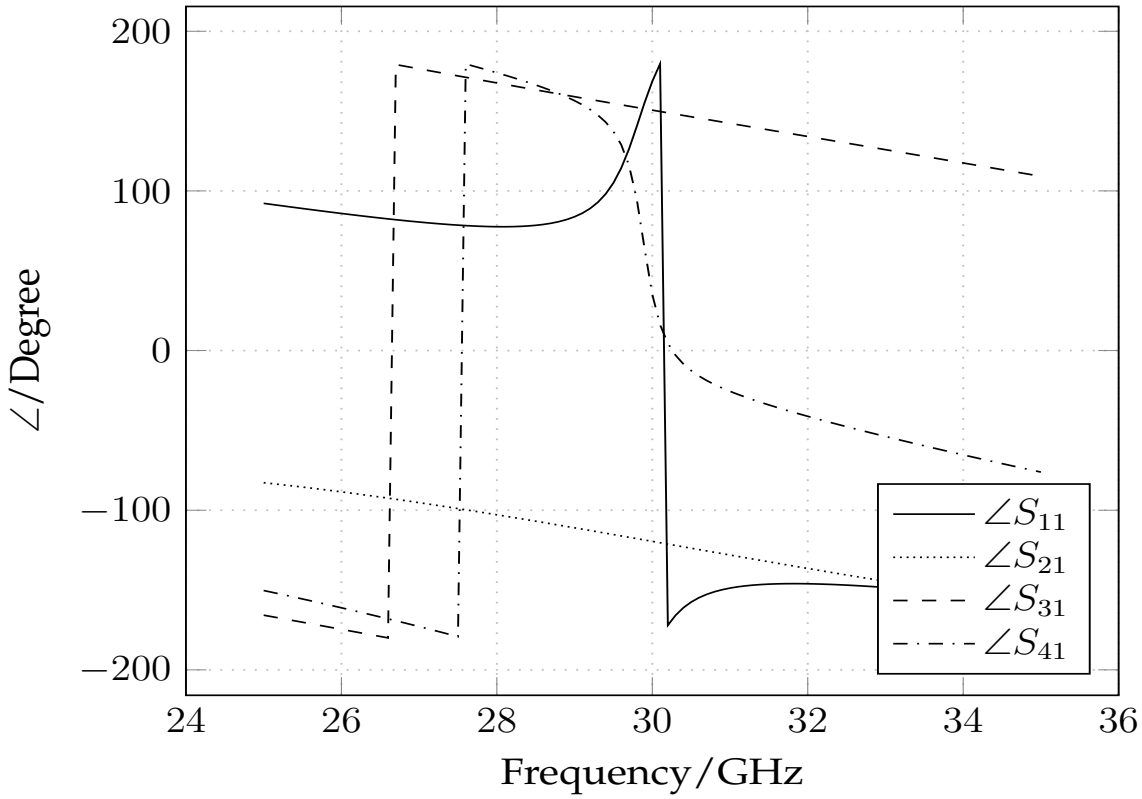

Fig. 4.7. CST Hybrid Phase with port 1 as reference

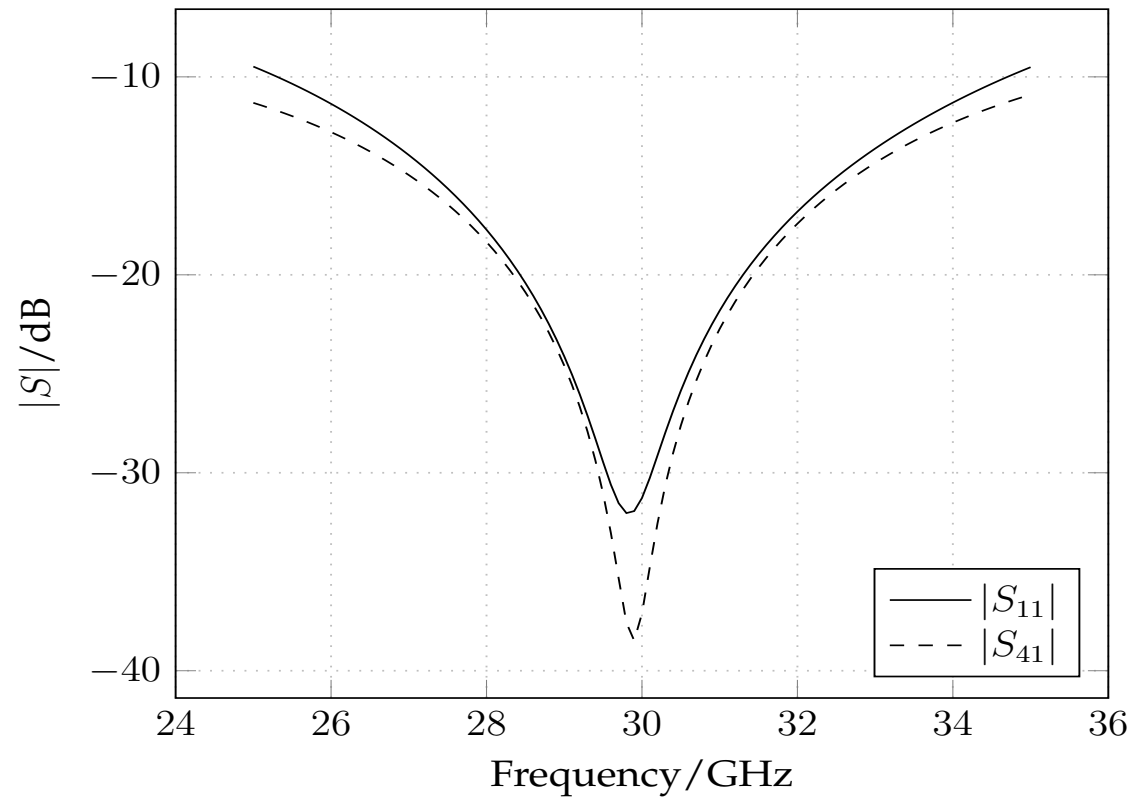

Fig. 4.8. Attenuation with port 1 as reference

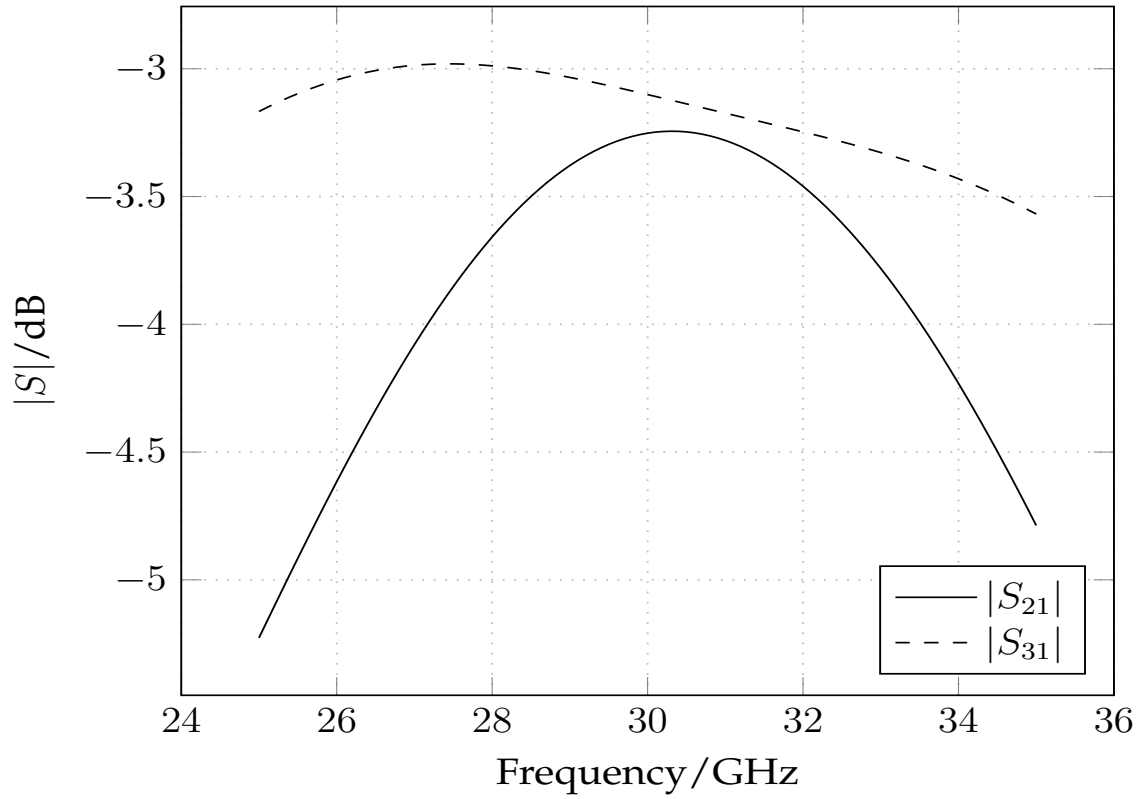

Fig. 4.9. Attenuation with port 1 as reference

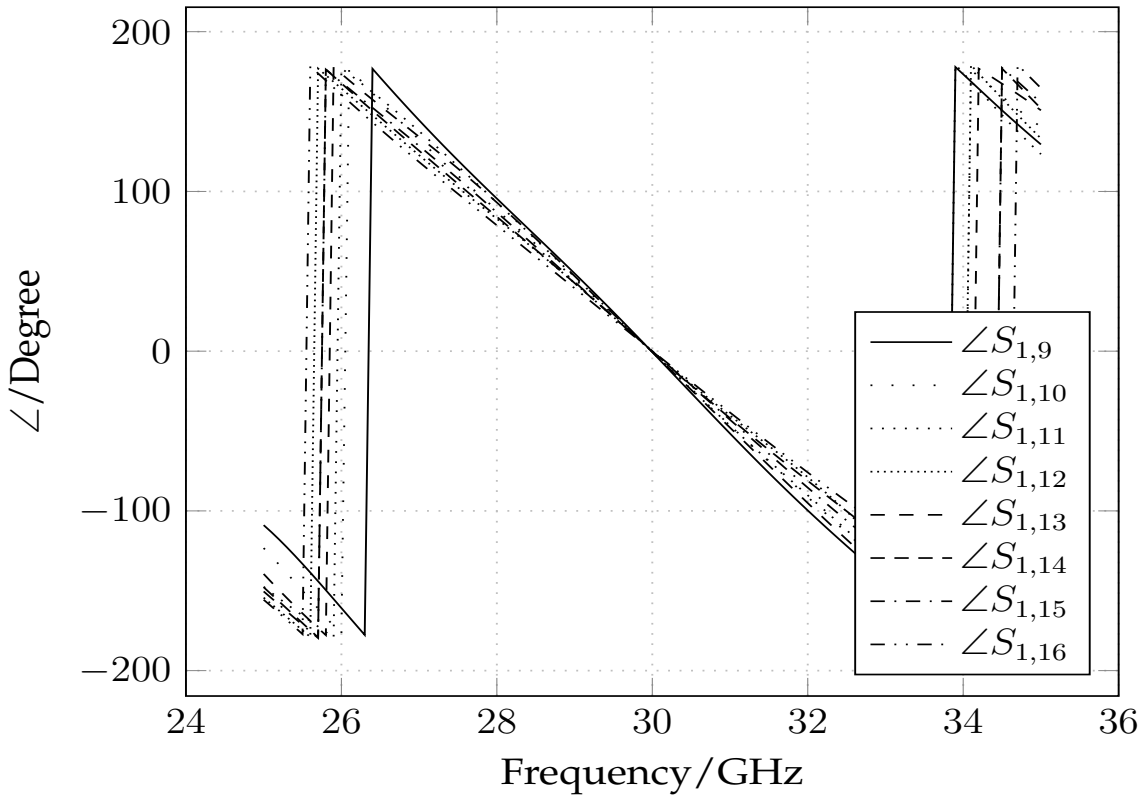

Fig. 4.10. Phase with port 1 as reference

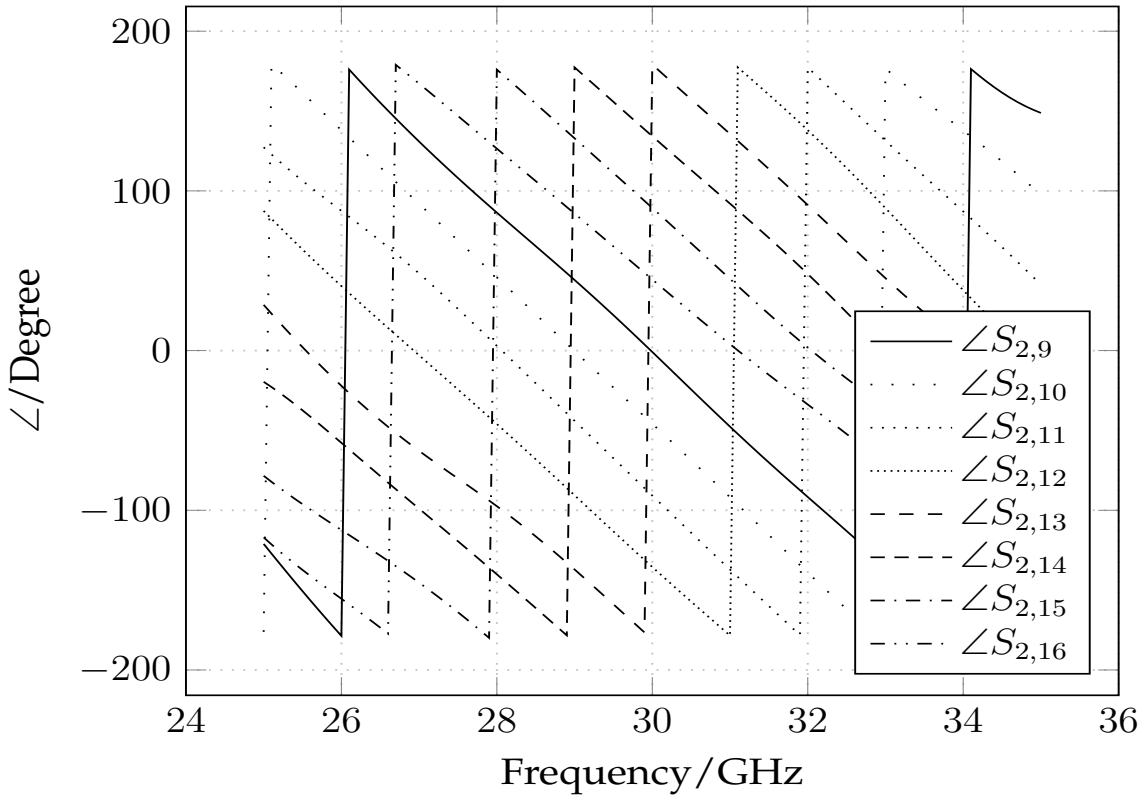

Fig. 4.11. Phase with port 2 as reference

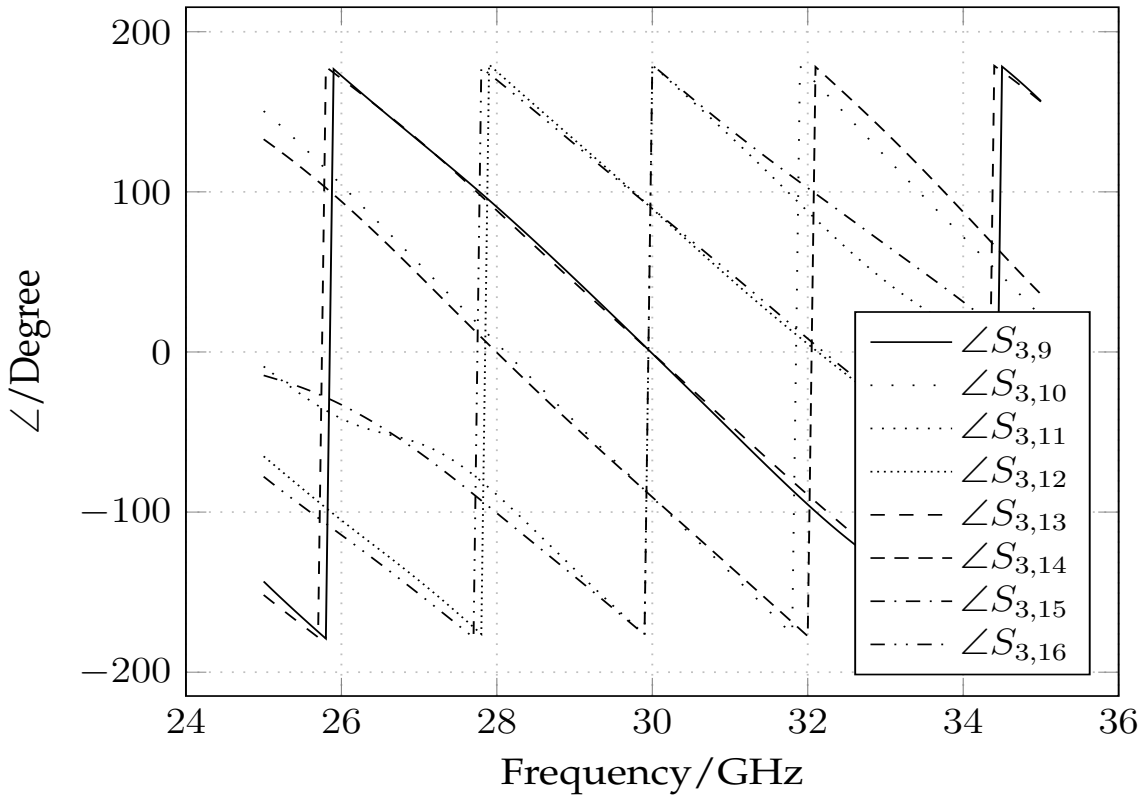

Fig. 4.12. Phase with port 3 as reference

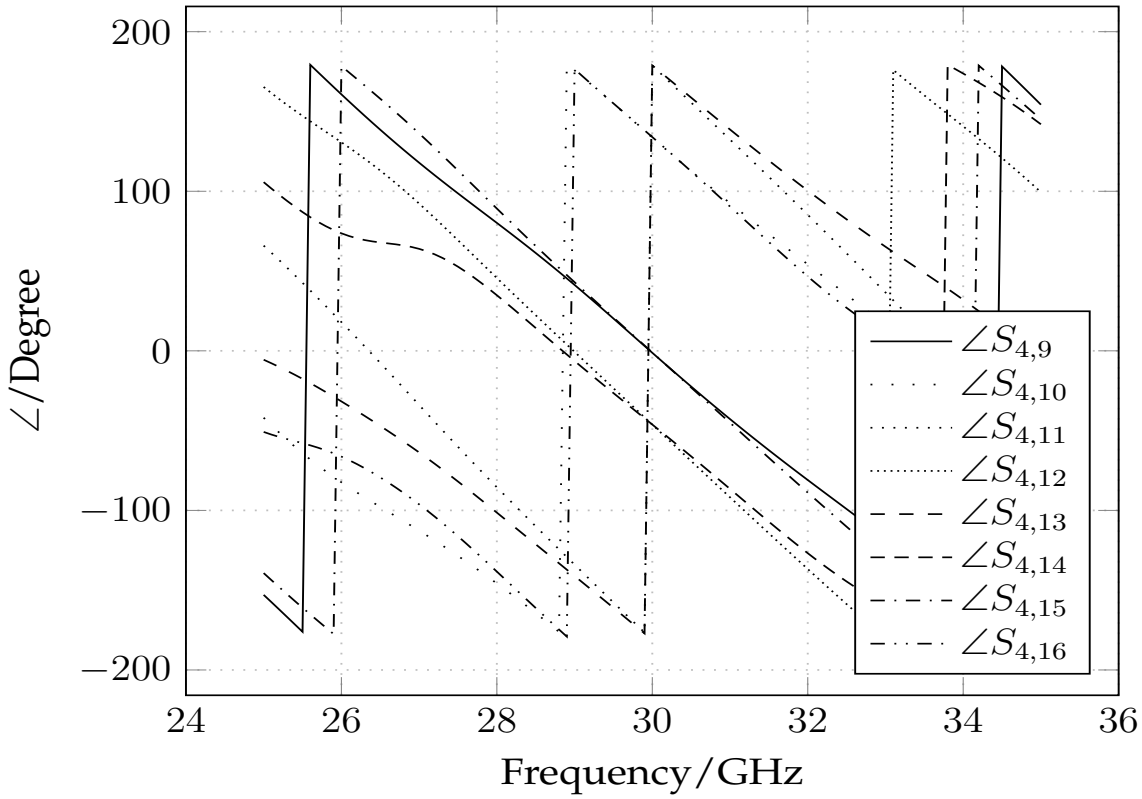

Fig. 4.13. Phase with port 4 as reference

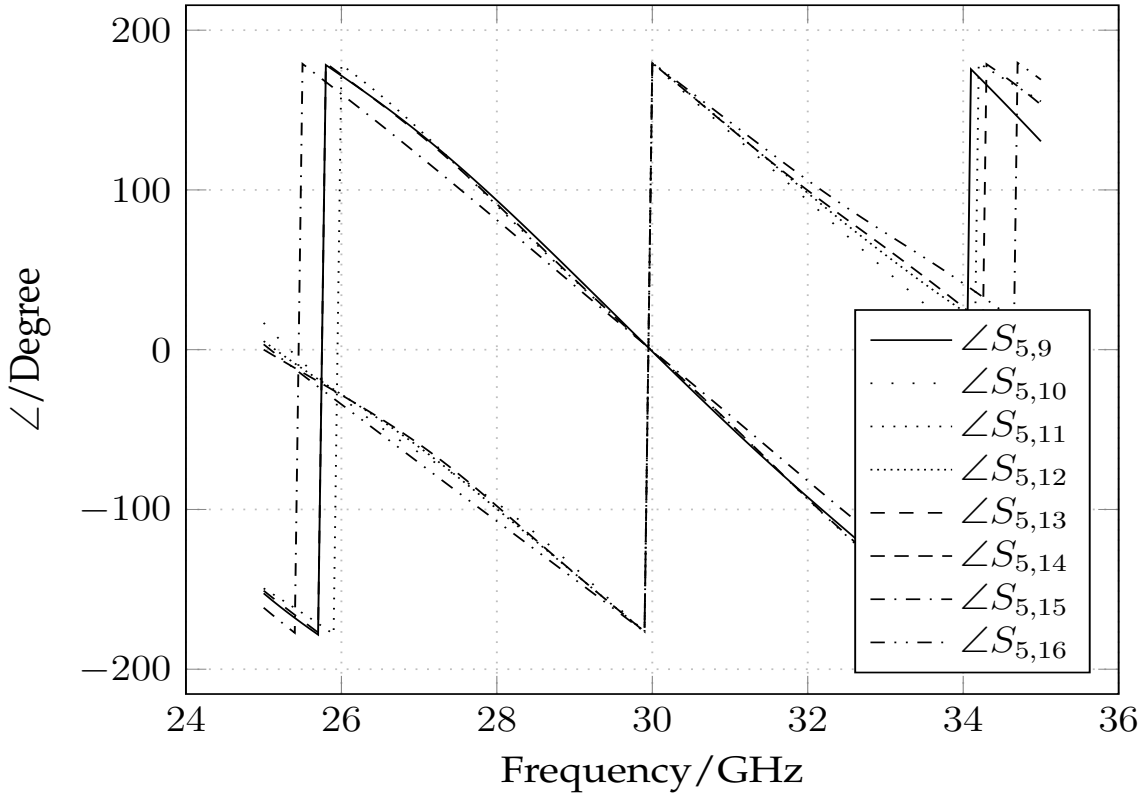

Fig. 4.14. Phase with port 5 as reference

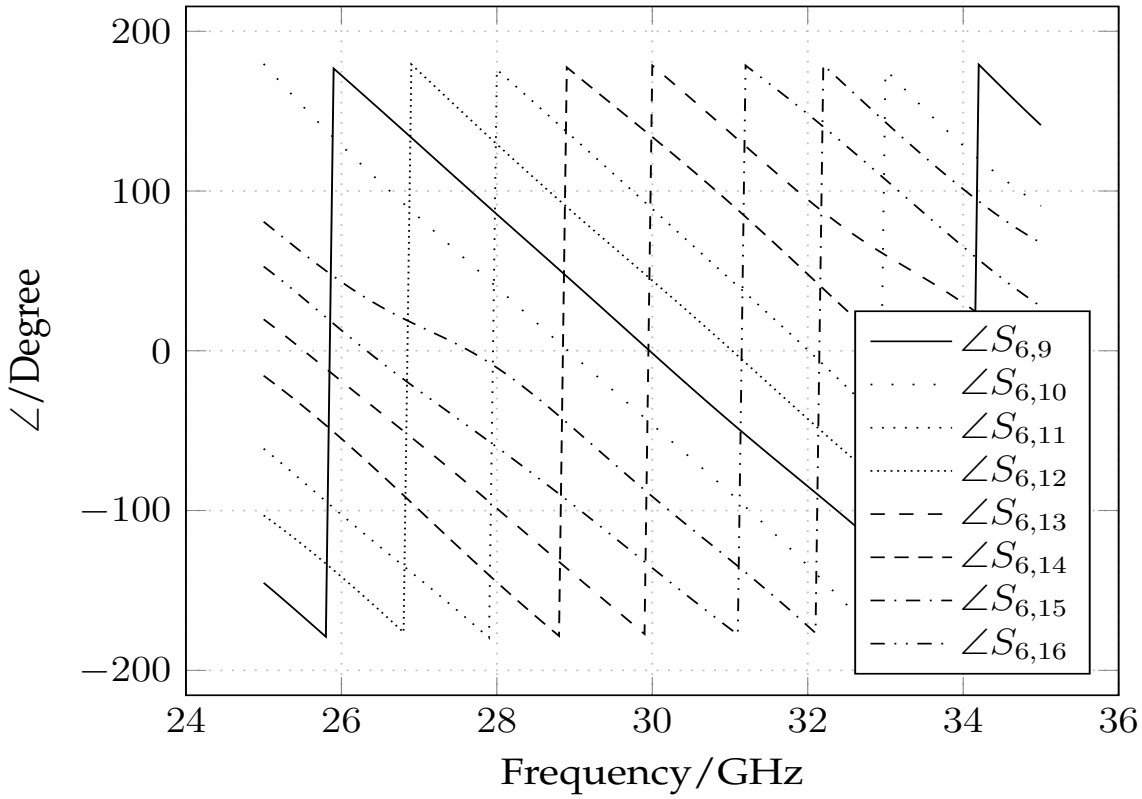

Fig. 4.15. Phase with port 6 as reference

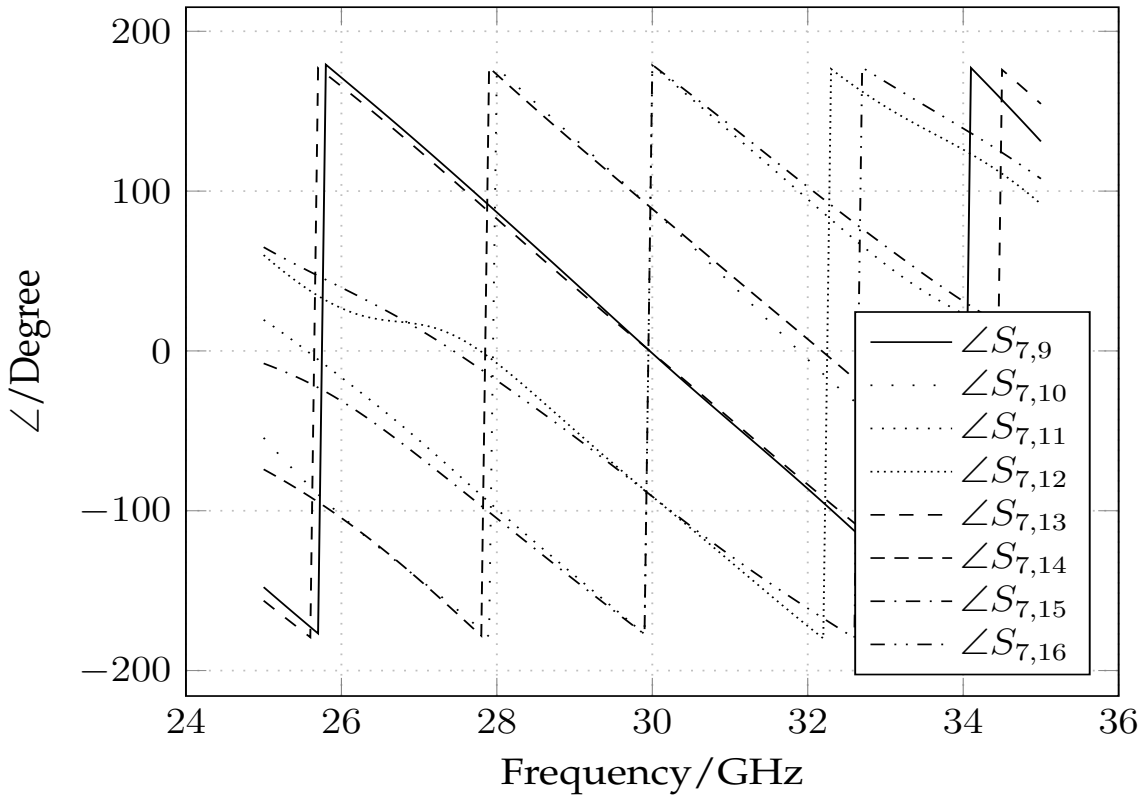

Fig. 4.16. Phase with port 7 as reference

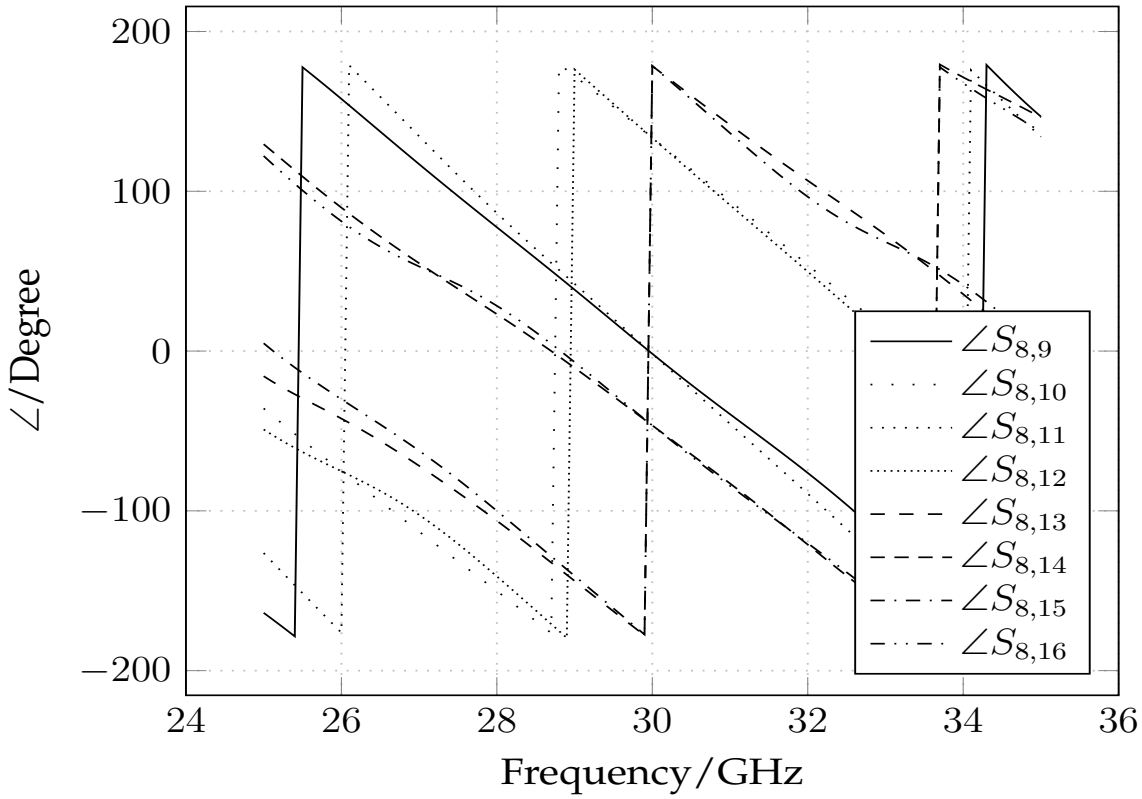

Fig. 4.17. Phase with port 8 as reference

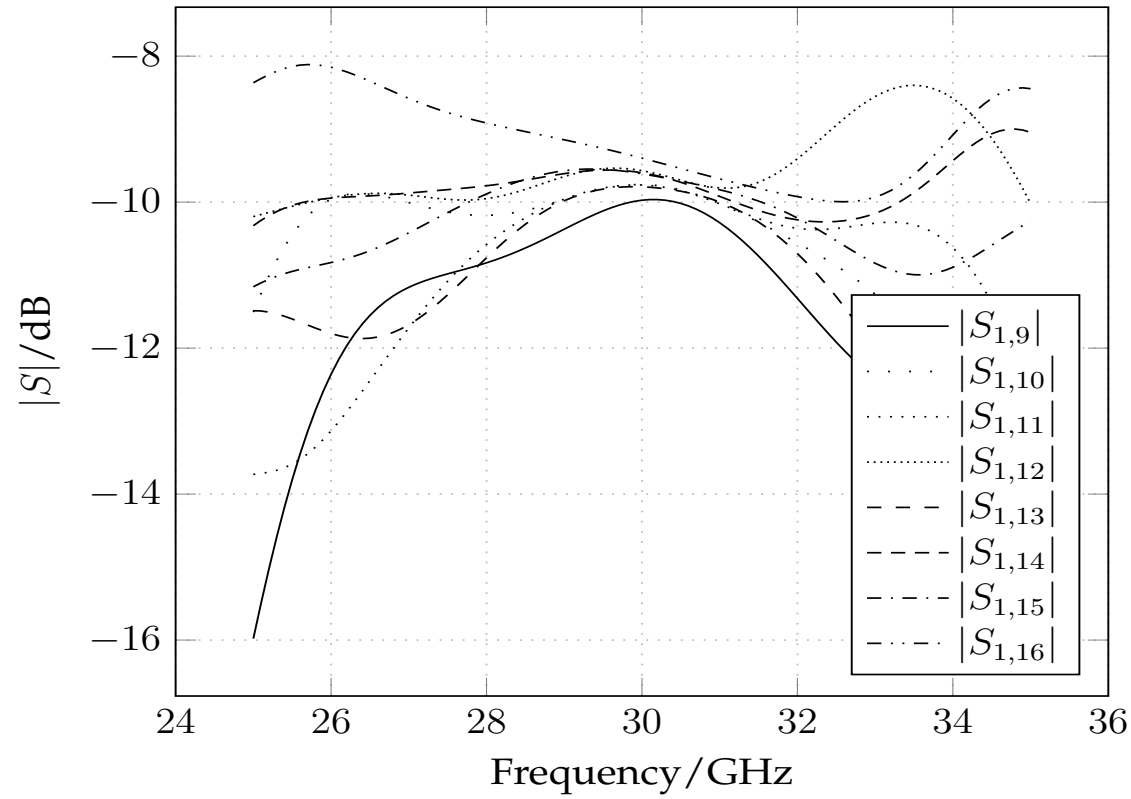

Fig. 4.18. Attenuation with port 1 as reference

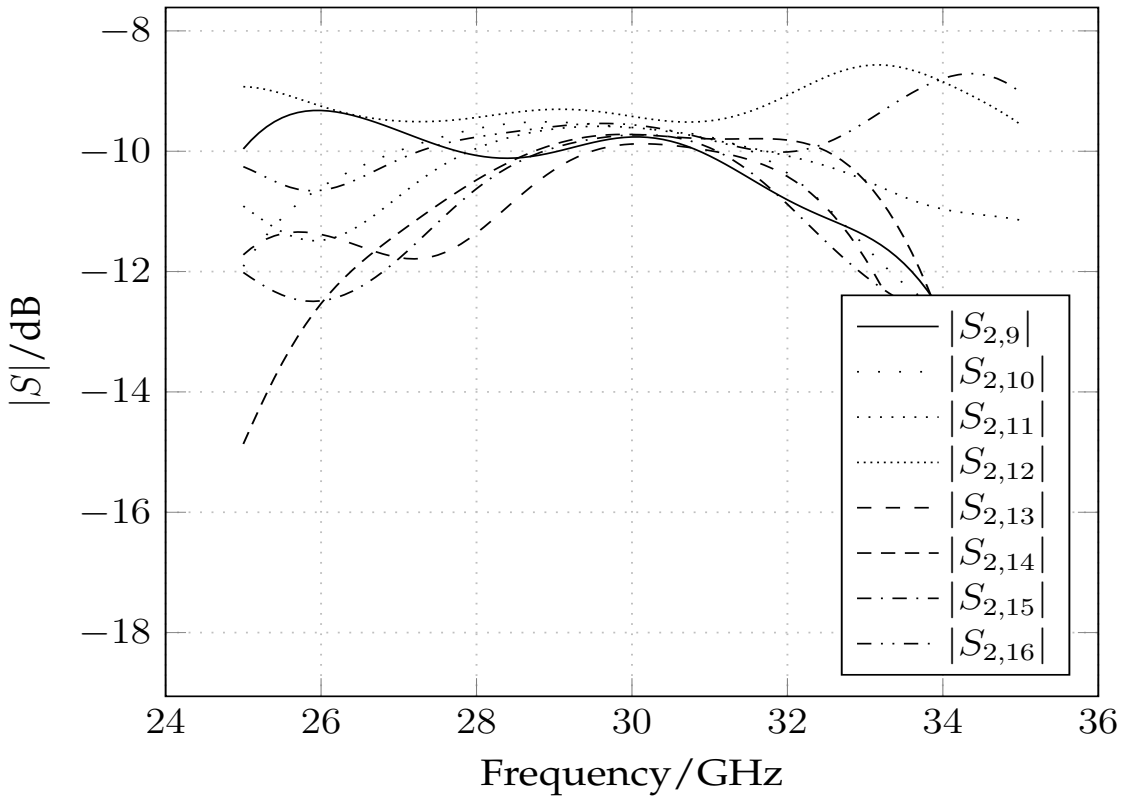

Fig. 4.19. Attenuation with port 2 as reference

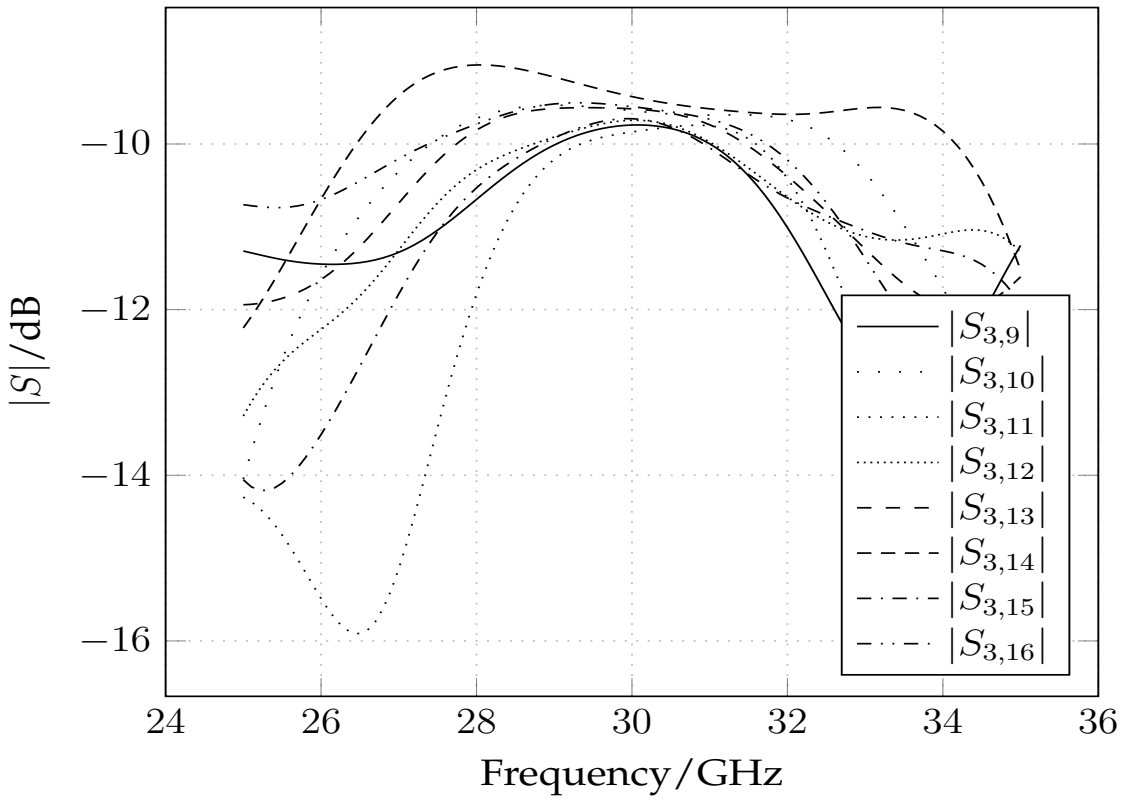

Fig. 4.20. Attenuation with port 3 as reference

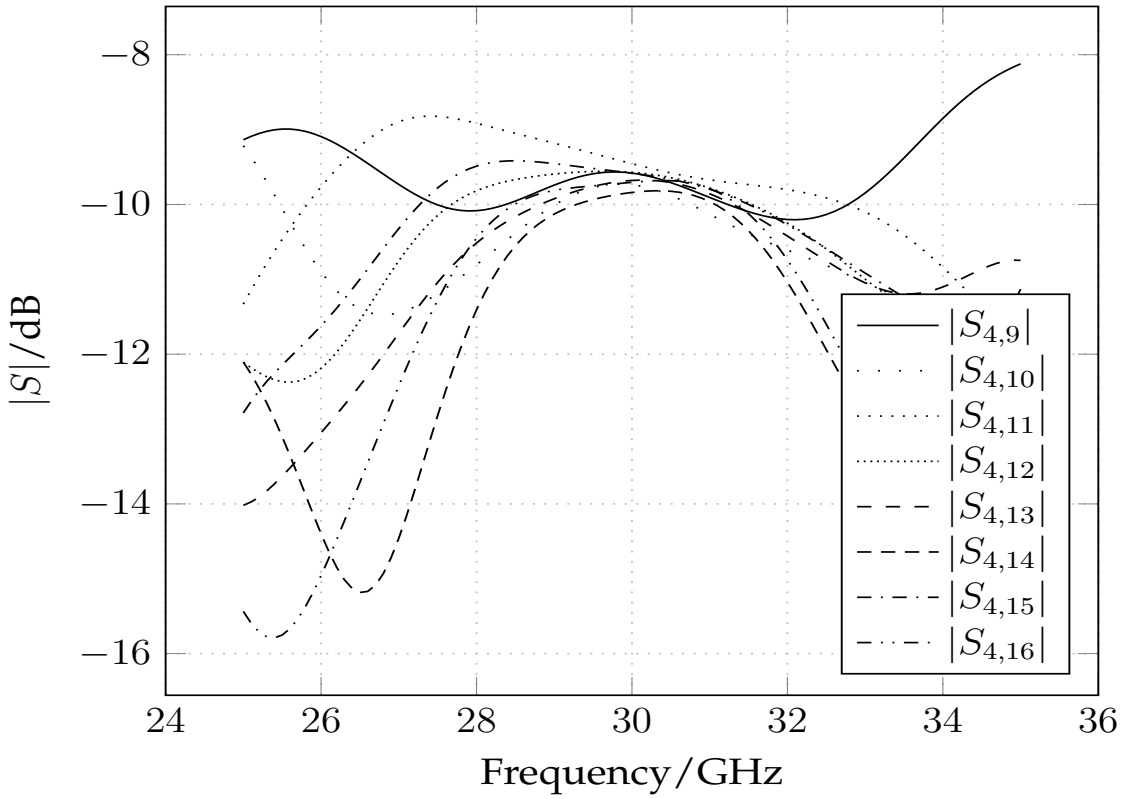

Fig. 4.21. Attenuation with port 4 as reference

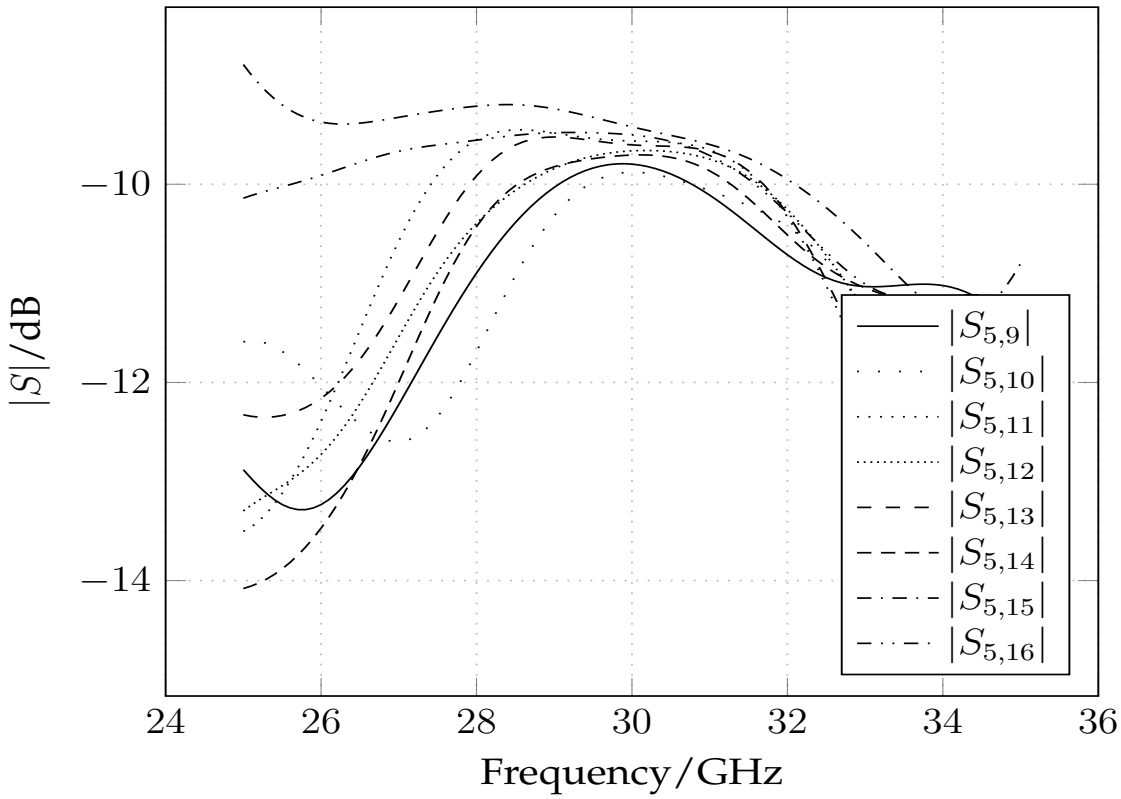

Fig. 4.22. Attenuation with port 5 as reference

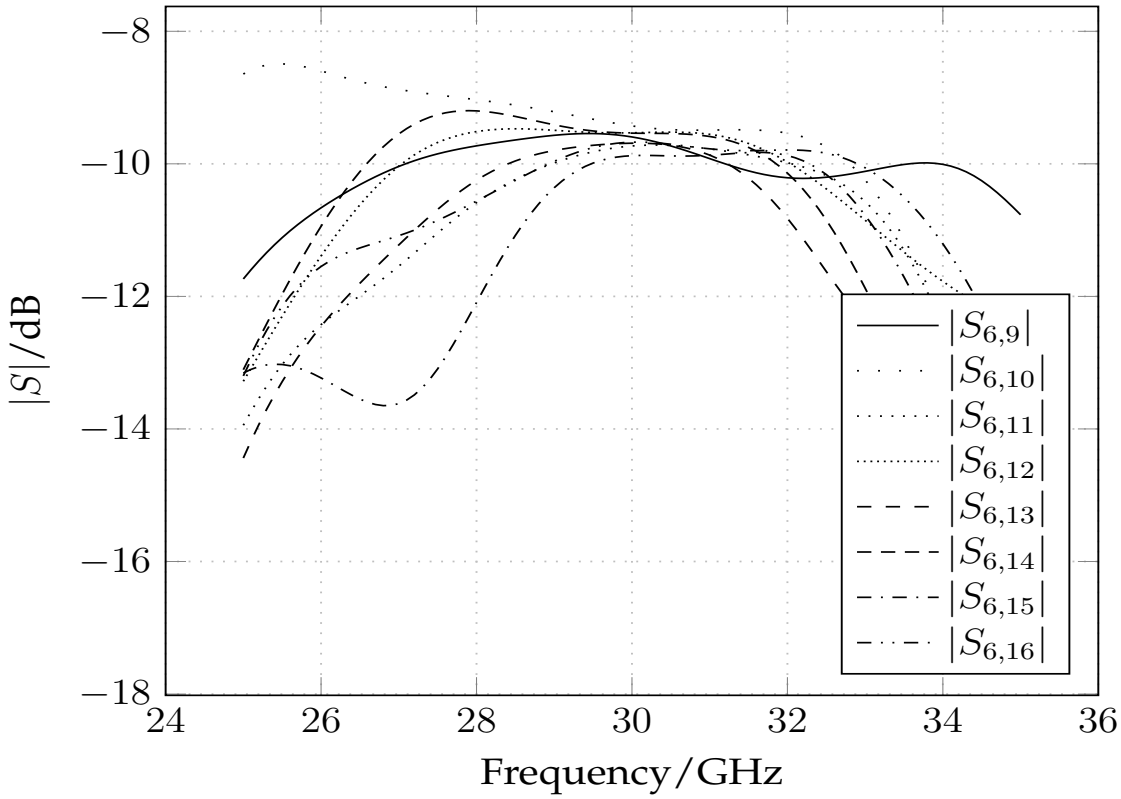

Fig. 4.23. Attenuation with port 6 as reference

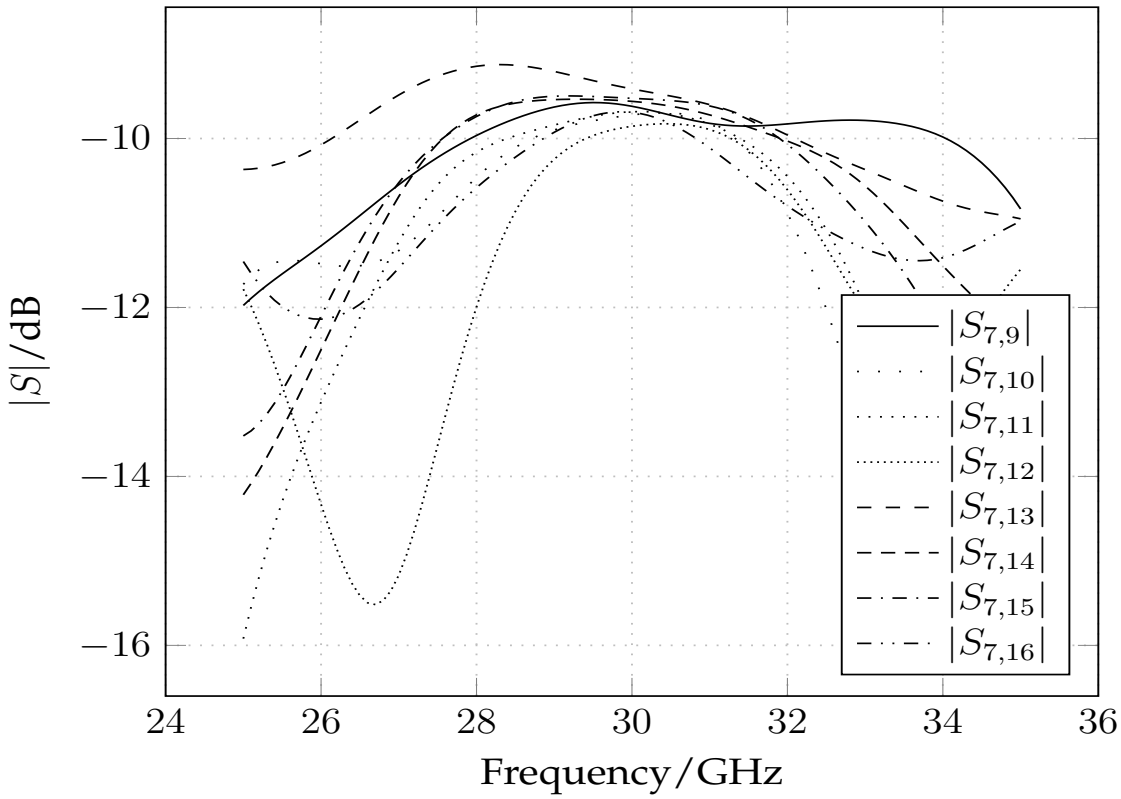

Fig. 4.24. Attenuation with port 7 as reference

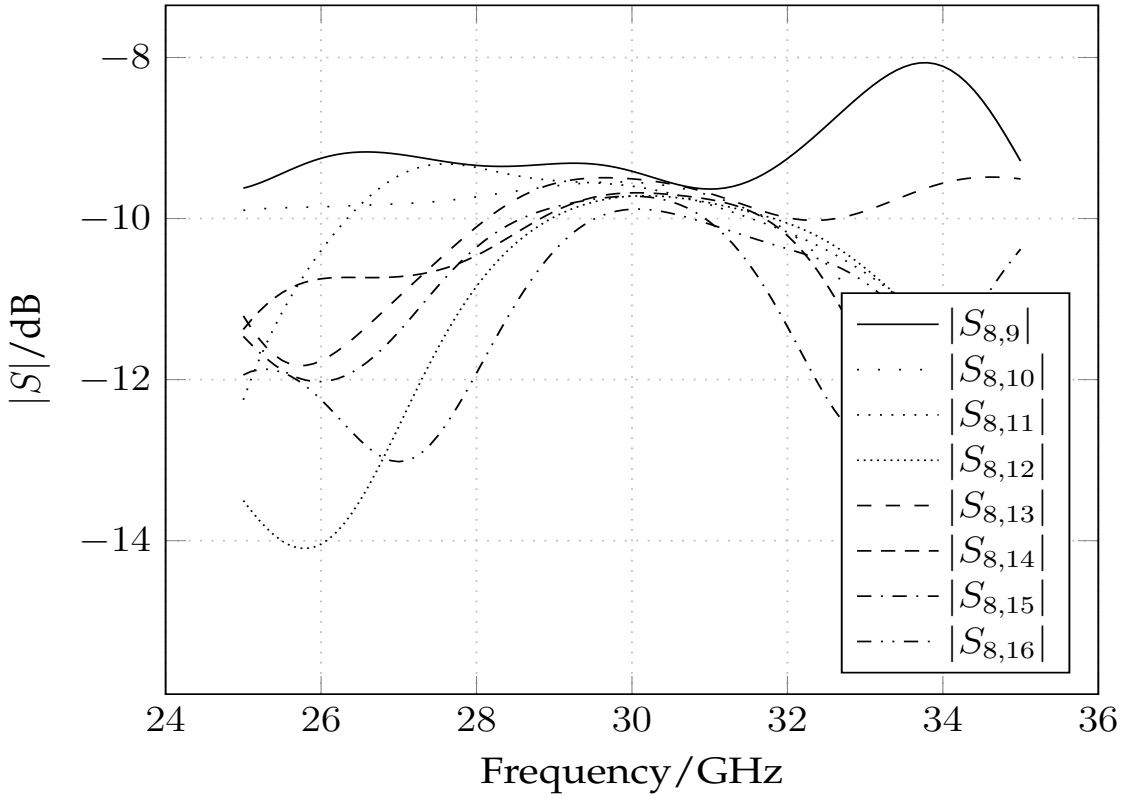

Fig. 4.25. Attenuation with port 8 as reference

The loss for each path is calculated by

$$|\boldsymbol{W}_{\mathrm{s}}| - |\boldsymbol{W}| = - \begin{bmatrix} 0.94 & 0.73 & 0.74 & 0.55 & 0.77 & 0.56 & 0.59 & 0.38 \\ 0.73 & 0.58 & 0.57 & 0.71 & 0.85 & 0.40 & 0.69 & 0.52 \\ 0.73 & 0.57 & 0.82 & 0.42 & 0.53 & 0.70 & 0.65 & 0.57 \\ 0.54 & 0.39 & 0.68 & 0.54 & 0.63 & 0.50 & 0.82 & 0.69 \\ 0.76 & 0.85 & 0.54 & 0.65 & 0.57 & 0.66 & 0.38 & 0.48 \\ 0.57 & 0.69 & 0.40 & 0.81 & 0.67 & 0.51 & 0.53 & 0.65 \\ 0.58 & 0.70 & 0.66 & 0.55 & 0.39 & 0.85 & 0.49 & 0.69 \\ 0.37 & 0.53 & 0.52 & 0.67 & 0.47 & 0.64 & 0.66 & 0.85 \end{bmatrix} \mathrm{dB}, \tag{4.4}$$

where $\boldsymbol{W}_{\mathrm{s}}$ is the simulation result.

4.2 Conclusion

A beam former made of 90° hybrids and delay lines is a very efficient solution for up to about 16 antennas at a considerable high center frequency. The size of the hybrids is frequency dependent and with each additional delay line and hybrid the losses increase. It is important to mention, that every hybrid acts as band pass filter. The more stages are used, the smaller the usable bandwidth will be. Nevertheless this is an extremely reliable solution, because no components with small mean time between failure (MTBF) are needed and no special adjustment after implementation is required. Compared to a solution with electrically adjusted phase shifters it is a robust and efficient solution.

5. Matching Strategies

5.1 Introduction

In the case of transmit amplifiers, it seems clear that *power matching* is the strategy one should follow in the design of matching networks, for one usually wants to extract all the generator's available power. To achieve efficiencies higher than 50% nowadays voltage matching is used for example in class C high power RF amplifiers.
For the case of a receive amplifier, the situation is more complicated. On the one hand, it seems that signal to noise ratio (SNR) is the all-important figure of merit for the receiver [36]. If this is so, then one should clearly follow the *noise matching* strategy in designing the matching network, rather than *power matching*. On the other hand, the *absolute level* of the output signal (voltage or current) is also important for the received and amplified signal has to be further processed by some kind of signal processing. If the signal level is too low, signal processing will not work anymore.
An immediately arising question is, therefore, why not go for power and noise matching at the same time? However, it has been shown long time ago [37], [38], that to design an amplifier which achieves power- and noise matching simultaneously while still providing reasonable gain, low noise figure and remaining stable, is next to impossible. This problem is caused by different mechanisms causing noise in a semiconductor, [39], [40].
If one cannot have noise- and power matching simultaneously, one may need to make a design decision which way to go. The fundamental trade off between information transfer i.e. minimum noise behaviour and power transfer has been investigated in [41] for a simple LNA model. Alternatively, one can ask what would be the optimum matching strategy which may well include noise and power matching as extreme cases. In this chapter, we look into these problems.

To elaborate, the analog signal is usually first converted into a digital signal by means of an ADC. The ADC requires its input signal to be within a certain range for proper operation. Because signal levels may be changing in time, one usually employs an automatic gain control (AGC) which follows the LNA. The purpose of the AGC is to keep the root mean square (RMS) of its output signal roughly constant by changing the amplification factor. However, the AGC has got a maximum amplification such that proper operation requires a *certain minimum signal level* coming out of the LNA [42]. One therefore has to ensure that, at the *output of the LNA*, both the

- signal to noise ratio, and
- the signal level

stay above some defined thresholds. While the latter's value is determined by the requirement of the ADC and the maximum amplification of the AGC, the minimum signal to noise ratio is determined by factors such as the modulation alphabet and channel code.

5.2 Choosing The Matching Strategy

Let us call $V_{\min}$, the minimum RMS voltage that must appear at the output of the LNA to drive the amplifier to full output with the AGC operating at full gain. It is more convenient, however, to use the normalized quantity:

$$\alpha_{\mathrm{g}} \;=\; \frac{V_{\min}^2}{4\mathrm{k}T\Delta f R_{\mathrm{G}}}, \tag{5.1}$$

which brings the minimum required signal level at the output of the LNA in relation to the strength of the noise signal received by the antenna. Herein, k is the Boltzmann constant, T is the antenna noise temperature, while Δf and R_{G} are the signal bandwidth and the real-part of the antenna impedance, respectively. Therefore, the aforementioned two goals become in mathematical notation:

$$\mathrm{SNR} \;\geq\; \mathrm{SNR}_{\min}, \tag{5.2}$$

$$\frac{\mathrm{E}[|v_{\mathrm{out}}|^2]}{4\mathrm{k}T\Delta f R_{\mathrm{G}}} \;\geq\; \alpha_{\mathrm{g}}, \tag{5.3}$$

where $\mathrm{SNR}_{\min}$ and α_{g} are given specifications. Per definition,

$$\mathrm{SNR} = \frac{\mathrm{SNR}_{\mathrm{av}}}{\mathrm{NF}} \tag{5.4}$$

with the noise figure (NF) of the LNA and $\mathrm{SNR}_{\mathrm{av}}$, the *available* SNR at the antenna port:

$$\mathrm{SNR}_{\mathrm{av}} = \frac{\mathrm{E}[|v_0|^2]}{4\mathrm{k}T\Delta f R_{\mathrm{G}}}, \tag{5.5}$$

with v_0 being the complex envelope of the antenna's open-circuit *desired signal* voltage. Substituting (5.5) into (5.4), the condition (5.2) can be rewritten as:

$$\frac{\mathrm{E}[|v_0|^2]}{4\mathrm{k}T\Delta f R_{\mathrm{G}}} \;\geq\; \mathrm{SNR}_{\min} \cdot \mathrm{NF}. \tag{5.6}$$

The complex envelope, v_{out}, of the LNA's output voltage consists of both signal and noise parts. Assuming noise and signal to be uncorrelated, their variances add up:

$$\mathrm{E}\left[|v_{\mathrm{out}}|^2\right] \;=\; \mathrm{E}\left[|v_0|^2\right] \cdot |A|^2 + 4\mathrm{k}T\Delta f R_{\mathrm{G}} \cdot \mathrm{NF} \cdot |A|^2, \tag{5.7}$$

where A is the voltage gain between the output of the LNA and the open-circuit voltage of the antenna. Substituting (5.7) into (5.3), the latter can be rewritten as:

$$\frac{\mathrm{E}[|v_0|^2]}{4\mathrm{k}T\Delta f R_{\mathrm{G}}} \;\geq\; \frac{\alpha_{\mathrm{g}}}{|A|^2} - \mathrm{NF}. \tag{5.8}$$

Taking (5.6) and (5.8) together into account, it follows that

$$\frac{\mathrm{E}[|v_0|^2]}{4\mathrm{k}T\Delta f R_\mathrm{G}} \;\geq\; \max\left(\mathrm{SNR}_\mathrm{min}\cdot\mathrm{NF}\;\;;\;\;\frac{\alpha_\mathrm{g}}{|A|^2}-\mathrm{NF}\right) \tag{5.9}$$

must hold for proper receiver operation. Note that NF and $|A|^2$ depend on the matching strategy:

- NOISE MATCHING: NF is *minimized* for the prize of *reduced gain* $|A|^2$
- POWER MATCHING: $|A|^2$ is *maximized* for the prize of *increased noise figure* NF.

Which matching strategy should one use then? Answer: the one for which

$$\max\left(\mathrm{SNR}_\mathrm{min}\cdot\mathrm{NF}\;\;;\;\;\frac{\alpha_\mathrm{g}}{|A|^2}-\mathrm{NF}\right) \tag{5.10}$$

is *minimum*. If we do not care for the signal level at all (by setting $\alpha_\mathrm{g}=0$), we see that noise matching is the winner. Yet, power matching will take the lead when α_g is increased large enough, i.e., for a large enough minimum signal level specification. The optimum choice between noise- and power matching strategies, therefore, depends on the pair

$$\left(\,\mathrm{SNR}_\mathrm{min},\;\alpha_\mathrm{g}\,\right),$$

while the pairs $(\mathrm{NF},|A|^2)$ for noise- and power matching, respectively, depend on the design of the LNA circuit. In the following, we give an illuminating example. Suppose that:

Strategy	noise figure, NF	gain, $\lvert A\rvert^2$
Noise matching	$1.58,\ (1.99\,\mathrm{dB})$	$4.75,\ (6.77\,\mathrm{dB})$
Power matching	$2.51,\ (4.00\,\mathrm{dB})$	$9.65,\ (9.84\,\mathrm{dB})$

With noise matching, the amplifier has a $2\,\mathrm{dB}$ better noise figure than with power matching. However, this comes at the price of the signal amplification being about $3\,\mathrm{dB}$ smaller. The optimum choice between noise- and power matching for this case is shown in Fig. 5.1 for different values of $\mathrm{SNR}_\mathrm{min}$ and α_g.

Example: Suppose the ADC requires an RMS input voltage of $1\,\mathrm{V}$. The AGC tries to keep this value constant by adjusting the amplification of the LNA output voltage. The maximum amplification shall be given by $100\,\mathrm{dB}$. The minimum required signal level at the output of the LNA is, therefore, $10\,\mu\mathrm{V}$. Assuming a half-wavelength dipole antenna with a noise temperature of $300\,\mathrm{K}$ and a signal bandwidth of $1\,\mathrm{MHz}$, we obtain a value of $\alpha_\mathrm{g}\approx 83$, or about $19\,\mathrm{dB}$. It then turns out from (5.10) that noise matching is preferable to power matching if the minimum required SNR is larger than about $8\,\mathrm{dB}$.

5.3 Optimum Matching Strategy

In general, neither noise- nor power matching are optimum, though. The optimum matching strategy would be to ensure that both the minimum required SNR and the minimum required signal level at the output of the LNA are met with the smallest possible

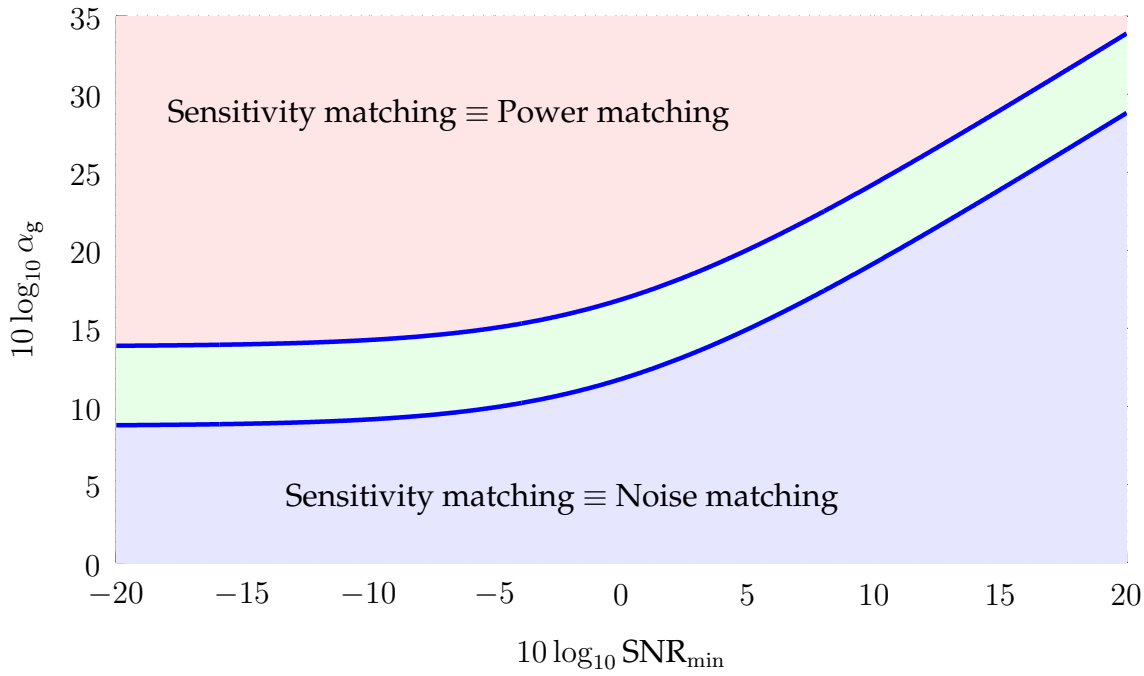

Fig. 5.1. Regions of optimality of noise-matching and power matching as special cases of sensitivity matching. In the area in the middle, sensitivity matching is different from both power- and noise-matching.

antenna desired signal voltage. For a given tuple $(\mathrm{SNR}_{\min}, \alpha_{\mathrm{g}})$, the optimum matching network, therefore, is obtained by solving

$$\min_{\text{matching network}} \max\left(\mathrm{SNR}_{\min} \cdot \mathrm{NF} \;;\; \frac{\alpha_{\mathrm{g}}}{|A|^2} - \mathrm{NF}\right). \tag{5.11}$$

As we will show later, both power- and noise matching are solutions of (5.11) but for different requirements $(\alpha_{\mathrm{g}}, \mathrm{SNR}_{\min})$. This is displayed in Figure 5.1. Note that NF and $|A|^2$ depend on the matching network and the amplifier circuit. A *joint design* of the amplifier and its matching network therefore looks promising.

5.3.1 Modeling

To be able to find the solution for (5.11) we have to establish NF and $|A|^2$ as a function of the parameters of the LNA and of the antenna. A circuit model is needed to derive these functions, see Fig. 5.2.

The antenna with $Z_{\mathrm{G}} = R_{\mathrm{G}} + \mathrm{j}X_{\mathrm{G}}$ and v_0 together with the matching twoport can be replaced by a transformed source with

$$Z'_{\mathrm{G}} = \frac{X_{12}^2}{R_{\mathrm{G}} + \mathrm{j}(X_{11} + X_{\mathrm{G}})} + \mathrm{j}X_{22}, \tag{5.12}$$

and

$$v'_0 = v_0 \frac{\mathrm{j}X_{12}}{R_{\mathrm{G}} + \mathrm{j}(X_{11} + X_{\mathrm{G}})}, \tag{5.13}$$

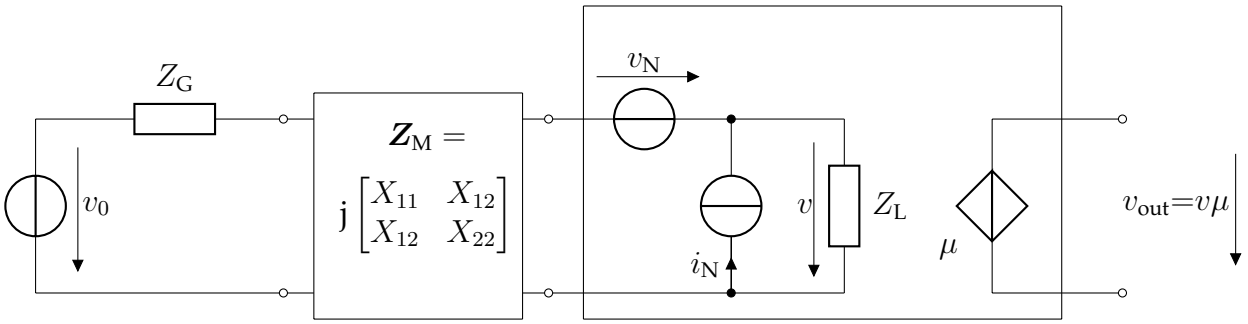

Fig. 5.2. Circuit model for antenna, lossless reciprocal matching twoport and LNA.

as shown in Fig. 5.3. Analysis leads to

$$\left|\frac{v_{\text{out}}}{v_0}\right|^2 = |A|^2 = \mu^2 \frac{R'_{\text{G}}}{R_{\text{G}}} \cdot \left|\frac{Z_{\text{L}}}{Z_{\text{L}} + Z'_{\text{G}}}\right|^2, \tag{5.14}$$

$$\text{NF} = 1 + \frac{\text{E}[|i_{\text{N}}|^2]}{4kT\Delta f R'_{\text{G}}}(R_{\text{N}}^2(1-|\rho|^2) + |Z'_{\text{G}} - \rho R_{\text{N}}|^2), \tag{5.15}$$

$$R_{\text{N}} = \sqrt{\frac{E[|v_{\text{N}}|^2]}{E[|i_{\text{N}}|^2]}} \tag{5.16}$$

and

$$\rho = \frac{E[v_{\text{N}} i_{\text{N}}^*]}{\sqrt{E[|v_{\text{N}}|^2]E[|i_{\text{N}}|^2]}} \tag{5.17}$$

have to be known. A measurement setup to determine R_{N} and ρ has been described in [43].

5.3.2 Problem Reformulation

First we reformulate (5.11) using an intermediate variable ζ as follows:

$$\min \zeta \;\; \text{s.t. } c \cdot \text{NF} \leq \zeta, \; \frac{\alpha_{\text{g}}}{|A|^2} \leq \zeta, \tag{5.18}$$

where $c = \text{SNR}_{\text{min}} + 1$. To accomodate the constraints the Lagrangian functional

$$L(\zeta, \lambda_1, \lambda_2) = \zeta + \lambda_1(c \cdot \text{NF} - \zeta) + \lambda_2 \left(\frac{\alpha_{\text{g}}}{|A|^2} - \zeta\right) \tag{5.19}$$

with $\lambda_1, \lambda_2 \geq 0$ has to be minimized with respect to t and maximized with respect to λ_1 and λ_2. The Karush Kuhn Tucker (KKT) conditions lead to

$$\frac{\partial L}{\partial \zeta} = 1 - \lambda_1 - \lambda_2 = 0, \tag{5.20}$$

$$\frac{\partial L}{\partial \lambda_1} = c \cdot \text{NF} - \zeta = 0, \tag{5.21}$$

$$\frac{\partial L}{\partial \lambda_2} = \frac{\alpha_{\text{g}}}{|A|^2} - \zeta = 0. \tag{5.22}$$

Next we have to compute the derivatives

$$\frac{\partial L}{\partial R'_{\mathrm{G}}} = 0, \ \frac{\partial L}{\partial X'_{\mathrm{G}}} = 0. \tag{5.23}$$

For X'_{G} and R'_{G} we get the solution

$$X'_{\mathrm{G}} = \gamma_{\mathrm{m}} \mathrm{Im}\{\rho\} R_{\mathrm{N}} - (1-\gamma_{\mathrm{m}}) X_{\mathrm{L}}, \tag{5.24}$$

$$R'_{\mathrm{G}} = \sqrt{\gamma_{\mathrm{m}} R_{\mathrm{N}}^2 (1-\mathrm{Im}\{\rho\}^2) + (1-\gamma_{\mathrm{m}}) R_{\mathrm{L}}^2 + \gamma_{\mathrm{m}}(1-\gamma_{\mathrm{m}})(\mathrm{Im}\{\rho\} R_{\mathrm{N}} + X_{\mathrm{L}})^2}, \tag{5.25}$$

where we combine the to Lagrangian multipliers λ_1 and λ_2 into one parameter

$$\gamma_{\mathrm{m}} = \frac{\frac{\lambda_1 c \mathrm{E}[|i_{\mathrm{N}}|^2]}{4kT\Delta f}}{\frac{\lambda_1 c \mathrm{E}[|i_{\mathrm{N}}|^2]}{4kT\Delta f} + \frac{\lambda_2 \alpha_{\mathrm{g}} R_{\mathrm{G}}}{\mu^2 |Z_{\mathrm{L}}|^2}}. \tag{5.26}$$

Now there are three different cases to distinguish:

$$\begin{aligned}
\lambda_1 = 0, \ \lambda_2 = 1, \ \zeta = \frac{\alpha_{\mathrm{g}}}{|A|^2} \qquad &\Rightarrow \text{power matching} \\
R'_{\mathrm{G}} = R_{\mathrm{L}}, \ X'_{\mathrm{G}} = -X_{\mathrm{L}}, \ \gamma_{\mathrm{m}} = 0 & \\
\lambda_1 = 1, \ \lambda_2 = 0, \ \zeta = c \cdot \mathrm{NF} \qquad &\Rightarrow \text{noise matching} \\
R'_{\mathrm{G}} = R_{\mathrm{N}} \sqrt{1-\mathrm{Im}\{\rho\}^2}, \ X'_{\mathrm{G}} = \mathrm{Im}\{\rho\} R_{\mathrm{N}}, \ \gamma_{\mathrm{m}} = 1 & \\
\lambda_1, \ \lambda_2 \neq 0, \ \zeta = c \cdot \mathrm{NF} = \frac{\alpha_{\mathrm{g}}}{|A|^2} \qquad &\Rightarrow \text{sensitivity matching} \\
0 < \gamma_{\mathrm{m}} < 1. &
\end{aligned} \tag{5.27}$$

In the case of sensitivity matching, we get a specific value for $\gamma_{\mathrm{m}} \in (0,1)$ from setting $c \cdot \mathrm{NF} = \frac{\alpha_{\mathrm{g}}}{|A|^2}$, which we plug in (5.24) and (5.25) to arrive at a second order equation for γ_{m} and therefore an optimum value Z'_{G} in closed form.

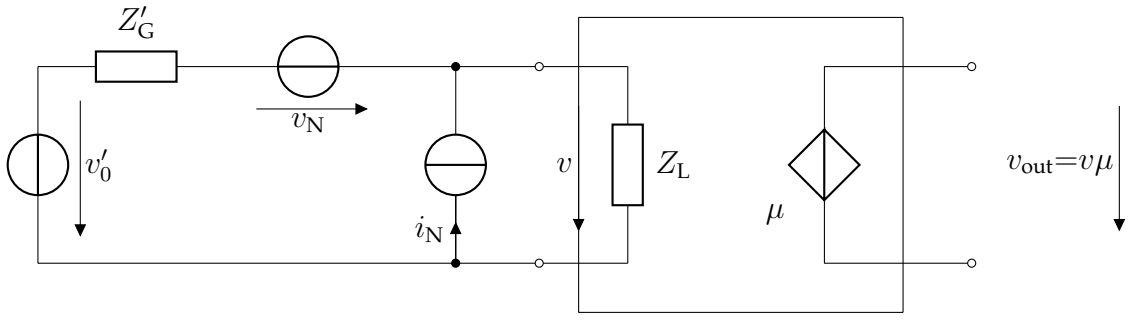

Fig. 5.3. LNA model driven by a signal source. The loading effect has been taken into account by the VCV's gain μ.

A T-circuit, shown in Fig. 5.4 seems to offer a reasonable topology for an implementation transforming Z_{G} to Z'_{G}. For there are two degrees of freedom, we need only two reactive elements. Fig. 5.5 shows a possible circuit topology. The output impedance of the

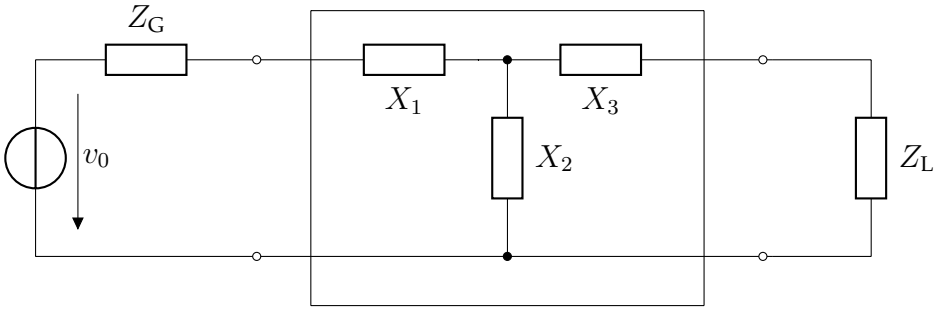

Fig. 5.4. Impedance matching network

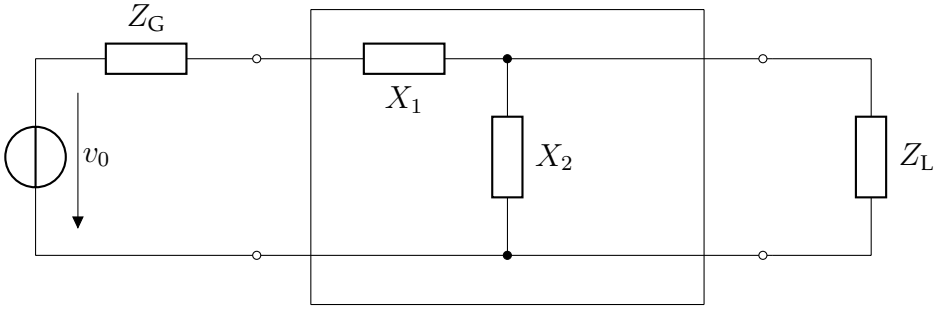

Fig. 5.5. Simple topology

matching network terminated by the source should be equal to

$$Z'_\mathrm{G} = \frac{\mathrm{j}X_2R_\mathrm{G} - X_2(X_\mathrm{G} + X_1)}{R_\mathrm{G} + \mathrm{j}(X_\mathrm{G} + X_1 + X_2)} = R'_\mathrm{G} + \mathrm{j}X'_\mathrm{G}. \tag{5.28}$$

Solving this system leads to:

$$X_1 = \frac{-b_\mathrm{q} \pm \sqrt{b_\mathrm{q}^2 - 4a_\mathrm{q}c_\mathrm{q}}}{2a_\mathrm{q}} \tag{5.29}$$

with the following variables

$$a_\mathrm{q} = R'_\mathrm{G} \tag{5.30}$$

$$b_\mathrm{q} = 2X_1X_\mathrm{G}R'_\mathrm{G} \tag{5.31}$$

$$c_\mathrm{q} = R'_\mathrm{G}(R_\mathrm{G}^2 + X_\mathrm{G}^2) - R_\mathrm{G}(R_\mathrm{G}'^2 + X_\mathrm{G}'^2), \tag{5.32}$$

on the first hand and on the other hand we have

$$X_2 = \frac{X'_\mathrm{G}R_\mathrm{G} + (X_\mathrm{G} + X_1)R'_\mathrm{G}}{R_\mathrm{G} - R'_\mathrm{G}}. \tag{5.33}$$

Note that $b_\mathrm{q}^2 \geq 4a_\mathrm{q}c_\mathrm{q}$ is assumed. Otherwise, an alternative topology with $X_1 = 0$ and $X_3 \neq 0$ has to be chosen.

5.4 Designing the System

For the realization, the A-band, which is identical to the former very high frequency (VHF) band, was chosen. At frequencies around $100\ \mathrm{MHz}$, lumped elements with a quality factor of 100 and even more are available. The matching network should be connected to the amplifier via an SMA connector. Power matching, noise matching and other designs could be plugged in without soldering and changing the amplifier itself. Each matching network can be set up on its own circuitboard.

5.4.1 Amplifier Design

The amplifier is a two stage common emitter circuit. It is a broadband amplifier, optimized for linearity, designed to work from $20\ \mathrm{MHz}$ to $1.5\ \mathrm{GHz}$, which uses the low noise transistor BFT66 in its input stage. Figure 5.6 shows the schematic of its first stage. Here, a $15\ \Omega$ emitter resistor and between base and collector $680\ \Omega$ and $1\ \mathrm{nF}$ are used for feedback. This causes lower gain, a higher noise figure but improves linearity and bandwidth very much. For bias a $15\ \mathrm{V}$ source is used, a $475\ \Omega$ resistor limits the collector current to $13\ \mathrm{mA}$ and a $100\ \mathrm{nF}$ ceramic capacitor blocks the RF.

If the collector current is increased to achieve better linearity the noise figure will rise, too [44]. If the base emitter diode current increases, R_N will move to lower values and more shot noise will be produced. Usually, input stages of measurement equipment like spectrum analyzers are optimized in a similar way. This kind of amplifier fits best to show the trade off. To keep its 3rd order intercept point (IP3) high the $2.7\ \mathrm{W}$ RF power transistor BFQ34 is used, collector to base and emitter feedback are also implemented, Fig. 5.7. In the 2nd stage, due to the higher signal power a much stronger feedback is implemented. By its biasing network, the collector current is adjusted to 50 mA.

5.4.2 Setting the Optimization Goal

Let us now set the required values both for SNR and the RMS voltage at the output of the amplifier. The necessary mimimum SNR is determined by the modulation format and the code, while the minimum amplifier output voltage V_min is determined by the required signal level at the ADC and the available AGC in between. As an example, we have chosen an $\mathrm{SNR}_\mathrm{min}$ of $10\ \mathrm{dB}$ and a V_min of $7.16\ \mu\mathrm{V}_\mathrm{RMS}$. All the parameters we need to compute α_g according to (5.1) are summarized in Table 5.1.

Parameter	Value
T	$290\ \mathrm{K}$
k	$1.38 \cdot 10^{-23}\ \frac{\mathrm{VAs}}{\mathrm{K}}$
Δf	$100\ \mathrm{kHz}$
$Z_\mathrm{G} = R_\mathrm{G}$	$50\ \Omega$
V_min	$7.16\ \mu\mathrm{V}_\mathrm{RMS}$
α_g	640
$\mathrm{SNR}_\mathrm{min}$	$10\ \mathrm{dB}$

Table 5.1. Source parameters

Parameter	Value
μ	12.59
$\mathrm{E}[\lvert i_\mathrm{N}\rvert^2]$	$2.6 \cdot 10^{-17}\mathrm{A}^2$
R_N	$20\ \Omega$
Z_L	$153 - \mathrm{j} \cdot 26\ \Omega$
ρ	$-0.9 - \mathrm{j} \cdot 0.127$

Table 5.2. Amplifier parameter

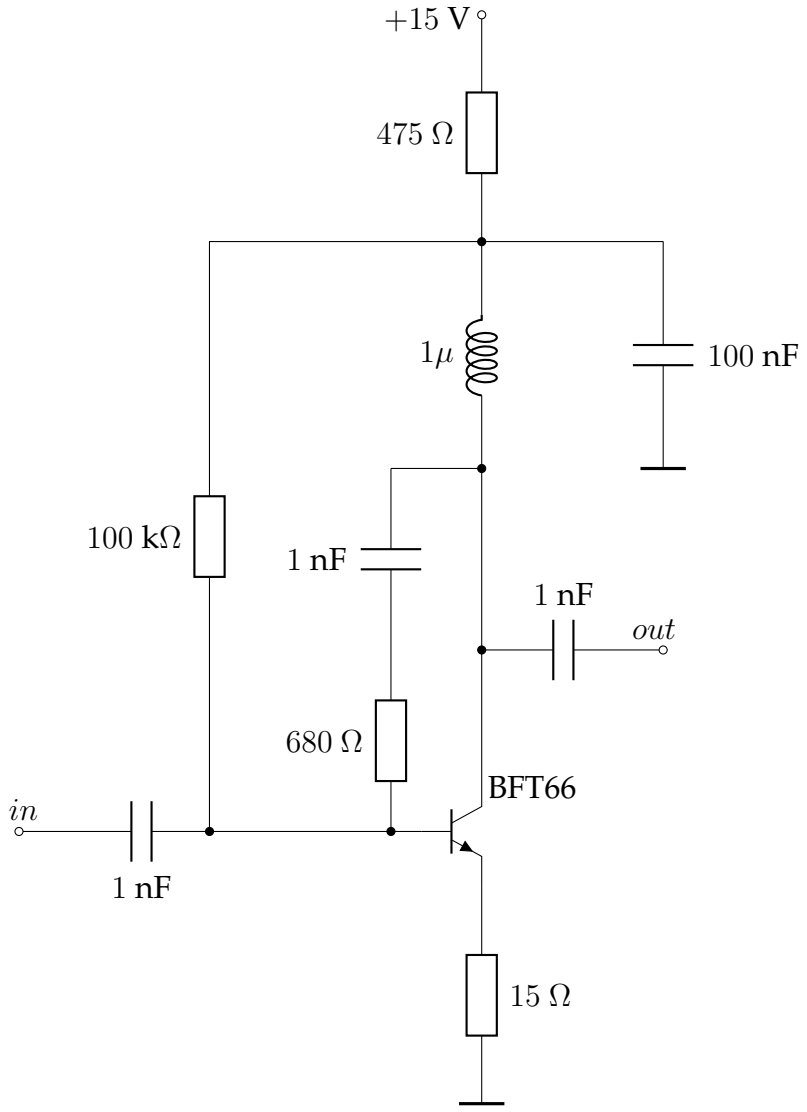

Fig. 5.6. Amplifier 1st stage

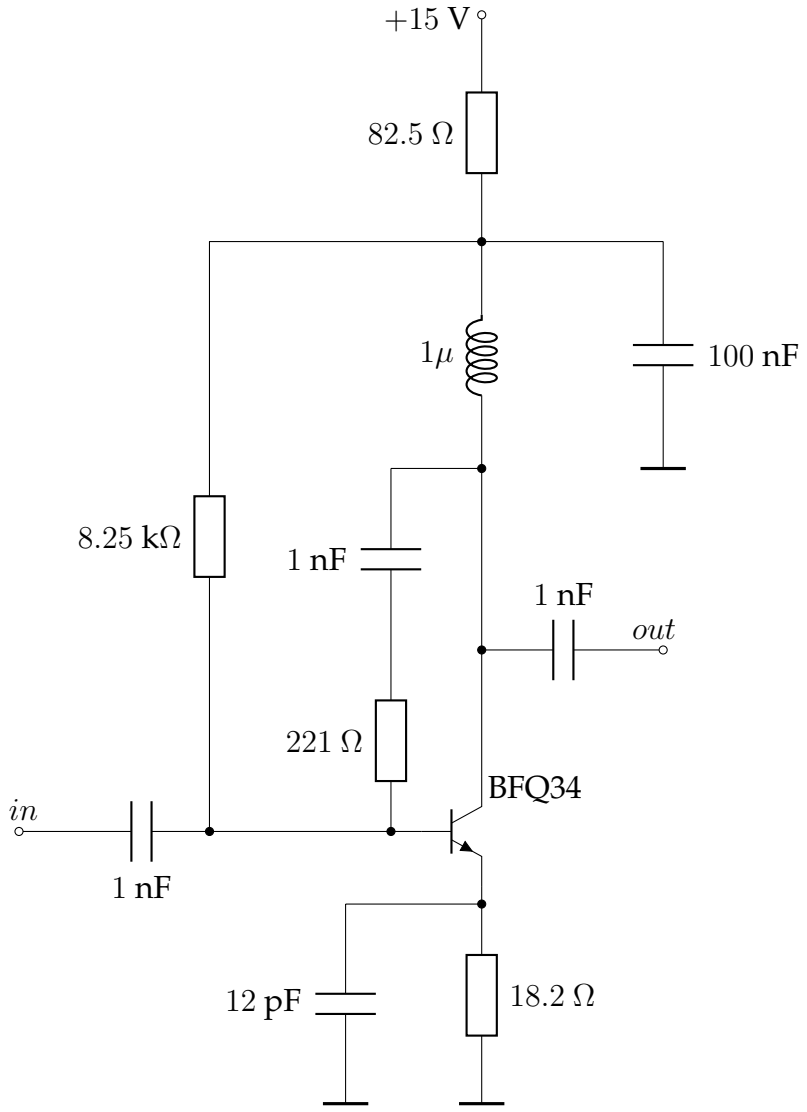

Fig. 5.7. Amplifier 2nd stage

This finally leads to $\alpha_g = 640$. Therefore, our optimization goal is to provide a source to the LNA such, that both, the $\text{SNR}_{\min}$ of 10 dB and the necessary $\alpha_g = 640$ can simultaneously be achieved with the lowest possible voltage v_0.

5.5 Realization

In order to verify the proposed matching strategy, a real amplifier is built in an electro magnetic interference (EMI) shielded box. For measuring the parameters, a spectrum analyzer, a network analyzer and two ultra low noise power supplies are used. Between the amplifier, described in section 5.4 and the spectrum analyzer an extreme low noise preamplifier is used. The measurement results are summarized in Table 5.2. From the parameters given in Table 5.2 we can design a matching twoport for the proposed sensitivity matching and compare the results with the well established power and noise matching:

$$\begin{aligned} \text{power matching } \gamma_m = 0 &: Z'_G = Z_L^* = (153 + j \cdot 26)\ \Omega \\ \text{noise matching } \gamma_m = 1 &: Z'_G = R_N(\sqrt{1 - \text{Im}\{\rho\}^2} + j \cdot \text{Im}\{\rho\}) = (19.84 - j \cdot 2.54)\ \Omega \\ \text{sensitivity matching } \gamma_m = 0.911 &: Z'_G = (50.1 + j6 \cdot 10^{-5})\ \Omega. \end{aligned} \tag{5.34}$$

The matching twoports for power and noise matching are shown in Fig. 5.8 and 5.9, while for sensitivity matching it turns out that the matching network collapses to just a through connection. This is a very desirable situation, where no reactive components are needed ($X_1 \to 0\ \Omega, X_2 \to \infty\ \Omega$), no losses associated with these reactances degrade the performance and no bandwith limitation is introduced by the matching network.

5.5.1 Matching Strategies

The amplifier has an input impedance of $Z_L = (153 - j \cdot 26)\ \Omega$. For power matching Z_L is transformed to $Z_G = 50\ \Omega$ as Fig. 5.8 shows. For noise matching the amplifier input must

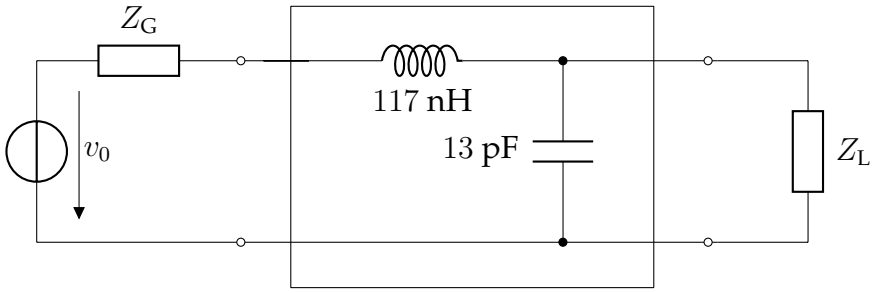

Fig. 5.8. Power matching

be connected to an impedance of $Z'_G = (19.84 - j \cdot 2.54)\ \Omega$ as shown in Fig. 5.9. According to our amplifier design, sensitivity matching now is quite simple: There is no matching twoport necessary, the antenna is directly connected to the LNA.

5.6 Measurement

The well established Y_N factor method will be used to verify our results. For this method of measurement, an uncorrelated calibrated diode noise source with an excess noise ratio (ENR) of 6.76 dB is connected via each matching network to the input of a spectrum

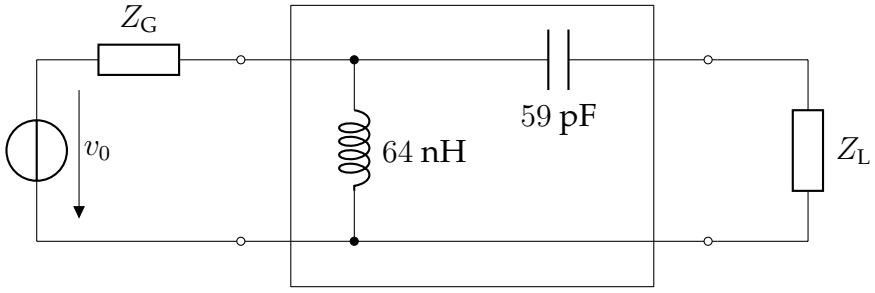

Fig. 5.9. Noise matching

analyzer via a further auxiliary low noise amplifier. When its power supply is turned off, the source produces noise like a 50 Ω resistor at $T_c = 290$ K. The reverse biased source diode will produce avalanche noise, with the power supply turned on. In this case the noise level at 100 MHz is equal to a 50 Ω resistor at $T_h = 1375$ K. With the reference temperature $T_0 = 290$ K, the ENR can be defined as:

$$\text{ENR} = \frac{T_h - T_c}{T_0}. \tag{5.35}$$

The amplifier and the noise source are fed with a low noise power supply. On the circuitboards of noise source and amplifier, there are additional low pass filters and each housing is shielded to prevent electromagnetic disturbance. This also called hot-cold method is used for measuring each kind of matching network. The value N_h (hot noise) at the amplifier's output port appears with the noise source supply turned on, N_c (cold noise) with its supply turned off. Y_N is the delta between hot and cold output power value,

Matching	Hot	Cold
Power	$-144.16\ \frac{\text{dBm}}{\text{Hz}}$	$-148.03\ \frac{\text{dBm}}{\text{Hz}}$
Sensitivity	$-144.54\ \frac{\text{dBm}}{\text{Hz}}$	$-149.10\ \frac{\text{dBm}}{\text{Hz}}$
Noise	$-144.70\ \frac{\text{dBm}}{\text{Hz}}$	$-149.61\ \frac{\text{dBm}}{\text{Hz}}$

Table 5.3. Measurement results

measured for each matching strategy of Table 5.3. According to Friis [45], gain G_p here is defined by the ratio of output and input power of an amplifier. If power matched, the source will only provide half of its open voltage and therefore the gain G_p is:

$$G_p = \frac{|A|^2}{4} \tag{5.36}$$

$$Y_N = \frac{N_X + kT_h\Delta f G_p}{N_X + kT_c\Delta f G_p} = \frac{N_h}{N_c} \tag{5.37}$$

With the Y_N factor and the ENR the amplifier's additional noise is:

$$N_X = kT_c\Delta f G_p \left(\frac{\text{ENR}}{Y_N - 1} - 1\right). \tag{5.38}$$

According to its definition the noise figure is then described by:

$$\text{NF} = \frac{kT_c\Delta f G_p + N_X}{kT_c\Delta f G_p} = \left(\frac{\text{ENR}}{Y_N - 1}\right). \tag{5.39}$$

The noise figure can be calculated, using (5.15) and be compared to the value from the analyzer, Table 5.4. The network analyzer helps us getting the gain in a two port measurement, the values are compared to the ones calculated with the help of (5.14), Table 5.5.

Matching	Measurement	Calculation
Power	5.18 dB	6.20 dB
Sensitivity	4.07 dB	4.00 dB
Noise	3.54 dB	3.46 dB

Table 5.4. Noise figure

Matching	Measurement	Calculation
Power	21.0 dB	20.96 dB
Sensitivity	19.6 dB	19.60 dB
Noise	17.2 dB	16.94 dB

Table 5.5. Gain, $10 \cdot \lg|A|^2$ dB

When noise matching an amplifier, a not negligible amount of signal energy is reflected from the amplifiers input, this causes a smaller gain, Table 5.5. Power matching is also not an optimal strategy, here no energy is reflected in an ideal case, but the related input noise floor is much higher, Table 5.6.

Matching	Measurement	Calculation
Power	$-168.8\ \frac{\text{dBm}}{\text{Hz}}$	$-167.80\ \frac{\text{dBm}}{\text{Hz}}$
Sensitivity	$-169.9\ \frac{\text{dBm}}{\text{Hz}}$	$-170.00\ \frac{\text{dBm}}{\text{Hz}}$
Noise	$-170.4\ \frac{\text{dBm}}{\text{Hz}}$	$-170.54\ \frac{\text{dBm}}{\text{Hz}}$

Table 5.6. Noise floor

Matching	Measurement	Calculation
Power	$-158.8\ \frac{\text{dBm}}{\text{Hz}}$	$-159.17\ \frac{\text{dBm}}{\text{Hz}}$
Sensitivity	$-160.0\ \frac{\text{dBm}}{\text{Hz}}$	$-160.00\ \frac{\text{dBm}}{\text{Hz}}$
Noise	$-157.6\ \frac{\text{dBm}}{\text{Hz}}$	$-157.88\ \frac{\text{dBm}}{\text{Hz}}$

Table 5.7. Sensitivity

Finally, we calculate the input sensitivity out of these results and see, that sensitivity matching provides us with the best sensitivity, see Table 5.7, i.e. we achieve our required SNR and signal level at the LNA output with a lower source voltage.

5.7 Conclusion

A new strategy of matching was presented. To this end, we first developed a mathematical model. In a second step, we designed an amplifier and implemented the system first on MATLAB and SPICE to simulate it. Finally, power matching, noise matching and sensitivity matching have been shown. The theoretical results have been compared with data obtained from measurement results and found to agree well. The new kind of matching is an efficient method to increase sensitivity of a receiving system. The design strategy was based on a given LNA and a given source. An interesting direction for research is designing the LNA for a given source such that the matching twoport becomes as simple as possible. Another important direction is to expand the methodology for matching multiports for multi antenna systems.

6. LNA Characterization

6.1 Introduction

6.1.1 Circuit Theoretic Model

A noisy two port can always be characterized by a noiseless one with two noise sources connected its ports. For modeling a noisy amplifier it is convenient to use the model depicted in Fig. 6.1 where two noise sources, current- and voltage source, are connected to the input of the amplifier [46][47][48]. There are four real parameters characterizing the

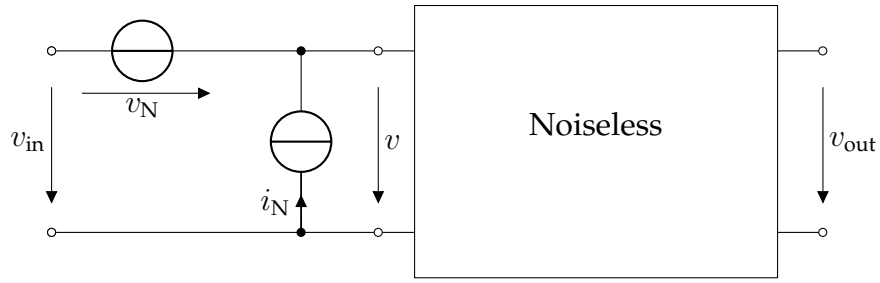

Fig. 6.1. External noise sources with noiseless two port

noise sources, i.e. the variances of both noise sources σ_{v}^2, σ_{i}^2 (6.1), the complex correlation coefficient ρ (6.2) and the noise resistance R_{N} (6.3) thereof

$$\sigma_{\mathrm{v}}^2 = \mathrm{E}\left[|v_{\mathrm{N}}|^2\right], \sigma_{\mathrm{i}}^2 = \mathrm{E}\left[|i_{\mathrm{N}}|^2\right], \tag{6.1}$$

$$\rho = \mathrm{Re}\{\rho\} + \mathrm{j} \cdot \mathrm{Im}\{\rho\} = \frac{\mathrm{E}[v_{\mathrm{N}} i_{\mathrm{N}}^*]}{\sigma_{\mathrm{v}} \sigma_{\mathrm{i}}} \tag{6.2}$$

$$R_{\mathrm{N}} = \frac{\sigma_{\mathrm{v}}}{\sigma_{\mathrm{i}}}. \tag{6.3}$$

Once these four parameters are known, the noise figure NF (6.4) of such an amplifier can be calculated [49] as a function of admittance of the source driving that amplifier

$$\begin{aligned} \mathrm{NF} = 1 + \frac{\sigma_{\mathrm{i}}^2}{4kT\Delta f} \frac{1}{G_{\mathrm{s}}} \\ (1 + R_{\mathrm{N}}^2 |Y_{\mathrm{s}}|^2 - 2R_{\mathrm{N}} \mathrm{Re}\{\rho\} G_{\mathrm{s}} + 2R_{\mathrm{N}} \mathrm{Im}\{\rho\} B_{\mathrm{s}}), \end{aligned} \tag{6.4}$$

where k, T and Δf are the Boltzmann constant, absolute temperature and the noise bandwidth respectively, while

$$Y_{\mathrm{s}} = G_{\mathrm{s}} + \mathrm{j} \cdot B_{\mathrm{s}} \tag{6.5}$$

is the source admittance.

6.1.2 Matching Strategies

When designing a front end (6.4) has to be minimized for noise matching, then $\frac{1}{R_{\mathrm{N}}}$ and $|Y_{\mathrm{s}}|$ have to be equal [50]. The minimum noise figure $\mathrm{NF}_{\mathrm{min}}$ is achieved with the optimum source admittance Y_{opt},

$$Y_{\mathrm{opt}} = G_{\mathrm{opt}} + \mathrm{j} \cdot B_{\mathrm{opt}} = \frac{1}{R_{\mathrm{N}}}(\sqrt{1 - \mathrm{Im}\{\rho\}^2} - \mathrm{j} \cdot \mathrm{Im}\{\rho\}) \tag{6.6}$$

$$\mathrm{NF}_{\mathrm{min}} = 1 + \frac{\sigma_{\mathrm{i}}^2}{2kT\Delta f} R_{\mathrm{N}}(\sqrt{1 - \mathrm{Im}\{\rho\}^2} - \mathrm{Re}\{\rho\}). \tag{6.7}$$

6.1.3 Standards for Measuring Noise

Already in 1960 basic standards on measuring noise of linear two ports have been devised by the institute of radio engineers (IRE) [51],[52], where again four real valued parameters are used to characterize noise. These four parameters are the optimum source admittance $Y_{\mathrm{opt}} = G_{\mathrm{opt}} + \mathrm{j} \cdot B_{\mathrm{opt}}$, the minimum noise figure $\mathrm{NF}_{\mathrm{min}}$ and a parameter called R_{n} (6.8)

$$R_{\mathrm{n}} = \sigma_{\mathrm{v}}^2 / 4kT\Delta f. \tag{6.8}$$

With that the noise figure for any source admittance $Y_{\mathrm{s}} = G_{\mathrm{s}} + \mathrm{j} \cdot B_{\mathrm{s}}$ reads

$$\mathrm{NF} = \mathrm{NF}_{\mathrm{min}} + \frac{R_{\mathrm{n}}}{G_{\mathrm{s}}}((G_{\mathrm{s}} - G_{\mathrm{opt}})^2 + (B_{\mathrm{s}} - B_{\mathrm{opt}})^2). \tag{6.9}$$

It can be shown that (6.9) and (6.4) are equivalent by using (6.6), (6.7) and (6.8). The proposed IRE measurement [51] needs a calibrated noise source for two different noise temperatures, a slide screw tuner as lossless matching two port between the noise source and the amplifier input and a power meter for measuring the amplifier output [53][54]. With an iterative procedure one has to find the optimum source admittance and at least one measurement with non optimum G_{s} and B_{s} to determine R_{n} [55]. Obviously, from the four parameters $\mathrm{NF}_{\mathrm{min}}, G_{\mathrm{opt}}, B_{\mathrm{opt}}$ and R_{n} one could compute the four parameters given in (6.1) and (6.2). But for carrying out the measurement a tunable matching two port, a so called slide screw tuner, which usually is narrow band and a calibrated noise source are needed [56].

6.1.4 The Alternative Characterization Approach

The alternative new approach needs as a minimum only four well defined terminations [31] for the amplifier input and a band limited power meter for the amplifier output. In a receiver its digital back end is used instead of the power meter. From the output power measured with only four different input terminations, e.g. two of them purely

resistive and two purely reactive, the four parameters (6.1), (6.2) can be computed, if S_{11} and $|S_{21}|$ of the amplifier under test are known.

The details of the new approach will be described in Section II together with extensions to improving the accuracy of the measurement by using a larger number of terminations and to find the input impedance

$$Z_{\text{in}} = \frac{1 + S_{11}}{1 - S_{11}} \tag{6.10}$$

without the need of measuring S_{11} with a network analyzer.

6.2 The New Concept

As a minimum $M = 4$ impedances are needed,
where $Z_{\text{m}} = R_{\text{m}} + \text{j} \cdot X_{\text{m}}$, $m = 1, ..., M$, Fig. 6.2.

First the value of Z_{in} obtained from the measured S_{11} is used. One has to be aware that an accurate measurement of S_{11} with a network analyzer may be difficult because of the low level of the reflected signal obtained by a directional coupler. Having more measurements with more than 4 terminations available, the initial value of Z_{in} from (6.10) can be updated. The power P_{m} delivered to the load resistor R is:

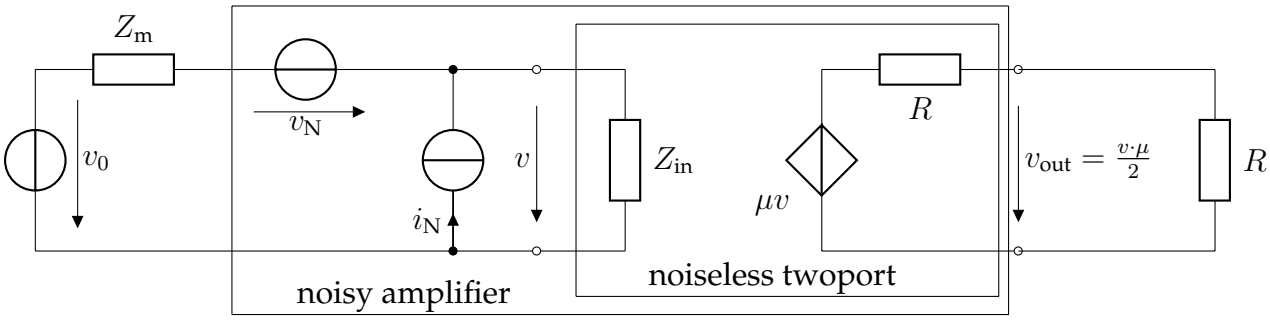

Fig. 6.2. Noisy Amplifier

$$\begin{aligned}
P_{\text{m}} &= \frac{\text{E}[|v_{\text{out}}|^2]}{R} = \frac{|\mu|^2}{4R}\text{E}[|v|^2] \\
&= \frac{|\mu|^2}{4R}\text{E}\left[\left|(v_0 + v_{\text{N}} + i_{\text{N}}Z_{\text{m}})\frac{Z_{\text{in}}}{Z_{\text{m}} + Z_{\text{in}}}\right|^2\right] \\
&= \frac{|\mu|^2|Z_{\text{in}}|^2}{4R|Z_{\text{m}} + Z_{\text{in}}|^2}(4kT\Delta f R_{\text{m}} + \text{E}[|v_{\text{N}}|^2] + \\
&+ \text{E}[|i_{\text{N}}|^2]|Z_{\text{m}}|^2) - 2(R_{\text{m}}\text{Re}\{\text{E}[v_{\text{N}}i_{\text{N}}^*]\} + \\
&+ X_{\text{m}}\text{Im}\{\text{E}[v_{\text{N}}i_{\text{N}}^*]\}).
\end{aligned} \tag{6.11}$$

For a short ($Z_{\mathrm{m}} = 0\ \Omega,\ v_0 = 0\ \mathrm{V}$) at the input

$$P_{\mathrm{m}} = P_{\mathrm{short}} = \frac{|\mu|^2}{4R}\mathrm{E}[|v_{\mathrm{N}}|^2]. \tag{6.12}$$

With an open ($Z_{\mathrm{m}} \to \infty\ \Omega,\ v_0 = 0\ \mathrm{V}$) at the input

$$P_{\mathrm{m}} = P_{\mathrm{open}} = \frac{|\mu|^2|Z_{\mathrm{in}}|^2}{4R}\mathrm{E}[|i_{\mathrm{N}}|^2]. \tag{6.13}$$

The noise parameter R_{N} can be determined from (6.12) and (6.13)

$$R_{\mathrm{N}} = \sqrt{\frac{\mathrm{E}[|v_{\mathrm{N}}|^2]}{\mathrm{E}[|i_{\mathrm{N}}|^2]}} = \sqrt{\frac{|Z_{\mathrm{in}}|^2 P_{\mathrm{short}}}{P_{\mathrm{open}}}}. \tag{6.14}$$

For a pure imaginary valued impedance (reactive termination) $\mathrm{j} \cdot X_{\mathrm{m}}$ at the input $\mathrm{Im}\{\rho\}$ is determined from $P_{\mathrm{j}\cdot X_{\mathrm{m}}}$

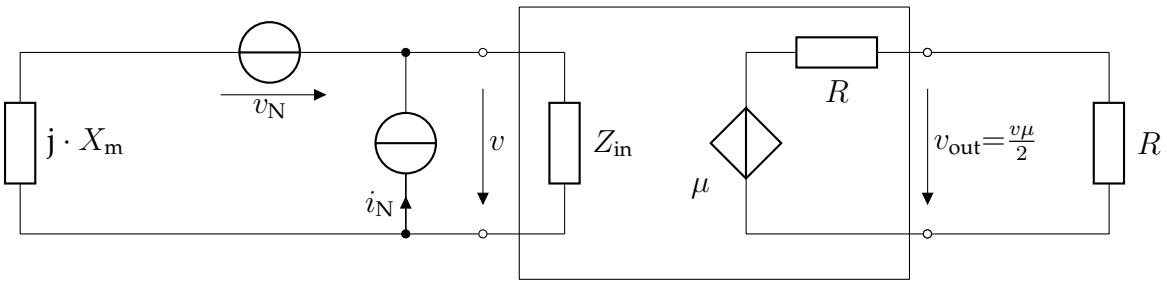

Fig. 6.3. Amplifier with pure reactive termination

$$\begin{aligned} P_{\mathrm{j}\cdot X_{\mathrm{m}}} =& \frac{|\mu|^2|Z_{\mathrm{in}}|^2}{4R|\mathrm{j}\cdot X_{\mathrm{m}} + Z_{\mathrm{in}}|^2}(\mathrm{E}[|v_{\mathrm{N}}|^2] + \\ &+ \mathrm{E}[|i_{\mathrm{N}}|^2]|X_{\mathrm{m}}|^2 - 2X_{\mathrm{m}}\mathrm{Im}\{\mathrm{E}[v_{\mathrm{N}}i_{\mathrm{N}}^*]\}). \end{aligned} \tag{6.15}$$

The second noise parameter $\mathrm{Im}\{\rho\}$ is

$$\begin{aligned} \mathrm{Im}\{\rho\} &= \frac{\mathrm{Im}\{\mathrm{E}[v_{\mathrm{N}}i_{\mathrm{N}}^*]\}}{\sqrt{\mathrm{E}[|v_{\mathrm{N}}|^2]\mathrm{E}[|i_{\mathrm{N}}|^2]}} \\ &= \frac{\left(\mathrm{E}[|v_{\mathrm{N}}|^2] + \mathrm{E}[|i_{\mathrm{N}}|^2]|X_{\mathrm{m}}|^2 - \frac{4P_{\mathrm{j}\cdot X_{\mathrm{m}}}R|\mathrm{j}\cdot X_{\mathrm{m}}+Z_{\mathrm{in}}|^2}{|\mu|^2|Z_{\mathrm{in}}|^2}\right)}{2X_{\mathrm{m}}\sqrt{\mathrm{E}[|v_{\mathrm{N}}|^2]\mathrm{E}[|i_{\mathrm{N}}|^2]}}. \end{aligned} \tag{6.16}$$

The optimum source impedance for noise matching (6.6) is

$$Z_{\mathrm{opt}} = R_{\mathrm{N}}(\sqrt{1 - (\mathrm{Im}\{\rho\})^2} + \mathrm{j}\cdot\mathrm{Im}\{\rho\}). \tag{6.17}$$

For a pure real valued impedance (resistive termination) R_{m}, $\mathrm{Re}\{\rho\}$ is determined from $P_{R_{\mathrm{m}}}$

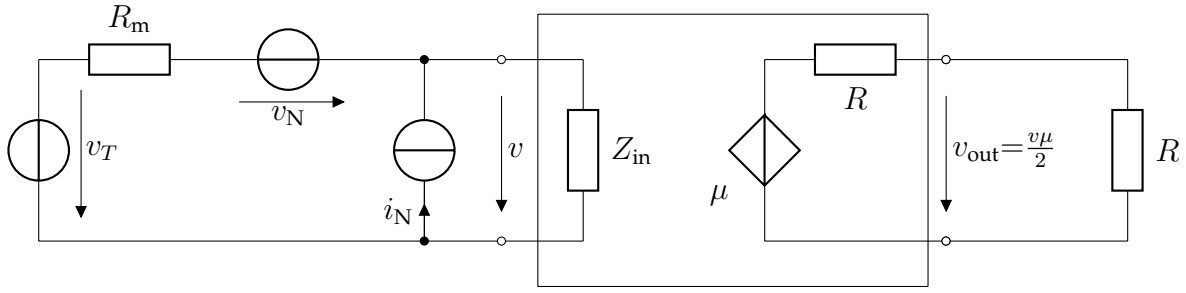

Fig. 6.4. Amplifier with resistive termination

$$P_{R_\mathrm{m}} = \frac{|\mu|^2|Z_\mathrm{in}|^2}{4R|R_\mathrm{m}+Z_\mathrm{in}|^2}(4kT\Delta f R_\mathrm{m} + \mathrm{E}[|v_\mathrm{N}|^2] + \\ + \mathrm{E}[|i_\mathrm{N}|^2]R_\mathrm{m}^2 - 2R_\mathrm{m}\mathrm{Re}\{\mathrm{E}[v_\mathrm{N}i_\mathrm{N}^*]\}). \tag{6.18}$$

Therefore, thermal noise [57] is modeled by voltage source v_T, Fig. 6.4, which is characterized by (6.19), where Δf is the bandwidth,

$$\mathrm{E}[|v_T|^2] = 4\mathrm{k}T\Delta f\mathrm{Re}\{Z_\mathrm{m}\}, \mathrm{E}[|v_T v_N^*|] = 0, \mathrm{E}[|v_T i_N^*|] = 0. \tag{6.19}$$

$$\mathrm{Re}\{\rho\} = \frac{\mathrm{Re}\{\mathrm{E}[v_\mathrm{N}i_\mathrm{N}^*]\}}{\sqrt{\mathrm{E}[|v_\mathrm{N}|^2]\mathrm{E}[|i_\mathrm{N}|^2]}} = \tag{6.20}$$

$$\frac{4kT\Delta f R_\mathrm{m} + \mathrm{E}[|v_\mathrm{N}|^2] + \mathrm{E}[|i_\mathrm{N}|^2]|R_\mathrm{m}|^2 - \frac{4P_{R_\mathrm{m}}R|R_\mathrm{m}+Z_\mathrm{in}|^2}{|\mu|^2|Z_\mathrm{in}|^2}}{2R_\mathrm{m}\sqrt{\mathrm{E}[|v_\mathrm{N}|^2]\mathrm{E}[|i_\mathrm{N}|^2]}}$$

With the fourth and last missing noise parameter $\mathrm{Re}\{\rho\}$, the minimum achievable noise figure NF_min, obtained at noise matching ($Z_G = Z_\mathrm{opt}$) is determined now.

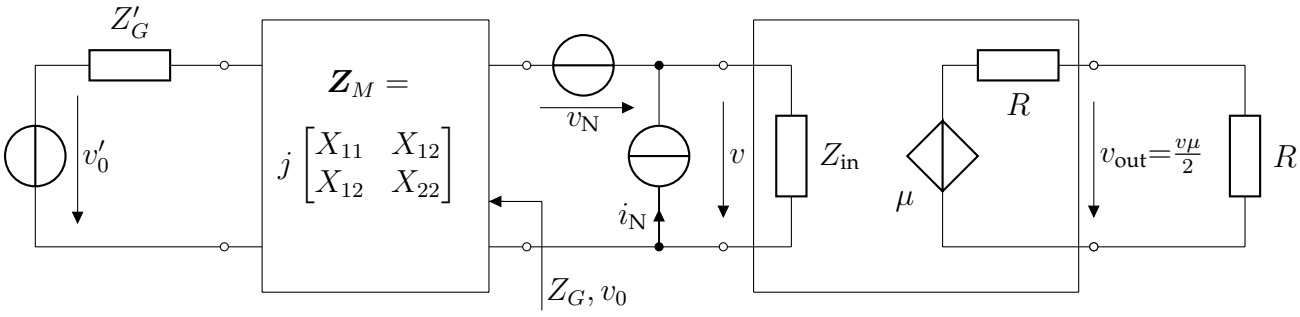

Fig. 6.5. LNA model driven by a signal source. The loading effect has been taken into account by the gain μ of the VCVS.

This example shows the basic concept, but there is no need to use ideal terminations. Devices with a known Z_m can be taken, nevertheless the input impedance must not exceed some hundred ohms at system center frequency [58]. To get $\mathrm{E}[|i_\mathrm{N}|^2]$ and $\mathrm{E}[|v_\mathrm{N}|^2]$, two input terminations are needed, they can either be resistive or reactive devices, but noiseless pure reactive ones should be preferred. For getting the imaginary part of the correlation coefficient $\mathrm{Im}\{\rho\}$ a reactive one and a resistive one to determine the real part

$\mathrm{Re}\{\rho\}$ are needed. A good choice for example would be $0\ \Omega, 50\ \Omega, +\mathrm{j}\cdot 50\ \Omega, -\mathrm{j}\cdot 50\ \Omega$. If ever possible, *many more than 4*, for example 10 measurement points should be used in order to improve accuracy, especially for the real part of the complex correlation coefficient $\mathrm{Re}\{\rho\}$. For the same reason it is advisable that several real valued impedances in the range from zero (short circuit) to some hundred ohms are used (e.g. $0\ \Omega, 22\ \Omega, 50\ \Omega, 100\ \Omega$) in conjunction with purely reactive impedance (both capacitive and inductive) (e.g. $\mathrm{j}\cdot[12\ \Omega, 26\ \Omega, 50\ \Omega, 120\ \Omega, -29\ \Omega, -43\ \Omega, -83\ \Omega]$). Note that the relationship between the open circuit voltage gain and the forward transmittance $|S_{21}|$ is given by:

$$\mu = \left(1 + \frac{R}{Z_{\mathrm{in}}}\right)|S_{21}|, \tag{6.21}$$

where R is used as the port reference resistance for specifying the S parameters, so $S_{12} = 0$ and $S_{22} = 0$.

Now, it is assumed that either S_{11} and $|S_{21}|$ or Z_{in} and μ are known from a previous measurement. Measure P_{m} for different values of Z_{m}, say Z_1, Z_2, Z_3 up to Z_M and define the vectors

$$\boldsymbol{p} = [P_1, P_2, P_3, ...P_M]^T, \tag{6.22}$$

$$\boldsymbol{g} = [\mathrm{Re}\{Z_1\}, \mathrm{Re}\{Z_2\}, \mathrm{Re}\{Z_3\}, ...\mathrm{Re}\{Z_M\}]^T, \tag{6.23}$$

$$\boldsymbol{g}_m = \left[|Z_{\mathrm{m}}|^2, 1, -2\mathrm{Re}\{Z_{\mathrm{m}}\}, -2\mathrm{Im}\{Z_{\mathrm{m}}\}\right]^T, \tag{6.24}$$

as well as the matrices:

$$\boldsymbol{G} = \begin{bmatrix} \boldsymbol{g_1^T} \\ \boldsymbol{g_2^T} \\ \boldsymbol{...} \\ \boldsymbol{g_M^T} \end{bmatrix} \tag{6.25}$$

$$\boldsymbol{\Phi} = \mathrm{diag}_{m=1}^{M} \left|\frac{1}{Z_{\mathrm{m}} + Z_{\mathrm{in}}}\right|^2. \tag{6.26}$$

With the help of these considerations the vector $\boldsymbol{p}$ can compactly be written as

$$\boldsymbol{p} = \frac{|Z_{\mathrm{in}}|^2|\mu|^2}{4R}\boldsymbol{\Phi}\left(\boldsymbol{G\theta} + 4\mathrm{k}T\Delta f\boldsymbol{g}\right), \tag{6.27}$$

where the noise parameters are put into the vector

$$\boldsymbol{\theta} = \left[\mathrm{E}[|i_{\mathrm{N}}|^2], \mathrm{E}[|v_{\mathrm{N}}|^2], \mathrm{Re}\{\mathrm{E}[|v_{\mathrm{N}}i_N^*|]\}, \mathrm{Im}\{\mathrm{E}[|v_{\mathrm{N}}i_N^*|]\}\right]. \tag{6.28}$$

6.2.1 Least Squares

Provided, that $\det(\boldsymbol{G}^{\mathrm{H}}\boldsymbol{G}) \neq 0$, one can solve this system of linear equations uniquely for $\boldsymbol{\theta}$ in the least square sense:

$$\boldsymbol{\theta}_{\mathrm{LS}} = \boldsymbol{G}^{+}\left(\frac{4R}{|Z_{\mathrm{in}}|^2|\mu|^2}\boldsymbol{\Phi}^{-1}\boldsymbol{p} - 4\mathrm{k}T\Delta f\boldsymbol{g}\right). \tag{6.29}$$

This means taking a starting value for Z_{in} or S_{11}, calculating the stochastic parameters, then recalculating the power $\boldsymbol{p}_{\mathrm{c}}$ based on these stochastic parameters for each termination.

With respect to Z_{in} this nonlinear system of equations can be solved and optimized for the lowest error $||\boldsymbol{p}_{\text{c}} - \boldsymbol{p}||_2^2$. The right value for Z_{in} is found when

$$Z_{\text{in}} = \arg\min_{Z_{\text{in}}} ||\boldsymbol{p}_{\text{c}} - \boldsymbol{p}||_2^2 \tag{6.30}$$

is solved.

6.2.2 Selected Tuples

A very interesting and realistic scenario is that e.g. a single measurement point is corrupted by electromagnetic interference or a defective termination. Assume just one value of measured power is wrong, the accuracy of the whole method would suffer. By selecting 4- tuples of P_{m} the corrupted measurement point can be properly identified. At least four different valued terminations are needed for determining four parameters, now a fifth impedance Z_5 is connected to the input. The output power becomes

$$P_5 = \frac{|Z_{\text{in}}|^2|A|^2}{4R|Z_5 + Z_{\text{in}}|^2}\left(4kT\Delta f\text{Re}\{Z_5\} + \boldsymbol{g}_5^T\boldsymbol{\theta}\right) \tag{6.31}$$

Substituting (6.29) in (6.31) it is obtained

$$\begin{aligned} P_5 = &\frac{1}{|Z_5 + Z_{\text{in}}|^2}\cdot \\ &\left(\frac{|Z_{\text{in}}|^2|\mu|^2kT\Delta f}{R}(\text{Re}\{Z_5\} - \boldsymbol{g}_5^T\boldsymbol{G}^{-1}\boldsymbol{g}) + \boldsymbol{g}_5^T\boldsymbol{G}^{-1}\boldsymbol{\Phi}^{-1}\boldsymbol{p}\right) \end{aligned} \tag{6.32}$$

and because

$$\text{Re}\{Z_5\} - \boldsymbol{g}_5^T\boldsymbol{G}^{-1}\boldsymbol{g} = 0, \tag{6.33}$$

it follows

$$P_5 = \frac{\boldsymbol{g}_5^T\boldsymbol{G}^{-1}\boldsymbol{\Phi}^{-1}\boldsymbol{p}}{|Z_5 + Z_{\text{in}}|^2}. \tag{6.34}$$

Note that once one set of these noise parameters $\boldsymbol{\theta}$ is known, the power P does *not* depend on the open circuit voltage gain μ anymore. That is why it is required that $|\mu|^2$ must be determined separately from a measurement of the amplifier's $|S_{21}|$ and an application of (6.21). However, Z_{in} can be determined from further measurement points of the output power. Because Z_{in} consists of two real quantities, at last one more impedance, Z_6 with its corresponding output power

$$P_6 = \frac{\boldsymbol{g}_6^T\boldsymbol{G}^{-1}\boldsymbol{\Phi}^{-1}\boldsymbol{p}}{|Z_6 + Z_{\text{in}}|^2} \tag{6.35}$$

is required. However, note from (6.35) and from the definition of $\boldsymbol{\Phi}$ in (6.26) that the output power depends on Z_{in} in a quadratic way. This may lead to multiple solutions from which one has to select the right one. This process can be simplified by requiring one more input impedance, Z_7 with corresponding output power.

$$P_7 = \frac{\boldsymbol{g}_7^T\boldsymbol{G}^{-1}\boldsymbol{\Phi}^{-1}\boldsymbol{p}}{|Z_7 + Z_{\text{in}}|^2}. \tag{6.36}$$

This resolves the ambiguities and there is a unique solution for Z_{in}. The solution of (6.31), (6.35) and (6.36), being a system of nonlinear equations, is rather involved analytically. Thus, it is proposed to simply solve it numerically:

$$Z_{\text{in}} = \arg\min_{Z_{\text{in}}} \sum_{m=5}^{7} \left(P_{\text{m}} - \frac{\boldsymbol{g}_7^T \boldsymbol{G}^{-1} \boldsymbol{\Phi}^{-1} \boldsymbol{p}}{|Z_7 + Z_{\text{in}}|^2} \right). \tag{6.37}$$

In total 7 impedance points are needed: $P_1, ..., P_7$ for seven impedances $Z_1, ..., Z_7$ in order to obtain Z_{in} numerically from (6.37), and afterwards the noise parameters from (6.29) with $|\mu|^2$ determined from (6.21) with the help of the value of Z_{in} (6.30) and a-priori knowledge of $|S_{21}|$. The accuracy of the measurement can be considerably improved if one uses more than 7 measurement measurement points of output power obtained from a wide range of different termination impedances. One can directly use the presented results in (6.37) and (6.29) if one chooses random combinations of 7 measurement points from the set of $M > 7$ measurement points, and computes estimates for Z_{in} and $\boldsymbol{\theta}$ from an appropriate averaging over the results obtained in the first step. An appropriate averaging in a two step procedure is proposed. First a selection of parameters is made such that only those parameters are chosen which jointly lie within the range of half the data centers around the respective median value. Second, an arithmetic mean is performed over the selection from the first step. For a precise formulation, the functionals are defined:

$$\text{Lo}(x, n) = a, \text{ such that} |\{x | x \leq a\}| = \frac{n}{4} \tag{6.38}$$

$$\text{Hi}(x, n) = a, \text{ such that} |\{x | x \geq a\}| = \frac{n}{4}. \tag{6.39}$$

Then the selection of Z_{in} from a number of K values is given by the list

$$\begin{aligned} (Z_{\text{in}} | (Lo(\text{Re}\{Z_{\text{in}}\}, K) \leq \text{Re}\{Z_{\text{in}}\} \leq Hi(\text{Re}\{Z_{\text{in}}\}, K)) \\ \wedge (Lo(\text{Im}\{Z_{\text{in}}\}, K) \leq \text{Im}\{Z_{\text{in}}\} \leq Hi(\text{Im}\{Z_{\text{in}}\}, K)))) \\ = \mathcal{L}_{Z_{\text{in}}} \end{aligned} \tag{6.40}$$

The final estimate of Z_{in} is then obtained by taking the arithmetic mean over the selection:

$$\bar{Z}_{in} = \text{mean}_{\mathcal{L}_{Z_{\text{in}}}} Z_{\text{in}}. \tag{6.41}$$

For the noise parameters one has similarly

$$\begin{aligned} \mathcal{L}_{\boldsymbol{\theta}} = (\boldsymbol{\theta} | (Lo(\theta_1, K') \leq \theta_1 \leq Hi(\theta_1, K')) \wedge \\ (Lo(\theta_2, K') \leq \theta_2 \leq Hi(\theta_2, K')) \wedge \\ (Lo(\theta_3, K') \leq \theta_3 \leq Hi(\theta_3, K')) \wedge \\ (Lo(\theta_4, K') \leq \theta_4 \leq Hi(\theta_4, K'))), \end{aligned} \tag{6.42}$$

where K' is the number of random selections of measurement tuples chosen to estimate $\boldsymbol{\theta}$. The final estimate of $\boldsymbol{\theta}$ is then obtained by taking the *arithmetic mean* over the selection:

$$\bar{\boldsymbol{\theta}} = \text{mean}_{\mathcal{L}_{\boldsymbol{\theta}}} \boldsymbol{\theta}. \tag{6.43}$$

A number of measurement points $M = 25$ is recommended, where about half should be essentially real valued with resistances ranging from 0 to about $200\ \Omega$. The other half should be reactive (both capacitive and inductive) with impedances in a similar range as the resistive impedances. A suitable choice for K and K' is

$$K = 10^3,\ K' = 10^4. \tag{6.44}$$

6.2.3 Static Failure of Forward Gain

Now $|S_{21}|$ is assumed to be wrongly estimated, which leads to an erroneous $|\mu|^2$. κ is the ratio between $|\mu_t|^2$, the true forward gain of the amplifier and $|\mu|^2$, the measured gain of the amplifier

$$\kappa = \frac{|\mu_t|^2}{|\mu|^2}. \tag{6.45}$$

When solving (6.29), both variances will also be scaled with κ

$$\kappa = \frac{\mathrm{E}[|i_N|^2]}{\mathrm{E}[|i_{Nt}|^2]} = \frac{\mathrm{E}[|v_N|^2]}{\mathrm{E}[|v_{Nt}|^2]} = \frac{|\mu_t|^2}{|\mu|^2}. \tag{6.46}$$

Imagine, the output of the low noise amplifier was connected to an ideal noiseless variable gain amplifier (VGA) with $S_{12} = 0$, so that the LNA sees the same impedance as output load as before. In this example Z_{opt} and Z_{in} remain unchanged, independent of the adjusted VGA gain. According to (6.30), R_N and $\mathrm{Im}\{\rho\}$ stay unchanged. $\mathrm{Re}\{\rho\}$ is calculated in dependence of the true value $\mathrm{Re}\{\rho_t\}$

$$\mathrm{Re}\{\rho\} = \mathrm{Re}\{\rho_t\} - 2\left(1 - \frac{1}{\kappa}\right) kT\Delta f \frac{1}{\mathrm{E}[|v_{Nt}|^2]\mathrm{E}[|i_{Nt}|^2]}. \tag{6.47}$$

(6.47) is put into (6.7) to show effects on the noise figure

$$\begin{aligned} \mathrm{NF} &= 1 + \kappa \frac{\mathrm{E}[|i_N|^2]R_N}{2kT\Delta f} \cdot \left(\sqrt{1 - (\mathrm{Im}\{\rho_t\})^2} - \mathrm{Re}\{\rho_t\}\right) \\ &\quad + \kappa(1 - \frac{1}{\kappa}) \\ &= \kappa \mathrm{NF}_t. \end{aligned} \tag{6.48}$$

If the forward gain is estimated in a wrong way, the input noise is certainly amplified with the true $|\mu_t|^2$ and the noise figure NF is calculated with $|\mu|^2$. So the calculated noise figure NF is also scaled with κ

$$\mathrm{NF} = \kappa \mathrm{NF}_t = \frac{|\mu_t|^2}{|\mu|^2} \cdot \mathrm{NF}_t. \tag{6.49}$$

With (6.46) and (6.48) $\mathrm{Re}\{\rho\}$ is calculated out of (6.7), where R_N and $\mathrm{Im}\{\rho\}$ remain constant and independent of κ:

$$\mathrm{Re}\{\rho\} = \sqrt{1 - \mathrm{Im}\{\rho_t\}^2} - \frac{2kT\Delta f}{\mathrm{E}[|i_{Nt}|^2]R_N} \cdot (\mathrm{NF}_t - \frac{1}{\kappa}) \tag{6.50}$$

With both variances vanishingly small in extreme low noise amplifiers $\mathrm{Re}\{\rho\}$ is very sensitive and reaches unbelievably huge values if $|\mu|^2$ is estimated a bit too small. If $|\mu|^2$ is estimated too big in this case and the input noise power calculated out of the measured output power would reach even lower values than thermal noise power, then there exists no solution for $\mathrm{Re}\{\rho\}$.

$$\frac{\partial \mathrm{Re}\{\rho\}}{\partial \kappa} = -\frac{2kT\Delta f}{\mathrm{E}[|i_{Nt}|^2]R_N} \cdot \frac{1}{\kappa^2} \tag{6.51}$$

As the derivation shows, the most difficult quantity to measure for very extreme low noise amplifiers certainly is $\mathrm{Re}\{\rho\}$. In a high noise amplifier, where $kT\Delta f$ is negligible, $\mathrm{Re}\{\rho\}$ is insensitive for gain errors. According to these considerations, getting $\mathrm{Im}\{\rho\}$ and R_N is no problem for both kinds of amplifiers. The interesting result is, that noise matching and power matching can be implemented without knowing $|S_{21}|$.

6.2.4 Broadband Systems

Many LNAs are used in narrow band receivers. In such a narrow band, noise spectral density can be assumed to be constant over frequency. For applications, where this assumption does not work, e.g. broad band systems, the broad band can always be divided into narrow bands. In practice the noise power vector $\boldsymbol{p}$ would be measured with a spectrum analyzer. By simply enabling the sweep mode, one gets $\boldsymbol{p}(f)$ and after applying the proposed algorithm each noise parameter is available as function of frequency: $\mathrm{E}[|v_\mathrm{N}(f)|^2]$, $\mathrm{E}[|i_\mathrm{N}(f)|^2]$, $\mathrm{Re}\{\rho(f)\}$, $\mathrm{Im}\{\rho(f)\}$.

6.3 Simulation

The two methods to determine the noise parameters (6.28) are very different in their sensitivity to a few erroneous measurements due to a defective termination (e.g. a broken soldering point or a short or an electromagnetic interference). To demonstrate the superiority of the selected tuples method with respect to such outliers a simulation scenario has been set up with following true parameters in Table 6.1. Power measurements are taken with 10 resistive and 10 reactive terminations which then are used as input both for the least squares and for the selected tuples method.

Parameter	Value
T	$300\ \mathrm{K}$
k	$1.38 \cdot 10^{-23}\ \frac{\mathrm{VAs}}{\mathrm{K}}$
Δf	$1\ \mathrm{MHz}$
R	$50\ \Omega$
$\lvert S_{21}\rvert$	7.7
$\mathrm{E}[\lvert v_\mathrm{N}\rvert^2]$	$6 \cdot 10^{-14}\ \mathrm{V}^2$
$\mathrm{E}[\lvert i_\mathrm{N}\rvert^2]$	$3 \cdot 10^{-16}\ \mathrm{A}^2$
R_N	$14.14\ \Omega$
$\mathrm{Re}\{\rho\}$	-0.35
$\mathrm{Im}\{\rho\}$	0.7
Z_in	$(85 - \mathrm{j} \cdot 40)\ \Omega$

Table 6.1. Setup parameters for the simulation

To emulate an outlier, one of the power values has been increased by $4\ \mathrm{dB}$. Such an outlier has quite a dramatic effect on results obtained with the least squares method, see Table 6.2, but almost no effect, if the selected tuples method is used, see Table 6.3.

The latter method is quite robust and has automatically removed the outlier in the selection process.

Parameter	Value
$\mathrm{E}[\lvert i_\mathrm{N}\rvert^2]$	$2.807 \cdot 10^{-16}$ A^2
R_N	20.916 Ω
$\mathrm{Re}\{\rho\}$	-0.1565
$\mathrm{Im}\{\rho\}$	0.4768
Z_in	$(98.02 - \mathrm{j} \cdot 46.13)$ Ω

Table 6.2. Solved by least squares

Parameter	Value
$\mathrm{E}[\lvert i_\mathrm{N}\rvert^2]$	$3.0003 \cdot 10^{-16}$ A^2
R_N	14.139 Ω
$\mathrm{Re}\{\rho\}$	-0.3499
$\mathrm{Im}\{\rho\}$	0.700
Z_in	$(84.99 - \mathrm{j} \cdot 39.99)$ Ω

Table 6.3. Solved by selected tuples

6.4 Measurement

6.4.1 The Spectrum Analyzer

For the measurement an EMI test receiver, a special kind of low noise spectrum analyzer, has been used as power meter, Fig. 6.6. For example the Rhode & Schwarz ESCS reaches its highest performance at a noise bandwidth of 0.74 MHz. For the measurement, the A-band, which is identical to the former VHF band, was chosen.

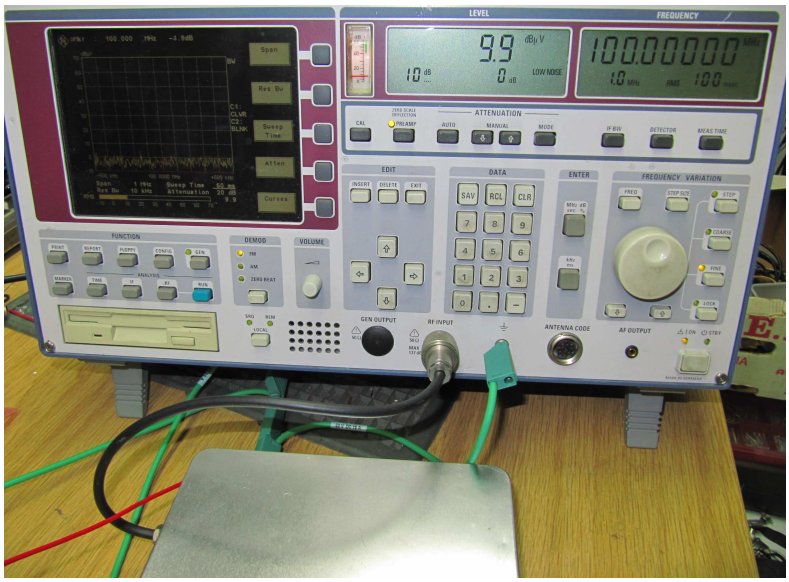

Fig. 6.6. Spectrum analyzer connected to amplifier box

6.4.2 Terminations

At frequencies around 100 MHz, lumped elements with a quality factor of 100 and even more are available. The terminations are connected to the amplifier by sub miniature version A (SMA) connectors. Each termination is mounted on its own SMA connector, see Fig. 6.7. Inductors were implemented as coils of 3 mm diameter made of 0.3 mm^2 silver wire, as capacitances RF ceramic capacitors have been used. Each resistive termination was compensated for this frequency band.

Fig. 6.7. Terminations

6.4.3 Cloning Amplifiers

Out of 150 pieces three transistors, BFT66, have been selected with equal current gain β and base to emitter forward voltage V_{be}. Three amplifiers have been built with almost identical parameters.

These amplifiers and two with quite different statistic parameters have been characterized in the following way with very good results: The RF encapsulated amplifier is put in an EMI shielded box. Shielding of cables and boxes have been tested with a RF Power transmitter to be sure there will be no electromagnetic interference, see Fig. 6.8.

6.4.4 Measuring Power

Parameter	Value
T	290 K
k	$1.38 \cdot 10^{-23}\ \frac{\text{VAs}}{\text{K}}$
Δf	0.74 MHz
R	50 Ω
Z_{in}	$(186 - \text{j}31.6)\ \Omega$
$\lvert S_{21}\rvert$	9.55

Table 6.4. System parameters

Parameter	Value
$\text{E}[\lvert v_{\text{N}}\rvert^2]$	$2.968 \cdot 10^{-13}\ \text{V}^2$
$\text{E}[\lvert i_{\text{N}}\rvert^2]$	$2.844 \cdot 10^{-17}\ \text{A}^2$
$\text{Re}\{\rho\}$	0.2730
$\text{Im}\{\rho\}$	0.1793
R_{N}	102 Ω

Table 6.5. Absolute amplifier parameter

First the system parameters seen in Table 6.4. Z_{in} and $|S_{21}|$ are determined in a previous measurement with a network analyzer. In the next step the output power is measured for each termination, a least square fit for $\boldsymbol{\theta}$ is done and finally $\boldsymbol{p}$ is calculated, Table 6.8,

then. The squared difference between calculated and measured power is minimized to get Z_{in}.

Z_{m}	u_{out}	p_{out}
$100\ \Omega$	$14.0\ \text{dB}\mu\text{V}$	$5.0 \cdot 10^{-13}\text{W}$
$50\ \Omega$	$13.0\ \text{dB}\mu\text{V}$	$4.0 \cdot 10^{-13}\text{W}$
$22\ \Omega$	$12.0\ \text{dB}\mu\text{V}$	$3.2 \cdot 10^{-13}\text{W}$
$0\ \Omega$	$10.3\ \text{dB}\mu\ \text{V}$	$2.1 \cdot 10^{-13}\text{W}$
$-\text{j} \cdot 29\ \Omega$	$10.7\ \text{dB}\mu\text{V}$	$2.3 \cdot 10^{-13}\text{W}$
$-\text{j} \cdot 43\ \Omega$	$10.9\ \text{dB}\mu\text{V}$	$2.5 \cdot 10^{-13}\text{W}$
$-\text{j} \cdot 83\ \Omega$	$12.0\ \text{dB}\mu\text{V}$	$3.2 \cdot 10^{-13}\text{W}$
$+\text{j} \cdot 12\ \Omega$	$10.3\ \text{dB}\mu\text{V}$	$2.1 \cdot 10^{-13}\text{W}$
$+\text{j} \cdot 26\ \Omega$	$10.4\ \text{dB}\mu\text{V}$	$2.2 \cdot 10^{-13}\text{W}$
$+\text{j} \cdot 50\ \Omega$	$10.7\ \text{dB}\mu\text{V}$	$2.4 \cdot 10^{-13}\text{W}$
$+\text{j} \cdot 120\ \Omega$	$12.5\ \text{dB}\mu\text{V}$	$3.6 \cdot 10^{-13}\text{W}$

Table 6.6. Output measurement

Termination	Amplifier 1	Amplifier 2
$122\ \Omega$	$14.23\ \text{dB}\mu\text{V}$	$14.43\ \text{dB}\mu\text{V}$
$100\ \Omega$	$14.08\ \text{dB}\mu\text{V}$	$14.23\ \text{dB}\mu\text{V}$
$50\ \Omega$	$13.23\ \text{dB}\mu\text{V}$	$13.38\ \text{dB}\mu\text{V}$
$22\ \Omega$	$12.23\ \text{dB}\mu\text{V}$	$12.48\ \text{dB}\mu\text{V}$
$0\ \Omega$	$10.73\ \text{dB}\mu\ \text{V}$	$10.88\ \text{dB}\mu\text{V}$
6.4 pF	$14.23\ \text{dB}\mu\text{V}$	$14.43\ \text{dB}\mu\text{V}$
11 pF	$13.38\ \text{dB}\mu\text{V}$	$13.58\ \text{dB}\mu\text{V}$
17 pF	$12.63\ \text{dB}\mu\text{V}$	$12.73\ \text{dB}\mu\text{V}$
20 pF	$12.43\ \text{dB}\mu\text{V}$	$12.53\ \text{dB}\mu\text{V}$
24 pF	$12.03\ \text{dB}\mu\text{V}$	$12.23\ \text{dB}\mu\text{V}$
38 pF	$11.53\ \text{dB}\mu\text{V}$	$11.48\ \text{dB}\mu\text{V}$
53 pF	$11.23\ \text{dB}\mu\text{V}$	$11.23\ \text{dB}\mu\text{V}$
72 pF	$11.13\ \text{dB}\mu\text{V}$	$11.23\ \text{dB}\mu\text{V}$
85 pF	$11.08\ \text{dB}\mu\text{V}$	$11.18\ \text{dB}\mu\text{V}$
103 pF	$11.03\ \text{dB}\mu\text{V}$	$11.13\ \text{dB}\mu\text{V}$
21 nH	$10.78\ \text{dB}\mu\text{V}$	$10.93\ \text{dB}\mu\text{V}$
32 nH	$10.78\ \text{dB}\mu\text{V}$	$10.88\ \text{dB}\mu\text{V}$
45 nH	$10.83\ \text{dB}\mu\text{V}$	$10.78\ \text{dB}\mu\text{V}$
81 nH	$10.98\ \text{dB}\mu\text{V}$	$11.08\ \text{dB}\mu\text{V}$
115 nH	$11.28\ \text{dB}\mu\text{V}$	$11.28\ \text{dB}\mu\text{V}$
145 nH	$11.68\ \text{dB}\mu\text{V}$	$11.68\ \text{dB}\mu\text{V}$
189 nH	$12.18\ \text{dB}\mu\text{V}$	$12.18\ \text{dB}\mu\text{V}$
240 nH	$13.13\ \text{dB}\mu\text{V}$	$12.98\ \text{dB}\mu\text{V}$

Table 6.7. Output measurement comparison

To validate the theory, the output power is now calculated according to (6.27) for each termination and compared to the measurement values. With these parameters shown in Table 6.5 the output power is calculated for any termination and the noise figure for any kind of matching network. The difference between measured power and power calculated is very small, Table 6.8, the test has been repeated several times with similar good results. With this method low noise amplifiers can be characterized in a quick and precise way. This powerful method helps improving both matching networks and amplifiers. Now, noise resistance and noise figure are determined. Here are the noise figure for noise matching NF_{min}, the required generator's impedance for noise matching Z_{NM} and the noise figure for power matching NF_{PM} calculated from these parameters, Z_{PM} is the impedance required for power matching, Table 6.9.

6.4.5 Outlook to MIMO Systems

A second amplifier with almost equal noise parameters was measured, Table 6.7 shows the output power measurement $P(Z_{\text{m}})$ at 90 MHz for $M = 23$ terminations. In a MIMO case, there will be several equal low noise amplifiers, so before starting the described algorithm at least two different kinds of fault check could be implemented. First the

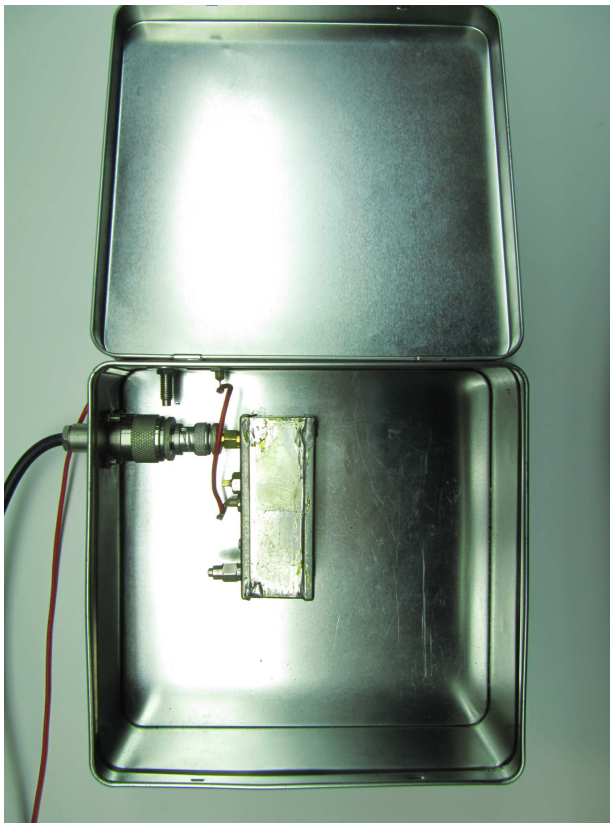

Fig. 6.8. Amplifier in a box

Z_{m}	Measurement	Calculation	Difference
$100\ \Omega$	$14.0\ \mathrm{dB}\mu\mathrm{V}$	$13.9969\ \mathrm{dB}\mu\mathrm{V}$	$-0.0031\ \mathrm{dB}$
$50\ \Omega$	$13.0\ \mathrm{dB}\mu\mathrm{V}$	$13.0286\ \mathrm{dB}\mu\mathrm{V}$	$+0.0286\ \mathrm{dB}$
$22\ \Omega$	$12.0\ \mathrm{dB}\mu\mathrm{V}$	$11.9473\ \mathrm{dB}\mu\mathrm{V}$	$-0.0527\ \mathrm{dB}$
$0\ \Omega$	$10.3\ \mathrm{dB}\mu\ \mathrm{V}$	$10.3236\ \mathrm{dB}\mu\mathrm{V}$	$+0.0236\ \mathrm{dB}$
$-\mathrm{j}\cdot 29\ \Omega$	$10.7\ \mathrm{dB}\mu\mathrm{V}$	$10.7258\ \mathrm{dB}\mu\mathrm{V}$	$+0.0258\ \mathrm{dB}$
$-\mathrm{j}\cdot 43\ \Omega$	$10.9\ \mathrm{dB}\mu\mathrm{V}$	$11.0177\ \mathrm{dB}\mu\mathrm{V}$	$+0.1177\ \mathrm{dB}$
$-\mathrm{j}\cdot 83\ \Omega$	$12.0\ \mathrm{dB}\mu\mathrm{V}$	$11.9358\ \mathrm{dB}\mu\mathrm{V}$	$-0.0642\ \mathrm{dB}$
$+\mathrm{j}\cdot 12\ \Omega$	$10.3\ \mathrm{dB}\mu\mathrm{V}$	$10.2800\ \mathrm{dB}\mu\mathrm{V}$	$-0.0200\ \mathrm{dB}$
$+\mathrm{j}\cdot 26\ \Omega$	$10.4\ \mathrm{dB}\mu\mathrm{V}$	$10.3389\ \mathrm{dB}\mu\mathrm{V}$	$-0.0611\ \mathrm{dB}$
$+\mathrm{j}\cdot 50\ \Omega$	$10.7\ \mathrm{dB}\mu\mathrm{V}$	$10.6965\ \mathrm{dB}\mu\mathrm{V}$	$-0.0035\ \mathrm{dB}$
$+\mathrm{j}\cdot 120\ \Omega$	$12.5\ \mathrm{dB}\mu\mathrm{V}$	$12.5135\ \mathrm{dB}\mu\mathrm{V}$	$+0.0135\ \mathrm{dB}$

Table 6.8. Measurement Results

Parameter	Value
$\mathrm{NF}_{\mathrm{min}}$	$1.3\ \mathrm{dB}$
Z_{NM}	$(100 + \mathrm{j}\cdot 18)\ \Omega$
$\mathrm{NF}_{\mathrm{PM}}$	$1.7\ \mathrm{dB}$
Z_{PM}	$(186 + \mathrm{j}\cdot 31.6)\ \Omega$

Table 6.9. Noise figures and source impedances

new amplifier can be compared to other amplifiers: Fig. 6.9 shows the output power $P(Z_\mathrm{m})$ for each pure imaginary valued termination and Fig. 6.10 for each pure real valued termination of three amplifiers of the same type. Here, the power contribution of the noise current source is dominating, so the output power reaches its lowest value near $Z_\mathrm{m} = 0\,\Omega$. When looking at the power measurement, e.g. Table 6.8 predictions about the correlation can be done: There is a minimum for $+\mathrm{j}\cdot 12\,\Omega$, so $\mathrm{Im}\{\rho\}$ must be small and positive valued, if it was negative, the minimum would be seen for the capacitive terminations. The values for the terminations should not exceed a few hundred ohms, because the curves get too flat or in other words the gradient of the function $P(Z_\mathrm{m})$ gets too low, Fig. 6.10.

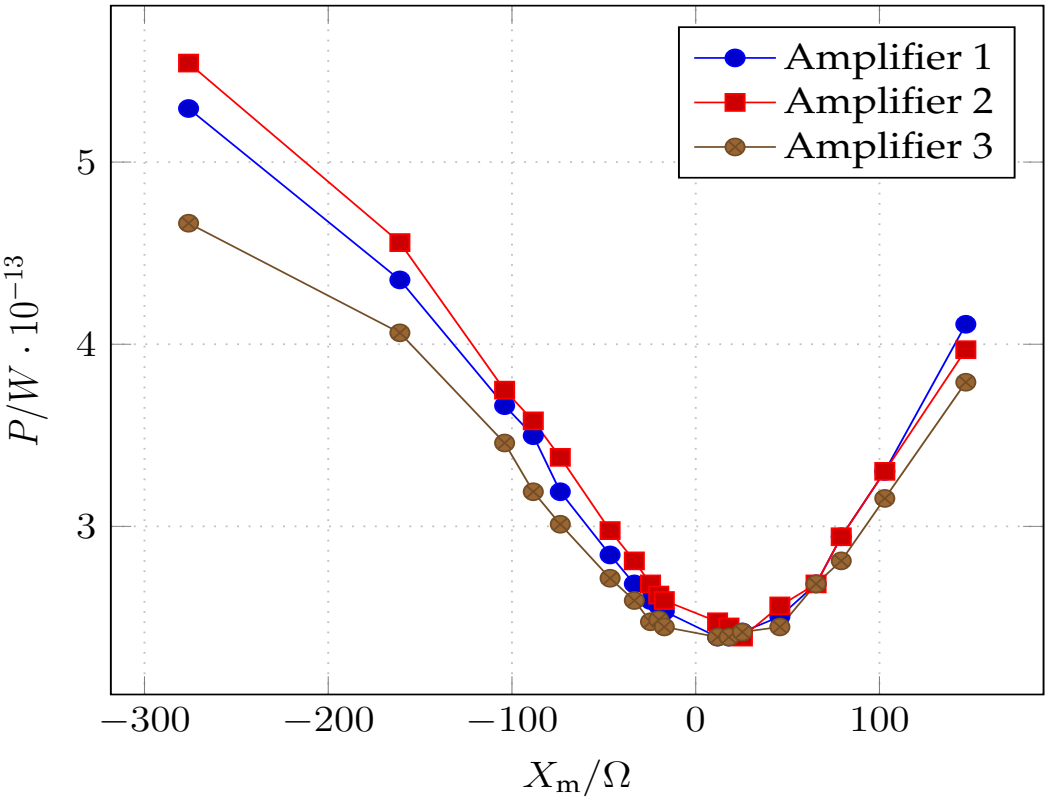

Fig. 6.9. P_m for imaginary valued terminations at 90 MHz

6.4.6 Identifying Corrupted Points of Measurement

One idea is taking two neighbor values, when resistance or reactance values are very close to each other, then the expected power values can also not vary in a big range and a tolerance limit Δ can be defined. Either for

$$X_{\mathrm{m}-1} = X_\mathrm{m} = X_{\mathrm{m}+1} \wedge R_{\mathrm{m}-1} \leq R_\mathrm{m} \leq R_{\mathrm{m}+1}, \tag{6.52}$$

or for

$$R_{\mathrm{m}-1} = R_\mathrm{m} = R_{\mathrm{m}+1} \wedge X'_{\mathrm{m}-1} \leq X_\mathrm{m} \leq X_{\mathrm{m}+1}, \tag{6.53}$$

$$\Delta \geq \left| \frac{P(Z_{\mathrm{m}-1}) + P(Z_{\mathrm{m}+1})}{2} - P(Z_\mathrm{m}) \right| \tag{6.54}$$

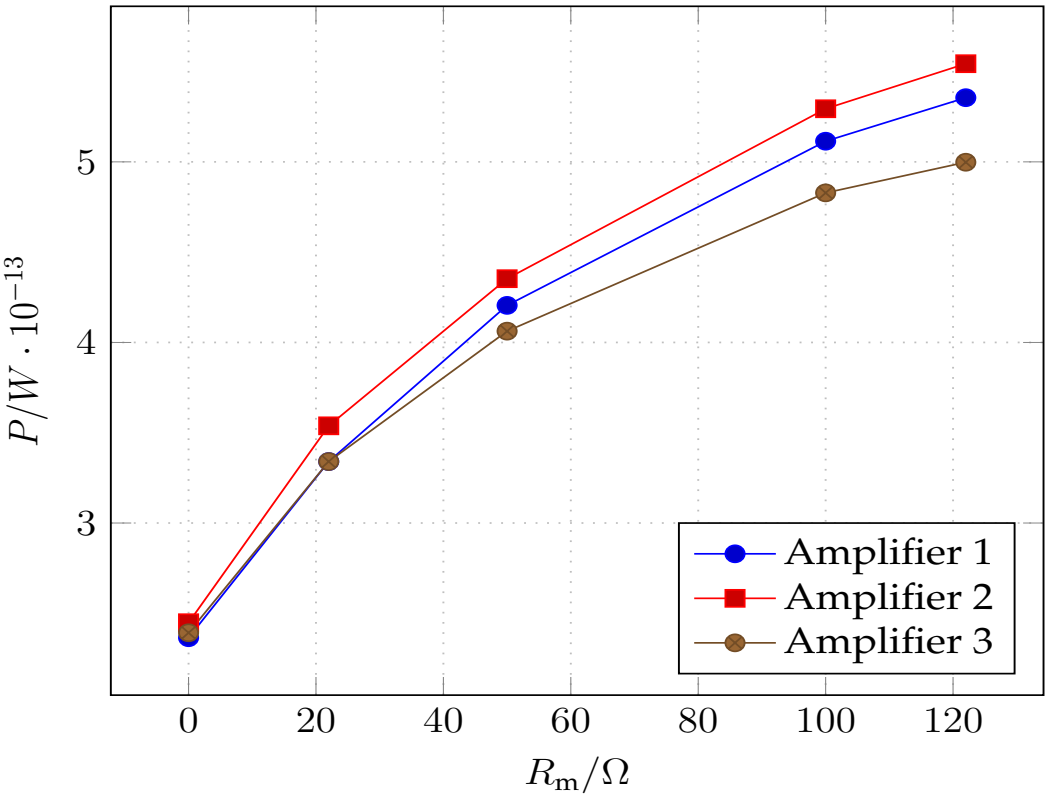

Fig. 6.10. P_m for real valued terminations at 90 MHz

can be applied. If L amplifiers are known, one can set a second tolerance limit Δ_F and each measurement that produced an outlier can be repeated and for example faulty terminations be identified, leading to a wrong value for P_x.

$$\Delta_F \geq \left| \frac{\sum_{l=0}^{L} P(Z_{lm})}{L} - P_x \right| \tag{6.55}$$

6.4.7 Accuracy

The accuracy of the spectrum analyzer is limited to 0.1 dB according to its data sheet. How many measurement points are needed to reach this limit? This analysis is done for the four stochastic parameters and an overdetermined system of the equations (6.29), tuples of 5 to 15 points of measurement out of 23 points and the calculation of the mean error $|\Delta P|$, Fig. 6.11. In other words: There are subsets of measurements with only 5, 6, 7,...15 terminations and the error compared to using all 23 measurements shows, that from 13 measurements in a tuple no further improvement of accuracy is achieved.

According to Fig. 6.11, 12 measurement points with both resistive and reactive terminations altogether would be a good choice. The accuracy of the characterization of the current noise source rises faster than for the voltage source, because the current source mainly influences the output power.

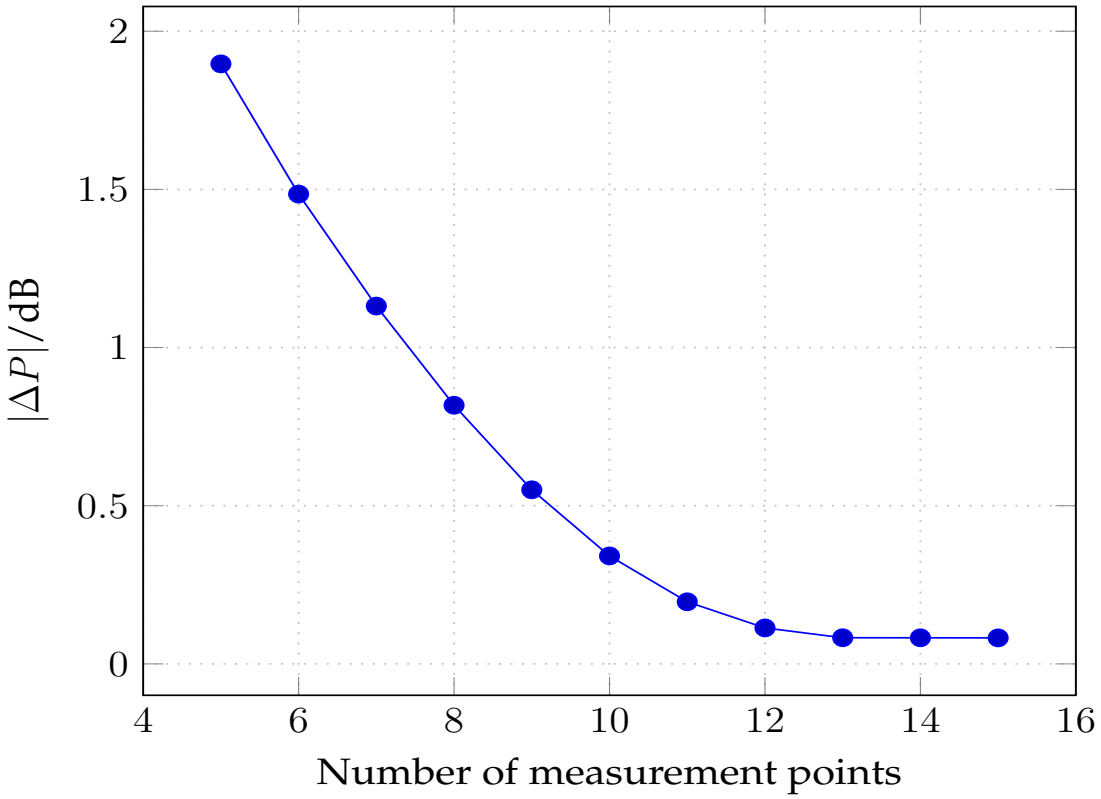

Fig. 6.11. Mean error

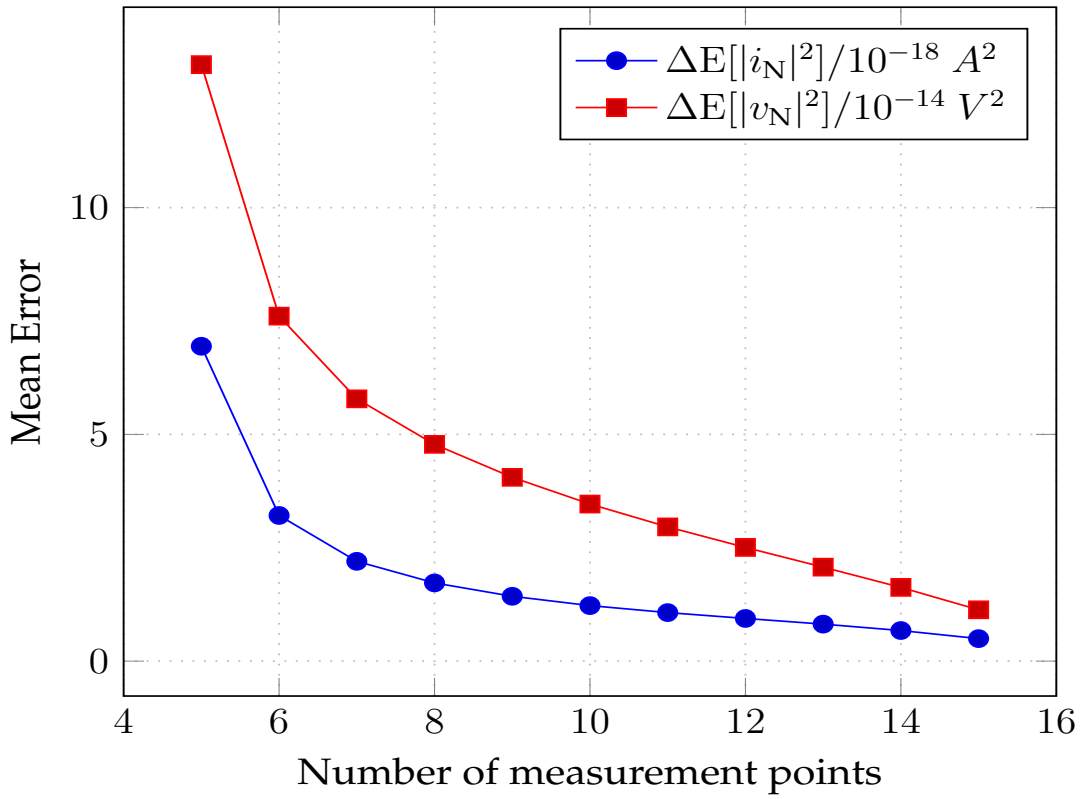

Fig. 6.12. Mean error of $\mathrm{E}[|v_\mathrm{N}|^2]$ and $\mathrm{E}[|i_\mathrm{N}|^2]$

6.5 Conclusion

In this chapter, a novel measurement technique and two methods of calculation, least squares and *selected tuples*, for stochastic and deterministic parameters of a low noise amplifier have been presented. No special input matching two port is necessary as in former established concepts. As proof of this new concept, a simulation, a comparison of both methods and the measurement results for three amplifiers have been shown. Therefore, stochastic parameters $\mathrm{E}[|v_\mathrm{N}|^2], \mathrm{E}[|i_\mathrm{N}|^2], \mathrm{Re}\{\rho\}, \mathrm{Im}\{\rho\}$ have been determined by least squares method for output power measurement points with different input terminations. The expected output power for each termination has been recalculated out of all calculated parameters and compared to the measurement. Numerically solving the nonlinear system of equations led to Z_in *at an extreme low power*. With these parameters, the noise figure is determined for any impedance. Near center frequency, the parameters are stable for a well designed amplifier, usually a measurement at one carrier frequency is enough for designing a typical standard matching network. When sweeping the power meter over frequency, each parameter can be determined as function of frequency. The gain is also determined by measuring at a different noise temperature.

7. Summary

A complete model of the analog parts for a communication receiver and transmitter system and its implementation has been developed. This model includes PA, LNA, DMN and hybrid beam forming. In the first part of this thesis, all well known classes of amplifiers, from A through F, have been discussed and analyzed, which led to new amplifier concepts, class M and N. In modern transceivers, these amplifiers are connected to antenna arrays. As already shown by colleagues and other researchers, therefore a DMN is necessary. As consequence, such a structure was implemented and optimized for efficiency. During this project, a new kind of highly efficient DMN was found. A design algorithm both for a lumped elements DMN and a strip line DMN has been laid out. The topology is usable both for receiver and transmitter purposes, due to its reciprocal behavior. In a complete system, the signal would pass the input of an LNA, after being amplified in the PA, matched in the DMN, transmitted by the array of antennas, received by an antenna array and fed to a DMN once more. As shown, power matching in the receiver's DMN is not necessarily the best strategy for achieving a high SNR. When going for noise matching, the chain gain can decrease and when obtaining power matching, usually more noise power will be amplified. In the most common case, when noise matching and power matching are obtained at two different points of impedance, the highest receiver sensitivity will be achieved with a new kind of matching, we call sensitivity matching. Therefore, a precise knowledge of the amplifier parameters is necessary. An easy new way of measuring these parameters out of the noise power is shown in the last chapter of the main part of this work. The big advantage of the new method is the extreme low hardware effort and its high accuracy. In particular, we can conclude that a transceiver system offers many points to be optimized, even if looking only at analog hardware topics. It will be the decision of design engineers to set up goal functions how the achieved gain in efficiency shall be distributed for lower power consumption, communication cell size and hardware price for example. New generations of researchers will keep on moving the frontier to regimes of higher data throughput, robustness and efficiency, since Heinrich Hertz started his world changing experiments in 1886.

Bibliography

[1] M. Lazarowik, "Anniversary of Birth of James Clerk Maxwell," in *Early day motion 2048*. UK Parliament, 2013.

[2] (2011, April) 1861: James Clerk Maxwell's greatest year. King's College London.

[3] J. C. Maxwell, "A dynamic theory of the electromagnetic field," *Philosophical Transactions of the Royal Society of London*, vol. VIII, pp. 459–511, 1865.

[4] ——, *A Treatise on Electricity and Magnetism*, W. D. Niven, Ed. Oxford, 1873.

[5] I. S. E. C. European Engineering Department, "Pioneers of Electrical Communication Heinrich Rudolf Hertz," *Electrical Communication*, vol. 6, pp. 63–77, 1927.

[6] H. Rukop, *Die Telefunkenröhren und ihre Geschichte*, Telefunken, Ed. Telefunken G. m. b. H., 1928.

[7] R. W. Hull, R. P. Haviland, W. W. Everett, O. N. Minot, and H. O. Stasis, "Correspondence," *IEEE Spectrum*, vol. 1, no. 4, pp. 164–173, April 1964.

[8] B. S. authors, "Abstracts of technical articles by Bell System authors," *The Bell System Technical Journal*, vol. 26, no. 3, pp. 682–690, July 1947.

[9] J. w. Han and M. Meyyappan, "The device made of nothing," *IEEE Spectrum*, vol. 51, no. 7, pp. 30–35, July 2014.

[10] N. O. Sokal, "RF power amplifiers-classes A through F," in *ELECTRO '96. Professional Program. Proceedings.*, Apr 1996, pp. 317–321.

[11] R. G. Harrison, "A Nonlinear Theory of Class C Transistor Amplifiers and Frequency Multipliers," *IEEE Journal of Solid-State Circuits*, vol. 2, no. 3, pp. 93–102, Sept 1967.

[12] J. Slatter, "An Approach to the Design of Transistor Tuned Power Amplifiers," *IEEE Transactions on Circuit Theory*, vol. 12, no. 2, pp. 206–211, Jun 1965.

[13] R. H. Johnston and A. R. Boothroyd, "High-frequency transistor frequency multipliers and power amplifiers," *IEEE Journal of Solid-State Circuits*, vol. 7, no. 1, pp. 81–89, Feb 1972.

[14] M. El-Said, "Analysis of tuned junction-transistor circuits under large sinusoidal voltages in the normal domain-Part II: Tuned power amplifiers and harmonic generators," *IEEE Transactions on Circuit Theory*, vol. 17, no. 1, pp. 13–18, February 1970.

[15] N. O. Sokal and A. D. Sokal, "Class E-A new class of high-efficiency tuned single-ended switching power amplifiers," *IEEE Journal of Solid-State Circuits*, vol. 10, no. 3, pp. 168–176, Jun 1975.

[16] A. Grama and D. Petreus, "A Matlab simulator tool for a class E power amplifier designed to generate plasma torch," in *2012 13th International Conference on Optimization of Electrical and Electronic Equipment (OPTIM)*, May 2012, pp. 1380–1385.

[17] S. Rashid, B. Dupaix, P. Watson, W. Gaber, V. J. Patel, A. Mattamana, S. Dooley, M. LaRue, and W. Khalil, "A Wide-Band Complementary Digital Driver for Pulse Modulated Single-Ended and Differential Bands Class-E PAs in 130 nm GaAs Technology," in *2016 IEEE Compound Semiconductor Integrated Circuit Symposium (CSICS)*, Oct 2016, pp. 1–4.

[18] T. Sowlati, C. A. T. Salama, J. Sitch, G. Rabjohn, and D. Smith, "Low voltage, high efficiency GaAs Class E power amplifiers for wireless transmitters," *IEEE Journal of Solid-State Circuits*, vol. 30, no. 10, pp. 1074–1080, Oct 1995.

[19] W. S. Kopp and S. D. Pritchett, "High efficiency power amplification for microwave and millimeter frequencies," in *IEEE MTT-S International Microwave Symposium Digest*, June 1989, pp. 857–858 vol.3.

[20] L. C. Hall and R. J. Trew, "Maximum efficiency tuning of microwave amplifiers," in *1991 IEEE MTT-S International Microwave Symposium Digest*, July 1991, pp. 123–126 vol.1.

[21] F. J. Martinez-Rodriguez, P. Roblin, Z. Popovic, and J. I. Martinez-Lopez, "Optimal Definition of Class F for Realistic Transistor Models," *IEEE Transactions on Microwave Theory and Techniques*, vol. 65, no. 10, pp. 3585–3595, Oct 2017.

[22] M. Gilasgar, A. Barlabé, and L. Pradell, "Highly efficient class-F RF power amplifiers with very low distortion," *URSI Radio Science Bulletin*, vol. 86, no. 4, pp. 21–31, Dec 2013.

[23] H. C. Chang, P. Roblin, J. A. Galaviz-Aguilar, J. C. N. Pérez, R. Pond, C. Xie, and S. J. Doo, "Asymmetrically-driven current-based chireix class-F power amplifier designed using an embedding device model," in *2017 IEEE MTT-S International Microwave Symposium (IMS)*, June 2017, pp. 940–943.

[24] C. Duvanaud, S. Dietsche, G. Pataut, and J. Obregon, "High-efficient class F GaAs FET amplifiers operating with very low bias voltages for use in mobile telephones at 1.75 GHz," *IEEE Microwave and Guided Wave Letters*, vol. 3, no. 8, pp. 268–270, Aug 1993.

[25] W. J. Chudobiak and D. F. Page, "Frequency and power limitations of Class-D transistor amplifiers," *IEEE Journal of Solid-State Circuits*, vol. 4, no. 1, pp. 25–37, Feb 1969.

[26] W. E. Frank, "New developments in high-frequency power sources," *IEEE Transactions on Industry and General Applications*, vol. IGA-6, no. 1, pp. 29–35, Jan 1970.

[27] S. A. El-Hamamsy, "Design of high-efficiency RF Class-D power amplifier," *IEEE Transactions on Power Electronics*, vol. 9, no. 3, pp. 297–308, May 1994.

[28] C. Schmidt and M. Roeblitz, "A performance comparison of sic power modules with schottky and body diodes," in *PCIM Europe 2017; International Exhibition and Conference for Power Electronics, Intelligent Motion, Renewable Energy and Energy Management*, May 2017, pp. 1–8.

[29] S. Sugimoto, "Ultra-High Speed Diode Switch for 50 GHz Band Utilizing Avalanche Breakdown of Varactor Diodes," in *1968 G-MTT International Microwave Symposium*, May 1968, pp. 91–98.

[30] Y. Amemiya, T. Sugeta, and Y. Mizushima, "Novel low-loss and high-speed diode utilizing an "Ideal" ohmic contact," *IEEE Transactions on Electron Devices*, vol. 29, no. 2, pp. 236–243, Feb 1982.

[31] B. Lehmeyer, M. T. Ivrlač, and J. A. Nossek, "LNA noise parameter measurement," in *Circuit Theory and Design (ECCTD), 2015 European Conference on*, Aug 2015, pp. 1–4.

[32] N. T. Larsen, "A new self-balancing DC-substitution RF power meter," *IEEE Transactions on Instrumentation and Measurement*, vol. IM-25, no. 4, pp. 343–347, Dec 1976.

[33] J. Bastl, "Analysis of Class M Power Amplifier," Master's thesis, 2017.

[34] F. Ayres, *Differential Equations*. McGraw-Hill Book Company, 1952.

[35] M. T. Ivrlač and J. A. Nossek, "On physical limits of massive miso systems," in *WSA 2016; 20th International ITG Workshop on Smart Antennas*, March 2016, pp. 1–7.

[36] C. Findeklee, "Array Noise Matching; Generalization, Proof and Analogy to Power Matching," *Antennas and Propagation, IEEE Transactions on*, vol. 59, no. 2, pp. 452–459, 2011.

[37] A. van der Ziel and J. W. Ero, "Small-signal, high-frequency theory of field-effect transistors," *Electron Devices, IEEE Transactions on*, vol. 11, no. 4, pp. 128–135, 1964.

[38] W. Bruncke and A. van der Ziel, "Thermal noise in junction-gate field-effect transistors," *Electron Devices, IEEE Transactions on*, vol. 13, no. 3, pp. 323–329, 1966.

[39] M. B. Das, "FET noise sources and their effects on amplifier performance at low frequencies," *IEEE Transactions on Electron Devices*, vol. 19, no. 3, pp. 338–348, Mar. 1972.

[40] A. Podell, "A functional GaAs FET noise model," *Electron Devices, IEEE Transactions on*, vol. 28, no. 5, pp. 511–517, 1981.

[41] F. Steiner, A. Mezghani, and J. Nossek, "Information theoretic analysis of concurrent information transfer and power gain," in *Circuits and Systems (ISCAS), 2012 IEEE International Symposium on*, May 2012, pp. 548–551.

[42] M. Ivrlač and J. Nossek, "Toward a circuit theory of communication," *Circuits and Systems I: Regular Papers, IEEE Transactions on*, vol. 57, no. 7, pp. 1663–1683, 2010.

[43] M. Ivrlač, B. Lehmeyer, J. Nossek, C. Hofmann, and B. Lankl, "Estimation of noise parameters in multi- antenna receivers using digitized samples," in *WSA 2013 - 17th International ITG Workshop on Smart Antennas*, 2013.

[44] H. Nyquist, "Thermal Agitation of Electric Charge in Conductor," *Physics Review*, vol. 32, pp. 110–113, 1928.

[45] H. T. Friis, "Noise figure of radio receivers," *Proc. IRE*, vol. 32, pp. 419–422, jul 1944.

[46] H. Rothe and W. Dahlke, "Theory of Noisy Fourpoles," *Proceedings of the IRE*, vol. 44, no. 6, pp. 811–818, June 1956.

[47] W. M. Leach, "Fundamentals of low-noise analog circuit design," *Proceedings of the IEEE*, vol. 82, no. 10, pp. 1515–1538, Oct 1994.

[48] M. Pospieszalski, "Interpreting Transistor Noise," *Microwave Magazine, IEEE*, vol. 11, no. 6, pp. 61–69, Oct 2010.

[49] M. T. Ivrlač and J. A. Nossek, "Toward a Circuit Theory of Communication," *IEEE Transactions on Circuits and Systems I: Regular Papers*, vol. 57(7), pp. 1663–1683, 2010.

[50] B. Lehmeyer, M. T. Ivrlač, A. Mezghani, J. A. Nossek, and B. Lankl, "On Matching Strategies for Wireless Receivers," in *Smart Antennas (WSA), 2014 18th International ITG Workshop on*, March 2014, pp. 1–6.

[51] I. S. 7.9, "IRE Standards on Methods of Measuring Noise in Linear Twoports, 1959," *Proceedings of the IRE*, vol. 48, no. 1, pp. 60–68, Jan 1960.

[52] H. Haus, W. Atkinson, G. Branch, W. Davenport, W. Fonger, W. Harris, S. Harrison, W. McLeod, E. Stodola, and T. Talpey, "Representation of Noise in Linear Twoports," *Proceedings of the IRE*, vol. 48, no. 1, pp. 69–74, Jan 1960.

[53] C. Motchenbacher and J. Connelly, *Low-Noise Electronic System Design*. New York: Wiley, 1993.

[54] H. Gao, K. Ying, M. K. Matters-Kammerer, P. Harpe, Q. Ma, A. van Roermund, and P. Baltus, "A 48-61 GHz LNA in 40-nm CMOS with 3.6 dB minimum NF employing a metal slotting method," in *2016 IEEE Radio Frequency Integrated Circuits Symposium (RFIC)*, May 2016, pp. 154–157.

[55] R. Cleriti, S. Colangeli, W. Ciccognani, M. Palomba, and E. Limiti, "Cold-source cryogenic characterization and modeling of a mHEMT process," in *Microwave Integrated Circuits Conference (EuMIC), 2015 10th European*, Sept 2015, pp. 41–44.

[56] J. Lange, "Noise Characterization of Linear Twoports in Terms of Invariant Parameters," *Solid-State Circuits, IEEE Journal of*, vol. 2, no. 2, pp. 37–40, Jun 1967.

[57] H. Nyquist, "Thermal Agitation of Electric Charge in Conductor," *Physics Review*, vol. 32, pp. 110–113, 1928.

[58] M. T. Ivrlač, B. Lehmeyer, J. A. Nossek, C. A. Hofmann, and B. Lankl, "Estimation of noise parameters in multi-antenna receivers using digitized signal samples," in *Smart Antennas (WSA), 2013 17th International ITG Workshop on*, March 2013, pp. 1–6.

List of Figures

List of Tables

Glossary

Term	Description	Units
	admittance	
α	DMN admittance	S
$\boldsymbol{Y}_{\mathrm{A}}$	antenna admittance matrix	S
β	DMN admittance	S
$\boldsymbol{\Phi}$	diagonal termination matrix	S^2
$\boldsymbol{Y}_{\mathrm{M}}$	DMN admittance matrix	S
Y_{opt}	optimum admittance	S
$\boldsymbol{Y}_{\mathrm{Ql}}$	lossy decoupler admittance matrix	S
$\boldsymbol{Y}_{\mathrm{Q}}$	ideal decoupler admittance matrix	S
Y_{s}	source admittance	S
$\boldsymbol{Y}$	admittance matrix	S
Y	admittance	S
	area	
A_j	actual diode area	m^2
	Butler	
$\boldsymbol{w}$	Butler coefficient	
$\boldsymbol{W}$	Butler matrix	
	capacitance	
C_{c}	antenna coupling capacitance	F
C_{e}	input shunt capacitance	F
C	capacitance	F
	conductance	
a	conductance	S
b	conductance	S
γ	conductance	S
G	conductance	S
G_{opt}	optimum conductance	S
G_{s}	source conductance	S
ξ	conductance	S
S	conductance	S
	constants	
β_{d}	triangle phase constant	$\frac{\mathrm{rad}}{\mathrm{m}}$
β_{p}	phase constant	$\frac{\mathrm{rad}}{\mathrm{m}}$

Term	Description	Units
β_s	star phase constant	$\frac{\mathrm{rad}}{\mathrm{m}}$
	correlation	
ρ_t	true correlation coefficient	
ρ	correlation coefficient	
	current	
I_0	replaced current	A
i_{L_S}	current amplitude	A
i_{AB1}	class AB transistor 1 collector current	A
i_{AB2}	class AB transistor 2 collector current	A
i_{ABR}	class AB resistor current	A
i_{ALR}	class $\mathrm{A_L}$ resistor current	A
i_{ALT}	class $\mathrm{A_L}$ transistor collector current	A
$\hat{I}$	current amplitude	A
i_{AR}	class A resistor current	A
i_{AT}	class A transistor collector current	A
$\boldsymbol{i}_\mathrm{a}$	antenna current vector	A
i_{B1}	class B transistor 1 collector current	A
i_{B2}	class B transistor 2 collector current	A
i_{BR}	class B resistor current	A
i_{CR}	class C resistor current	A
i_{CT}	class C transistor collector current	A
i_{D1}	class D transistor 1 collector current	A
i_{D2}	class D transistor 2 collector current	A
I_{DC}	DC current	A
i_{DR}	class M resistor current	A
i_{DR}	class D resistor current	A
i_d	drain current	A
i_{EC}	class E capacitor current	A
i_{ER}	class E resistor current	A
i_{ET}	class E transistor collector current	A
i_{FC}	class F resonator current	A
i_{FR}	class F resistor current	A
i_{FT}	class F transistor collector current	A
I_{load}	load current	A
i_{MC}	class M transistor collector current	A
i_{MD}	class M diode current	A
i_d	model drain current	A
I_{OP}	operating point current	A
i_R	resistor current	A
i_{sd}	schottky diode current	A
I_{max}	maximum current	A
$\boldsymbol{i}$	current vector	A
	energy	
E_{L_S}	energy stored in L_S	J
ΔE	energy difference	J

Term	Description	Units
E_{in}	input energy	J
E_{load}	load energy	J
E_{OP}	operating point energy	J
E_{r}	recovered energy	J
	frequency	
B_{w}	bandwidth	Hz
Δf	bandwidth	Hz
f	frequency	Hz
f_0	fundamental frequency	Hz
	gain	
μ_{t}	true gain factor	
μ	gain factor	
G_{p}	power gain	
A	voltage gain	
	impedance	
$\boldsymbol{G}$	noise contribution matrix	
$\boldsymbol{g}_{\mathrm{m}}$	noise contribution vector	
$\boldsymbol{g}$	real part of impedances vector	Ω
$\boldsymbol{Z}_{11}$	subimpedance matrix	Ω
$\boldsymbol{Z}_{12}$	subimpedance matrix	Ω
Z_1	impedance of 1st termination	Ω
$\boldsymbol{Z}_{21}$	subimpedance matrix	Ω
$\boldsymbol{Z}_{22}$	subimpedance matrix	Ω
Z_2	impedance of 2nd termination	Ω
Z_3	impedance of 3rd termination	Ω
Z_4	impedance of 4th termination	Ω
Z_5	impedance of 5th termination	Ω
$\hat{Z}$	absolute impedance value	Ω
$\boldsymbol{Z}_a$	antenna impedance matrix	Ω
Z_{d}	triangle line impedance	Ω
Z'_{G}	generator impedance	Ω
Z_{G}	generator impedance	Ω
$\boldsymbol{Z}_{\mathrm{in}}$	input impedance matrix	Ω
Z_{L}	load impedance	Ω
Z_{m}	m-th termination impedance	Ω
Z_{NM}	impedance for noise matching	Ω
$\boldsymbol{Z}_{\mathrm{opt}}$	optimum impedance matrix	Ω
Z_{PM}	impedance for power matching	Ω
Z_0	reference impedance	Ω
Z_{ss}	strip line impedance	Ω
Z_{s}	star line impedance	Ω
Z_m	impedance of m-th termination	Ω
	inductance	
L_{S}	inductance supply	H
H	inductance	H

Term	Description	Units
	length	m
l	length	m
l_s	star side length	m
l_d	triangle side length	m
w	stripline width	m
	mathematical variable	
Δ_F	tolerance limit	
Δ	tolerance limit	
γ_m	matching variable	
α_g	goal variable	
κ_ssq	sine to square ratio	
κ	ratio	
λ_1	Lagrangian multiplier	
λ_2	Lagrangian multiplier	
λ_A	area scaling factor	
λ_W	width scaling factor	
l	counter	
m	counter	
m	counter	
ϕ	phase angle	
a_q	quadratic equation variable	
b_q	quadratic equation variable	
c_q	quadratic equation variable	
Q	quality factor	
ζ	goal variable	
	noise parameter	
Θ_LS	least squares noise parameter vector	
Θ	noise parameter vector	
Y_N	noise variable	
	physical constant	
e	Euler constant	2.718281828
j	imaginary unit	
$\mathrm{k_B}$	Boltzmann constant	$1.38065^{-23}\,\frac{\mathrm{J}}{\mathrm{K}}$
π	circular unit	3.14159265
	power	
P_1	noise power for 1st termination	W
P_2	noise power for 2nd termination	W
P_3	noise power for 3rd termination	W
P_4	noise power for 4th termination	W
P_5	noise power for 5th termination	W
N_c	noise power cold	W
P_h	noise power hot	W
P_m	noise power for m-th termination	W
N_X	unknown noise power	W
P_short	power value, input shorted	W

Term	Description	Units
P_{open}	power value, input open	W
$\boldsymbol{p}_{\text{c}}$	calculated noise power vector	W
$\boldsymbol{p}$	noise power vector	W
P_{x}	wrong power value	W
P_{AC}	alternating power	W
P_{B}	battery supply power	W
P_{DC}	direct power	W
$P_{\text{diss max}}$	maximum power dissipated	W
$P_{\text{diss min}}$	minimum power dissipated	W
P_{diss}	dissipated power	W
P_{in}	input power	W
P_{out}	output power dissipated	W
P_{R}	power dissipated by resistor	W
P_{T}	power dissipated by transistor	W
P	power	W
	reactance	
X_{11}	input reactance	Ω
X_{12}	transfer reactance	Ω
X_1	output reactance	Ω
X_{21}	transfer reactance	Ω
X_{22}	output reactance	Ω
X_2	output reactance	Ω
X_3	output reactance	Ω
X'_{G}	transformed generator reactance	Ω
X_{G}	generator reactance	Ω
X_{L}	load reactance	Ω
X_{m}	m-th termination reactance	Ω
	resistance	
R_0	reference resistance	Ω
R_{D}	drain resistance	Ω
R_{S}	source resistance	Ω
R_{ds}	drain source resistance	Ω
R'_{G}	transformed generator resistance	Ω
R_{G}	generator resistance	Ω
R_{n}	IRE noise resistance	Ω
R_{L}	load resistance	Ω
R_{m}	m-th termination resistance	Ω
R_{N}	noise resistance	Ω
R	resistance	Ω
	scattering parameter	
$\boldsymbol{S}_{3_{\text{dB}}}$	3 dB Hybrid scattering matrix	
$\boldsymbol{S}_{90^\circ}$	90° Hybrid scattering matrix	
$S_{i,j}$	scattering parameter	
$\boldsymbol{S}$	scattering matrix	
	signal	

Term	Description	Units
$\boldsymbol{a}$	signal vector	
$\boldsymbol{b}$	signal vector	
	susceptance	
B_{g}	susceptance	S
B_{c}	susceptance	S
B_{e}	susceptance	S
B_{s}	susceptance	S
$\boldsymbol{A}$	susceptance matrix	S
$\boldsymbol{B}$	susceptance matrix	S
$\boldsymbol{C}$	susceptance matrix	S
B_{opt}	optimum susceptance	S
B_{s}	source susceptance	S
B	susceptance	S
B_{d}	susceptance	S
	temperature	
T_0	reference temperature	K
T_{c}	cold temperature	K
T_{h}	hot temperature	K
T_{N}	noise temperature	K
T	temperature	K
	time	
T	period duration	s
t	time	s
	variance	
$\mathrm{E}[\lvert i_{\mathrm{Nt}}\rvert^2]$	true variance of noise current	A^2
$\mathrm{E}[\lvert i_{\mathrm{N}}\rvert^2]$	variance of noise current	A^2
$\mathrm{E}[\lvert v_{\mathrm{out}}\rvert^2]$	variance of output voltage	V^2
$\mathrm{E}[\lvert v_0\rvert^2]$	variance of antenna voltage	V^2
$\mathrm{E}[\lvert v_{\mathrm{Nt}}\rvert^2]$	truevariance of noise voltage	V^2
$\mathrm{E}[\lvert v_{\mathrm{N}}\rvert^2]$	variance of noise voltage	V^2
σ_{i}^2	variance of noise current	A^2
σ_{v}^2	variance of noise voltage	V^2
	voltage	
v_0'	transformed generator voltage	V
v_0	generator voltage	V
v_{L_∞}	voltage L infinity	V
v_{ABN}	class AB node N voltage	V
v_{ABR}	class AB resistor voltage	V
v_{ALN}	class $\mathrm{A_L}$ node N voltage	V
v_{ALR}	class $\mathrm{A_L}$ resistor voltage	V
$\boldsymbol{v}_{\mathrm{a}}$	antenna voltage vector	V
v_{AN}	class A node N voltage	V
v_{AR}	class A resistor voltage	V
V_{be}	base emitter voltage	V
v_{BN}	class B node N voltage	V

Term	Description	Units
v_{BR}	class B resistor voltage	V
V_{B}	battery supply voltage	V
v_{CN}	class C node N voltage	V
v_{CR}	class C resistor voltage	V
V_{dbc}	base collector breakdown voltage	V
V_{dbe}	base emitter breakdown voltage	V
v_{DN}	class D node N voltage	V
v_{DR}	class D resistor voltage	V
v_{ds}	drain source voltage	V
v_{EN}	class E node N voltage	V
v_{ER}	class E resistor voltage	V
v_{FN}	class C node N voltage	V
v_{FR}	class C resistor voltage	V
v_{gs}	gate source voltage	V
v_{in}	input voltage	V
V_{min}	minimum voltage	V
v_{MN}	class M node N voltage	V
v_{MR}	class M resistor voltage	V
V_{OP}	operating point voltage	V
V_{PP}	peak to peak voltage	V
V_{P}	peak voltage	V
v_{R}	voltage at resistor	V
v_{sig}	signal voltage	V
v_{sn}	sinus signal voltage	V
v_{sq}	square wave signal voltage	V
$\boldsymbol{v}$	voltage vector	V

AC alternating current 9

ADC analog to digital converter 10

ADS advanced design system by Keysight 66

AGC automatic gain control 118

CST Computer Simulation Technology 83

DAC digital to analog converter 10

DC direct current 4

DFT discrete fourier transform 102

DMN decupling and matching network 61

DSP digital signal processor 10

EMI electro magnetic interference 128

ENR excess noise ratio 128

FET field effect transistor 12

FT fourier transform 51

HFT chair of high frequency engineering 88

HIFI high fidelity 23

IF intermediate frequency 14

IP3 3rd order intercept point 125

IRE institute of radio engineers 132

KKT Karush Kuhn Tucker 122

LF low frequency 17

LNA low noise amplifier 106

MATLAB matrix laboratory 50

MOS-FET metall oxide field effect transistor 13

MTBF mean time between failure 117

MWS microwave studio by Computer Simulation Technology 66

NF noise figure 119

OP point of operation 13

OpAmp operational amplifier 21

PA power amplifier 10

PAE power added efficiency 57

RF radio frequency 12

RMS root mean square 118

SMA sub miniature version A 141

SMD surface mounted device 80

SNR signal to noise ratio 118

SPICE LTspice by Linear Technology 50

TUM technical university of Munich 88

VHF very high frequency 125